Optically Resonant Structures for the Enhancement of Polycrystalline PbSe Photoconductors

A Dissertation Presented to the Faculty of the Graduate School

University of Missouri-Columbia

In Partial Fulfillment of the Requirements for the Degree

Doctor of Philosophy

_____

by

Justin Stewart Grayer

Dr. Randy Curry, Dissertation Supervisor

December 2018

The undersigned, appointed by the dean of the Graduate School, have examined the dissertation entitled

Optically Resonant Structures for the Enhancement of

Polycrystalline PbSe Photoconductors

presented by Justin Stewart Grayer, a candidate for the degree of doctor of philosophy, and hereby certify that, in their opinion, it is worthy of acceptance.

_____
Dr. Randy Curry
Department of Electrical and Computer Engineering

_____
Dr. David Bryan
Department of Electrical and Computer Engineering

_____
Dr. Justin Legarsky
Department of Electrical and Computer Engineering

_____
Dr. Mark Prelas
Department of Electrical and Computer Engineering

_____
Dr. Jacob A. McFarland
Department of Mechanical and Aerospace Engineering

Dedicated to Sarah.

Acknowledgements

My journey into higher education started over 13 years ago, so there are too many people to thank for the successes and experience gained along the way here. Instead, I would like to specifically acknowledge a few major influencers and supporters. First I would like to thank my mother, Carla. You raised me, gave me the means and encouragement to support myself, and have been in my corner through this whole process. As my first teacher, you instilled in me the drive and will to pursue my dreams. Without you, this achievement would not have been possible.

I would also like to thank the teachers, instructors, and professors I have learned from throughout my academic career. I have been influenced by you all, and my academic success serves as a testament to your expertise and ability to pass on your knowledge to your students. I want to especially acknowledge Dr. Gavin King. Thank you for giving a technician the chance to learn and grow in the early years of your laboratory. The opportunities you helped provide me enabled me to gain the knowledge and experience I needed to become a better-rounded engineer.

The Professor I would like to thank most of all is my advisor, Dr. Randy Curry. Though you have only been my advisor for a short time, you have been a mentor to me for several years, and it has been a pleasure getting to know and learn from you. Thank you for expanding my scientific understanding into the realm of high power electromagnetics, and giving me the freedom to explore my own path. Most of all, thank you for agreeing to be my advisor and helping me through this process. I would also like to give my sincerest gratitude to Dr. David Bryan. Thank you for reading and

commenting on the many drafts of this dissertation. Your suggestions were invaluable in bringing this document to what it is today.

I would like to give a special thanks to my WIRED team members and collaborators for helping with film growth, fabrication, and early characterization studies of our PbSe films. I would also like to thank the DARPA MTO program office and the Air Force Reasearch Laboratory (AFRL) for your valuable suggestions and insight during this investigation.

The most important person to acknowledge and give my most sincere gratitude would be my friend, my rock, my wife, Sarah. You have been there since the beginning, and have stayed on this journey with me over the years. This process has been long, and at times challenging. Yet, you have encouraged me, built me up, and bolstered my resolve when I needed it. Thank you for all that you've done, all that you do, and all that you are.

Contents

Figures

Tables

Abstract

The mid-wave infrared (MWIR) regime of the electromagnetic spectrum is attractive for long-range imaging systems due to the atmospheric window between 3 and 5 μm. Due to ambient thermal background, it is often necessary to operate sensor systems below room temperature to achieve an adequate signal-to-noise ratio (SNR). This cooling requirement adds size, weight, and complexity to systems in which these parameters are at a premium. In this work I investigated two methods for optically enhancing the absorptive properties of lead selenide (PbSe) photoconductive films to increase the operating temperature up to 290 K, thereby mitigating system cooling requirements. By employing surface plasmon resonant (SPR) and embedded reflective structures, we were able to demonstrate enhanced responsivity and raise the operating temperature to room-temperature. Sensitivity was observed to increase by a factor of three for SPR enhanced detectors, and up to two-times at room temperature in detectors with an embedded Pt back reflector. Moreover, PbSe detectors with SPR discs operating at room temperature were observed to have responsivity comparable to reference detectors at 230 K. Photoconductors with the embedded Pt back reflector had a performance at room temperature that was similar to the reference detector at 250 K. Herein, I discuss my design process, as well as the fabrication of these resonant structures. Also discussed are the measurement and test results I obtained from surface plasmon and embedded reflector enhanced PbSe detectors. In this dissertation, I present results that demonstrate the viability of SPR and interference structures as mechanisms for increasing the operating temperature of PbSe MWIR photodetectors up to 290 K.

Chapter 1: Introduction

1.1 Introduction of Lead Selenide

Materials like mercury cadmium telluride (HgCdTe), indium antimonide (InSb), and lead selenide (PbSe) are often employed as mid-infrared (MWIR) materials [1-4, 16-19]. Due to the large amount of ambient thermal background between 3 µm and 5 µm of the electromagnetic spectrum, MWIR detector materials are typically operated at cryogenic temperatures to minimize noise. This cooling requirement adds cost and complexity to a detector subsystem. For instance, HgCdTe and InSb operate at 77 K, which requires an integrated cryocooler adding size, weight, and power draw to the system. Further, the cost of the cryocooler system can often times be a significant fraction of the total cost of the system, including a decrease in reliability and lower lifetime. In these detector materials performance is prioritized over system cost and complexity, limiting their use and utility to research and defense applications. However, there is now a new focus in military, commercial, and consumer industries for near-room temperature, high sensitivity IR detector technology. As an alternative to HgCdTe and InSb, PbSe-based detectors can serve to mitigate the stringent cooling requirement.

Polycrystalline PbSe is a IV-VI material typically employed for MWIR detectors. PbSe is grown using well-established chemical bath deposition techniques, and photodetectors based on PbSe operate at temperatures between 230 K and 250 K for adequate signal-to-noise performance [5-9, 11, 13, 14-16]. Sensitivity is an important figure of merit when discussing infrared detectors. The specific detectivity D*, a measure of detector sensitivity, of PbSe based detectors has been reported to be as high as 4 ×

10^{10} $cm\sqrt{Hz}/W$ at 230 K [14, 15], making its near room temperature performance comparable to other detector materials, such as InSb [16], at cryogenic temperatures. Specific detectivity, with units of $cm \cdot \sqrt{Hz}/W$ or Jones, for a detector material is given by equation 1.1,

$$D^* = \frac{\sqrt{A_d \Delta f} \, \eta_e q}{V_n h\nu} = \frac{\sqrt{A_d \Delta f} \, \Re(h\nu)}{V_n} \tag{1.1}$$

where A_d is the area of the detector in cm^2, Δf is the bandwidth in Hz, η_e is the external quantum efficiency, q is the electric charge constant (1.602×10^{19} C), V_n is the measured noise typically given in units of current or voltage depending on the type of measurement, and $h\nu$ is the energy of the photons in joules incident on the detector [3, 16]. The variable $\Re(h\nu)$ in equation 1.1 is the energy dependent responsivity, which can also be used as a standalone figure of merit for detector sensitivity. This quantity has been utilized as one of the major figures of merit during this investigation.

In an alternative treatment proposed by Phillips, D* can be related to the carrier density n_{th} in cm^{-3}, the absorption coefficient α in cm^{-1}, and carrier lifetime τ given in seconds of the detector material as shown in equation 1.2 [9].

$$D^* = \frac{\eta_e q}{h\nu \sqrt{\frac{2n_{th}}{\alpha\tau}}} \tag{1.2}$$

An examination of Phillips model in equation 1.2 shows that the sensitivity of a detector material can be improved by increasing the material absorption, yet this parameter is a material dependent property which cannot be readily improved without changing the material system. As an alternative, structures based on surface plasmon resonance and thin film interference have been embedded into PbSe films to affect their

absorptive properties with the goal of increasing the operating temperature from between 230 K and 250 K up to 290 K without affecting the material composition.

Herein, I demonstrate up to three-times the sensitivity of reference detectors as a result of embedding surface plasmon resonant discs into PbSe films. Detectors utilizing a back reflector to increase the intensity of interference effects in the films showed a factor of two-times increase in responsivity over reference detectors at room temperature. Both techniques resulted in raising the operating temperature of PbSe devices to 290 K. This increased operating temperature was confirmed by observing greater responsivity in devices with surface plasmon resonant disc arrays at room temperature over that of reference PbSe detectors at 230 K. The same comparison was made for a PbSe detector with an embedded Pt reflector, and its performance was found to be comparable to the reference detector response at 250 K. In this dissertation, I demonstrate that resonant structures based on either surface plasmon resonance or interference techniques increase the MWIR sensitivity of PbSe photoconductors to levels well above the current state-of-the-art.

The details of my investigation are presented in the following order. A brief introduction to both structures is given in the remainder of this chapter. In chapter 2, the baseline characteristics of the PbSe films and reference detectors we investigated are discussed and established. In chapters 3 and 4 the theoretical background of surface plasmon resonance and thin film interference structures is provided. In chapter 5 the modeling and simulation process for selecting the parameters, as well as the predicted absorption enhancement, for resonance-enhanced PbSe films is presented. The

experimental results of this investigation are presented in chapter 6. In chapter 7, major

findings are summarized, and future enhancement schemes are briefly discussed.

1.2 Resonant Structures for Optical Management

Resonant structures for light manipulation have been used extensively for

applications such as anti-reflection coatings [24], laser cavities [25-26], and enhancement

of optical detector sensitivity [27-29]. These structures typically rely on the principle of

wave interference in which two waves that have a direct phase relationship occupy the

same space at the same time, thereby resulting in a third wave with an amplitude that can

be less than, equal to, or greater than the two incident waves [30-31]. When waves

interfere they follow the superposition principle that states if there exist solutions W_1 and

W_2 to the wave equation, described in detail in Chapter 4, then their sum (W_1+W_2) must

also be a solution to the wave equation. The degree and type of interference can be

categorized into constructive interference for additive effects, and destructive interference

for resultant waves in which the amplitude is less than the combined amplitudes of the

incident waves.

These interference phenomena can be observed and engineered from the

macroscopic to the nanoscale. Interference cavities in which the refractive index and

thickness of stacked layers are engineered to alter the transmission, reflection, or

absorption of a film or substrate are examples of a macroscopic resonant structures [32-

33]. A relatively new class of structures that take advantage of surface plasmon resonance

yields increased near-field intensity and increased scattering of the incident wave [34-35].

In this work, I investigated both the back reflector interference structure and the

plasmonic disc structure. Structures were embedded into the PbSe detector films to

increase the path length and field intensity in the PbSe layer for improved sensitivity. These structures were chosen and designed such that there would be little impact to the material composition of the PbSe film. The goal of this work was to demonstrate room temperature performance comparable to that of baseline PbSe detectors at lower temperatures. In the following sections, the plasmonic disc structure and back reflector interference structure are introduced.

1.2.1 Introduction to Surface Plasmon Resonance

To explain the losses of ballistic electrons passing through a metal, Pines and Bohm considered the quantization of coupled oscillations between free electrons in a metallic solid in 1952 [34]. Since then, this particle, which they dubbed the plasmon, has come to be known as a volume or bulk plasmon. Plasmons can be defined as coupled oscillations of free electrons in metals, as well as some dielectric materials, that can oscillate at material specific eigenfrequencies [22, 34-38].

When light interacts with a dielectric material it will do so with three primary elementary particles. The first interaction we will discuss is the exciton [12]. Consider a semiconductor medium with a bandgap energy E_g given in joules. For a photon to be absorbed by the material, its energy must be greater than that of the bandgap,

$$h\nu_{photon} = \frac{hc}{\lambda} \geq E_g \qquad (1.3)$$

where h is Planck's constant ($6.626 \times 10^{-34} Js$), ν_{photon} is the frequency of the incident photon in Hz, c is the speed of light in a vacuum ($2.998 \times 10^8 m/s$), and λ is the wavelength in µm. From equation 1.3, it is evident that there is a cutoff wavelength for the photonic response for dielectric and semiconductor materials shown in equation 1.4.

$$\lambda_{cutoff} = \frac{hc}{E_g} \tag{1.4}$$

If light at the cutoff wavelength λ_{cutoff} is absorbed by the dielectric, an electron at the top of the valence band will then be excited to the bottom of the conduction band leaving a positively charged core called a hole. This bound electron-hole pair is called an exciton, and the interaction between a photon and an exciton is called an exciton polariton [12, 20-23].

Light can also couple to frequencies caused by coupled lattice vibrations in solids that manifest as excess heat [21-22]. The elementary particles of these lattice vibrations are called phonons, and, with respect to light frequencies, are categorized as either longitudinal optical or transverse optical. The interaction between a photon and phonon is called a phonon polariton.

Finally, the third interaction, which is the focus of one of the enhancement mechanisms of this investigation, is the coupling between longitudinal density fluctuations of free electrons in a metal and a photon. Defined above, these coupled density fluctuations in a metal are called plasmons. Surface plasmon polaritons (SPP) are excitations between photons and plasmons at and near the interface between a metal and a dielectric [34-38]. When light interacts with a surface plasmon, the result is an evanescent wave that decays away from the interface in both the metal and host dielectric material. These waves can either be stationary waves (localized surface plasmon polaritons) or traveling waves (surface plasmon polaritons) depending on the effective spatial dimension of the supporting structure [39]. The energy of the light must be resonant with that of the surface plasmons to create a surface plasmon polariton.
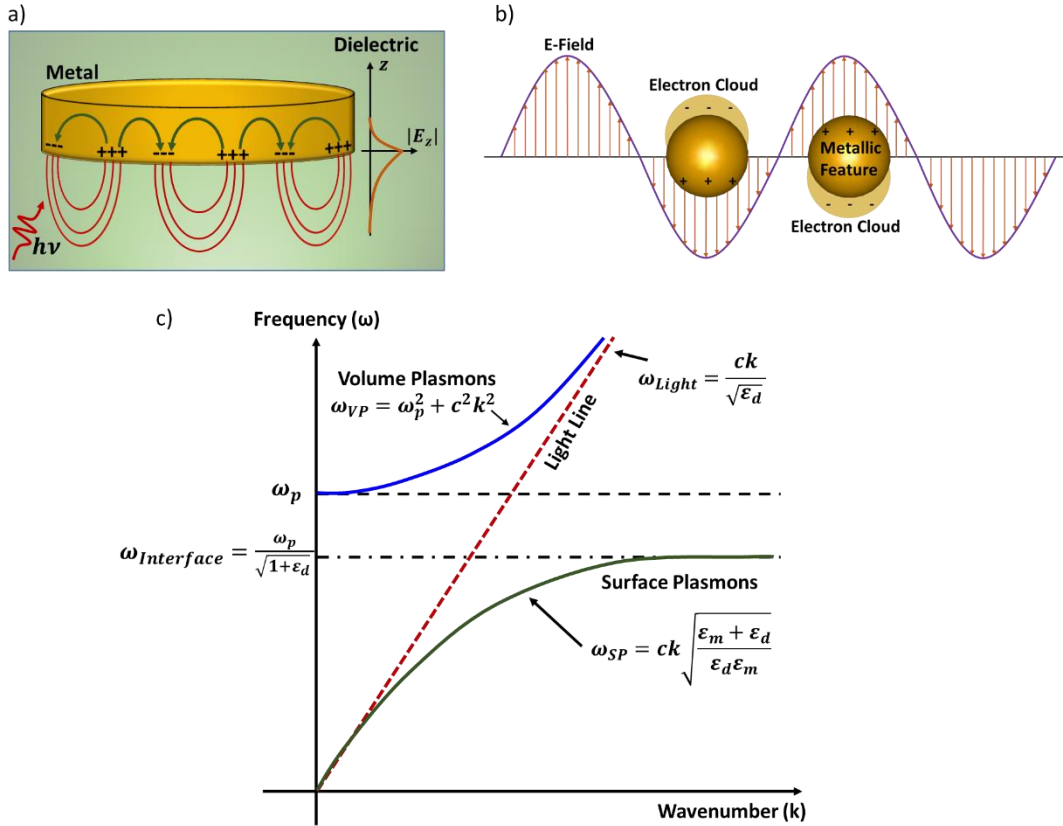
Figure 1. Depiction of a) surface plasmon polaritons at the metal/dielectric interface, b) coupled oscillations of free electrons in a metal surface feature in response to a resonant electric field, and c) surface plasmon polariton dispersion relations [34, 54].

Figure 1 contains several drawings of surface plasmon polaritons. In figure 1a surface plasmons are excited by a resonant photon generating a surface plasmon polarition, which results in an evanescent wave in both the metal and the dielectric host. Figure 1b depicts the coupled oscillations of free electrons in a metallic surface feature due to a resonant electric field. Of note are the dispersion relations shown in figure 1c. The light line (red, dashed) adheres to equation 1.5, which states the angular frequency of an incident photon is related to the wavenumber k, the speed of light c, and is reduced by the square root of the relative permittivity ε_d of the host dielectric material.

$$\omega_{Light} = \frac{ck}{\sqrt{\varepsilon_d}} \qquad (1.5)$$

The wavenumber of the surface plasmon, except for low frequencies, is always larger than that of the light line [22, 34]. The wavenumber is directly proportional to energy, therefore surface plasmons, in general, have a larger energy than the light line. Recall that energy is proportional to the square of momentum, so there must be additional momentum added to an incident photon to excite a surface plasmon. This momentum mismatch can easily be observed from the solid green trace in figure 1c, which follows the relationship of equation 1.6,

$$\omega_{SP} = kc\sqrt{\frac{\varepsilon_m+\varepsilon_d}{\varepsilon_m\varepsilon_d}} \qquad (1.6)$$

where ε_m is the relative permittivity of the metal. It is clear from equations 1.7 and 1.8 that one method to compensate for this momentum mismatch is to change the surrounding dielectric, thereby raising the wavenumber of the incident photon [40]. As a photon propagates through a host dielectric material, its wavenumber will be altered by the permittivity of the propagation medium. When it reaches the metal-dielectric interface, assuming such an interface exists, part of the wave is reflected. If the momentum of the photon meets the resonance condition, then an evanescent wave that decays away from the interface is created in both the host dielectric and metal structure [41]. In contrast, the solid blue trace above the light line represents the dispersion relations, shown in equation 1.7, of volume or bulk plasmons,

$$\omega_{VP} = \sqrt{\omega_p^2 + c^2k^2} \qquad (1.7)$$

where ω_p is the plasma frequency of the metal. Bulk plasmons are not easily excited, because their dispersion relations lie above the light line. This is due to the large energy

mismatch between typical photons of interest (visible-IR), and bulk plasmons. Consider the resonance condition given in equation 1.8,

$$\hbar\omega_p = \hbar\omega \qquad (1.8)$$

where the $\hbar$ is Planck's constant (6.626×10^{-34} Js) reduced by 2π, the left hand side is the energy of the bulk plasmon, and the right hand side is the energy of a photon. The typical energy for bulk plasmons in a metal is ~10 eV, so it would take a photon in the UV to excite volume plasmons [54]. Moreover, the photons would have to propagate into the bulk of the metal, and reflection at the surface of the metal can prohibit this propagation. Therefore, in general, the resonance condition for volume plasmons in equation 1.8 is not readily met by conventional means.

Surface plasmon resonant structures offer two primary benefits of which this study takes advantage. These include increased scattering to extend the optical path length thereby increasing the absorption, and enhanced localized field intensity to increase the absorption and number of photogenerated carriers within the sensing material [35]. Indeed, gold (Au) nanodisc arrays embedded in HgCdTe [42] and in HgSe colloidal quantum dots [43] have been reported to yield up to a five-fold multiplication in detector responsivity. The plasmonic disc structure is attractive for sensor systems due to the increase in scattering cross-section, wavelength selectivity, and large increase in near-field intensity it offers. Moreover, its simple shape can be fabricated quickly on a relatively large scale using techniques such as photolithography [38]. The surface plasmon resonant frequency red-shifts as the refractive index of the host material increases. Therefore, PbSe is an excellent candidate for infrared plasmonic structures, due to its large index of refraction (n~5) [44]. Typically, these structures are utilized in the

UV and visible where the plasma frequency of metals like Au and Ag occur [45]. However, by altering either the size, morphology, metal, or host material these resonances can be shifted to the MWIR and LWIR regimes [40, 46].

Utilizing numerical and finite element techniques, discussed in Chapter 4, I designed and tailored plasmonic disc arrays into PbSe for increased MWIR sensitivity. Described in Chapter 2, the oxide layer is typically roughened using reactive ion etching (RIE) to ensure the PbSe films adhere to the Si substrate during deposition. The typical peak-to-peak roughness after this process is 500 nm. In an effort to reduce the roughness of PbSe films, I proposed and helped develop a new process utilizing nanosphere lithography for SiO_2 roughening [38]. This new process was deemed to be a necessary step to preserve the coherence properties of surface plasmon polaritons within the PbSe films [53]. Described in Appendix A, the nanosphere roughening process lead to a factor of five decrease in the peak-to-peak roughness in PbSe films. With help from collaborators, PbSe detectors with embedded Pt disc arrays were fabricated. Described in Chapter 6, I measured the material properties and detector performance of these devices, and compared them to my previous measurements, shown in Chapter 2, on PbSe reference detectors. I observed room temperature responsivity that was a factor of three above the reference detector under the same test conditions. Moreover, the observed room temperature responsivity in the detectors with embedded Pt disc arrays was found to be greater than that of the reference detector at 230 K. Furthermore, I compared modeled and measured results to develop optimization and future enhancement strategies discussed in Chapter 7.

1.2.2 Introduction to Thin Film Interference and the Back Reflector

Interference is of particular interest in PbSe thin films, due to the presence of multiple layers with varying indices of refraction which will be described in Chapters 2 and Chapter 4. The index of refraction of PbSe was stated above without derivation. However, to understand the effects on an incident wave as it propagates through the film, it is important to understand where the index comes from, as well as how it relates to other film properties. Described in Chapter 2, the films we investigated were composed of three semiconductor layers on top of a Si substrate. These layers, in order from the bottom, are SiO_2, PbSe, and PbI_2, and each is on the order of 300 nm to 1 µm thick depending on process conditions. The substrate, by comparison, is much larger having a thickness of approximately 250-450 µm. Due to the large substrate thickness and sub-wavelength thickness of the layers, it can be assumed that the constituent parts of an incident beam of light that are reflected or transmitted have a direct phase relationship and are coherent with respect to one another [30]. Further, due to the fact that the wavelength of incident light in the infrared regime is much larger than the interatomic spacing between the atoms that make up the films the interaction of incident light with the films can be assumed to span many unit cells, allowing the use of a macroscopic treatment. The derivation of interference within thin films will be discussed in Chapter 4, however, it is important to briefly describe the benefits of incorporating an artificial structure within PbSe to enhance sensitivity.

When light propagates from a lower to a higher refractive index medium, the waves will undergo a phase shift of 180 degrees upon reflection [47]. The transmitted wave will be refracted according to Snell's law [30]. When the beam travels from a lower

index, such as air or vacuum, to a higher index, such as PbI$_2$ or PbSe, the light will bend toward the normal at the refracted angle. This refracted angle becomes the angle of incidence for the second interface, where part of the light will again be reflected and part will be transmitted.

If the refractive index of the medium immediately following the second interface is lower than that of the preceding medium, then the wave will retain its current phase upon reflection. The reflected beam will then propagate through the medium a second time, and refract bending at an angle away from the normal as it exits the film. In fact, the beam that emerges will do so at the same angle as the first reflected wave (this is also true of the incident and transmitted angle). Now, the first reflected wave, which has undergone a π phase shift, and the second reflected wave can interfere resulting in an intensity that deviates from the intensities of the original waves.

Consider the representation of the multilayer films depicted in figure 2. For now, we will only discuss those light beams that undergo normal path deviation in an ideal thin film, so the roughness of the PbSe film will be ignored. This assumption will be true for at least part of the light beam, even in rough films, as it will propagate through the film without deviation. Let the initial phase of the light as it passes from air to the PbI$_2$ layer be regarded as 0 radians. At the air-PbI$_2$ interface, part of the light will be reflected and part of the light will be transmitted. The amount of light reflected and transmitted can be calculated by using the Fresnel equation, shown in equation 1.9, to calculate the reflectance [48].

$$R = \left| \frac{n_0 - n_1}{n_0 + n_1} \right|^2 \qquad (1.9)$$
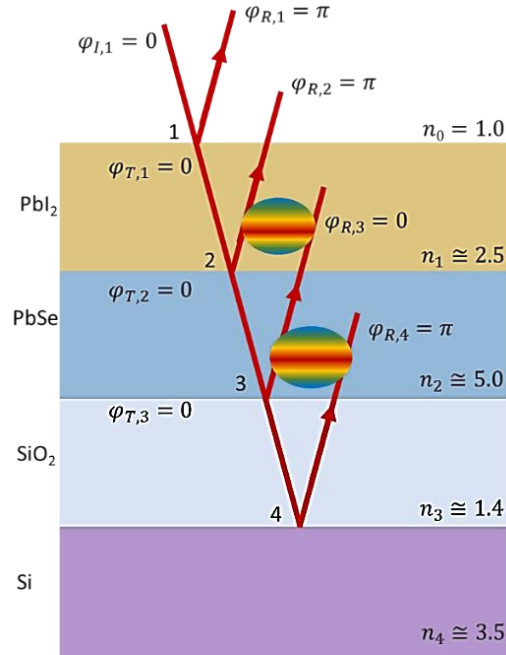
Figure 2. Interference in idealized PbSe thin films on Si substrate.

Assuming the interfaces are non-absorbing, the transmittance can be found by taking the difference between 1 and the calculated reflectance. Therefore, at the air-PbI$_2$ interface, 18% of the light will be reflected and 82% will be transmitted. Upon reflection, there will be a π radian phase shift due to PbI$_2$ having a larger refractive index than air. The transmitted beam as it approaches the PbI$_2$-PbSe interface will also undergo a phase shift upon reflection, with approximately 11% of the light being reflected from the interface. This reflected ray upon exiting the PbI$_2$ layer has the ability to constructively or destructively interfere with the first reflected ray. This pattern will repeat through the film, with the reflectances of the PbSe-SiO$_2$ interface and the SiO$_2$-Si interface being 32% and 18%, respectively. There will be another π phase shift at the Si-SiO$_2$ interface, which will interfere with the reflected ray in the PbSe layer. Further, the reflected ray in the PbI$_2$ layer can also interfere with the reflected ray from the PbSe layer. Described in detail in Chapter 4, it is clear from the Fresnel reflections and the existing phase shifts

13

that the layer thicknesses can be tuned such that a significant portion of the light has a distinct probability of interference, resulting in increased field intensity in the PbSe layer.

Figure 2 illustrates the regions in which interference can occur in baseline PbSe films. However, there are two limitations with respect to interference enhancement in baseline PbSe films. First, the layers need to be engineered to specific thicknesses to fully realize the enhancement. The chemical bath deposition process, though repeatable on the whole, has wide variation from deposition to deposition that can lead to inhomogeneity in layer thickness and composition [9, 11]. Furthermore, the sensitization process lacks the precision for optically precise tailoring of layer thickness. The second limitation is the amount of light that is available to reflect back into the film for interference. Described in chapter 2, the PbSe films investigated herein have an absorption of ~30%. The reflectance at each layer, shown in table 1, is a fraction of the light incident at each interface. Considering the absorption in PbSe and the reflectance at each interface, 23% of light would be lost to the substrate. Therefore, the resultant intensity increase from constructive interference can be weak.

Table 1. Calculated interface reflectance and reflection-induced phase shifts in investigated PbSe films.

PbSe Film Interface	Reflectance	Phase Shift
Air-PbI$_2$	18%	π
PbI$_2$-PbSe	11%	π
PbSe-SiO$_2$	32%	0
SiO$_2$-Si	18%	π

To address these shortcomings, I have explored the addition of an embedded metallic reflector, which will be referred to as a back reflector. The back reflector is attractive as a PbSe enhancement mechanism due to its ease of fabrication, wide area coverage, wavelength selectivity, and large increase in absorption and field intensity [49-

51]. The difference in the PbSe structure with the embedded metallic reflector is minimal. The metal reflector, in this case Pt, is located on top of the substrate, with the remaining layers having their same order on top of the reflector. The SiO_2 layer serves two purposes in this configuration. The first is similar to that of the baseline film in that it insulates the underlying layer from PbSe, and the second is as a dielectric spacer with which to change the thickness of the film to selectively tune the resonant enhancement [9, 52]. Stated above, approximately 23% of an incident light beam would transmitted to the substrate after the PbSe film. With a metallic reflector it is possible for all of the light that propagates through the PbSe film to be reflected back into the active layer resulting in increased intensity of constructive interference effects.

To investigate the effect of this increased interference intensity on the sensitivity of PbSe, I have designed and tailored Pt back reflector films for increased MWIR sensitivity using numerical and finite element methods. Assuming smooth films and sharp interfaces, the back reflector sets up a plane-parallel cavity within the PbSe film. However, the rough nature of these PbSe films causes light to scatter randomly as it propagates through them. This scattering can affect the optical path length within the films, and reduce the effectiveness of the cavity. The nanosphere lithography process, described in Appendix A, for roughening the SiO_2 was also used here to prepare PbSe substrates for the back reflector structure. With help from collaborators, PbSe films with an embedded Pt back reflector were deposited and fabricated into photoconductive devices. Described in Chapter 6, I measured the detector performance of these devices, and compared them to measurements I made previously on the PbSe reference detector. I observed room temperature responsivity that was a factor of two above the reference

detector under the same test conditions. Furthermore, two distinguishable peaks were

observed, and confirmed to be the result of constructive interference within the PbSe

film. I also observed the room temperature responsivity in detectors with an embedded Pt

back reflector to be comparable to the reference detector at 250 K. Modeled and

measured results were compared to develop optimization and future enhancement

strategies discussed in Chapter 7.

Chapter 1 References

[1]   J. C. Leachtenauer, and R. G. Driggers, *Surveillance and reconnaissance imaging systems: Modeling and Performance Prediction*. Norwood, MA: Artech House, Inc, 2004.

[2]   Spectral Sciences, Inc. [online] Available: http://modtran.spectral.com/modtran_home#plot. [Accessed Sept. 11, 2018]

[3]   K. Kasunic, *Optical Systems Engineering*. McGraw-Hill Education, 2011.

[4]   C. J. Willers, *Electro-Optical Systems Analysis and Design*, Bellingham, WA: SPIE Press, 2013.

[5]   D. A. Kondas, "Introduction to Lead Salt Infrared Detectors," Technical Report ARFSD-TR-92024, US Army Armament Research, Development, and Engineering Center, 1993.

[6]   G. Vergara, et al. "Polycrystalline lead selenide: the resurgence of an old infrared detector," Opto-Electronics Review, 15(2), 110-117, 2007.

[7]   D. J. Lovell, "Development of Lead Salt Detectors." American Journal of Physics 37, 467, 1969.

[8]   Thanikaikarsan, et al. "Growth and Characterization of Lead Selenide Thin Films." J. Mater. Electron. 23, 1562-1568, 2012.

[9]   S. –S., Yoo, et al. "High Operating Temperature MWIR Photodetecotrs Development Using Polycrystalline PbSe Technology," presented at The U.S. Workshop on the Physics and Chemistry of II-VI Materials, Chicago, IL, 2017.

[10]   J. Phillips, "Evaluation of the Fundamental Properties of Quantum Dot Infrared Detectors." Journal of Applied Physics, 91 (7), 4590-4594, 2002.

[11]   M. –H., Jang, "Effect of Sensitization on PbSe IR Detector Materials Properties." Manuscript submitted to J. of Elect. Mat., 2017.

[12]   D. A. Neamen, *Semiconductor Physics and Devices: Basic Principles, 3rd Ed*, New York, NY: McGraw Hill, 2003.

[13]   J. N. Humphrey and R. I. Petritz, "Photoconductivity of Lead Selenide: Theory of the Mechanism of Sensitization." Physical Review, vol 105, no 6, 1957.

[14]   P. Kuman, et. al. "PbSe Mid-IR Photoconductive Thin Films (Part 1): Phase Analysis of the Functional Layer." Journal of Alloys and Compounds, 724, 316-326, 2017.

[15]   Lihuazhao, et al. "Understanding Sensitization Behavior of Lead Selenide Photoconductive Detectors by Charge Separation Model." Journal of Applied Physics, 115, 084502, 2014.

[16]   P. R. Norton, "Photodetectors," in *McGraw-Hill's Handbook of Optics,* 3rd ed., Vol. 2, New York: McGraw-Hill, 2010, pp. 24.3-24.100.

[17]   E. Hergert, "Detectors: Guideposts on the Road to Selection," in *the Photonics Directory*, 5nd Ed. Laurin Publishing, 2006.

[18]   R. A. Smith, "Detectors for Ultraviolet, Visible, and Infrared Radiation," Applied Optics, Vol. 4, No. 6, 1965.

[19]   A. Rogalski, M. Kopytko, and P. Martyniuk, *Antimonide-based Infrared Detectors: A New Perspective*, Bellingham, WA: SPIE Press, 2018.

[20]   R. A. Serway, C. J. Moses, and C. A. Moyer, "The Solid State," in *Modern Physics*, 3rd ed, Belmont, CA: Borrks/Cole-Thomson Learning, 2005.

[21]   C. Kittel, *Introduction to Solid State Physics*, Hoboken, NJ: John Wiley and Sons, Inc. 2005.

[22]   M. P. Marder. *Condensed Matter Physics,* 2nd ed. Hoboken, NJ: John Wiley and Sons, Inc. 2010.

[23]   D. J. Lovell, "The Development of Lead Salt Detectors," American Journal of Physics, Vo. 37, No. 2, 1957.

[24]   K. Rabinovitch and A. Pagis, "Multilayer antireflection coatings: theoretical model and design parameters," Applied Optics, Vol. 14, No. 6, 1975.

[25]   W. T. Silfvast, *Laser Fundamentals*, New York, NY: Cambridge University Press, 2000.

[26]   C. C. Davis, *Lasers and Electro-Optics: Fundamentals and Engineering*, 2nd ed. New York, NY: Cambridge University Press, 2014.

[27]   K. K. Choi, et al. "Electromagnetic modeling and resonant detectors and arrays." Infrared Physics & Technology 70, 2015.

[28]   K. K. Choi, et al. "Resonant structures for infrared detection." Applied Optics, Vol. 56, No. 3, 2017.

[29]   K. K. Choi, et al. "Resonator-quantum well infrared photodetectors." Appl. Phys. Lett. 103, 201113, .2013.

[30]   E. Hecht, *Optics*, 4th ed. New York: Addison-Wesley, 2002.

[31]   R. E. Fischer, et al. *Optical Systems Design*, 2nd ed. SPIE Press, McGraw Hill, 2008.

[32] M. S. Rauscher, et al. "Dual-channel mid-infrared sensor based on tunable Fabry-Perot filters for fluid monitoring applications." Sensors and Actuators B, 259, 2018.

[33] E. Gayo and J. Frutos, "Interference filters as an enhancement tool for infrared thermography in humidity studies of building elements." Infrared Physics and Technology 38, 1997.

[34] D. Sarid and W. Callner, *Modern Introduction to Surface Plasmons: Theory, Mathematical Modeling, and Applications*. New York, NY: Cambridge University Press, 2010.

[35] J. Alda and G. Boremann. *Infrared Antennas and Resonant Structures,* Billingham, WA: SPIE Press, 2017.

[36] A. A. Toropov and T. V. Shubina, Plasmonic *Effects in Metal-Semiconductor Nanostructures*. Great Clarendon, Oxford, United Kingdom: Oxford University Press, 2015.

[37] E. Li and H. Chu, *Plasmonic Nanoelectronics and Sensing*. United Kingdom: Cambridge Press, 2014.

[38] J. Jahns and S. Helfer, *Introduction to Micro- and Nanooptics*. Hoboken, NJ: John Wiley and Sons, Inc., 2012.

[39] W. A. Murray and W.L. Barnes, "Plasmonic Materials." Adv. Mater. 19, 3771-3782, 2007.

[40] Z Jaksˇicˊ, et al. "Red Shifting Approach for Nanoplasmonic Enhancement of Semiconductor Infrared Detectors." Proc. 28th International Conference on Microelectronics, Serbia, 2012.

[41]   H. N. Daghestani and B. W. Day, "Theory and applications of Surface Plasmon
         Resonance, Resonant Mirror, Resonant Waveguide Grating, and Dual
         Polarization Interferometry Biosensors," Sensors, 10, 9630-9646, 2010.

[42]   J. Liang, et al. "Modeling of HgCdTe photoconductive infrared detector with
         metallic nanostructures." IEEE, NUSOD, 2014.

[43]   X. Tang, et al. "Plasmon resonance enhanced colloidal HgSe quantum dot
         filterless narrowband photodetectors for mid-wave infrared." J. Mater. Chem. C,
         5, 362-369, 2017.

[44]   G. Bauer and H. Krenn, "Lead Selenide (PbSe)," in Palik, E.D. Editor, Handbook
         of Optical Constants of Solids, (Vol. 1, pp. 517 – 523). San Diego, CA. United
         States: Academic Press, Inc. 1985.

[45]   A. J. Wood, "Fabrication and Characterization of a Plasmonic Grating Platform
         for Enhanced Fluorescence Biosensor Applications," PhD Thesis, University of
         Missouri, Columbia, MO, 2016.

[46]   D. W. Peters, et al. "Plasmonic Nanoantennas for Enhanced Midwave and
         Longwave Infrared Imaging," Proc. Of SPIE, Vol. 9467, 2015.

[47]   OP-Tec: National Center for Optics and Photonics Education, *Fundamental of
         Light and Lasers*, 2nd ed. Texas: Op-TEC, 2013.

[48]   Balanis, C.A. *Advanced Engineering Electrodynamics*, 2nd Edition. Wiley, 2012.

[49]   S. Jain, et al. "Broadband absorption enhancement in ultra-thin crystalline Si solar
         cells by incorporating metallic and dielectric nanostructures in a back reflector,"
         Pro. Photovolt: Res. Appl., Vol. 23, 2015.

[50]   J. Piotrowski and A. Piotrowski, "Uncooled infrared photodetectors in Poland,"
         Opto-Electron. Rev., 14, no. 1, 2006.

[51]   J. J. Talghader, A. S. Gawarikar, and P. R. Shea, "Spectral selectivity in infrared
         thermal detection," Light: Science & Applications, Vol. 1, 2012.

[52]   X. Tang, M. Ackerman, and P. Guyot-Sionnest, "Thermal Imaging with Plasmon
         Enhanced HgTe Collidal Quantum Dots Photovoltaic Devices," manuscript nn-
         2018-03871g submitted to ACS Nano, 2018.

[53]   G. A. Farias and A. A. Maradudin, "Effect of surface roughness on the attenuation
         of surface polaritons on metal films," Phys. Rev. B 27, 1983.

[54]   V. M. Shalaev, "Introduction to Metal Optics," Lecture from ECE 695 at Purdue
         University, 2006. [Online]. Available:
         https://nanohub.org/resources/1852/download/2006.10.05-ece695s-l09.pdf.
         [Accessed: Sept. 25, 2017].

Chapter 2: Lead Selenide (PbSe) as a Detector Material

PbSe has been studied extensively since WWII for military applications. German scientists were very interested in the military applications of infrared technology, pursuing with intense fervor lead-salt technology [48-49]. Research Efforts in Germany, led by Edgar W. Kutzcher, focused on lead sulfide (PbS). Kutzcher observed high SWIR sensitivity in PbS crystallites, which were capable of bolometer caliber operation. His work would lead to passive IR detectors employed by Germany during WWII for aircraft and ship detection. These detectors were a leap forward in military technology, making the invisible IR spectrum a tool to be exploited. To extend the spectral sensitivity range of PbS, which was limited to 1 µm – 3.3 µm, PbSe was investigated by German scientists leading to appreciable sensitivity at 77 K. The development of PbSe detectors opened up the IR spectrum, spanning the SWIR to MWIR and beyond, with spectral sensitivity from 1 µm - 7 µm. In parallel to German efforts, British scientists reported excellent sensitivity in PbSe; not only at cryogenic temperatures, but at room temperature with a cutoff up to 5 µm [49]. In the early 1940's, the United States in parallel started to take interest in Pb-salt based infrared technology. The National Defense Research Committee (NDRC) was formed with the express purpose of developing and understanding infrared technology. Spearheaded by Robert J Cashman, efforts were focused on PbS photoconductive cells [48]. Cashman was a pioneer in his field, developing and optimizing chemical deposition techniques for Pb-salt synthesis. He discovered that the sensitivity of PbS could be enhanced by synthesizing films in an oxygen rich atmosphere. It should be noted that this was a precursor to the current sensitization process used for Pb-salts [12].

Immediately following WWII, military interest in Pb-salts saw a decline, with research efforts being focused more on optimizing the chemical synthesis and understanding the material characteristics than on device improvement. In 1947, however, the US Navy contracted with the Eastman Kodak company to develop PbS cells as a result of their successful demonstration of long range detection of the thermal signature of the Dove missile, an air-to-air ordnance [49]. Around the same time, Henry Levinston and his graduate students at Syracuse University were investigating the photoconductive nature of PbSe and PbTe. Starting in 1948, the Naval Ordnance Laboratory (NOL) took on a decade long charge of determining the photoconductive and material nature of PbSe and PbS [48-49]. Between 1960 and 1980, new, more expensive technologies caused a decline in Pb-salt research, and, by the mid-1980s, Pb-salts had taken a back seat to compounds like InSb and HgCdTe [49-50]. As mentioned above, these materials typically offer greater infrared sensitivity at the cost of added system complexity and cryogenic operating temperatures. Seeing a resurgence in recent years, PbSe is attractive for both military and space-based applications due to its low-cost and high-temperature operation over the 3-5 µm atmospheric window.

The PbSe films discussed herein are comprised of three semiconductor layers grown on single side polished silicon (Si) substrates. First, a $0.5 - 1.5$ µm thick silicon-dioxide (SiO_2) layer is grown on top of the Si substrate by plasma enhanced chemical vapor deposition (PE-CVD). Reactive ion etching (RIE) is used to etch the SiO_2 layer to a surface roughness of approximately 500 nm peak-to-peak. This roughening step is necessary for adequate adhesion of PbSe to the substrate during deposition. A process based on chemical bath deposition methods is then used to synthesize lead acetate

trihydrate ($Pb(C_2H_3O_2)_2$) and optical grade selenourea (($H_2N)_2C=Se$) into a PbSe film with an approximate thickness of 1 μm. The PbSe films then undergo sensitization by oxidation and halogenation at 420 $^{\circ}$C and 350 $^{\circ}$C, respectively. The halogen used for sensitization for these films is iodine, thereby converting approximately half of the PbSe film into lead iodide (PbI_2) [1-2].

2.1 PbSe Crystal Structure

To begin the discussion of PbSe films, let the film during the various processes of synthesis be identified by the monikers "as-grown", "oxidized", and "sensitized". Samples of the film from various processes are shown in figure 3a. The as-grown PbSe looks grey in color, while oxidized PbSe has a blue hue. When the sensitization process leads to a uniform conversion, the PbI_2 has a slight yellow tint. If the film is over iodized then the top film will look completely yellow, and can lead to decreased sensitization. Depicted in figure 3b, the films consist of three layers on top of a Si substrate, with a total film thickness, including the SiO_2 layer, of ~ 2 μm. The films are polycrystalline in nature, so the atoms within crystallites are arranged periodically, while the areas between grains show very little order [13].
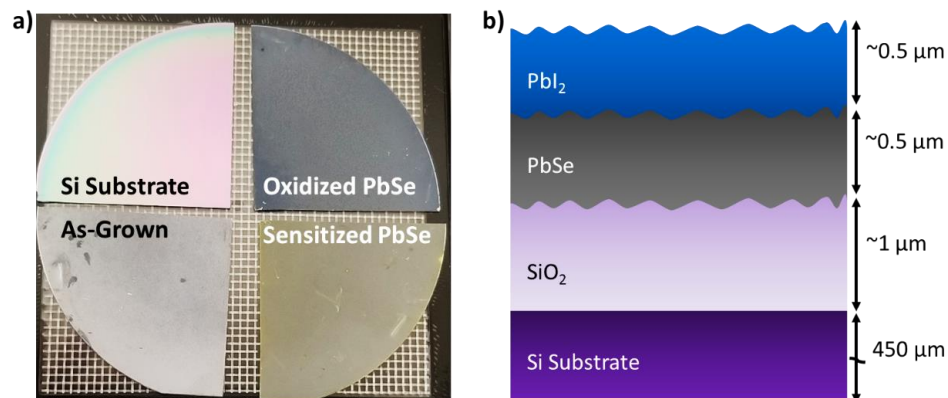
Figure 3. PbSe films grown by chemical bath deposition for this investigation; a) Shown from left to right are the Si substrate (top-left), as-grown PbSe film (bottom-left), oxidized PbSe film (top-right), and sensitized PbSe film (bottom-left); b) Depiction of sensitized PbSe film cross-section.

An energy dispersion spectroscopy (EDS) map [3] collected during our early studies of the sensitized PbSe film is shown in figure 4 [1]. The green points in the top image indicate the presence of Pb throughout the film, as expected. The other colored points represent Se (magenta), oxygen (yellow), iodine (cyan), and carbon (red). The bottom of the figure contains point clouds representing the density and location of each secondary compound. As expected, the Se and I portions are on top of each other, representing the interface between PbSe and PbI_2. This interface is semi-sharp, with gradients of each compound permeating into the opposite layer. The oxygen seen in the bottom of the film is associated with the SiO_2 layer beneath the PbSe. Oxygen is also seen throughout the film, which is where the PbSe has been converted to oxygenated-lead compounds during oxidation [2]. Interestingly, a large amount of carbon is found throughout the film. These carbon molecules play a crucial role in the PbSe sensitization process.
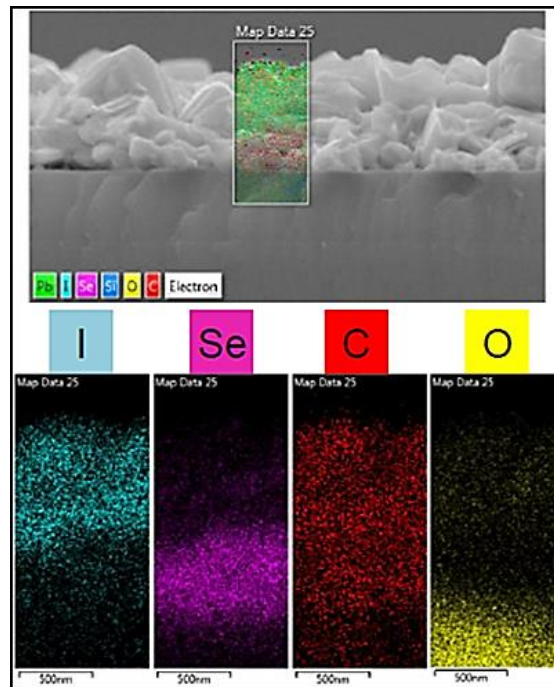
Figure 4. EDS map depicting the polycrystalline nature of, as well as the interface between, the PbSe and PbI$_2$ within the film after sensitization [1].

26

During the synthesis process, the crystal structure of PbSe thin films undergoes various changes. Jang, et al. used x-ray diffraction to show that the films start out with a polycrystalline face-centered cubic (FCC) phase, while the oxidized films show evidence of the conversion of part of the film to monoclinic or orthorhombic $PbO_2(SeO_3)$ depending on the oxidation time [2]. After iodine halogenation, the PbI_2 layer contains a polytype 12R crystal structure [4]. Figure 5 depicts the different crystalline structures contained within the films.
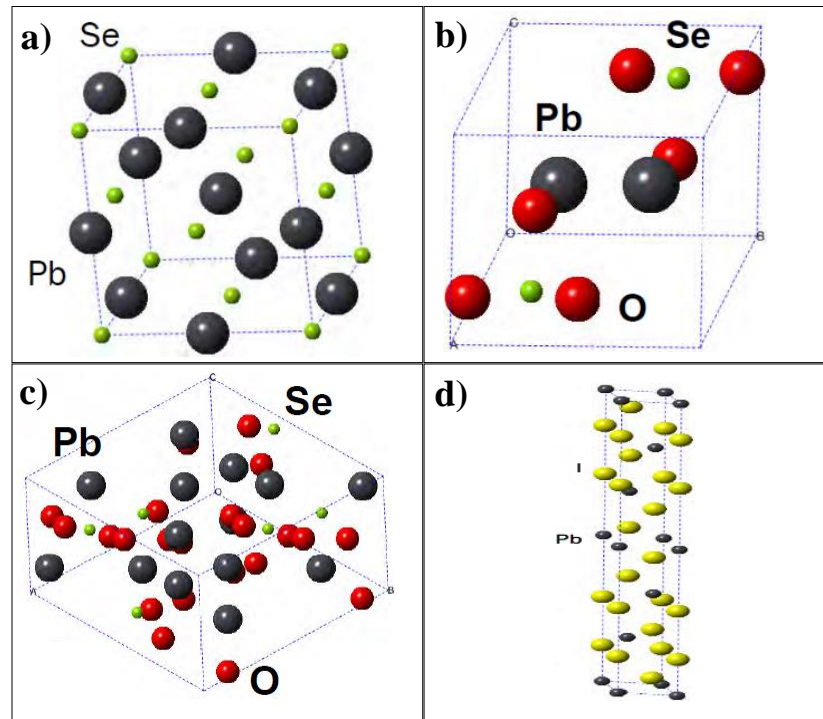
Figure 5. Depiction of crystal structure of PbSe films; a) as-grown PbSe, b) monoclinic $Pb_3O_2(SeO_3)$, c) orthorhombic $Pb_3O_2(SeO_3)$, d) polytype 12R PbI_2 [2].

We collected secondary electron images (SEI), shown in figure 6, on the oxidized and sensitized PbSe films during this investigation using scanning electron microscopy (SEM). From figure 6a, the grain size of PbSe crystallites range from ~0.3-1µm. It would seem from figure 6b that the crystallite size increases to 0.5-3µm after the sensitization step. However, as reported in [5] and [6] for similar PbSe films, the grain

size tends to decrease while the agglomeration of microcrystallites increases during the iodine sensitization process.
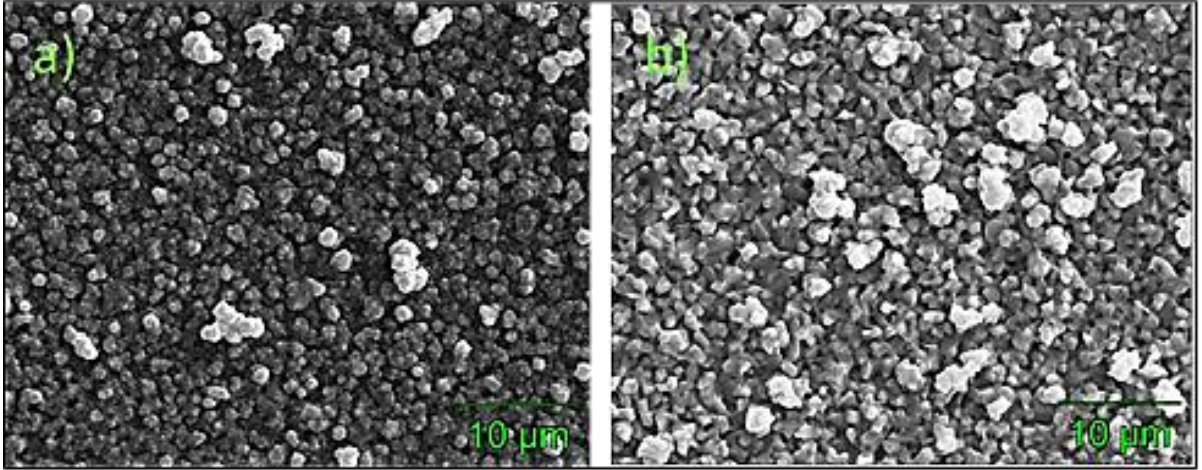
Figure 6. Secondary electron images obtained using a scanning electron microscope on the of a) oxidized, and b) sensitized PbSe films of this study. During the iodine sensitization process, crystallite size is reduced while the number and size of crystallite agglomerations increases.

High resolution transmission electron microscope (HRTEM) images were also collected by our collaborators from the same sensitized PbSe films. Figure 7a shows agglomerations larger than 500 nm, reinforcing the SEI results. Interestingly, a carbon shell is observed in figure 7b and 7c, which has an oxidation temperature-dependent thickness of 10-20 nm and surrounds both the PbSe and PbI_2 crystallites [2]. The carbon shell is formed by organic precursors in the lead acetate, which are incorporated during the deposition process. This carbon shell may contribute to photoconduction by either the barrier or charge separation models [7-8]. Carriers may move from the PbSe grains to the carbon shell, which acts as a thin conductive layer making it necessary for high sensitivity PbSe detectors.
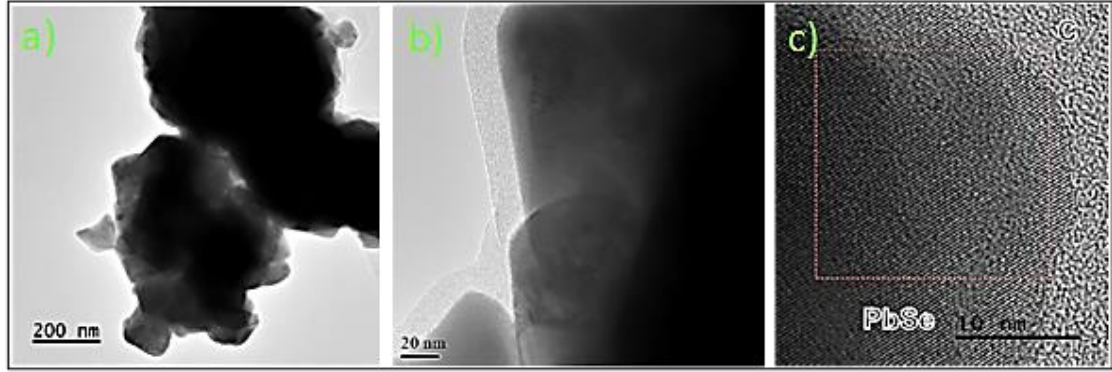
Figure 7. HRTEM images collected on sensitized PbSe films of this study. a) PbSe crystallite agglomerations after sensitization, b) carbon shell surrounding PbSe crystallite for 400 °C oxidation, and c) reduced carbon shell after 420 °C oxidation.
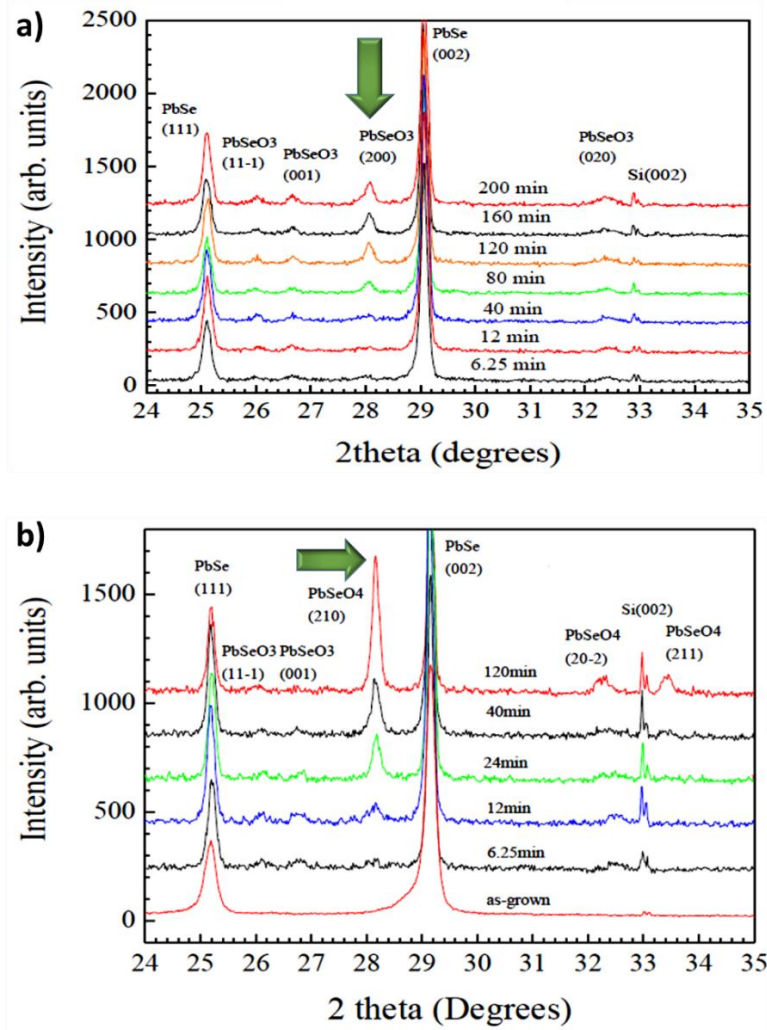
Figure 8. The XRD spectra of oxidized PbSe films as a function of time and temperature [2, 9]. When the oxidization temperature is increased from a) 400 °C to b) 460 °C, the PbSeO₃ compound is converted to PbSeO₄. Longer times can lead to over oxidation, and decreased film sensitivity.

Another function this carbon layer serves is to protect the crystallites from over oxidation during the sensitization process [2, 9]. X-ray diffraction (XRD) spectra were collected on these films by our collaborators as a function of oxidation time and temperature [2]. As the oxidation temperature increases the $PbSeO_3$ peak becomes $PbSeO_4$, and the carbon shell shrinks [2, 9]. The conversion can be seen in figure 8 when comparing samples oxidized at 400 $^\circ$C (top) and 460 $^\circ$C (bottom). It is also evident from figure 8 that the oxidation time is an important factor in determining the amount of incorporated oxygen in the film. As the time increases from 6.25-200 min, both the $PbSeO_3$ and $PbSeO_4$ peaks grow significantly. This increase in peak amplitude can have a detrimental effect on the sensitivity of the PbSe films, emphasizing the need for the optimization and control of sensitization conditions [9].

2.2 **Photoconduction in PbSe**

To first approximation, the band structure of these PbSe thin films can be found using the electron affinity rule [10]. The PbSe has a bandgap of 0.29 eV, while PbI_2 has a bandgap of 2.41 eV [7, 11]. Furthermore, shown below, PbSe is an n-type material and PbI_2 p-type [12]. PbSe and PbI_2 conduction bands are both considered to be parallel to the vacuum level. Moreover, the straddling case for heterojunctions is assumed. Using this configuration, the electron affinity, defined as the energy difference between the bottom of the conduction band and the vacuum level [12], for PbSe χ_{PbSe} is greater than that of PbI_2 χ_{PbI_2}. The electron affinity for both materials can be used to find the difference in the conduction band energies by equation 2.1.

$$\Delta E_c = e(\chi_{PbSe} - \chi_{PbI2}) \tag{2.1}$$

The valence band offset, shown in equation 2.2, can be found using the difference of the

bandgap energies and equation 2.1.

$$\Delta E_v = E_{gPbI_2} - E_{gPbSe} - \Delta E_c = \Delta E_g - \Delta E_c \qquad (2.2)$$
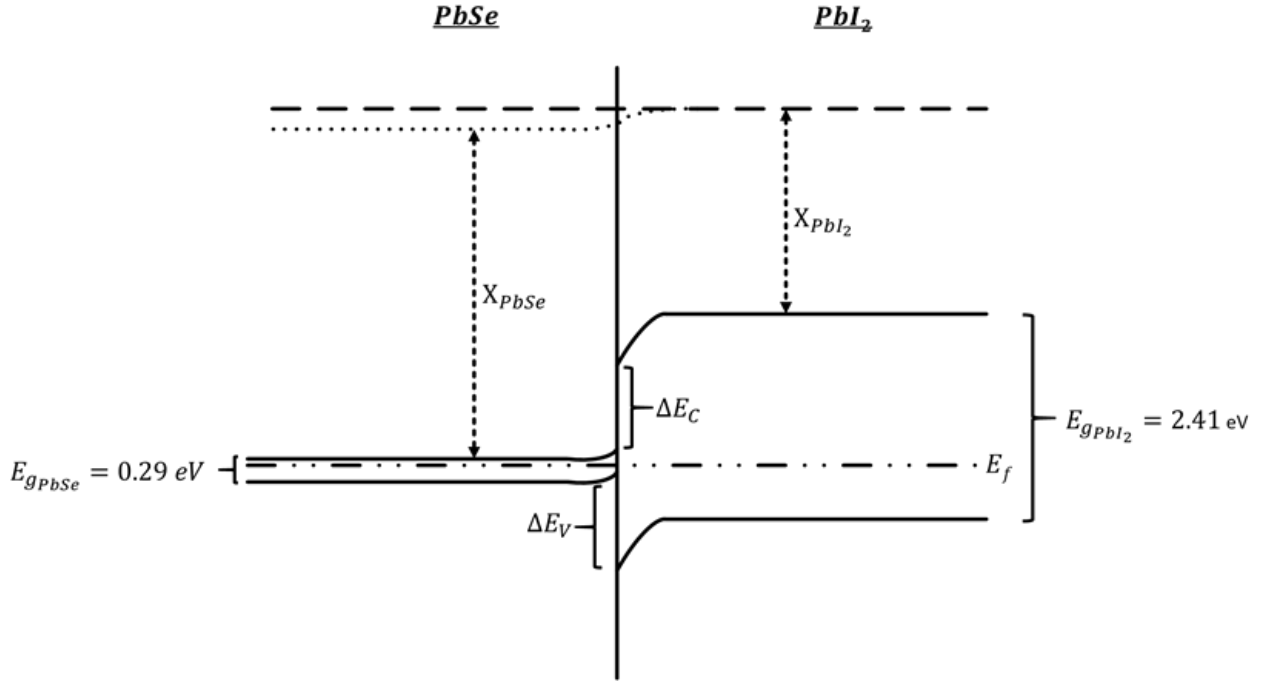
Figure 9. Qualitative band diagram sketch of PbSe photoconductive films obtained using the electron affinity rule. When PbSe and PbI₂ form an interface, the Fermi-level of the system lowers enabling increased hole flow.

When these two materials are brought together, the Fermi-levels align and

electrons from PbSe will flow into PbI₂, while at the same time holes from PbI₂ will flow

into PbSe creating a space-charge or depletion region [12-13]. Band bending occurs at the

junction, which is a result of the change in the vacuum level due to the alignment of the

Fermi-levels. Figure 9 shows the author's qualitative drawing of the band structure in

PbSe films constructed by using the band gaps of PbSe and PbI₂, as well as equations 2.1

and 2.2. It should be noted that the PbSe films that were grown for this study are

polycrystalline and porous, so the interface may not be as sharp as that depicted in figure 9. In fact, the interface observed in the EDS map of figure 4 is semi-sharp with gradients of PbSe and PbI$_2$ appearing close to the interface in the opposite layer. This band structure is important for PbSe conduction, because, as will be discussed shortly, when PbSe and PbI$_2$ meet the Fermi-level of the PbSe lowers reducing the resistance to hole flow and increasing the effectiveness of minority carrier traps [12].

We fabricated PbSe detectors to be configured as photoconductors, such that the material conductivity changes upon illumination resulting in a detectable change in current under an applied electric field [10, 13]. Even with its long history photoconduction in PbSe is still a subject of rich investigation [2, 15]. Empirical evidence, described shortly, suggests that the oxygen trap model proposed by Humphrey and Petritz is the dominant model [12].

As described above, PbSe films are grown by chemical bath deposition, and then sensitized by oxidation and halogenation. Humphrey and Petritz analyzed the properties of as-grown, oxidized, and halogenated films [12]. They found their as-grown PbSe films to be n-type, and after oxidation the films were converted to p-type. This is an important finding, because it suggests that the photocurrent generating carriers are holes [10]. Humphrey hypothesized that oxidation resulted in the incorporation of impurities, which acted as electron-traps near the PbSe conduction band. If the trap decay time is greater than the hole-to-contact transit time, then these traps decrease the probability of recombination, and therefore increase the recombination lifetime [16]. In general, equation 1.4 shows that the longer the carrier lifetime the better the performance of the

photoconductor. Halogenation lowers the Fermi-level thereby increasing the flow of holes in the valence band leading to increased photocurrent [10, 12-13].

2.2.1 PbSe Carrier Concentration, Mobility, Resistivity, and Film Type

The Hall Effect, discovered by E. H. Hall in 1879, was used to determine the type, concentration, and mobility of majority carriers within a semiconductor [10, 17]. The basic principles of the Hall Effect starts from the Lorentz force **F** in units of newtons (N) shown in equation 2.3.

$$\boldsymbol{F} = -q(\boldsymbol{E} + \boldsymbol{v} \times \boldsymbol{B}) \tag{2.3}$$

Here, q is the charge constant (1.602×10^{-19} coulombs), **E** is the electric field in V/cm, $\boldsymbol{v}$ is the velocity, in cm/s, of the charge as it moves through the electric field **B** in units of Gauss. For a Hall measurement, a current-carrying semiconductor is placed within a magnetic field with an orientation orthogonal to the current flow. Charge build up on one side of the semiconductor induces an electric field. In steady state, the force from the electric field and magnetic field balance, resulting in a Lorentz force of 0 N. The built up electric field, known as the Hall field, produces the Hall voltage V_H, shown in equation 2.4, across the semiconductor in a direction perpendicular to both the direction of current flow and the magnetic field,

$$|V_H| = Ed = \frac{iB}{qnd} \tag{2.4}$$

where E is the magnitude of the electric field in V/cm, d is the thickness of the sample in cm, i is the magnitude of the current flowing through the semiconductor in amps, B is the magnitude of the magnetic field, and n is the carrier density in units of cm^{-3}. The sign of the Hall voltage can be used to determine the majority carrier type in the semiconductor.

If V_H is negative then the semiconductor is n-type, and the semiconductor is p-type if it is positive. The V_H can be used to find the Hall coefficient R_H, which is an alternative way of determining the carrier type as described in equation 2.5.

$$R_H = \frac{-V_H d}{BI}$$

(2.5)

For p-type semiconductors R_H will be negative, and R_H will be positive for n-type [17]. Another important quantity for determining carrier dynamics in semiconductors is the resistivity ρ, defined as the product of the sheet resistance in Ω/square and the sample thickness in cm, which for our films is 1×10^{-4} cm. Shown in equation 2.6, the resistivity is needed to determine majority carrier mobility μ with units of cm^2/Vs.

$$\mu = \frac{R_H}{\rho}$$

(2.6)
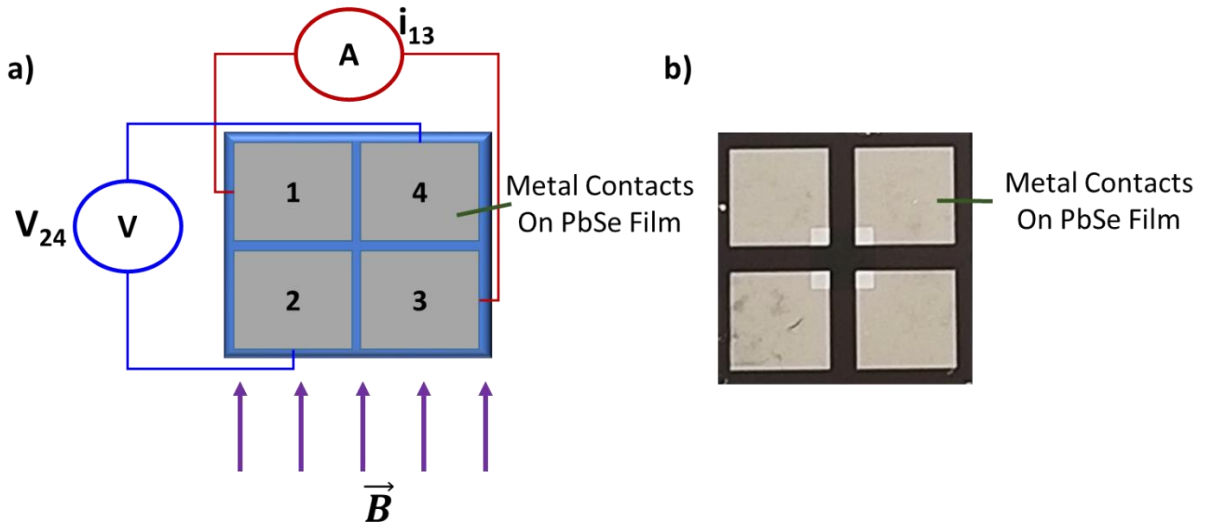
Figure 10. Van der Pauw configuration for measuring Hall parameters; b) PbSe device for Hall measurements where the metal contacts are placed in the four-corners of the PbSe film.

To determine the material properties of the investigated PbSe films, I performed temperature dependent Hall measurements. Metal contacts, in this case made of palladium (Pd), were deposited on the four corners of a 1 cm $\times$ 1 cm sensitized PbSe

device with a film thickness of 1×10^{-4} cm. The Hall measurement configuration was that of the Van der Pauw method as depicted in figure 10.

First, the current, denoted as i_{13}, is applied across terminals 1 and 3, while at the same time the voltage, denoted as V_{24}, is measured across terminals 2 and 4. Using Ohm's law, R_A is the resistance determined with i_{13} and V_{24}. Next, R_B is found in a similar fashion by applying the current across terminals 2 and 4, and measuring the voltage across terminals 1 and 3. Known as the Van der Pauw equation, equation 2.7 shows that R_A and R_B can be used to determine the sheet resistance R_S.

$$1 = e^{-\pi R_A/R_S} + e^{-\pi R_B/R_S} \qquad (2.7)$$

To determine the Hall voltage, the sample was placed within a magnetic field of 8000 Gauss, and a source meter was used to apply a current of 500 nA across terminals 1 and 3. The voltage measured across terminals 2 and 4 was the Hall voltage. The configuration was then switched and the current was applied across terminals 2 and 4, while the voltage was measured across terminals 1 and 3. The two values for the Hall voltage were compared to ensure the measurements were consistent.

Table 2. PbSe film characteristics determined by Hall measurements.

Film	Carrier Density (cm^{-3})	Carrier Mobility (cm^2/Vs)	Sheet Resistance (Ω/sq)	Resistivity (Ω-cm)	Hall Coefficient (cm^3/C)	Film Type
As-Grown	2.76×10^{18}	69.99	320	0.032	2.24	n
Oxidized	3.92×10^{17}	44.59	3570	0.357	15.92	n
Sensitized (290 K)	3.03×10^{15}	1.46	1.41×10^7	1410	-2060	p
Sensitized (270 K)	5.66×10^{14}	2.85	3.86×10^7	3860	-11000	p
Sensitized (230 K)	4.03×10^{14}	3.64	4.26×10^7	4260	-15500	p
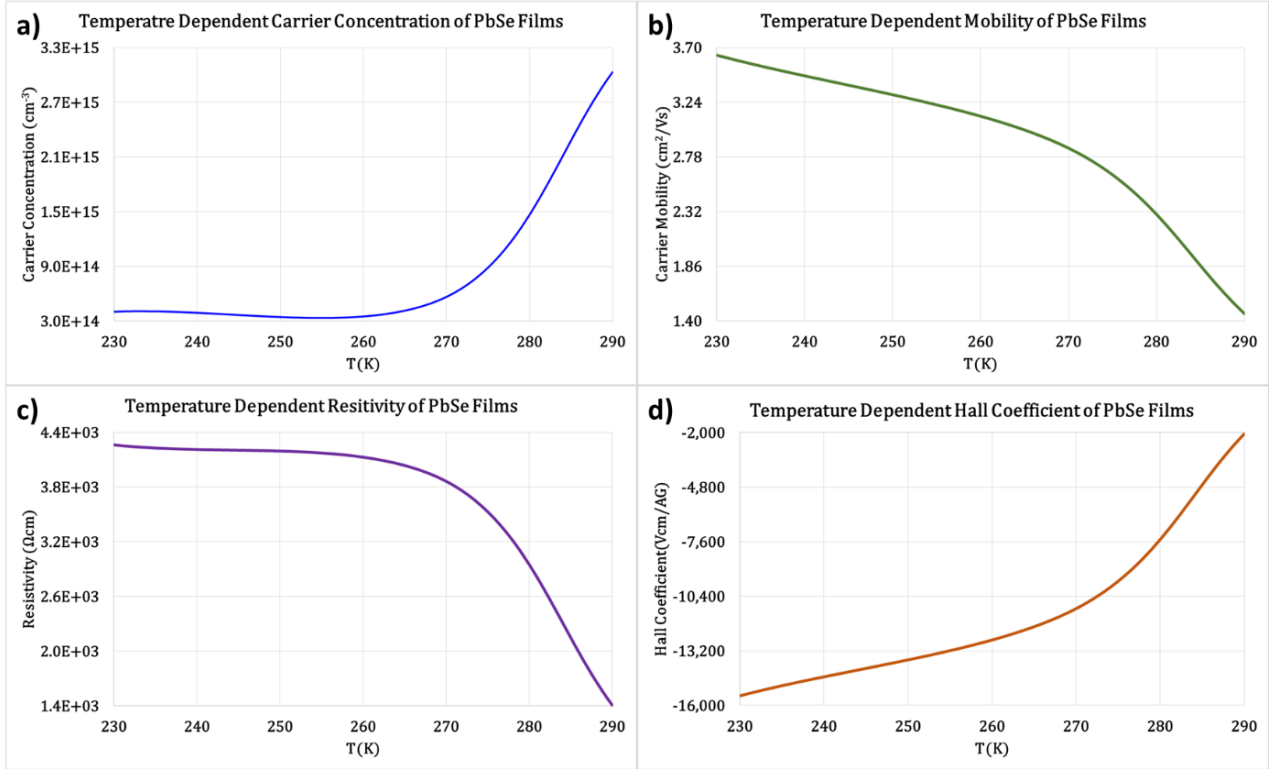
Figure 11. Temperature dependent a) carrier concentration, b) carrier mobility, c) film resistivity, and d) Hall coefficient in sensitized PbSe films. Trends indicate sensitivity increases at lower temperatures.

Table 2 contains room-temperature results we collected and analyzed from as-grown and oxidized PbSe, as well as temperature dependent data of our sensitized devices. These results seem to support the oxygen trap model proposed by Humphrey and Petritz [12]. As-grown films show an n-type carrier concentration on the order of 10^{18} cm^{-3}. After oxidation, the free-carrier concentration reduces by approximately an order of magnitude (10^{17} cm^{-3}), suggesting a trapping mechanism. Finally, after sensitization the carrier-concentration reduces by roughly two orders-of-magnitude down to ~10^{15} cm^{-3}, and the polarity switches to p-type. Moreover, the carrier mobility decreases from 70 cm^2/Vs in as-grown films to 45 cm^2/Vs in oxidized films, further supporting electron trapping by oxygen impurities. Mobility then decreases to 1.5 cm^2/Vs in sensitized films. The data presented in table 2 seems to confirm that the incorporation of PbI$_2$ results in

more effective oxygen traps, and lowers the Fermi-level of PbSe thereby increasing the flow of holes in these p-type films.

The temperature dependent results show expected behavior [10]. As the temperature decreases, the free carrier density, which is dependent on thermal energy k_bT, reduces. This leads to an increase in mobility, as well as an increase in resistance. Figure 11 shows plots of the carrier concentration, resistivity, and mobility as a function of temperature for sensitized PbSe films as presented in table 2. The carrier concentration and resistivity change linearly with a steep slope from 290 K to 275 K, approach an inflection point at 270 K, then level off as the temperature approaches 230 K. Recall from equation 1.4 in Chapter 1 that the sensitivity is inversely proportional to free carrier density. The trend in the carrier concentration and resistivity suggest that there should be similar sensitivity between 260 K and 230 K. However, the mobility shows a linear increase from 260 K down to 230 K. Photocurrent is directly proportional to carrier mobility, so as the temperature decreases sensitivity increases [18].

2.2.2 Minority Carrier Lifetime

Minority carrier lifetime is an important property for photoconductive detectors. Indeed, its importance is presented in equation 1.4 of Chapter 1 where the higher the minority carrier lifetime the higher the detector sensitivity. To determine this important material property, I measured carrier lifetime of our PbSe films using the photoconductive decay method (PCD) [19], and for comparison my collaborators utilized time resolved photoluminescence (TRPL) [20]. In the PCD method, the circuit depicted in figure 12 is used to measure the change in voltage across a load resistor over time as the PbSe detector is transversely illuminated by pulsed laser light. To ensure the

measured signal was indicative of the PbSe lifetime, the laser wavelength was selected to be greater than the absorption cutoff of PbI$_2$ [11]. The carrier lifetime is defined as the time for the excess carrier concentration n in cm^{-3}, generated from the formation of electron-hole pairs during excitation, to decay to a value of approximately 36.7% (1/e) of its initial value n$_0$,

$$n(t) = n_0 \, exp\left(-\frac{t}{\tau}\right) \tag{2.8}$$

where t is the time in seconds within a single period over which the measurement is taken. In the photoconductive decay method, n is proportional to the measured voltage V, such that

$$V(t) = V_0 \, exp\left(-\frac{t}{\tau}\right). \tag{2.9}$$

The value of the carrier lifetime τ, with units typically given as μs or ns, can be found by fitting an exponential decay curve, shown in equation 2.10, to the measured decay of the voltage.

$$y(t) = y_0 \, exp(-Ax) \tag{2.10}$$

By equating equations 2.9 and 2.10 it is evident that y$_0$ is V$_0$ and Ax is equal to t/τ from a similarity argument. Taking the natural log of both sides, and rearranging equation 2.10 results in the value of the lifetime shown in equation 2.11.

$$\tau = \frac{t}{ln\left(\frac{V_0}{V(t)}\right)} \tag{2.11}$$

Lead selenide test detectors were fabricated as described in Appendix A, with a 7 mm × 7 mm active area, and metal contacts on either side of sensitized film. Figure 13 shows the observed photoconductive decay curve. The test detector was biased using a 9

V battery, while the active area was illuminated by a model B071 pulsed laser from *Power Technology, Inc.* with a wavelength of 980 nm, pulse repetition frequency of 100 Hz, pulse width of 20 ns, and a measured average power of 1.3 mW [47]. The decay spectra was normalized to 1, and an exponential fit was used to determine the lifetime as described above.
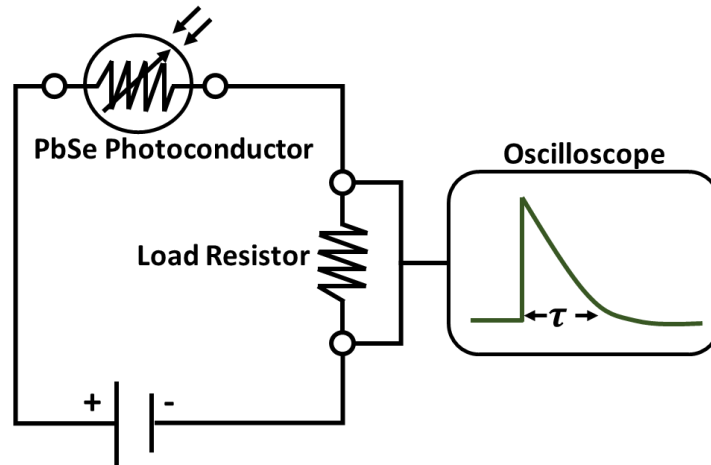
Figure 12. Bias circuit for measuring minority carrier lifetime in PbSe films.
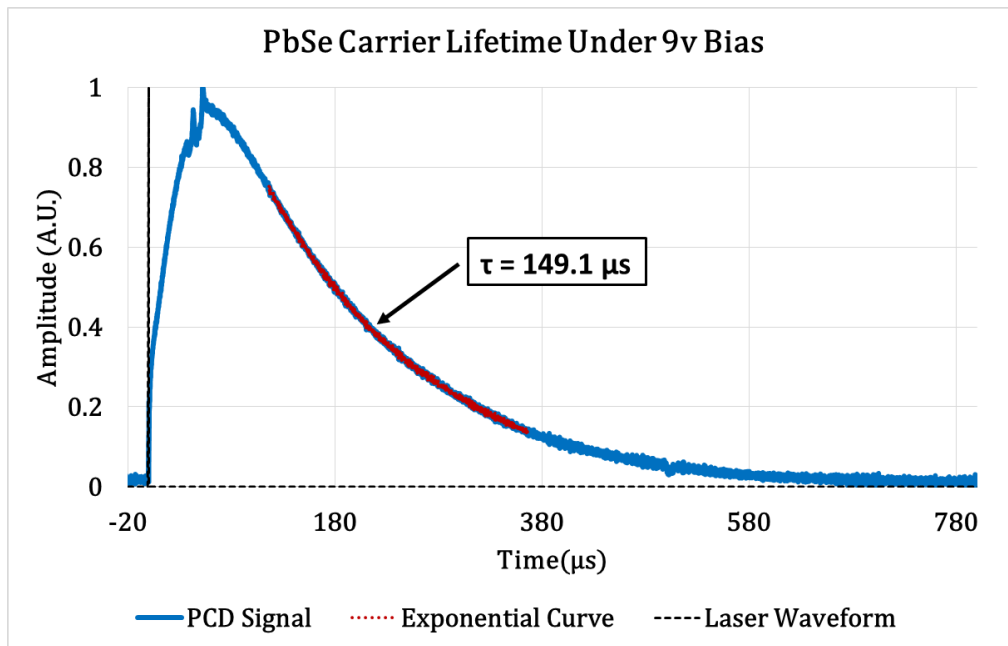
Figure 13. The room temperature PCD curve observed by transversely illuminating a PbSe test detector with pulsed laser light, and measuring the change in voltage across a load resistor connected in series. The carrier lifetime was extracted by fitting an exponential curve (red trace) to the decay data (blue trace).

For sensitized PbSe detectors, the carrier lifetime as measured by the PCD method was found to be ~149 µs. We have previously reported that the carrier lifetime of these detectors varies from 30 µs to greater than 150 µs at room temperature depending on deposition conditions and metal contacts [7]. This is quite large when compared to previously reported carrier lifetimes of 2 - 10 µs in other PbSe films [14, 12].

I verified carrier lifetime by also measuring the RC-time constant, and ensuring it was longer than the measured PCD decay time. In a configuration similar to that of the PCD method, the RC time constant was found by measuring the decay time across the load resistor as the bias circuit was pulsed using an arbitrary waveform generator (AWG) [21]. In this configuration, the sample is kept dark such that the observed signal is only due to the electrical pulse from the AWG. Figure 14 shows the configuration of an RC-time constant measurement, and figure 15 shows the RC-time constant data for the same detector under similar test conditions as figure 13.
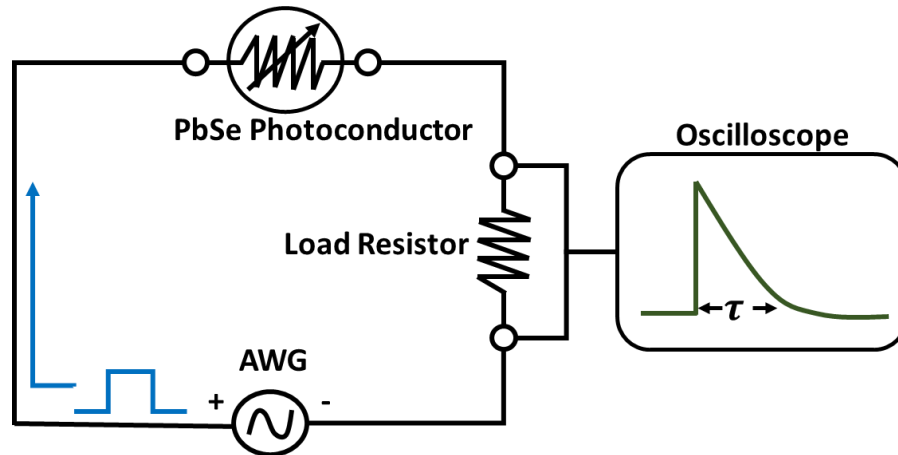
Figure 14. An RC-time constant measurement setup.
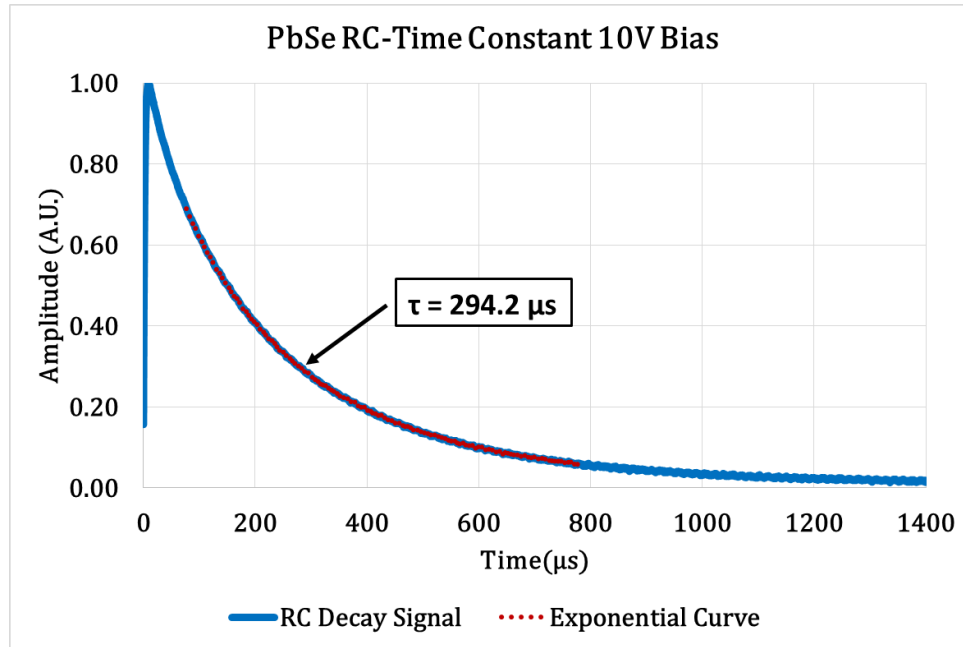
Figure 15. The RC-decay curve measured across the PbSe detector as it was pulsed by an AWG. The decay curve shows a factor of two increase over that of the PCD measurement, distinguishing the measured lifetime from the RC time constant.

The RC-time constant was calculated to be 294 µs using a 100 Hz pulse with an amplitude of 10 V to electrically excite the detector without illumination. The PCD carrier lifetime for the same detector biased from 9-25V was found to be 149-168µs. The drift velocity of holes is in the direction of the applied electric field [10, 13]. Therefore, assuming oxygen trapping is the dominant mechanism for photoconduction, when the bias is increased across the PbSe detector, the drift current increases further reducing the probability of recombination. Notice that the measured RC-time constant is only two-times greater than the measured carrier lifetime. As a final verification for the measured lifetime, the carrier lifetime found by the PCD method was subtracted from the RC-time constant yielding a difference of 145.1 µs. This difference is within 2.7% of the calculated carrier lifetime, which shows the measured PCD curve and RC-decay curve were indeed distinguished from one another, confirming the validity of the results.

Depicted in figure 16, our collaborators measured time resolved photoluminescence (TRPL) on the same PbSe devices [20]. PbSe test detectors were placed at the focus of a 100x microscope objective. A pulse signal, with pulse repetition frequency of 100 kHz, was sent from an arbitrary waveform generator (AWG) to trigger both the laser, and the start of the measurement time. The beam from a 1.064 µm laser with a pulse width of 20 ns was reflected off of a long-wavelength pass dichroic mirror into the entrance aperture of the microscope objective. The beam was focused onto the sample to excite carriers and produce photoluminescence. The photoluminescence signal, which consisted of longer wavelength light than that of the pump beam, was collected by the microscope objective and projected through the dichroic mirror onto the detector head. Similar to the PCD method, the signal decay was monitored over time and analyzed to determine the carrier lifetime. In contrast to the PCD method, the PbSe detector was not biased during this measurement.
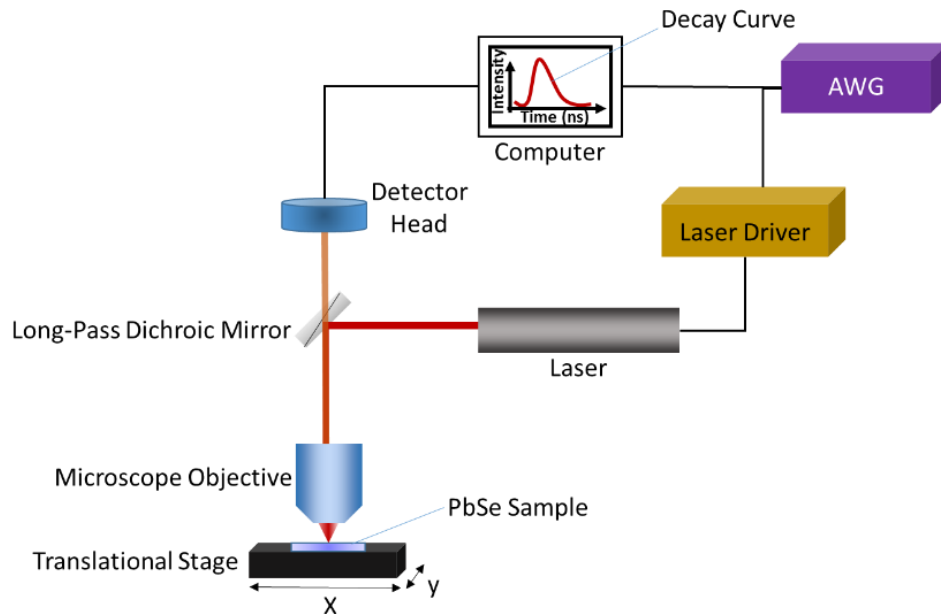
Figure 16. Time resolved photoluminescence setup for carrier lifetime measurements on PbSe test detectors.

42

The observed decay curve from TRPL measurements is shown in figure 17. The decay of the trace is not smooth like in figures 13 and 15. Therefore, the lifetime was estimated by simply finding the 1/e point after the peak of the intensity was reached. The lifetime determined by TRPL was found to be 92 ns, which is three orders-of-magnitude less than the PCD results suggested. Ahrenkiel observed the same disparity when comparing PCD and TRPL results obtained from measuring polycrystalline HgCdTe thin films [22]. The difference between the results of the two techniques can be understood, again, by carrier trapping. The TRPL measurement requires radiative recombination, and is therefore not sensitive to carrier traps. The density of states of the trap level is too low for an appreciable photoluminescence signal at room temperature [22]. However, PCD is very sensitive to carrier trapping, because it measures the decay of current carriers through the semiconductor material. Furthermore, depending on the type of metal contacts, the barrier height, and therefore the carrier lifetime, will change [7].
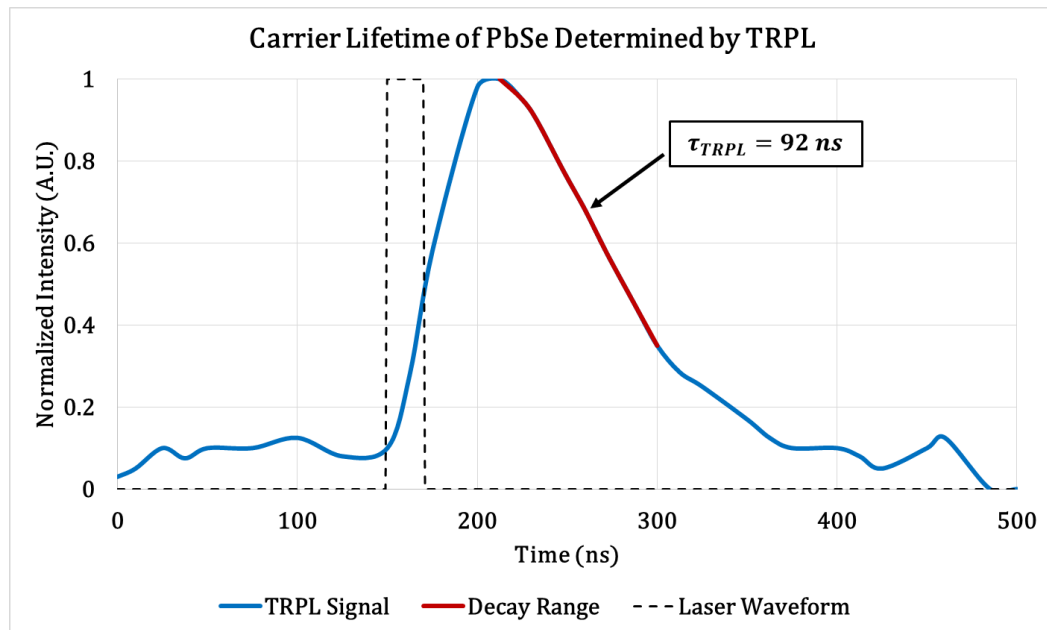
Figure 17. Observed TRPL decay curve for PbSe test detector at room temperature. Results show a three-order-of-magnitude disparity compared to those of the PCD method due to carrier trapping.

Another photoconduction model has been proposed by Kuman and Lihuazhao [15, 23]. Their charge separation model suggests that the core of the PbSe polycrystalline grains is n-type, while the surface is p-type. The p-type carriers flow in one direction in the spacing between grains, while the n-type carriers flow between the grains in the opposite direction thereby separating the charges leading to long lived carrier lifetimes and greater performance. There are, however, differences between the PbSe films on which [14] and [23] report and the films we have investigated. The largest difference between the films of this investigation and those reported in literature is the fact that the films in the literature start as p-type, and then become n-type in as-grown and sensitized samples. Furthermore, the charge separation model assumes iodine acts as a dopant to increase the number of carriers in the film. Though the charge separation model is feasible, the experimental evidence presented above seems to suggest that the films we investigated adhere more to the oxygen trap model of Humphrey and Petritz [12].
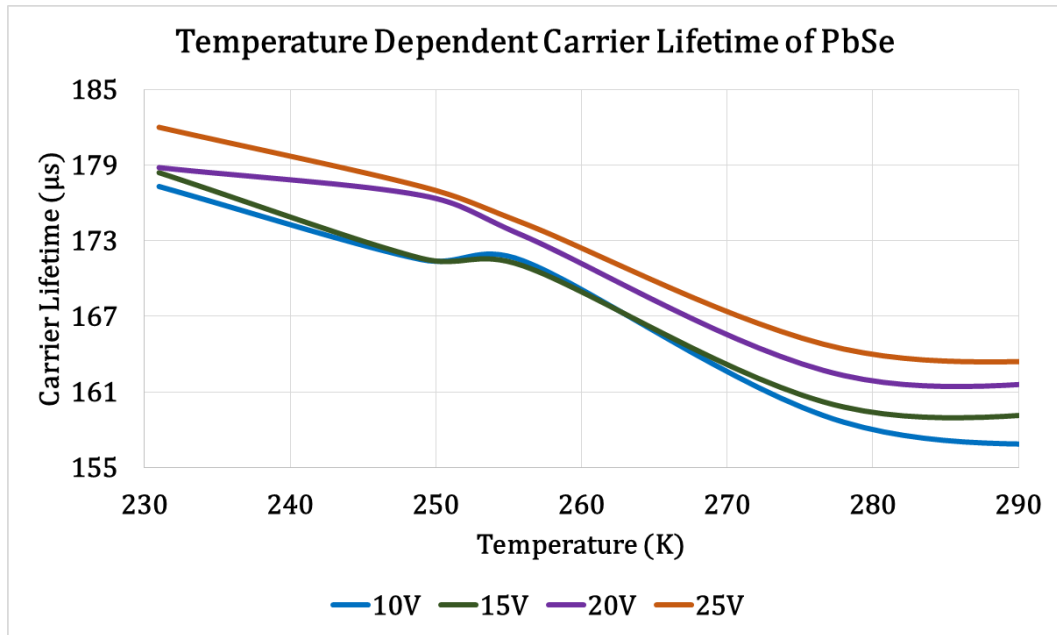
Figure 18. Observed temperature and bias dependence of the carrier lifetime of PbSe test detectors measured using the PCD method.

In addition to room temperature measurements, I also measured the temperature dependence of the carrier lifetime. Test detectors were mounted in a thermoelectric cooler (TEC) dewar assembly, and the carrier lifetime was measured at 290 K, 270 K, 250 K, and 230 K at bias levels between 10 V and 25 V. The data in figure 18 shows that for all biases, the carrier lifetime increases with decreasing temperature. This result is expected, because the excess carrier concentration should decrease as the temperature decreases due to its energy (k_bT) dependence [10, 13]. Of note is the fact that the total increase in carrier lifetime from 290 K to 230 K was only found to be 30 µs. This small increase suggests that the performance of these PbSe films at room temperature is similar to that of 230 K, and only a small enhancement is needed for comparable performance at room temperature.

2.3 Absorption in PbSe
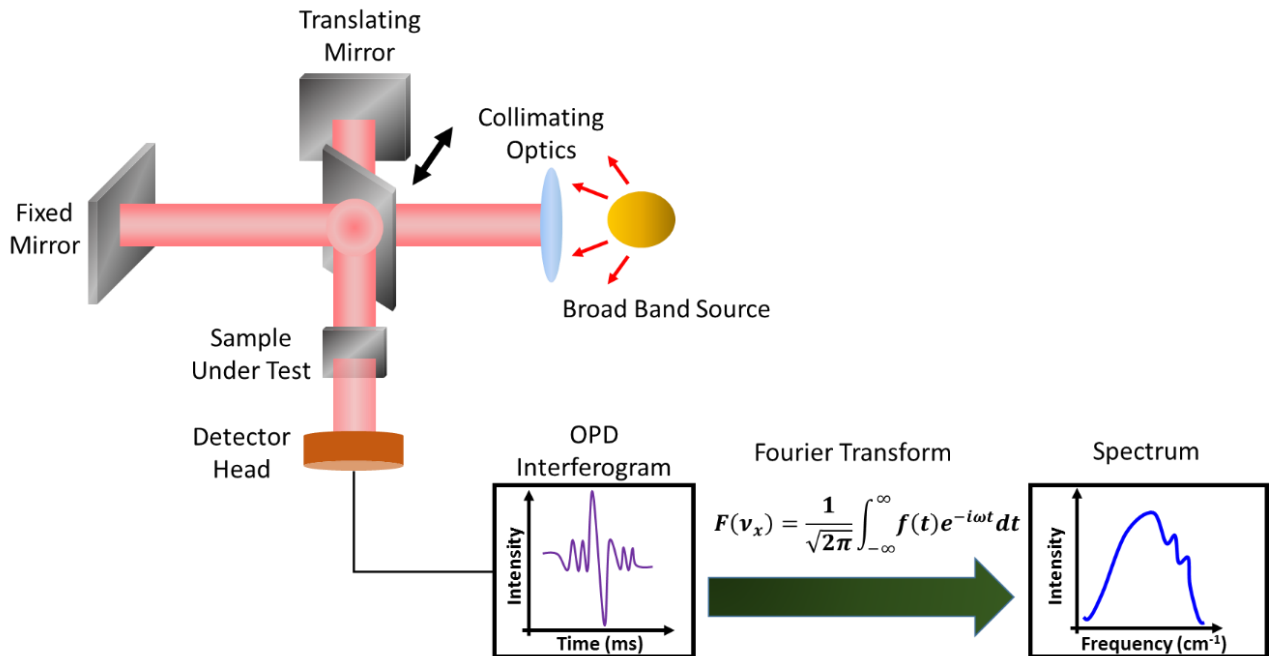
Figure 19. Depiction of FTIR measurement.

Recall that the baseline films within this study have a peak-to-peak surface roughness of 500 nm. This roughness makes it difficult to determine the absorption using methods such as Fourier transform infrared spectroscopy (FTIR). Depicted in figure 19, during an FTIR measurement, light from a blackbody emitter is transmitted through a Michelson interferometer where one leg of the interferometer is translated back and forth to modulate the signal in time creating an optical path difference between the beams of the two legs [24-25]. When using a broadband blackbody source, the resulting interferogram will contain peaks corresponding to constructive interference for the regions of zero-path difference. This interferogram is analyzed via a Fourier transform shown in equation 2.12, which relates the time spectrum $f(t)$ to the spatial frequency spectrum $F(v_x)$, to determine the spectral content, as well as intensity, of the resulting spatial frequency spectrum in units of cm^{-1}. The transmittance, reflectance, and absorbance of a sample can be determined by placing it in the optical path before the detector.

$$F(v_x) = \frac{1}{\sqrt{2\pi}} \int_{-\infty}^{\infty} f(t)e^{-i\omega t} dt \qquad (2.12)$$

Transmission spectra are relatively simple to determine, yet scattering by diffuse and rough surfaces can lead to indistinguishable spectral features [25]. Moreover, when the absorption or reflection coefficients are desired, without a priori knowledge of either the absorbance or reflectance, the quantity that can be determined with certainty is the optical density OD which includes contributions from reflection, including scattering, and absorption. The optical density is given by equation 2.13,

$$OD = -\log(T) \qquad (2.13)$$

where T is the measured transmission with a maximum value of 1. One way to circumvent this limitation and determine the absorption within thin films is to insert the sample in the middle of an integrating sphere, and sense the transmitted light output by the sphere [26]. The inside of an integrating sphere is made of a diffuse Lambertian scattering surface, which is a surface that scatters in all directions evenly resulting in a uniform output. When a sample is put within an integrating sphere, the incident light will propagate through the input port and undergo Fresnel reflections at the interfaces within the film. All of the incident light will be scattered and reflected out of the integrating sphere onto an optical detector, so the only attenuation will be from absorption within the sample material. Using this configuration, the light from an FTIR auxiliary port was focused onto the input port of an integrating sphere with a sensitized PbSe sample suspended from one of the sample ports. The output of the integrating sphere was positioned in front of a HgCdTe MWIR detector cooled to 77 K. The signal of the detector was then input to the external detector port of the FTIR for analysis.

To measure the absorption in these films, I inserted sensitized PbSe film samples into a gold integrating sphere with a spectral reflectance from 1 µm – 20 µm of greater than 95%. To ensure minimal absorption by outside sources, the sample was suspended from one of the sphere sample ports by a gold wire. Using equation 2.14, the absorption in the film was determined.

$$A = 1 - 10^{-OD} = 1 - 10^{log(T)} \qquad (2.14)$$

Figure 20 shows the absorption spectra obtained from one of our sensitized PbSe film samples. The maximum absorption above the cutoff wavelength at 4.3 µm is 35% across the 3-5 µm spectral band. The decrease in absorption around 3.2 µm and 4.3 µm is

associated with H_2O and CO_2 in the atmosphere [27-28]. Further, the increase in

absorption between 4.8 µm and 6.0 µm is associated with carbon impurities in the

underlying SiO_2 [29]. Assuming a maximum absorption of 100%, these results suggest

the theoretical maximum in-band absorption enhancement below the cutoff wavelength is

a factor of approximately 2.85. Moreover, these results also suggest the maximum

external quantum efficiency in baseline PbSe detectors without resonant structures at

room temperature is 35%. However, as will be discussed shortly, the observed quantum

efficiency in baseline PbSe detectors was much lower due to both radiative and non-

radiative carrier recombination [10].
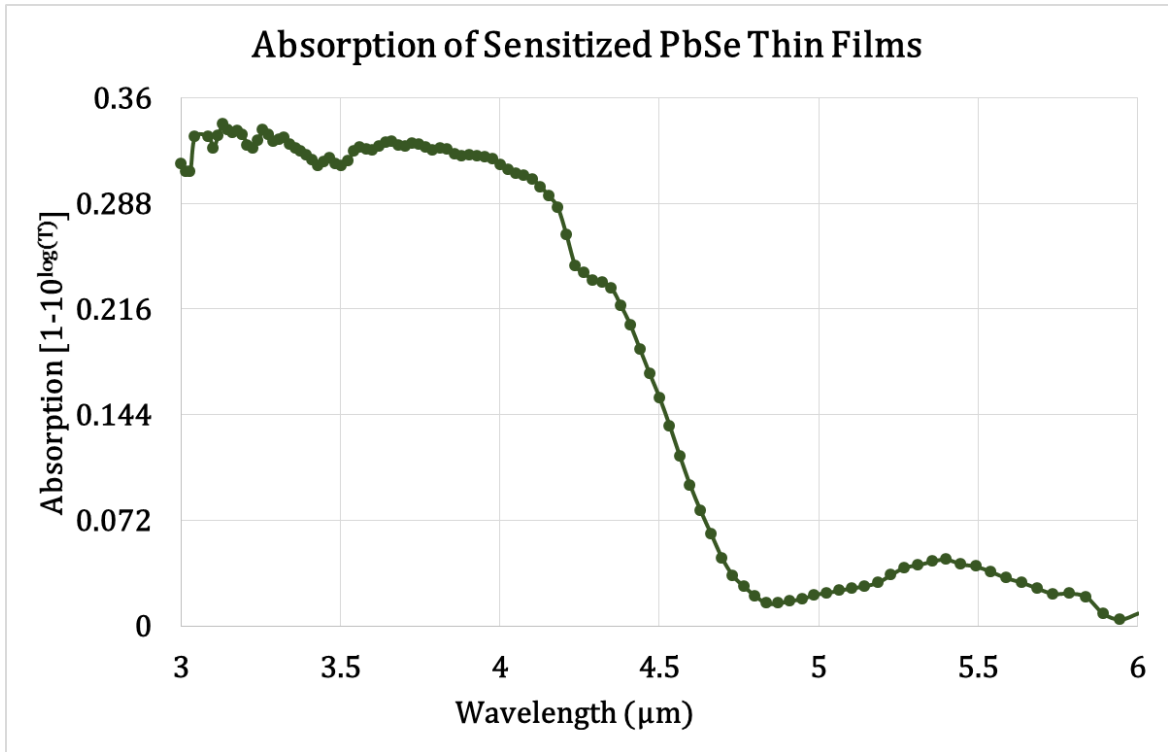
Figure 20. Absorption spectrum of investigated PbSe thin films at 290 K determined by FTIR with integrating sphere.

2.4 **Performance of Baseline PbSe Test Detectors**

An important parameter for understanding the performance of infrared photoconductors is the wavelength dependent photoresponse. I measured the spectral response of PbSe test detectors using the same bias circuit configuration as that depicted in figure 12. The output from the bias circuit was input into an *AMETEK Scientific Instruments* model 5210 lock-in amplifier, the output of which was then used as the auxiliary detector input for a *Nexus* model 870 Fourier transform infrared spectrometer. The responsivity $\Re$ was measured over a spectrum of 10000 cm^{-1} to 1800 cm^{-1} (1 µm – 5.5 µm). I calculated the FTIR source power spectral density by measuring the spectral response of a *Thor Labs* model FDPSE2X2 2 mm x 2 mm PbSe photoconductor, interpolating the response curve derived from information in the detector manual, and taking the quotient between the measured and interpolated curves [30]. The calculated source power can be seen in figure 21.
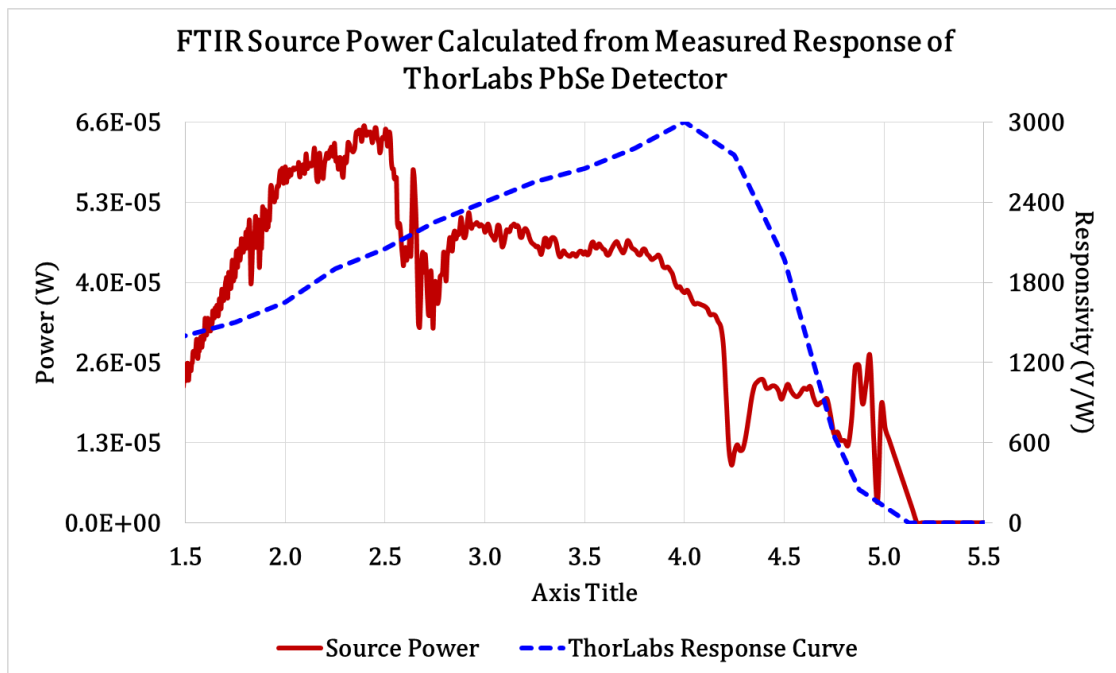
Figure 21. Reported Thor Labs responsivity (blue, dashed), and calculated FTIR source power spectrum (red, solid).
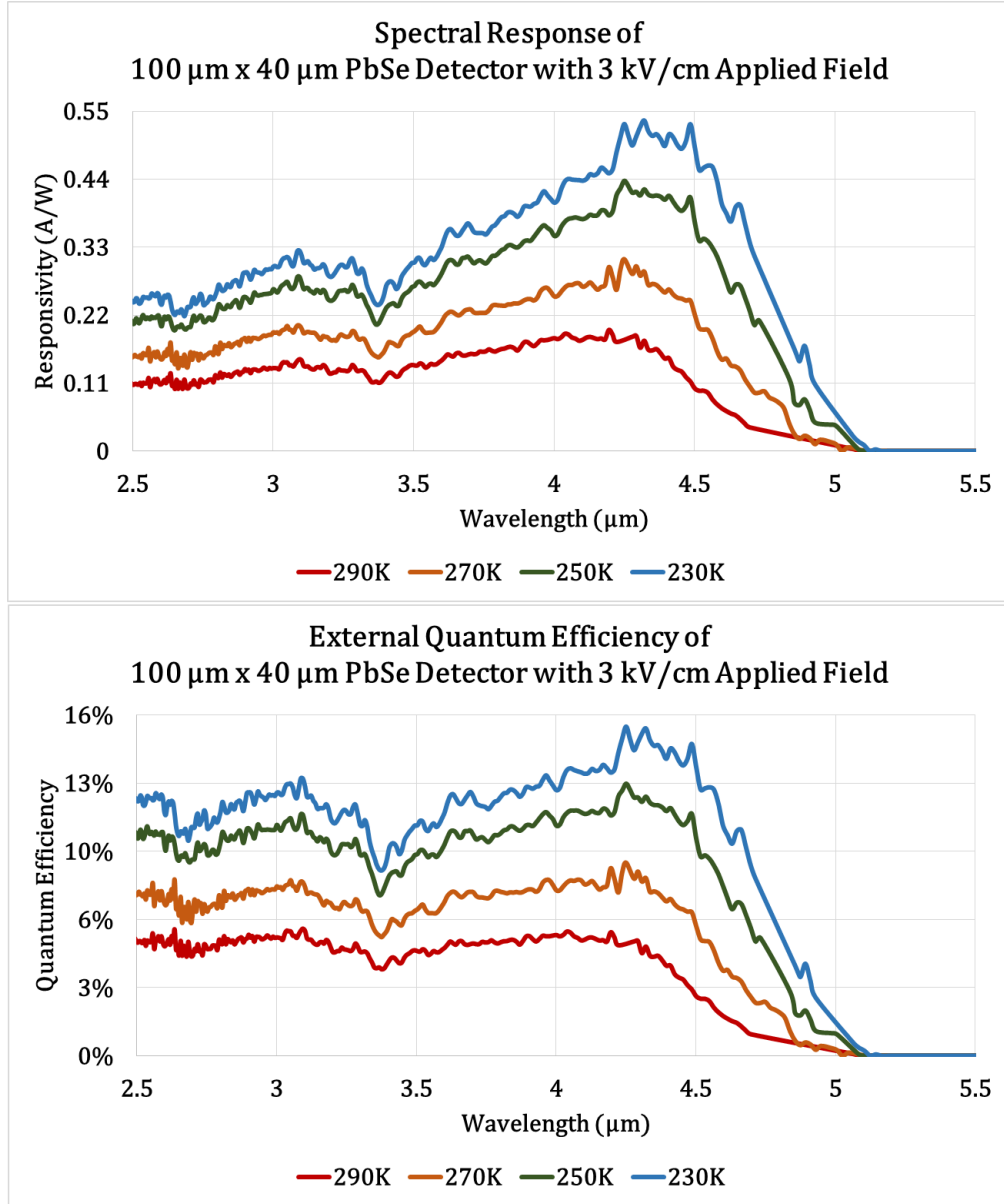
Figure 22. Measured responsivity and external quantum efficiency of a 100 μm x 40 μm PbSe test detector under an applied electric field of 3.3 kV/cm at ambient temperatures of interest.

The change in voltage across the 11 MΩ load resistor R_{load} was measured as the

PbSe test detector was illuminated, and $\mathfrak{R}$, with units of A/W, was found using equation

2.15,

$$\mathfrak{R}(\lambda) = \frac{V_m(\lambda)A_{TLPbSe}}{P_s(\lambda)R_{load}A_{PbSeTD}} \qquad (2.15)$$

where V_m is the measured voltage difference upon illumination across the load resistor R_{load} in ohms, A_{TLPbSe} is the area of the reference detector in cm^2, P_s is the calculated source power in watts, λ is the wavelength in µm, and A_{PbSeTD} is the area of the PbSe detector under test in cm^2. From the responsivity, the external quantum efficiency, defined as the ratio of the number of carriers that contribute to photocurrent to the number of incident photons, can be found by using equation 2.16.

$$\eta_e = \frac{\Re h\nu}{q} \tag{2.16}$$

Figure 22 shows the spectral response and quantum efficiency for a 100 µm x 40 µm detector under an applied field of 3 kV/cm at temperatures ranging from 290 K down to 230 K. The peak responsivity and external quantum efficiency at 4.3 µm and 230 K were found to be 0.55 A/W and 15%, respectively. Notice the decrease in response and quantum efficiency at ~3.4 µm. To be discussed in detail in Chapter 4, this drop in sensitivity is due to optical interference. These are the baseline values from which the sensitivity enhancement gained by incorporating optically resonant structures into PbSe photoconductors were measured.

2.5 **Dispersion relations of PbSe**

The dispersion relations, which define how the complex index of refraction of a material changes with the illumination wavelength, determine the behavior of electromagnetic waves as they pass through and interact with the material [31-32]. Reflection and transmission are most often associated with the real part of the complex index, whereas absorption is associated with the imaginary part. The complex index of refraction m is given by equation 2.17,

$$m = n + i\kappa \qquad\qquad (2.17)$$

where n is the real part of the index, κ is the imaginary part, and i denotes the imaginary

number $\sqrt{-1}$. Typically, ellipsometry is used to determine the optical constants of the

thin film materials [33].

Table 3. Bauer and Krenn's PbSe dispersion relations at an ambient temperature of 290 K.

Wavelength (µm)	n	k
2	4.7	0.25
2.066	4.7	0.254
2.254	4.7	0.238
2.48	4.7	0.45
2.583	4.9	0.4
2.695	4.88	0.25
2.755	4.883	0.22
2.818	4.885	0.22
2.952	4.895	0.22
3.024	4.9	0.22
3.1	4.91	0.22
3.179	4.85	0.219
3.263	4.93	0.225
3.444	4.95	0.22
3542	4.95	0.199
3647	4.96	0.194
3757	4.97	0.189
3875	4.98	0.173
4000	4.97	0.127
4275	4.95	0.0572
4428	4.94	0.0353
4592	4.94	0.00917
4769	4.94	0.00285
4959	4.92	0.00154
5166	4.9	0.00138
5391	4.83	0.00128
5636	4.86	0.0012

However this technique requires the angle of reflected light to be determinate, and random scattering from the roughness in these films makes this measurement difficult. Therefore, for PbSe, the room temperature complex index of refraction, shown in table 3, was taken from Bauer and Krenn [34].

It has been reported that the PbSe cutoff wavelength undergoes a redshift as the ambient temperature decreases [1, 7, 37]. This redshift is due to a decrease in the bandgap energy at lower temperature, which is unique to PbSe and other lead-salt materials [36-37]. To understand and estimate how the complex index of refraction of PbSe changes with temperature, I quantified the red-shift in cutoff wavelength utilizing photoluminescence (PL) spectroscopy to observe the change in bandgap with temperature.

In photoluminescence spectroscopy, a semiconductor material is illuminated by either CW or pulsed laser light. If the energy of the incident beam is greater than that of the bandgap, an electron in the valence band can absorb an incoming photon and be excited into the conduction band of a direct bandgap semiconductor [10, 13, 17]. Unless the energy of excitation is equal to that of the bandgap, the electron will be excited to an energy state above the bottom of the conduction band leaving a positively charged core or hole at the top of the valence band. The time for the electron to relax to a lower energy level, known as the metastable state, will be on the order of picoseconds [38-39]. This transition process is non-radiative, and will not result in a photon. The electron will remain in the metastable state, which in semiconductors corresponds to the bottom of the conduction band, for time periods on the order of 10s of microseconds where it becomes part of a bound electron-hole pair known as an exciton [13]. If the semiconductor

material under test is a direct bandgap material, defined as a material in which the bottom

of the conduction band and the top of the valence band are aligned in momentum space,

the electron will decay, recombine with its corresponding hole, and undergo the process

of annihilation resulting in an emitted photon with an energy that matches the energy

difference between the metastable state and the valence band [17, 39]. The

photoluminescence process is depicted in figure 23, and a depiction of the PL setup is

shown in figure 24.

Sensitized PbSe test films were mounted in a closed cycle dewar-cooler assembly,

and illuminated by a 1.064 µm neodymium-doped yttrium aluminum garnet (Nd:YAG)

laser at an incident angle of 45°. The resulting PL signal was emitted in the direction

perpendicular to the sample face, and was detected by an FTIR spectrometer. Figure 25

shows the observed spectrum at various temperatures.
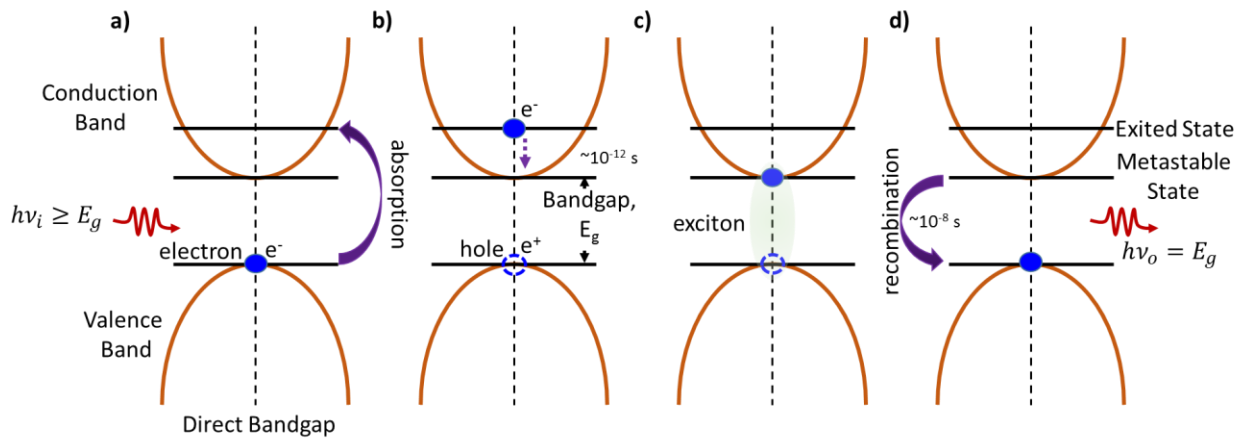
Figure 23. Graphical depiction of photoluminescence process in a direct bandgap semiconductor: a)
electrons are excited to a state above the bottom of the conduction band upon absorption of pump photons;
b) the electron undergoes non-radiation relaxation down to the bottom of the conduction band; c) an
exciton is created between the electron at the bottom of the conduction band and holes at the top of the
valence band; d) the electron relaxes from the metastable state recombining with the hole and the atom
emits a photon with an energy of E_g.
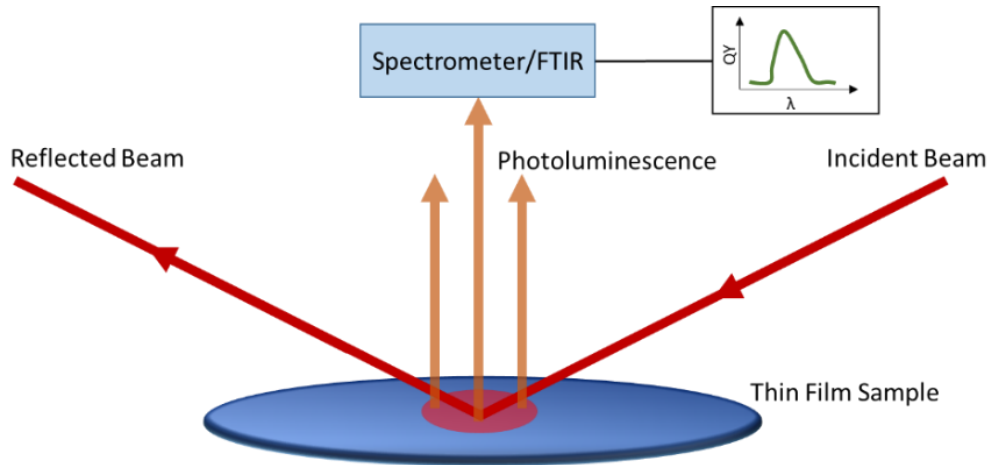
Figure 24. Graphical depiction of a photoluminescence setup.
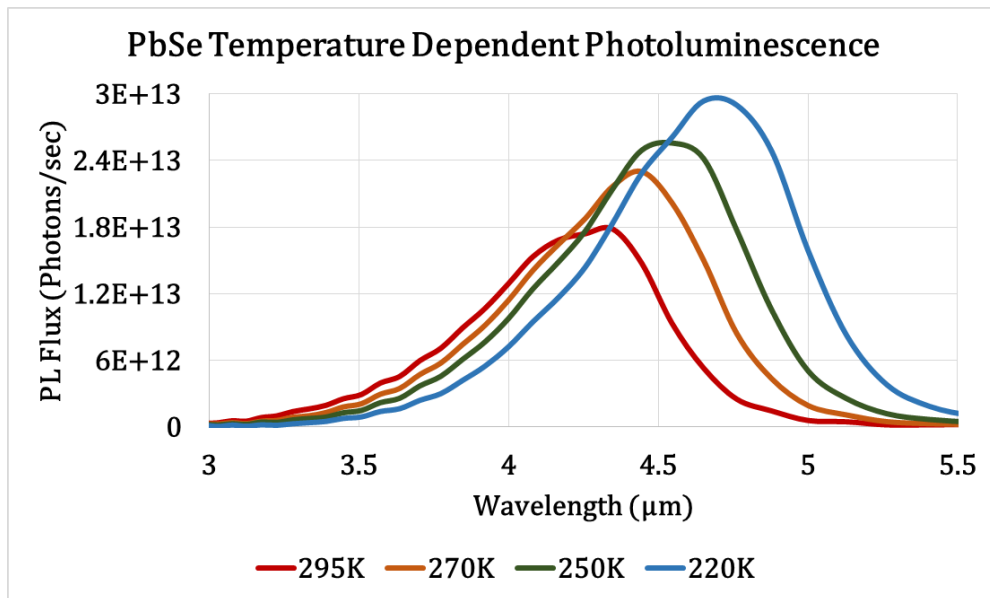
Figure 25. Measured temperature dependent photoluminescence of sensitized PbSe films.

Described above, the peak of the PL spectrum is associated with the bandgap energy, while the amplitude is the emitted photon flux. The results in figure 25 are red-shifted, yet still show good agreement with those presented in [36]. This redshift can be quantified by dividing the peak energy or wavelength value at a given temperature by that at room temperature. Table 4 contains red-shift scaling factors, which were utilized to estimate how the dispersion relations change with temperature. Also of note in figure 25

is the inverse relationship between emitted photon flux and temperature. Discussed above, this trend follows the same behavior observed in the responsivity and quantum efficiency of fabricated PbSe detectors.

Table 4. Temperature dependent scaling factor calculated from the PL spectra of investigated PbSe films.

Temperature (K)	Max Flux (Photons/s)	E_g Wavelength (µm)	Red-shift Scaling Factor
290	1.74e13	4.256	1
270	2.30e13	4.445	1.044
250	2.56e13	4.546	1.068
230	2.81e13*	4.647*	1.092*
220	2.81e13	4.652	1.093
*Estimated from surrounding temperature values			
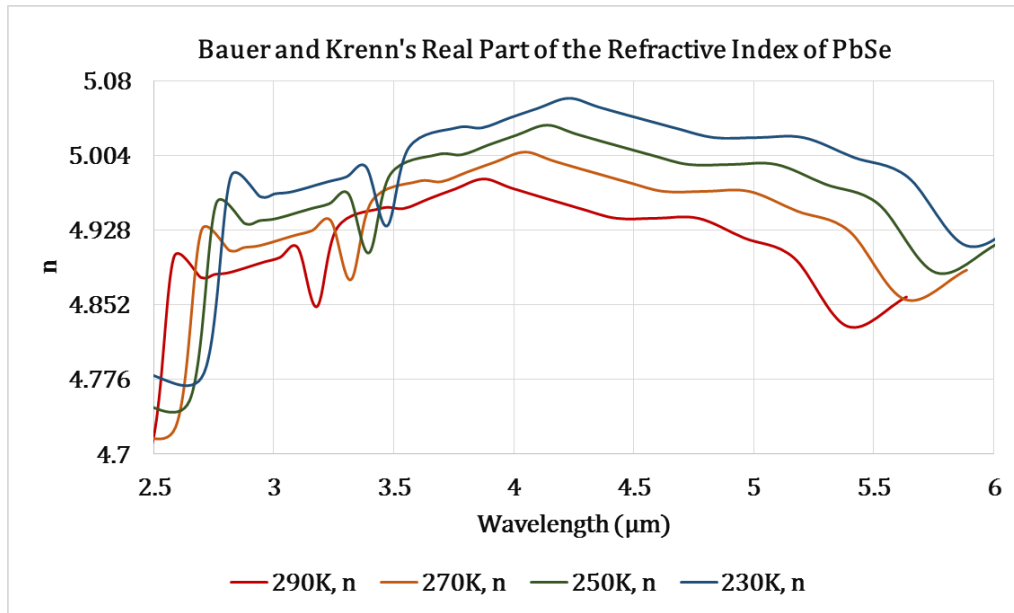
Figure 26. The real part of the index of refraction of PbSe from 2.5 µm to 6 µm at temperatures of interest.

To estimate how the amplitude of the complex index of refraction changes with temperature, the real part and the imaginary part must be considered separately. The real part of the index of refraction changes with temperature T according to a constant of proportionality called dn/dT, which for PbSe was found in the literature to be

$$\frac{1}{n_0}\left(\frac{dn}{dT}\right) = -28x10^{-5} \ K^{-1},$$
(2.18)

where n_0 is defined as the index of refraction at room temperature [35]. From equation

2.16, the dispersion relations of table 3, and the red-shift scaling factors in table 4 the real

part of the index of refraction between 2.5 µm and 6 µm was calculated. The resulting

temperature dependence of the real part of the index of refraction from 290 K down to

230 K is shown in figure 26.
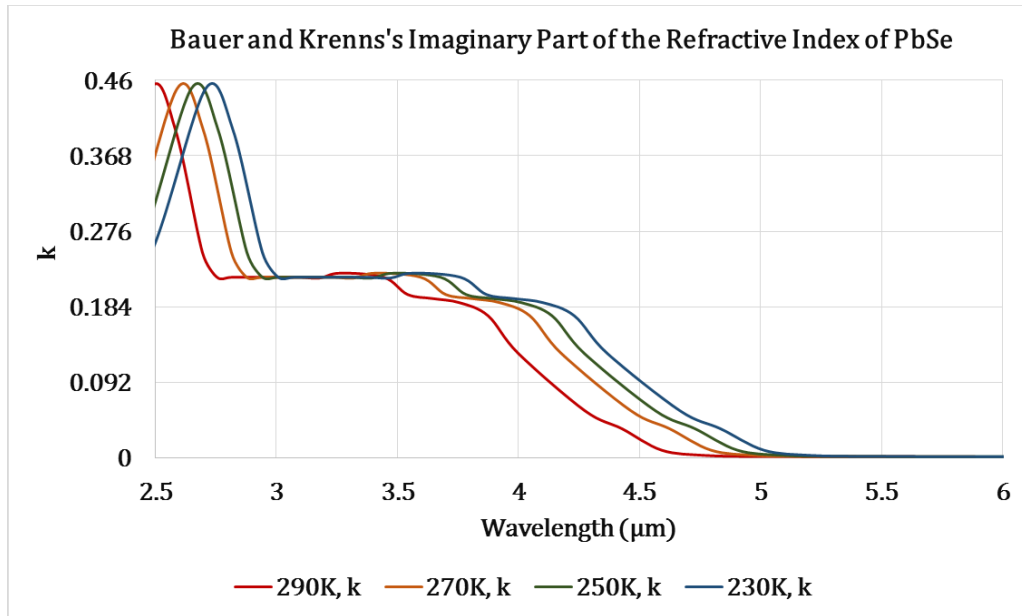
Figure 27. The imaginary part of the index of refraction of PbSe between 2 µm and 6 µm at the temperatures of interest.

A first assumption for the imaginary part of the index of refraction might be to

consider figure 22, and observe that the response increases as the temperature decreases.

Therefore, the imaginary part must increase. However, if this assumption were to be true,

the absorption would also increase. Instead, consider the effect of temperature on the

carrier concentration shown in table 2. The thermal energy dependence would suggest

that the recombination rate should decrease, therefore increasing the performance of the

detector. The increase in performance in the material relates to a quantity known as the internal quantum efficiency, which is defined as the ratio of the number of carriers that contribute to photocurrent to the number of carriers generated upon photoexcitation [13]. The external quantum efficiency shown in figure 22 can also be defined as the product of the internal quantum efficiency and the absorption of the semiconductor material. Therefore, the assumption for this study is that the absorption remains constant, while the internal quantum efficiency is inversely proportional to temperature. The temperature dependence of the imaginary part of the index of refraction for PbSe according to Bauer and Krenn's dispersion relations and the red-shift scaling factors in table 4 are shown in figure 27.

When comparing the EQE of figure 22 and the k-values of figure 27, the overall shape of the response should be the same. In figure 22 the cutoff wavelength is approximately 4.6 µm. Bauer and Krenn's dispersion relations, however, have a cutoff at room temperature around 4.25 µm [33]. Their dispersion relations suggest a cutoff closer to the bandgap energy of 0.29 eV (4.27 µm) of PbSe, however the measured absorption from the films shows a 1.08x redshift in the cutoff wavelength. Recall, however that the investigated films herein have a three-layer polycrystalline structure. Therefore, the discrepancy is associated with additional absorptive states within the bandgap leading to what are known as mid-gap states and the Urbach tail [40-41]. When an electron near the top of the valence band is excited to an energy state close to the conduction band in a disordered material, it can experience thermal fluctuations that blur the well-defined edges of both bands. This blurring leads to additional energy states, as well as an exponential tail that has effects on the absorption coefficient α. Considering these films

are polycrystalline and highly disordered, I shifted the wavelength of Bauer and Krenn's dispersion relations by taking the cutoff wavelength of the measured absorption and dividing by the cutoff wavelength they report. The resulting dispersion relations are shown in figure 28. The cutoff and knee wavelengths at 290 K are now in agreement with the measured absorption spectra of figure 20.
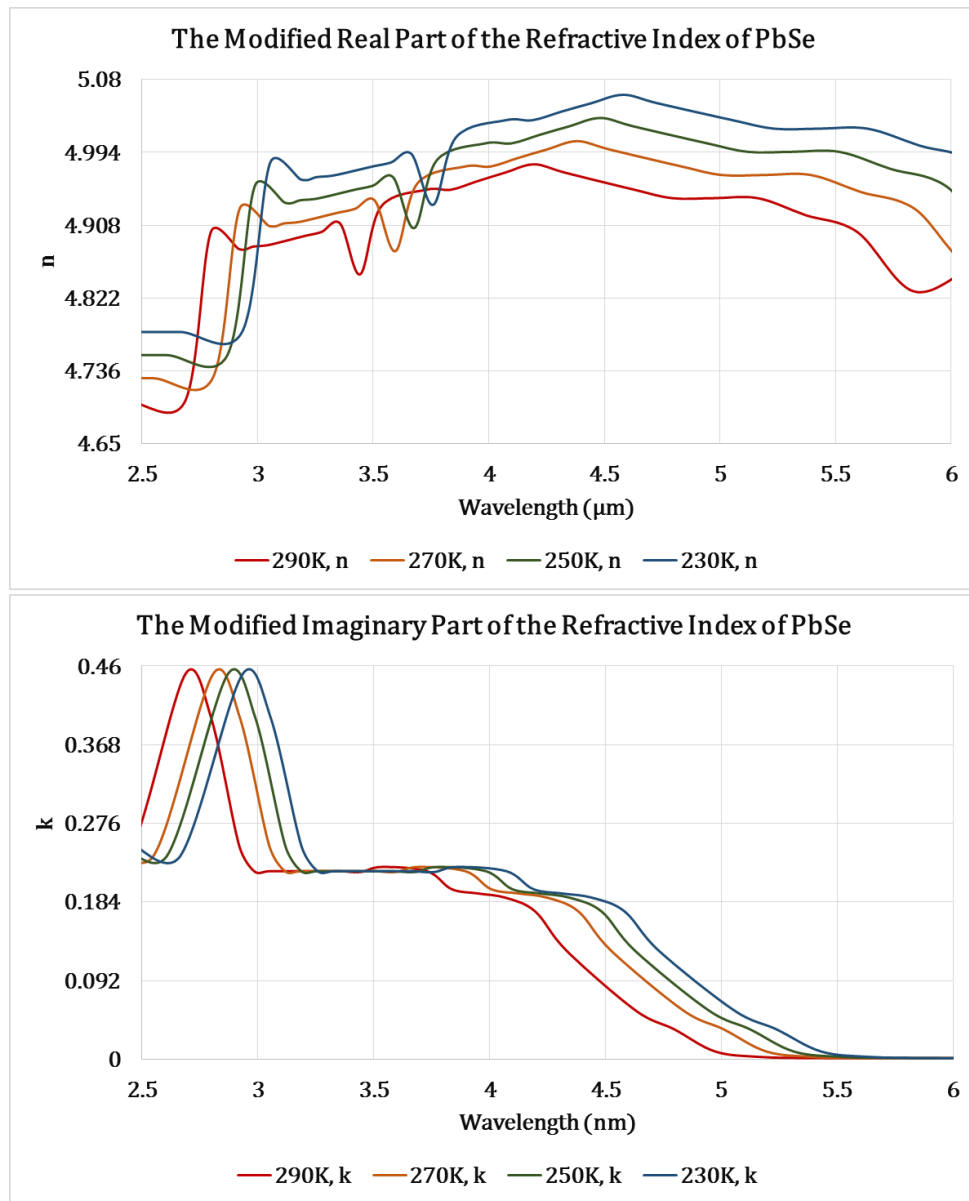
Figure 28. Modified dispersion relations of PbSe.

There are several important features to acknowledge in figure 28. The k-values have been kept constant across temperature to be consistent with the assumption that absorption should be approximately constant across temperatures. Further, the shape of the k-value spectra are similar to the measured EQE spectra, which is expected because EQE is dependent on the absorption within the material. Finally, for resonant structures, especially with respect to surface plasmon resonance and resonant cavities, the index of the host material is one of the primary parameters that governs the resonant behavior [31, 42]. These modified dispersion relations that describe the PbSe films we investigated have been used extensively in numerical and finite element modeling of films with embedded resonant structures to predict the optical parameters, device performance, and theoretical absorption enhancement.

Recall from figure 3 that the baseline structure of the PbSe films discussed herein (from bottom up) is Si substrate, SiO_2, PbSe, and PbI_2. The dispersion relations of PbSe have already been discussed, however the other dispersion relations must also be known to accurately model and predict the optical properties of the films. To ensure the modeled absorption was only from PbSe, the k-values for Si, SiO_2, and PbI_2 were excluded from this investigation. This assumption closely approximates the real system, because all three compounds are wide bandgap materials and therefore transparent in the band of interest. The index of refraction of Si is approximately 3.45, while the index of refraction of SiO_2 is approximately 1.4 in the MWIR band [43-44]. The real part of the index of refraction of PbI_2 is between 2.3 and 2.5 in the MWIR regime [11, 45-46], so for this study PbI_2 was taken to be 2.5. In these films, the index of refraction alternates from lower to higher values multiple times as light propagates through them. As I have

previously discussed in Chapter 1, this will cause constructive and destructive interference fringes within the film which can be tailored to selectively enhance the in-band performance of PbSe.

Chapter 2 References

[1]   S. –S., Yoo, et al. "High Operating Temperature MWIR Photodetectors

Development Using Polycrystalline PbSe Technology," presented at The U.S.

Workshop on the Physics and Chemistry of II-VI Materials, Chicago, IL, 2017.

[2]   M. –H., Jang, ""Effect of Sensitization on PbSe IR Detector Materials

Properties." Manuscript submitted to J. of Elect. Mat., 2017.

[3]   B. Hafner, "Energy Dispersive Spectroscopy on the SEM: A Primer," University

of Minnesota [online], Available:

http://www.charfac.umn.edu/instruments/eds_on_sem_primer.pdf [accessed Oct.

30, 2018].

[4]   R. S. Mitchell, "Structural polytypism of lead iodide and its relationship to screw

dislocations." Z. Kristallogr. Cryst. Mater. Vol. 111, Iss. 1-6, 1959.

[5]   Z. I. Smirnova, et al. "Effect of an Iodine-Containing Additive on the

Composition, Structure, and Morphology of Chemically Deposited Lead Selenide

Films." Physics of the Solid Stat, Vol. 56, No. 12, 2014.

[6]   Y. Suh and S. –H. Suh, "Effect of iodine doping in the deposition solution and

iodine vapor pressure in the sensitization treatment on the properties of PbSe

films." Optical Engineering, Vol. 56, No. 9, 2017.

[7]   J. Grayer, P. Martin, M. Kramer, and S. –S. Yoo, "Material and Device

Characterization of High-Temperature PbSe Photoconductive films," presented at

Military Sensing Symposia, Gaithersburg, MD. 2018

[8]   S. Horn, et al. "Reaching for the sensitivity limits of uncooled and minimally

cooled thermal and photon infrared detectors." Proc. Of SPIE, Vol. 5783, 2005.

[9] M. Kramer, et al. "Effect of Temperature on the Sensitization of Lead Selenide," presented at the Northrop Grumman Corporation Materials Forum, Rolling Meadows, IL. 2017.

[10] D. A. Neamen, Semiconductor Physics and Devices: Basic Principles, 3rd Ed, New York, NY: McGraw Hill, 2003.

[11] R. Ahuja, et al. "Electronic and Optical Properties of Lead Iodide." J. Appli. Phys., Vol. 92, No 12, 2002.

[12] J. N. Humphrey and R. I. Petritz, "Photoconductivity of Lead Selenide: Theory of the Mechanism of Sensitization." Physical Review, Vol. 105, No. 6, 1957.

[13] J. Singh, *Optoelectronics: An Introduction to Materials and Devices,*" New York: McGraw-Hill Companies, Inc. 1996.

[14] P. R. Norton, "Photodetectors," in McGraw-Hill's Handbook of Optics, 3rd ed., Vol. 2, New York: McGraw-Hill, 2010, pp. 24.3-24.100.

[15] Lihuazhao, et al. "Understanding sensitization behavior of lead selenide photoconductive detectors by charge separation model." J. of Appl. Phys., Vol. 115, 084502, 2014.

[16] W. V. Roosebroeck, "Current-Carrier Transport and Photoconductivity in Semiconductors with Trapping," Physical Review, Vol. 119, No. 2, 1960.

[17] M. P. Marder. Condensed Matter Physics, 2nd ed. Hoboken, NJ: John Wiley and Sons, Inc. 2010.

[18] V. D. Mihailetchi, J. Wilderman, and P. W. M. Blom, "Space-Charge Limited Photocurrent," Physical Review Letters, Vol. 94, 126602, 2005.

[19] Y. Nishina and G. C. Danielson, "Measurements of Minority Carrier Lifetimes in Semiconductors," Ames Laboratory ISC Technical Report ISC-926, 1957.

[20] W. K. Metzger, et al. "Time-Resolved Photoluminescence and Photovoltaics," presented at the DOE Solar Energy Technologies Program Review, Denver, CO. 2004.

[21] S. Dunford. "Calculating the Time Constant of an RC Circuit," Undergraduate Journal of Mathematical Modeling: One+2, Vol. 2, Iss. 2, Art. 3, 2010.

[22] R. K. Ahrenkiel, "Analysis of Techniques for Measuring Carrier Recombination Lifetime," presented at the US Department of Energy Conference on Energy Efficiency and Renewable Energy, 2013.

[23] P. Kuman, et al. "PbSe Mid-IR Photoconductive Thin Films (Part 1): Phase Analysis of the Functional Layer," Journal of Alloys and Compounds, Vol. 724, 2017.

[24] Thermo Scientific, *Advanced FT-IR spectroscopy: Principles, Experiments, and Applications*, Thermo Scientific Instruments, LLC, 2012.

[25] P. R. Griffiths and J. A. Haseth, *Fourier Transform Infrared Spectrometry*, 2nd ed, Hoboken, NJ: John Wiley & Sons, Inc. 2007.

[26] T. A. Blake, et al. "Methods for quantitative infrared directional-hemispherical and diffuse reflectance measurements using an FTIR and commercial integrating sphere," Applied Optics, Vol. 57, No. 3, 2018.

[27] M. Falk and A. G. Miller, "Infrared spectrum of carbon dioxide in aqueous solution," Vibrational Spectroscopy, Vol. 4, Iss. 1, 1992.

[28]   M. Falk and T. A. Ford, "Infrared Spectrum and Structure of Liquid Water,"
       presented at the Symposium on Molecular Structure and Spectroscopy,
       Columbus, OH, 1965.

[29]   B. Shokri, M. A. Firouzjah, and S. I. Hosseini, "FTIR analysis of silicon dioxide
       thin film deposited by metal organic-based PECVD," presented at the 19th
       International Symposium on Plasma Chemistry, 2009.

[30]   Thor Labs "FDPSE2x2 Lead Selenide Photoconductor User Guide," Rev C, pg 8,
       2017.

[31]   E. Hecht, *Optics*, 4th ed. New York: Addison-Wesley, 2002.

[32]   I. Chambouleyron and J. M. Marinez, *Handbook of Thin Film Materials; ch 12*,
       edited by H.S. Nalwas, Academic Press, 2001.

[33]   J. H. W. G. Boer, *Spectroscopic infrared ellipsometry: components, calibration
       and application*, Eindhover: Technische Universiteit Eindhoven, 1995.

[34]   G. Bauer and H. Krenn, "Lead Selenide (PbSe)", in Palik, E.D. Editor, *Handbook
       of Optical Constants of Solids*, (Vol. 1, pp. 517 − 523). San Diego, CA. United
       States: Academic Press, Inc. 1985.

[35]   S. Adachi, *Optical Properties of Crystalline and Amorphous Semiconductor:
       Materials and Fundamental Principles*, New York, New York: Springer, 2012.

[36]   N. M Ravindra, S. Auluck, and V. K. Srivastava, "Temperature dependence of the
       energy gap in PbS, PbSe, and PbTe," Phys. Sat. Sol. (a) 52, K151, 1979.

[37]   Z. Dashevsky, et al. "Mid-infrared photoluminescence of PbSe film structures up
       to room temperature," Proc. Of SPIE, Vol. 7142, 71420L-1, 2008.

[38]   K. Bhatnagar, "Nanogap Embedded Silver Gratings for Surface Plasmon Enhanced Fluorescence," M.S. Thesis, University of Missouri, Columbia, MO, 2012.

[39]   J. R. Laokowicz, *Principles of Fluorescence Spectroscopy*, 3rd ed. Springer, 2006.

[40]   A. Lukyanov, et al. "Structural origin of the midgap electronic states and the Urbach tail in Pnictogen-Chalcogenide glasses," J. Phys. Chem. B, 2018.

[41]   Sadigh, et al. "First-principles calculation so of the Urbach tail in the optical absorption spectra of silica glass," Phys. Rev. Lett. PRL 106, 027401, 2011.

[42]   D. Sarid and W. Challner, *Modern Introduction to Surface Plasmons: Theory, Mathematical Modeling, and Applications*, New York, NY: Cambridge University Press, 2010.

[43]   H. H. Li, "Refractive index of silicon and germanium and its wavelength and temperature derivatives." J. Phys. Chem. Ref. Data 9, 1993.

[44]   J. Kischkat, et al. "Mid-infrared optical properties of thin films of aluminum oxide, titanium dioxide, silicon dioxide, aluminum nitride, and silicon nitride." Appl. Opt. 51, 2012.

[45]   A. E. Dugan and H. K. Henisch, "Dielectric Properties and Index of Refraction of Lead Iodide Single Crystals". J. Phys. Chem. Solids. Pergamon Press, Great Britain, 1967.

[46]   L. Glasser, et al. "Dielectric Properties of Lead Iodide". J. Chem. Soc. (A), 1967.

[47]   Power Technology, Inc., "IQ1C100(LD2191)," 2018. [Online]. Available: https://www.powertechnology.com/b071.html. [Accessed; Nov. 9, 2018].

[48]   D. A. Kondas, "Introduction to Lead Salt Infrared Detectors," Technical Report
        ARFSD-TR-92024, US Army Armament Research, Development, and
        Engineering Center, 1993.

[49]   D. J. Lovell, "The Development of Lead Salt Detectors," American Journal of
        Physics, Vo. 37, No. 2, 1957.

[50]   G. Vergara, et al. "Polycrystalline lead selenide: the resurgence of an old infrared
        detector," Opto-Electronics Review, 15(2), 110-117, 2007.

Chapter 3: Surface Plasmon Resonance

3.1 Electrodynamics and Light-Matter Interaction

In Chapter 1, surface plasmons and surface plasmon resonance was defined without derivation. Hence, the electrodynamic relationships for surface plasmons are discussed in detail in this chapter. Equations 3.1-3.4 show the familiar Maxwell's equations in differential form [1-4].

$$\nabla \cdot \boldsymbol{D} = \rho \tag{3.1}$$

$$\nabla \cdot \boldsymbol{B} = 0 \tag{3.2}$$

$$\nabla \times \boldsymbol{E} = -\frac{\partial \boldsymbol{B}}{\partial t} \tag{3.3}$$

$$\nabla \times \boldsymbol{H} = \boldsymbol{J} + \frac{\partial \boldsymbol{D}}{\partial t} \tag{3.4}$$

Equation 3.1, Gauss's law, relates the electric flux density **D** to the charge density ρ. Equation 3.2 is Gauss's law of magnetism, where **B** is the magnetic flux density, which states that there are no magnetic monopoles. Equation 3.3, Faraday's law, shows that a change in the electric field **E** induces a change in **B** and vice versa. Finally, Ampere's law, from equation 3.4, shows that a change in the magnetic field **H** is related to the change in **D**, in addition to the electric current density **J**.

Maxwell's equations are not complete without the constitutive relationships, given in equations 3.5-3.7,

$$\boldsymbol{D} = \varepsilon \boldsymbol{E} = \varepsilon_0 \varepsilon_r \boldsymbol{E} \tag{3.5}$$

$$\boldsymbol{B} = \mu \boldsymbol{H} = \mu_0 \mu_r \boldsymbol{H} \tag{3.6}$$

$$\boldsymbol{J} = \sigma \boldsymbol{E} \tag{3.7}$$

where ε_0 is the vacuum permittivity which is equal to 8.854×10^{-12} F/m, ε_r is the relative dielectric constant of the material, μ_0 is the vacuum permeability which is equal to $4\pi \times 10^{-7}$ H/m, μ_r is the relative permeability of the medium assumed to be one for all calculations, and σ in Siemens/cm is the specific conductivity which represents power loss in a material. The discussion of surface plasmons deals with the phenomena that occur at the interface between dielectric and metallic media. Therefore, we must consider the boundary conditions for solving Maxwell's equations [4].

3.2 Surface Plasmon Polaritons

Consider a spherical metal particle located on the surface of a dielectric medium. Light incident on the metallic particle will either be reflected, scattered and diffracted, or absorbed by this metallic surface feature [4-5]. Here, a distinction has been made between reflection (back scattering) and forward scattering, but in general scattering and reflection are synonymous. If the frequency of the incident light is such that it meets the plasmonic resonance condition, then either radiative or non-radiative evanescent waves will be induced at the interface between the dielectric and metallic particle [4-6]. If scattering and diffraction dominate, then evanescent waves will radiate and decay from the interface into the near field of the dielectric [4-5].

3.2.1 Spherical Particles in the Quasi-Static Limit

In the limit that the radius of the particle is much smaller than the wavelength of incident light ($r \ll \lambda$), a classical approach can be employed for determining the surface plasmon (SP) resonance of a material system [7-8]. In the classical limit, the response of surface plasmons is due to induced polarization of the metal particle by an external

driving field [4-5, 7-10]. Moreover, the incident light can be treated as a plane wave, and the metallic particle can be treated as a dipole oscillating with a resonant frequency ω_p known as the plasma frequency.

3.2.1.1 Drude-Lorentz Model of Metals

To discuss the metallic particle, we draw on the Drude-Lorentz, also known as the free-electron, model [4-6, 11]. For this model, the conduction electrons in a metal are treated as a gas of free, non-interacting carriers that undergo relaxation through collisions with the metal lattice and other scatterers [4-6]. We can describe the dynamics of these free electrons using Newton's equation of motion shown in equation 3.8,

$$m\frac{d^2x}{dt^2} = -\frac{m}{\tau}\frac{dx}{dt} - qE_{tot}(t) \tag{3.8}$$

where m is the effective electron mass in the metal, x is the displacement distance during oscillation, q denotes the electric charge constant, and τ is the decay time which accounts for electron scattering. The term E_{tot} represents the total electric field, including the incident and induced fields acting on the electrons in the metal, and is given by equation 3.9.

$$E_{tot}(t) = Re\{E_{tot}(\omega)\,exp(-i\omega t)\} \tag{3.9}$$

It is important to note how the interaction between the metal and the incident field is dependent on the field frequency ω. The spatial displacement of the electrons during oscillation is also a function of frequency, and is given by equation 3.10.

$$x(\omega) = \frac{qE_{tot}(\omega)}{m(\omega^2+\frac{i\omega}{\tau})} \tag{3.10}$$

Assuming a 2D density of states and an electron density of N, the polarization P induced in the metal particle by the incident light is given by equation 3.11.

$$P(\omega) = -qx(\omega)N \tag{3.11}$$

Recall from equation 3.1 that the electric flux density is a product of the permittivity and the electric field in metals. Using the Drude-Lorentz model, the magnitude of the electric flux density in a metal is given by equation 3.12.

$$D(\omega) = \varepsilon(\omega)E_{tot}(\omega) = \varepsilon_\infty(\omega)E_{tot}(\omega) + 4\pi P(\omega) \tag{3.12}$$

The above relationship leads to the metal permittivity, shown in equation 3.13, as described in the Drude-Lorentz model. This relationship is needed to describe the surface plasmon resonance condition [4-6, 7-10].

$$\varepsilon(\omega) = \varepsilon_\infty(\omega) - \frac{\omega_p^2}{\omega^2 + \frac{i\omega}{\tau}} \tag{3.13}$$

The first term on the right hand side of equation 3.13, ε_∞, represents the high-frequency permittivity limit of the metal, and ω_p is the bulk plasma frequency of the metal given by equation 3.14.

$$\omega_p = \sqrt{\frac{4\pi q^2 N}{\epsilon_\infty m}} \tag{3.14}$$

It is important to remark on the time constant τ, and how it relates to SPs at this point. Notice how if τ approaches infinity, then the denominator of the right side is only a function of the frequency of the incident light. This implies the surface plasmons have an infinite lifetime, and will have sharp resonances at the plasma frequency. However, if τ is finite, then plasmon resonances become broadened around a specific frequency that

depends on the surrounding material and the plasma frequency of the metal [4]. The surface plasmon resonance lifetimes of various metals will be revisited shortly.

For completeness, we can now revise equations 3.9 and 3.10 to include the contributions from the external E_{ext} and induced fields. The total electric field and spatial displacement of electrons in a metal due to an external field is shown in equations 3.15 and 3.16.

$$E_{tot} = E_{ext}(\omega) + \frac{4\pi Nqx(\omega)}{\varepsilon_\infty} \tag{3.15}$$

$$x(\omega) = \left(\omega^2 + \frac{i\omega}{\tau} - \frac{4\pi Nq^2}{\varepsilon_\infty m}\right) = \frac{q}{m}E_{ext}(\omega) \tag{3.16}$$

3.2.1.2 Metal Spheres in the Classical Limit

From the classical or quasi-static treatment a metallic particle can be treated as a dipole oscillator with a resonant frequency ω_p [4-5]. Here, the incident light is considered to be a plane wave with a uniform field distribution. In other words, we will ignore the spatial distribution of intensities of the incident field, and only consider the time dependence.

In the quasi-static limit, we can use equation 3.17, Laplace's equation, for the static potential to solve for the electric field in spherical coordinates given in equation 3.18.

$$\nabla^2 \Phi = 0 \tag{3.17}$$

$$\mathbf{E} = -\nabla \Phi \tag{3.18}$$

If the incident plane wave is polarized along the x-direction, then the lowest order

solution for the total field is that of an induced dipole [4]. Inside the metal sphere, the

electric potential is given by equation 3.19,

$$\Phi_{in} = A_p x \tag{3.19}$$

where A_p is the amplitude of the potential, and x is the displacement. Therefore, the

electric field inside the metal sphere is given by equation 3.20 [4-5].

$$\boldsymbol{E}_{in} = -A_p\hat{x} = -A_p(\hat{r}sin\theta cos\varphi + \hat{\theta}cos\theta cos\varphi - \hat{\varphi}sin\varphi) \tag{3.20}$$

Outside the sphere, the field potential, shown in equation 3.21, is given by the sum of the

contributions from the external and induced dipole fields,

$$\Phi_{out} = -Ex + \frac{C_{DP}}{r^2}sin\theta cos\varphi \tag{3.21}$$

where r is the radius of the spherical particle, and C_{DP} is the amplitude of the dipole

potential. Using equation 3.18 and 3.21, the electric field outside of the particle is given

by equations 3.22 and 3.23.

$$\boldsymbol{E}_{out} = E\hat{x} - C_{DP}\left[\frac{\hat{x}}{r^3} - \frac{3x}{r^5}(x\hat{x} + y\hat{y} + z\hat{z})\right] \tag{3.22}$$

$$\boldsymbol{E}_{out} = E(\hat{r}sin\theta cos\varphi + \hat{\theta}cos\theta cos\varphi - \hat{\varphi}sin\varphi) + $$
$$\frac{C_{DP}}{r^3}(2\hat{r}sin\theta cos\varphi - \hat{\theta}cos\theta cos\varphi + \hat{\varphi}sin\varphi) \tag{3.23}$$

Due to the fact that the host material and metallic sphere have different dielectric

properties, there will be an induced charge that perturbs the incident electric field. Shown

in equation 3.24 and 3.25, there is continuity across the sphere boundary between the

tangential component of the electric field E_t and the normal component of the

displacement field E_n, respectively,

$$E_{t_{outside}} = E_{t_{inside}} \tag{3.24}$$

$$E_{n_{outside}} = \frac{\varepsilon_m}{\varepsilon_d} E_{n_{inside}} \tag{3.25}$$

where ε_m is the frequency dependent relative permittivity of the metal sphere, and ε_d is the relative permittivity of the host dielectric material, which is assumed to be constant in the quasi-static model [5]. Therefore, we can relate the static A_p and induced C_{DP} amplitudes using equations 3.26 and 3.27.

$$A_p = -\left(\frac{3\varepsilon_d}{2\varepsilon_d + \varepsilon_m}\right) E \tag{3.26}$$

$$C_{DP} = \frac{r^3(\varepsilon_m - \varepsilon_d)}{2\varepsilon_d + \varepsilon_m} E \tag{3.27}$$

The relative dielectric constant of the metal, shown in equation 3.28, has both a real and imaginary part, which relate to the phenomena of scattering and absorption.

$$\varepsilon_m = \varepsilon'_m + i\varepsilon_m'' \tag{3.28}$$

Equations 3.26 and 3.27 lead to the polarizability of the metal, which is defined as the ability for carriers within the metal to align into dipoles. Shown in equation 3.29, the polarizability α is highly dependent on the complex permittivity of the metal and the host material.

$$\alpha(\omega) = \frac{4\pi\varepsilon_0\varepsilon_d C_{DP}}{E} = (4\pi\varepsilon_0\varepsilon_d)r^3\left(\frac{\varepsilon_m - \varepsilon_d}{2\varepsilon_d + \varepsilon_m}\right) \tag{3.29}$$

Notice, that as the denominator in equation 3.29 goes to zero, then the polarizability approaches infinity, and the plasmonic resonance condition for spherical metallic particles is reached [4-10]. In real metals, the polarizability would approach a maximum, yet still adhere to the same resonance condition shown in equation 3.30 [34-35].

$$\varepsilon'_m(\omega) \cong -2\varepsilon_d \qquad \text{(3.30)}$$

Equation 3.30 states that the surface plasmon resonance condition for spherical

particles occurs when the frequency of the incident light is such that the real part of the

complex permittivity of the metal is negative, with an amplitude that is two-times that of

the surrounding dielectric [4-10, 21-22, 30, 36]. Notice the resonance condition in the

classical limit is independent of size. The size independence is due to the omission of

retardation effects in the metal [4-5]. As will be discussed shortly this is not the case for

larger particles, and resonances will shift to lower frequencies as particle sizes increase

[5, 7, 12-15]. Also of note for the quasi-static limit is that we assume the incident light

only couples to dipole resonances [4-5]. However, when the theory is expanded into the

Mie regime, light can also couple to multi-pole resonances.

To get a glimpse of how surface plasmons can greatly increase the field strength

of the incident light, consider the peak field intensity. The spatial location of the peak

field intensity will be located where the sphere and the dielectric medium meet ($\varphi =$

$0, \theta = \pi/2$). At resonance, the electric field outside the sphere is given by equation 3.31.

$$\boldsymbol{E}_{out} = \left[1 + \frac{2(\varepsilon_m - \varepsilon_d)}{2\varepsilon_d + \varepsilon_m}\right] E\hat{r} = \left[\frac{3\varepsilon'_m}{i\varepsilon''_m}\right] E\hat{r}. \qquad \text{(3.31)}$$

The imaginary part of equation 3.31 represents the losses in the metal, so for metals in

which the losses are small ($|\varepsilon'_m| \gg |\varepsilon''_m|$), the maximum predicted field enhancement at

resonance on the surface of the particle is given by equation 3.32 [4],

$$\left|\frac{E_{SP}}{E_0}\right| \cong 3\left|\frac{\varepsilon'_m}{\varepsilon''_m}\right| \qquad \text{(3.32)}$$

where E_{sp} represents the field on the metallic sphere surface due to surface plasmons, and

E_0 represents the incident field. The relationship in equation 3.32 is a first approximation

for how large the electric field at the surface of a metallic sphere in a host material can be. Consider the carrier generation rate G_L, with units of cm^{-3}s^{-1}, for photoconductors shown in equation 3.33,

$$G_L = (1 - e^{-\alpha x})I_{ph,0}\eta_i A_{detector} \tag{3.33}$$

where α is the absorption coefficient in units of inverse length, x is the distance into the semiconductor material, $I_{ph,0}$ is the incident photon irradiance (photons/cm^{2}s), η_i is the internal quantum efficiency defined as the ratio of the current-contributing carriers to the total number of generated carriers, and $A_{detector}$ is the effective area of the detector [44]. The quantity of interest is the incident photon irradiance $I_{ph,0}$ which is related to the optical intensity I_0 with units of W/cm^2 by equation 3.34,

$$I_{ph,0} = \frac{I_0}{h\nu} \tag{3.34}$$

where $h\nu$ is the photon energy [2, 44]. The incident optical intensity I_0 is related to the square of the incident electric field $\mathbf{E_0}$ by equation 3.35,

$$I_0 = \frac{1}{2}c\varepsilon_d\varepsilon_0|\mathbf{E}|^2 \tag{3.35}$$

where c is the speed of light ($2.998 \times 10^8 \ m/s$), and ε_0 is the permittivity of free space ($8.854 \times 10^{-12} \ F/m$) [1-3]. If the intensity of the incident light is related to the electric field strength, then through the excitation of surface plasmons the electric field strength is increased by a factor of $\left|\frac{E_{SP}}{E_0}\right|$ at resonance. The square of this electric field enhancement can then be used to derive the excess carrier generation rate G_{L_SP} in surface plasmon enhanced photoconductive detectors by equation 3.36.

$$G_{L,SP} = \frac{(1-e^{-\alpha x})c\varepsilon_0\varepsilon_d\left(\left|\frac{E_{SP}}{E_0}\right|\right)^2|E_0|^2\eta_i A_{detector}}{2h\nu} = \left|\frac{E_{SP}}{E_0}\right|^2 G_L \qquad (3.36)$$

The importance of equation 3.32 can be seen by examining equations 3.36, and observing that the square of the electric field enhancement at resonance acts as an effective gain coefficient for the number of generated excess carriers. For instance, an electric field enhancement of 10 at the surface of the metal sphere would result in a $100\times$ increase in the carrier generation rate, while a field enhancement of 20 would result in a factor of 400 more carriers being generated in the same amount of time over the dielectric host material alone. To the best of the author's knowledge as of the time of this writing, the author was the first to explicitly derive and present this relationship [45]. It should be noted that this relationship was one of the theoretical motivations for investigating surface plasmon resonance for enhanced sensitivity in PbSe photoconductors.

Recall that the major interactions that can occur when light is incident on the metallic particle are reflection, scattering, and absorption. In the quasi-static limit, we ignore the contribution from back-scattering, and only deal with forward-scattering and absorption. In this case, the incident plane wave will be partially transmitted without deviation, partially absorbed, and partially scattered.

The first term to be considered is the absorption cross-section σ_{abs}, which is defined as the total power absorbed by the particle, normalized to the intensity of the incident plane wave. Recall that the imaginary part of equation 3.28 represents absorption in the metal. Therefore the imaginary part of the complex polarizability α'' is also

representative of absorption, leading to the relationship for the absorption cross-section

shown in equation 3.37,

$$\sigma_{abs} = \frac{k\alpha''}{\varepsilon_0} \cong \frac{(12\pi k r^3)\varepsilon_d \varepsilon_m''}{(2\varepsilon_d + \varepsilon_m')^2} \tag{3.37}$$

where $k = \sqrt{\varepsilon_d}\, k_0 = \frac{\sqrt{\varepsilon_d}\, 2\pi}{\lambda_0}$ is the wavenumber of the incident plane wave in the

surrounding medium in units of inverse length, r represents the radius of the sphere in

cm, and the units of σ_{abs} are cm^2. The scattering cross-section σ_{sca} is similarly defined,

with the total scattered power being normalized to the intensity of the incident plane

wave, in equation 3.38.

$$\sigma_{sca} = \frac{k^4 |\alpha|^2}{6\varepsilon_0^2} \cong \frac{8k^4 r^6}{3} \left| \frac{\varepsilon_m - \varepsilon_d}{\varepsilon_m + 2\varepsilon_d} \right|^2 \tag{3.38}$$

The sum of the scattering and absorption cross-sections, shown in equation 3.39, is called

the extinction cross-section, which represents the total power coupled to a surface

plasmon modes normalized to the intensity of the incident plane wave.

$$\sigma_{ext} = \sigma_{abs} + \sigma_{sca} \tag{3.39}$$

Of note are the units of σ_{abs}, σ_{sca}, and σ_{ext}, which are that area. An intuitive

evaluation of the benefits offered by SPPs can be made by examining what is known as

the efficiency or Q-factor. The Q-factor is the ratio of a given cross-section to the

geometrical cross-section G of the particle. For spherical particles, the geometrical cross-

section is the area of a circle, so the Q-factors associated with surface plasmon resonance

are given by equations 3.40-3.42.

$$Q_{abs} = \frac{\sigma_{abs}}{G} = \frac{\sigma_{abs}}{\pi r^2} \tag{3.40}$$

$$Q_{sca} = \frac{\sigma_{sca}}{G} = \frac{\sigma_{sca}}{\pi r^2} \qquad (3.41)$$

$$Q_{ext} = \frac{\sigma_{ext}}{G} = \frac{\sigma_{ext}}{\pi r^2} \qquad (3.42)$$

Equations 3.40 – 3.42 represent an effective gain factor over the dielectric without metallic nanoparticles. This gain factor will be one of the primary metrics for analytically evaluating the plasmonic response for different metals in PbSe.

3.2.2 Ellipsoids

It is important to also discuss ellipsoidal particles in the quasi-static limit, because the particle geometry and orientation with respect to the incident light plays a significant role in determining the resonant frequency [4-10, 12-16]. Ellipsoids are defined mathematically by equation 3.43,

$$\frac{x^2}{A^2} + \frac{y^2}{B^2} + \frac{z^2}{C^2} = 1 \qquad (3.43)$$

where A, B, and C are the lengths in their respective directions, and x, y, and z are defined in equations 3.44-3.46.

$$x = A\cos\theta\sin\phi \qquad (3.44)$$

$$y = B\sin\theta\cos\phi \qquad (3.45)$$

$$z = C\cos\phi \qquad (3.46)$$

Here, θ and ϕ are are contained within the intervals [0, 2π] and [0, π], respectively [17]. In the special case of ellipsoids in which two of the axes are equal, the shape is called a spheroid. Spheroids are of particular interest, because their shape factors S, described shortly, can be found analytically [4-5, 18-19, 22-23, 30, 45].

There are two cases of spheroids to be considered. The first is the prolate

spheroid, in which the relationship between the radii can be defined as in equation 3.47.

$$C > A = B \tag{3.47}$$
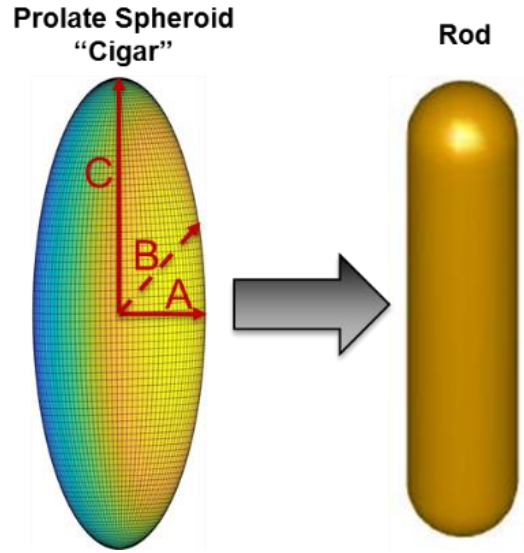
Figure 29. Depiction of a prolate spheroid, which is an analogue of the rod structure.

Figure 29 shows a graphical representation of the prolate spheroid. As the radii of the two

ends start to match the radii of A and B, the shape becomes a rod. Conversely, as the radii

of the two ends become smaller and smaller, the prolate spheroid takes on a cigar-like

shape. Therefore, prolate spheroid is an analogue for a nanorod, which has many

interesting plasmonic properties [18-19, 22-23].

The second spheroidal shape of interest is the oblate spheroid. For the oblate

spheroid, the radii follow the relationship as given in equation 3.48.

$$A = B > C \tag{3.48}$$

These structures have a pancake-like shape as the dimension C becomes smaller. When C becomes larger, the shape is that of a disc making oblate spheroids acceptable analogues for discs. A graphical representation of the oblate spheroid is shown in figure 33.
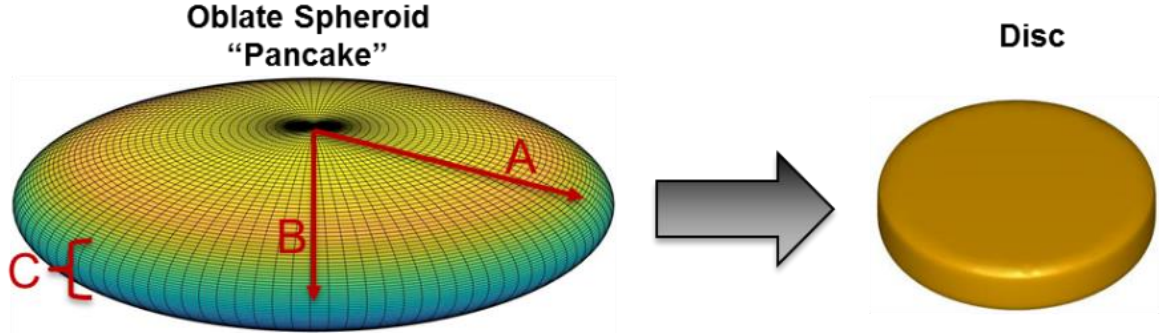
Figure 30. Depiction of an oblate spheroid, which is an analogue of the disc structure.

Returning to the discussion on surface plasmon resonance, the polarizability for ellipsoids is now a tensor quantity dependent on orientation, size, and shape. For the x, y, and z directions, the polarizability is given by equations 3.49-3.51,

$$\alpha_x = \frac{(4\pi\varepsilon_0\varepsilon_d)ABC(\varepsilon_m-\varepsilon_d)}{3[\varepsilon_d+S_x(\varepsilon_m-\varepsilon_d)]} \tag{3.49}$$

$$\alpha_y = \frac{(4\pi\varepsilon_0\varepsilon_d)ABC(\varepsilon_m-\varepsilon_d)}{3[\varepsilon_d+S_y(\varepsilon_m-\varepsilon_d)]} \tag{3.50}$$

$$\alpha_z = \frac{(4\pi\varepsilon_0\varepsilon_d)ABC(\varepsilon_m-\varepsilon_d)}{3[\varepsilon_d+S_z(\varepsilon_m-\varepsilon_d)]} \tag{3.51}$$

where $S_{x,y,z}$ are the shape factors in the x-, y-, and z-directions given by equations 3.52-3.54.

$$S_x = \frac{ABC}{2}\int_0^\infty \frac{ds}{(s+A^2)^{\frac{3}{2}}+(s+B^2)^{\frac{1}{2}}+(s+C^2)^{\frac{1}{2}}} \tag{3.52}$$

$$S_y = \frac{ABC}{2}\int_0^\infty \frac{ds}{(s+A^2)^{\frac{1}{2}} +(s+B^2)^{\frac{3}{2}}+(s+C^2)^{\frac{1}{2}}} \tag{3.53}$$

$$S_z = \frac{ABC}{2} \int_0^\infty \frac{ds}{(s+A^2)^{\frac{1}{2}} + (s+B^2)^{\frac{1}{2}} + (s+C^2)^{\frac{3}{2}}} \tag{3.54}$$

Equation 3.55 provides a convenient relationship between the shape factors, making

analytical calculations of spheroids possible.

$$S_x + S_y + S_z = 1 \tag{3.55}$$

Consider an x-polarized plane wave incident on a prolate-spheroid. Then the shape factor

in the x-direction reduces to the equation 3.56,

$$S_x = \left(\frac{1}{1 - r_{asp}^2}\right) - \frac{r_{asp}}{\left(1 - r_{asp}^2\right)^{\frac{3}{2}}} sin^{-1} \sqrt{1 - r_{asp}^2}$$

$$= \frac{(1-e^2)}{e^2} \left[\frac{1}{2e} ln\left(\frac{1+e}{1-e}\right) - 1\right] \tag{3.56}$$

where r_{asp} is the aspect ratio given as the ratio of the x-dimension to that of the y- or z-

dimensions, and e is the eccentricity given as $1 - r_{asp}^{-2}$. Now, the y- and z-shape factors

can be found by utilizing the relationship in equation in equation 3.55, the results of

which are shown in equation 3.57.

$$S_y = S_z = \frac{1 - S_x}{2} \tag{3.57}$$

Recall that the resonant plasmonic frequency for spheres in the quasi-static limit

is only dependent on the properties of the metal comprising the sphere and the host

material. The resonance condition for ellipsoids, however, includes the shape factors and

is given by equation 3.58,

$$\varepsilon_m' \cong \varepsilon_d \left(1 - \frac{1}{S_i}\right) \tag{3.58}$$

where the subscript i on the shape factor denotes the direction under consideration. There are several key observations that can be made from equation 3.58. First, in addition to the properties of the metal and host material, the resonance condition now depends on the shape factor. So, depending on the morphology of an ellipsoidal particle, the resonance can be tuned to longer wavelengths [7-18-19]. Further, there will be three different resonance conditions corresponding to the different directions. Therefore, the resonance will be dependent on shape and orientation of the spheroidal structures, as well as the polarization of incident light. It should be noted that if the x-, y-, and z-axes are equal, equation 3.58 reduces to equation 3.30.

To gain an intuitive understanding for how the shape of a particle affects the resonance condition, we continue the discussion of prolate-spheroids. As the aspect ratio increases, the surface charges at either end of the particle become more separated [4, 18-19]. If the incident plane wave is polarized along the major axis of the spheroid, then the shape factor decreases and the energy of the resonant mode decreases red-shifting the resonant wavelength. In other words, the surface charges at either side of the particle are repulsive, and pushing them further apart decreases the energy in the particle-system [4]. The SP resonance will now occur for wavelengths in which $\varepsilon_m{}'$ is more negative. In general, lengthening a particle will cause the resonance along the lengthened direction to shift to longer wavelengths [7-8]. Another phenomenon, known as the "lightning rod" effect, which describes the increase in the local field strength in a rod-like particle, also occurs at the ends of the particle [4, 18-19]. The field strength is inversely proportional to length, so in the limiting case in which the ends of a rod-like particle become like zero-

dimensional needle points the field strength would become infinite. Of course, for a real particle, the ends would have some finite dimension.

Another important system is the dual- or multi-particle system [4, 14, 20-21]. Similar to the ellipsoidal particle, the resonance condition is polarization and orientation dependent. For simplicity, we consider a dual-particle system of discs positioned adjacent to each other with a small gap between them. If these discs are illuminated by a plane wave polarized along the axis between the discs, their surface charges become attractive [20-21]. Moving the particles closer together would then reduce the energy in the system, and thus shift the resonance to longer wavelengths. Conversely, if the plane wave is polarized perpendicular to the axis between the particles, then the energy in the system increases and the resonant wavelength is blue shifted [4, 20]. In either case, due to the small gap, a very large electric field will accumulate between the particles [22]. This phenomenon is called the dual-dipole effect [4, 20-22].

3.2.3 Plasmonics in the Mie Regime

The quasi-static or Rayleigh regime is a subset of Mie theory. The upper limit of the classical regime typically occurs when the particle size is between 1% [4] and ~10% [7] of the wavelength. When the particle or structure size approaches the wavelength of light, then Mie theory must be used. In the Mie regime, resonances are dependent on morphology and size, where in general the resonance redshifts for larger particles [12-13]. Further, the relaxation time of plasmons in the metal must now be considered [4]. As the relaxation time decreases, the resonances become broadened [4-5, 23-24]. Moreover, where we only considered the dipole resonance in the quasi-static limit, we must now consider multi-pole resonances [4-5, 12-13]. For a detailed derivation of Mie theory, see

[12-13]. For now, the scattering, extinction, and absorption cross-sections will be given without derivation. Assuming plane wave illumination, the scattering, extinction, and absorption cross-sections in Mie theory are given by equations 3.59 − 3.61,

$$\sigma_{sca} = \frac{2\pi}{k_m^2} \sum_{l=1}^{\infty} (2l+1)(|a_l|^2 + |b_l|^2) \qquad (3.59)$$

$$\sigma_{ext} = \frac{2\pi}{k_m^2} Re\{\sum_{l=1}^{\infty} (2l+1)(a_l + b_l)\} \qquad (3.60)$$

$$\sigma_{abs} = \sigma_{ext} - \sigma_{sca} \qquad (3.61)$$

where l indicates the multi-pole resonant mode (for a dipole, l=1), a_l and b_l are the Mie coefficients representing scattering, and the wavenumber k_m is related to the size parameter χ by equation 3.62 [4],

$$\chi = k_m r \qquad (3.62)$$

where for a sphere r represents the radius. There are in fact four Mie coefficients that represent scattering (a_l, b_l), backscattering (c_l), and absorption (d_l) [13]. The coefficients c_l and d_l represent the internal fields of the particle, while a_l and b_l coefficients coincide with the external/scattered fields of the particle. Modifying equations 3.40 − 3.42 to account for the new size parameter χ, the Q-factors for scattering, absorption, and extinction can be found.

3.3 Investigating the Plasmonic Response in PbSe

Shown in Chapter 2, PbSe has a bandgap of 0.29 eV. For this investigation, the detector films are sensitized with iodine, forming a top layer of PbI_2 which has a bandgap of ~2.4 eV. The band of interest for these detector materials is in the mid-infrared (3-5 μm), so from equation 1.4 in Chapter 1 it is clear that light incident on the detector films should pass through the PbI_2 and be absorbed by the PbSe. Keeping this in mind,

assuming uniform plane wave illumination, oblate spheroids have been modeled in PbSe

using *MATLAB* scripts I developed, which can be found in appendix B. Stated in Chapter

1, the plasmonic disc was selected as the structure of choice due to its ease of fabrication,

demonstrated sensor enhancement in the literature, wavelength selectivity, and large

near-field intensity increase [25-26]. Using the Sellmeier equation, the index of refraction

n for PbSe in the 3-5 μm range is given by equation 3.63 [27].

$$n^2 - 1 = \frac{21.1\lambda^2}{\lambda^2 - 1.37^2} \tag{3.63}$$

For 3 μm, the index of refraction of PbSe was calculated to be 5.27, and for 5 μm the

index of refraction was found to be 4.88. For the following calculations a uniform index

over the spectral band of interest was assumed, so the calculated average refractive index

of 5.07 was used over the 3 μm and 5 μm band. The Sellmeier equation, as opposed to the

full dispersion relations, was used for simplicity as a first approximation for numerical

calculations. It should be noted that the following results include only the resonance

conditions and Q-factors in PbSe. Later, the effect of nanostructures on the absorption of

PbSe will be treated in a more rigorous fashion using the finite element analysis method.

3.3.1 Dispersion Relations of Drude Metals

To determine a suitable metal for surface plasmon resonance in PbSe, various

Drude metals were investigated. Using the compiled and tabulated constants for the

Lorentz-Drude model from Rakic, the dispersion relations have been found for Ag, Al,

Au, Ni, Pd, and Pt [28]. The complex permittivity was determined using equation 3.64

and 3.65, where the former is the single oscillator permittivity, and the latter accounts for

many oscillators within the metal.

$$\varepsilon_{r0}(\omega) = 1 - \frac{\Omega_p^2}{\omega^2 - i\omega\Gamma_0} \tag{3.64}$$

$$\varepsilon_r(\omega) = \varepsilon_{r0} + \sum_{i=1}^{m} \frac{f_i \omega_p^2}{(\omega_i^2 - \omega^2) + i\omega\Gamma_i} \tag{3.65}$$

Here, $\Omega_p = \sqrt{f_0}\omega_p$ is the intraband transition, also known as the free-electron, plasma frequency, f is the oscillator strength which is an indication of the probability of absorption in the transition between the energy levels of individual oscillators, Γ is the damping constant, ω_i is the oscillator frequency, ω_p is the bulk, also known as the bound-electron, plasma frequency, and ω is the probe frequency. Specific oscillators are denoted by i, where Rakic has divided the calculation between the bulk and individual oscillators within the metal [28]. To compare and evaluate all variables without difficulty, they are provided in units of energy (eV). The complex index was found by taking the square root of equation 3.65. The *MATLAB* scripts the author developed for the calculation of the dispersion relations of these metals can be found in Appendix B.

The properties of plasmonic structures, as well as their host material, not only govern the resonance, but also govern the surface plasmon dynamics [4, 32]. Important surface plasmon properties include the propagation distance D_{SP}, the phase velocity V_{SP}, and the surface plasmon lifetime τ_{SP} [4]. The propagation distance, given in equation 3.66, for an ideal metal is a measure of the length over which the metal can support the propagation of surface plasmons before their amplitude decays to 1/e of their initial value.

$$D_{SP} \cong \frac{2\varepsilon_m'^2}{(\varepsilon_d)^{\frac{3}{2}}\varepsilon_m'' k_0} \tag{3.66}$$

The surface plasmon phase velocity is given in equation 3.67, which is needed to find the surface plasmon lifetime by equation 3.68,

$$V_{SP} = \frac{\omega}{k_{SP}} = c \sqrt{\frac{\varepsilon_d + \varepsilon_m}{\varepsilon_d \varepsilon_m}} \qquad (3.67)$$

$$\tau_{SP} = \frac{D_{SP}}{V_{SP}} \cong \frac{2(\varepsilon_m')^2}{\omega \varepsilon_d \varepsilon_m''} \qquad (3.68)$$

where ω is the angular frequency of the incident light wave, k is the wavenumber, ε_d is the relative dielectric constant of the host material, and ε_m' and ε_m'' are the real and imaginary parts of the relative permittivity of the metal, respectively. Stated above, the surface plasmon lifetime is an important parameter that is inversely proportional to the width of resonant peaks, defined as the full-width-at-half-maximum (FWHM). Surface plamons can be limited by decay mechanisms such as nonradiative decay due to electron-hole pairs generated in the metal [34], as well as a loss of phase coherence due to scattering mechanisms [35]. In general, in real metals with finite surface plasmon lifetimes, a shorter-lived lifetime leads to a broader resonance peak with lower Q-factors and electric field enhancement [36].

To determine the MWIR surface plasmon properties of the metals listed above, I calculated the surface plasmon propagation distance, surface plasmon phase velocity normalized to the speed of light in vacuum, and surface plasmon lifetime. The results of this calculation were used to evaluate which metal was best suited for surface plasmon enhanced PbSe detectors. The host material was assumed to be PbSe with a refractive index of 5.07.

Table 5 shows the calculated results at the cutoff wavelength (4.3 µm) of PbSe, and figure 31 - figure 33 show the trend from 2.5 µm – 6 µm. We find that Ag, Al, and Au have the highest surface plasmon characteristics, with the calculated propagation distance reaching as high as ~50 µm and the surface plasmon lifetime being as high as

800 ns. In contrast, the calculated characteristics for Ni, Pd, and Pt showed a factor of 5-to 10-times lower propagation distance and lifetime compared to that of Ag, Al, and Au. These results suggest the metals in the top part of table 5 will yield sharper resonances with higher field-enchantment than those in the bottom half of the table.

Table 5. Calculated surface plasmon characteristics for various metals embedded in PbSe.

Metal	D_{SP} at 4.3 μm (μm)	V_{SP}/c at 4.3 μm	τ_{SP} at 4.3 μm (ns)
Ag	48.4	0.200	818
Al	42.7	0.199	722
Au	35.6	0.201	602
Ni	4.13	0.208	697
Pd	8.27	0.205	101
Pt	6.48	0.207	110
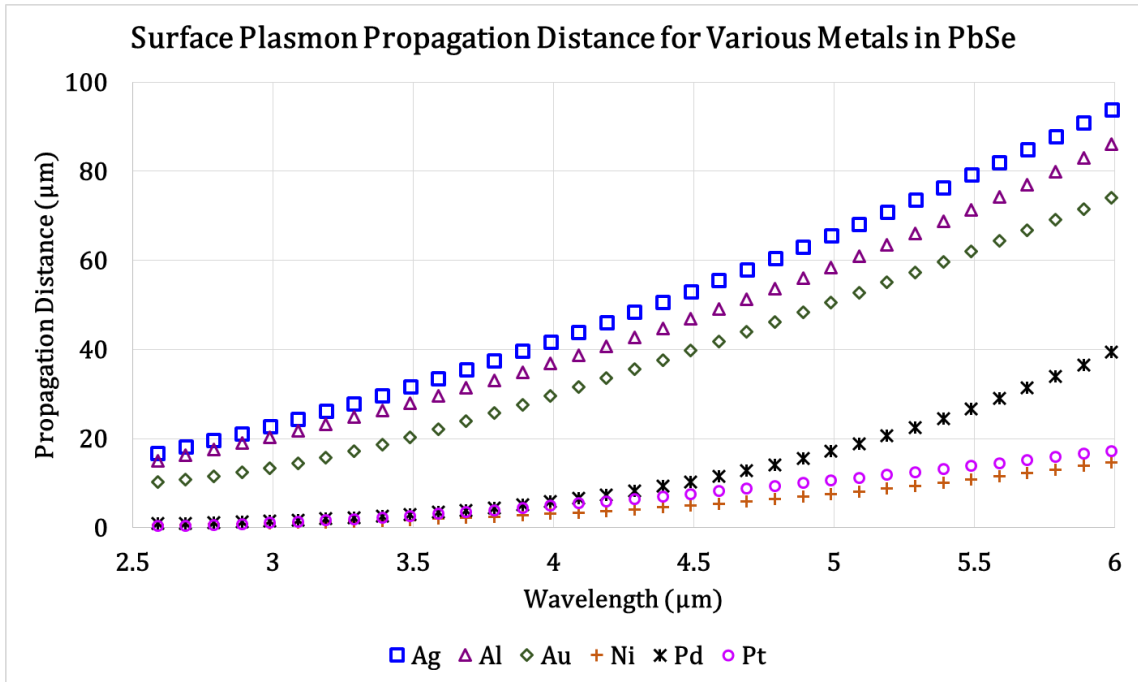
Figure 31. Surface plasmon propagation distance for various metals embedded in PbSe.

The observed trends from the calculated surface plasmon characteristics, shown in figure 31 - figure 33, show that the surface plasmon propagation distance and lifetime increase with wavelength for all the metals. This is however an idealization, and does not account for surface roughness or the change of the refractive index of PbSe with wavelength. Moreover, these calculations do not account for morphology or size of the metallic structures, which can have a significant effect on the surface plasmon characteristics [34]. In addition to surface roughness and morphology considerations, the PbSe deposition and sensitization process must also be considered. Nobel metals like Au have been found in previous experiments to diffuse into our PbSe films during the sensitization process. Therefore, metals like Pt, though their enhancement may not be as great as the nobel metals, were found to offer a feasible alternative for fabricating surface plasmon resonant structures into PbSe detectors.
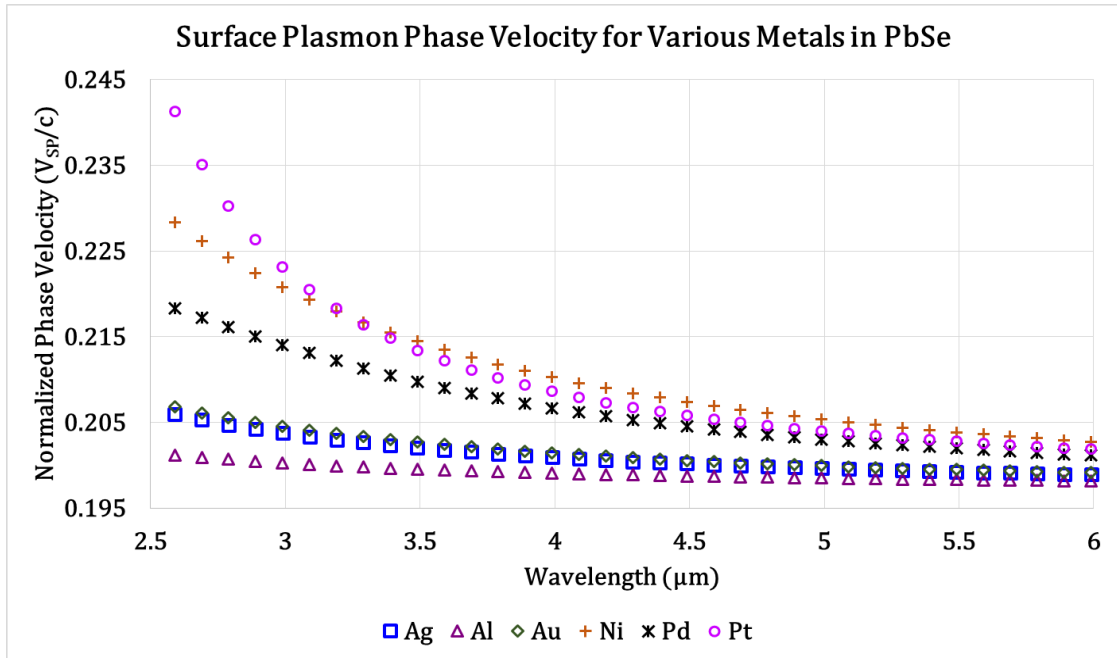
Figure 32. Phase velocity normalized to the speed of light in vacuum of surface plasmons for various metals in PbSe.

The nanodisc is polarization independent if transversely illuminated from above, assuming the disc is oriented such that its circular face is perpendicular to the propagation vector of the incident light wave [4-5, 25-26]. Assuming the source of the light wave is above the disc and traveling in the –z-direction, the face of the nanodisc is a circle of radius A. The dimension C is half the thickness of the disc, and the aspect ratio is $r_{asp} = A/C$. Mentioned above, the nanodisc is relatively simple to fabricate with techniques such as electron beam lithography, photolithography, and nanosphere lithography [21, 30].
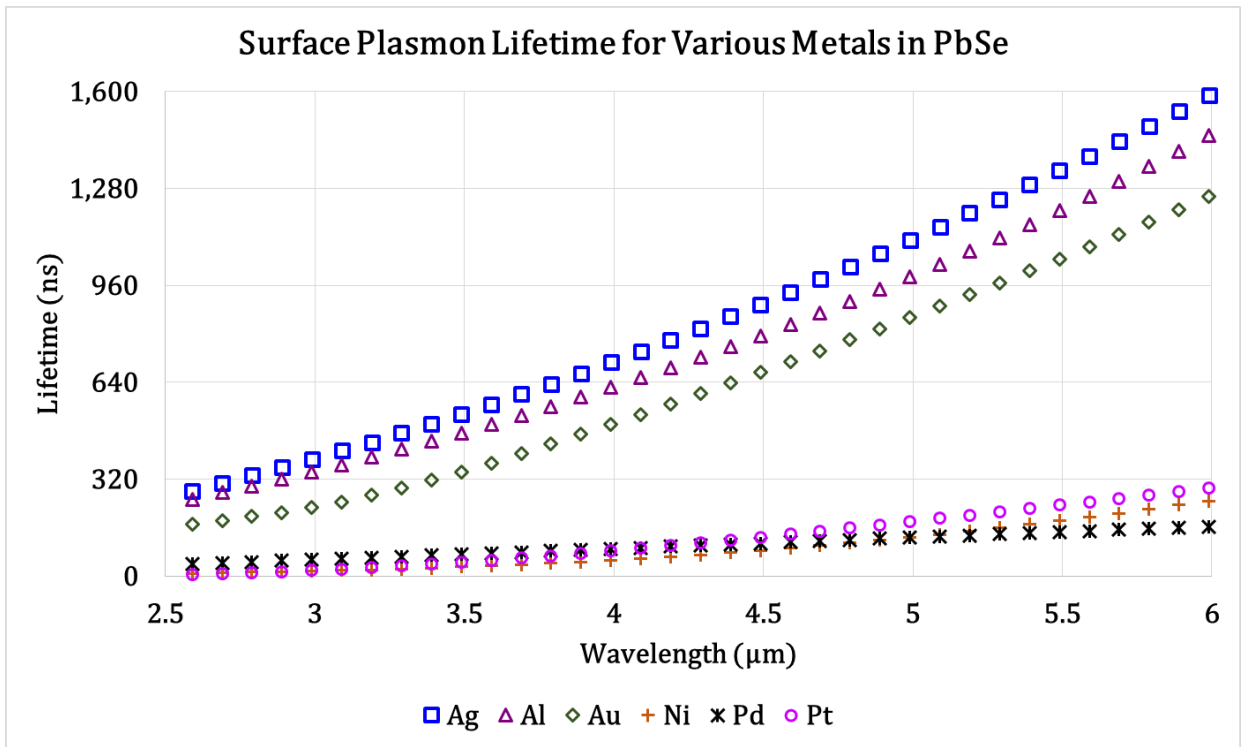
Figure 33. Surface plasmon lifetime for various metals in PbSe.

Due to their polarization independence, relative ease of fabrication, and demonstrated enhancement in similar materials, this investigation was focused on the nanodisc structure. Recall that the SiO$_2$ layer of the films is roughened to a peak-to-peak

value of 500 nm to ensure the PbSe adheres to the substrate. Coupled with the inherent roughness of the polycrystalline grains of PbSe, this surface roughness permeates throughout the PbSe film. Therefore, it would be difficult to adequately fabricate structures within the PbSe layer. The limitation stems from the coherent nature of surface plasmons [4-5, 33, 34-35]. Surface plasmons have a degree of coherence, and the waves of which they are comprised retain a direct phase relationship for short distance within the near-field of the structure surface. The surface roughness of the metal can act as scattering centers, thereby changing the path length of various parts of the traveling evanescent waves reducing their coherence length [31-32]. In fact, if the surface is too rough it may negate any surface plasmon enhancement. Therefore, the nanodiscs in this study will be considered at the PbSe/SiO$_2$ interface. Practically, discs were fabricated on smooth SiO$_2$, and a newly developed roughening procedure, described in Appendix A, was performed around the discs.

For the investigation of PbSe films, nanodiscs were modeled numerically using the quasi-static derivation described above. For a structure located at an interface between two dielectric materials, the effective index of the host material is the average of the two materials [22, 37-39]. Therefore, the effective index of refraction at the interface between PbSe and SiO$_2$ over the 3-5 µm band is considered to be 3.24, because SiO$_2$ has an in-band refractive index of 1.41. Figure 34 shows the comparison of extinction cross-sections of nanodiscs with aspect ratios of 10, 13, 15, 18, and 20. As the aspect ratio increases, the resonance peak red-shifts to longer wavelengths as would be expected. It was found in figure 34 that an increasing the aspect ratio of the Pt nanodisc from 10 to 20 lead to a resonance peak that coincides with the PbSe absorption edge at 4.27 µm.

Furthermore, the peaks become broader suggesting a decreased surface plasmon lifetime [4, 35]. Finally, the amplitude of the extinction cross-section increases with aspect ratio due to the increased diameter.
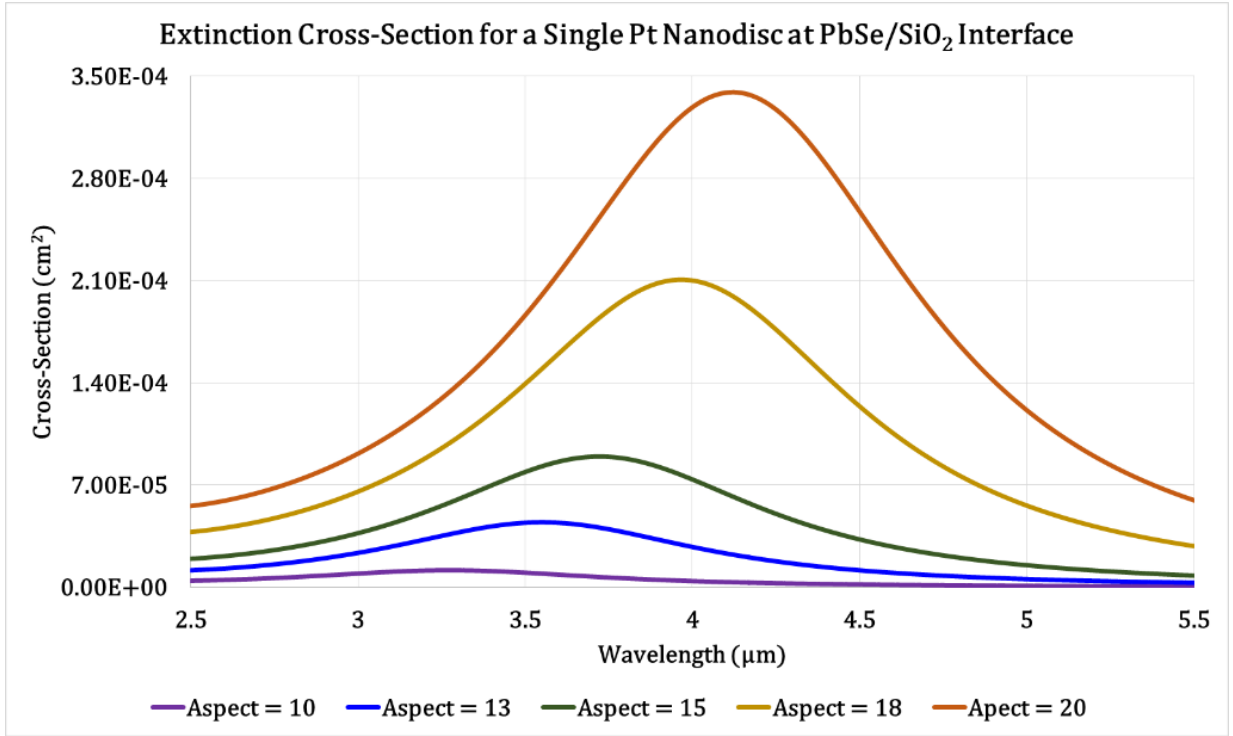
Figure 34. Extinction cross-section of a single Pt nanodisc at the PbSe/SiO₂ interface. Resonance peak red-shifts with wavelength, demonstrating wavelength selectivity for designing surface plasmon resonant disc structures for detector enhancement.

For the Pt discs in figure 34 it would seem that an aspect ratio of 20 would be the optimum design choice, because the resonance peak coincides with the absorption edge of PbSe and has the largest amplitude. However, the PbSe absorption edge also coincides with the atmospheric CO_2 absorption notch [33]. If the resonance is slightly blue shifted, then the peak can still be within the PbSe spectral sensitivity band while remaining close the absorption edge. To this end, an aspect ratio between 13 and 18 would be preferred.

I also calculated the field enhancement of Pt discs at the PbSe-SiO$_2$ interface. Using the *MNPBEM MATLAB* toolbox, a freely available simulation tool which uses the boundary element method to calculate the solution to Maxwell's equations using surface charges, the near-field intensity enhancement $\frac{|E|^2}{|E_0|^2}$ was calculated [40-41]. Moreover, this tool was also used to observe the effect of the incident illumination angle on the scattering cross-section and field-enhancement. Modeled discs were 250 nm in diameter and 20 nm thick, which resulted in an aspect ratio of 12.5.
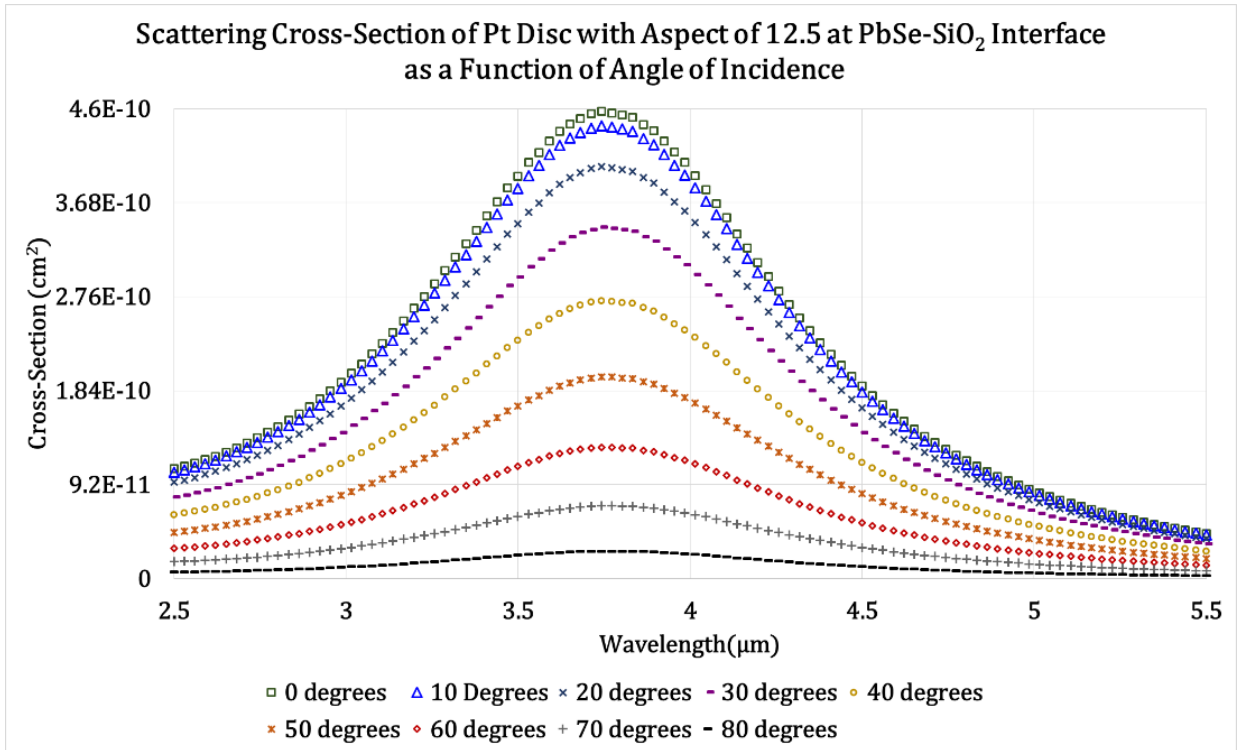
Figure 35. Calculated scattering-cross section for surface plasmon resonant discs at the PbSe-SiO$_2$ interface as a function of incident illumination angle.

The calculated scattering cross-section as a function of incident illumination angle is shown in figure 35. For all angles, the resonance was found to be 3.7 µm, which is slightly red-shifted from the results shown in figure 34. Further, the amplitudes differ by

several orders-of-magnitude, with the quasi-static calculation yielding more idealistic results. The discrepancy is due to the different algorithms used for the calculation. In figure 34 the quasi-static limit was used, while in figure 35 the more rigorous boundary element method was used. Nevertheless, the results yield similar resonances. Of note in figure 35 is the fact that the maximum scattering-cross section was found at a normal angle of incidence. This is an important feature of the plasmonic disc structure, because the investigated PbSe detectors are designed to be illuminated at normal incidence.
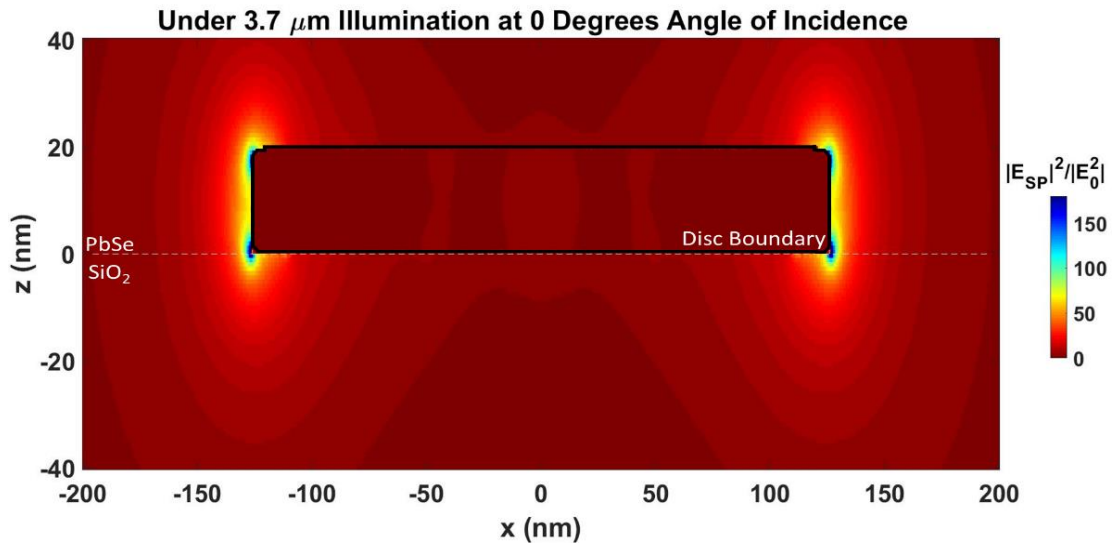
Figure 36. Field intensity enhancement map of a Pt disc located at the SiO_2-PbSe interface illuminated with a 3.7 µm plane wave at normal incidence

The electric field intensity enhancement for a Pt disc illuminated at normal incidence with an excitation wavelength of 3.7 µm is shown in figure 36. The near-field intensity enhancement, which is the square of equation 3.31 modified by the morphology of the disc, is predicted be as high as 200 on the disc surface, and up to 75 a distance of 25 nm into the PbSe layer. Distances of ~90 nm into the PbSe layer still experience a near field intensity enhancement greater than that of the incident field. Even on the inside of the

discs, which shows the induced field intensity indicative of surface plasmon resonance, a small field intensity increase is observed. The field intensity enhancement map shown in figure 36, which was only considered as an ideal approximation, showed that an appreciable increase in absorption and carrier generation in the investigated PbSe films was feasible.

Before moving on from this chapter, there are a couple of important comments to make with respect to figure 34 - figure 36. The calculated results assumed an aspect ratio of 12.5, yet the question may arise as to how large the disc diameter can be and still show the same surface plasmon resonance characteristics. Part of the answer comes down to the limitation of the fabrication techniques to be employed. For instance, for larger structures, ultraviolet (UV) photolithography might be chosen for its relatively quick process and ability to cover large areas [42-43]. Yet, if UV photolithography is chosen, there is a limit as to how small the structures can be accurately reproduced in photoresist, which is dependent on the minimum feature size of the mask and the diffraction limit for the wavelength of the UV light. Modeling is a powerful tool for assessing what aspect ratio is required and/or desired for the particular application and spectral band. From there, the limits of the fabrication technique will dictate the actual size of the structure.

The second discussion point, which is closely related to the first, is wavelength selectivity. The spectral band of interest and the bandwidth are dependent on the application for which a detector system will be used. Figure 34 demonstrates the wavelength selectivity offered by the surface plasmon resonant disc structure. Depending on the application, spectral band, and bandwidth of interest, the structure can be designed and tailored.

Chapter 3 References

[1]   J. D. Jackson, *Classical electrodynamics*, New York: Wiley, 1999.

[2]   J. D. Griffiths, *Introduction to electrodynamics*, Upper Saddle River, N.J: Prentice Hall, 1999.

[3]   C. A. Balanis, *Advanced Engineering Electromagnetics*,1ˢᵗ Ed., Hoboken, NJ: John Wiley and Sons, Inc. 1989.

[4]   D. Sarid and W. Challner, *Modern Introduction to Surface Plasmons: Theory, Mathematical Modeling, and Application*, New York, NY: Cambridge University Press, 2010.

[5]   A. A. Toropov and T. V. Shubina, *Plasmonic Effects in Metal-Semiconductor Nanostructures*, Great Clarendon, Oxford, United Kingdom: Oxford University Press, 2015.

[6]   M. P. Marder, *Condensed Matter Physics*, 2nd ed., Hoboken, NJ: John Wiley and Sons, Inc., 2010.

[7]   Z. Jaksˇicˊ, et al. "Red Shifting Approach for Nanoplasmonic Enhancement of Semiconductor Infrared Detectors." Proc. 28th International Conference on Microelectronics, Serbia, 2012.

[8]   A. Battaglia, et al. "Light scattering by Gaussian particles: Rayleigh-ellipsoid approximation," J. of Quantitative Spectroscopy and Radiative Transfer, 63, 1999.

[9]   P. Berini and A. Olivieri, "Plasmonic Optoelectronics on Si." Proc. Of SPIE, Vol. 9163, 2014.

[10]   W. A. Murray and W. L. Barnes, "Plasmonic Materials." Adv. Mater. 19, 2007.

[11]   C. Kittel, Introduction to Solid State Physics, Hoboken, NJ: John Wiley and Sons, Inc. 2005.

[12]   Evan, Amato. University of California San Diego, Scripps Institute of Oceanography, Department of Atmospheric and Climate Sciences 251: Radiation The Atmosphere Ch3 Class Notes

[13]   C. Matzler, "MATLAB Functions for Mie Scattering and Absorption," Institut fur Angewandte Physik, Research Report No 2002-08, 2002.

[14]   P. Strobbia, et al. "Recent advances in plasmonic nanostructures for sensing: a review," Optical Engineering, Vol. 54, No. 10, 2015.

[15]   N. Pere-Laperne, et al. "Infrared Plasmonic Detectors." Proc. of SPIE, Vol. 7945, 2011.

[16]   https://nanocomposix.com, visited 2/24/2018

[17]   W. E. Weisstein, "Spheroid." From MathWorld - A Wolfram Web Resource [online]. Available: http://mathworld.wolfram.com/Spheroid.html [Accessed: Sept. 11, 2018].

[18]   E. S. Kooij and B. Poelsema, "Shape and size effects in the optical properties of metallic nanorods," Phys. Chem. Chem. Phys., Vol. 8, 2006.

[19]   J. S. Sekhon and S. S. Verma, "Rational Selection of Nanorod Plasmons: Material, Size, and Shape Dependence Mechanism for Optical Sensors," Plasmonics, Vol. 7, 2012.

[20]   T. Atay, J. –H. Song, and A. V. Nurmikko, "Strongly Interacting Plasmon Particle Pairs: From Dipole-Dipole Interaction to Conductively Coupled Regime," Nano Lett., Vol. 4, No. 9, 2004.

[21]   Y. Li, *Plasmonic Optics Theory and Applications*, Tutorial Texts in Optical
         Engineering, Vol. TT110. SPIE Press. Billingham, WA., 2017.

[22]   J. A. Schuller, et al. "Plasmonics for extreme light concentration and
         manipulation," Nature Materials, Vol. 9, 2010.

[23]   V. Juve, et al. "Size-Dependent Surface Plasmon Resonance Broadening in
         Nonspherical Nanoparticles: Single Gold Nanorods," Nano Lett., Vol. 13, No. 5,
         2013.

[24]   T. J. −Y. Derrien, et al. "Properties of Plasmon Polaritons on lossy metals:
         Lifetimes, periods, and excitation conditions," J. of Opt., Vol. 18, No. 11, 2016

[25]   X. Tang, et al. "Plasmon resonance enhanced colloidal HgSe quantum dot
         filterless narrowband photodetectors for mid-wave infrared," J. Mater. Chem. C,
         5, 2017.

[26]   J. Liang, et al. "Modeling of HgCdTe photoconductive infrared detector with
         metallic nanostructures." IEEE, NUSOD, 2014.

[27]   Polyansky, M. RefractiveIndex.info.
         https://refractiveindex.infor/?shelf=main&book=PbSe&page=zemel

[28]   Rakic´, et al. "Optical Properties of Metallic Films for Vertical Cavity
         Optoelectronic Devices," Applied Optics, Vol. 37, No. 22, 1998.

[29]   A. I. Golovashkin, and G. P. Motulevich, "Optical Properties of Lead in the
         Visible and Infrared Spectral Ranges," Sov. Phys. Jet P 26, 1968.

[30]   J. Alda and G. Boremann, *Infrared Antennas and Resonant Structures*,
         Billingham, WA: SPIE Press, 2017.

[31]   G. A. Farias and A. A. Maradudin, "Effect of surface roughness on the attenuation of surface polaritons on metal films," Phys. Rev. B 27, 1983.

[32]   A. Degiron and D. R. Smith, "Numerical simulations of long-range plasmons," Optics Express, Vol. 14, No. 4, 2006.

[33]   M. Falk and A. G. Miller, "Infrared spectrum of carbon dioxide in aqueous solution," Vibrational Spectroscopy, Vol. 4, Iss. 1, 1992.

[34]   U. Freibig and M. Vollmer, *Optical Properties of Metal Clusters*, Berlin: Springer-Verlag, 1995.

[35]   M. Perner, et al. "Optically induced damping of the surface plasmon resonance in gold colloids," Phys. Rev. Lett., Vol. 78, 1997.

[36]   T. Klar, et al. "Surface-plasmon resonances in single metallic noanparticles," Phys. Rev. Lett., Vol. 80, 1998.

[37]   P. Strobbia, et al. "Recent advances in plasmonic nanostructures for sensing: a review," Optical Engineering, 54(10), 100902, 2015.

[38]   H. N. Daghestani and B. W. Day, "Theory and applications of Surface Plasmon Resonance, Resonant Mirror, Resonant Waveguide Grating, and Dual Polarization Interferometry Biosensors," Sensors, 10, 2010.

[39]   E. Li and H. Chu, Plasmonic Nanoelectronics and Sensing, United Kingdom: Cambridge Press, 2014.

[40]   U. Hohenester and A. Trugler, "MNPBEM-A Matlab toolbox for the simulation of plasmonic nanoparticles," Computer Physics Communications, Vol. 183, Iss. 2, 2012.

[41]   J. Waxenegger and U. Hohenester, "Plasmonics simulations with the MNPBEM toolbox: Consideration of substrates and layer structures," Computer Physics Communications, Vol. 193, 2014.

[42]   S. A. Campbell, *Fabrication Engineering at the Micro- and Nanoscale*, Fourth Edition, Oxford University Press, New York, 2013.

[43]   M. J. Madou, *Fundamentals of Microfabrication: The Science of Miniaturization*, Second Edition. CRC Press, 2002.

[44]   J. D. Vincent, et al. *Fundamentals of Infrared and Visible Detector Operation and Testing*, 2nd Ed., John Wiley and Sons, 2015.

[45]   J. Grayer and S.-S. Yoo, "Investigation of nanoplasmonic antenna for increased performance of high temperature operation PbSe photoconductors," Proceedings of SPIE, Vol. 10722, 2018.

Chapter 4: Thin Film Interference and the Back Reflector

4.1 Derivation of the Refractive Index and Absorption Coefficient

In Chapter 3, the interaction of light with matter was explained from the perspective of the plasma frequency in metals. The discussion is now expanded to the provenance of the refractive index of materials. Consider a beam of light incident on a semiconductor material. When the light wave interacts with the particles in the film there is an induced dipole moment due to the oscillation of the incident electric field. Let the variable **P** represent this resulting polarization from the induced dipole, such that the effective charge ρ and the current density are given by equations 4.1 and 4.2, respectively.

$$\rho = -\nabla \cdot \boldsymbol{P} \tag{4.1}$$

$$\boldsymbol{j} = \frac{\partial \boldsymbol{P}}{\partial t} \tag{4.2}$$

Accounting for polarization effects, Maxwell's equations are now given by equations 4.3-4.6,

$$\nabla \cdot \boldsymbol{E} = -\frac{(\nabla \cdot \boldsymbol{P})}{\varepsilon_0} \tag{4.3}$$

$$\nabla \times \boldsymbol{E} = -\frac{\partial \boldsymbol{B}}{\partial t} \tag{4.4}$$

$$\nabla \cdot \boldsymbol{B} = 0 \tag{4.5}$$

$$c^2 \nabla \times \boldsymbol{B} = \frac{\partial}{\partial t}\left(\frac{\boldsymbol{P}}{\varepsilon_0} + \boldsymbol{E}\right) \tag{4.6}$$

where the variable for the speed of light, which can be found from the electric permittivity and magnetic susceptibility of free space by $c = (\varepsilon_0 \mu_0)^{-1/2}$, is included to simplify the derivation [9]. By taking the curl of both sides in equations 4.4 and 4.6, the

electric and magnetic fields can be decoupled leading to the wave equations for the electric and magnetic fields. The traveling wave solutions for the electric and magnetic fields take on the form of equations 4.7 and 4.8,

$$\boldsymbol{E} = \boldsymbol{E_0}exp[i(\omega t - k \cdot r)] \tag{4.7}$$

$$\boldsymbol{H} = \boldsymbol{H_0}exp[i(\omega t - k \cdot r)] \tag{4.8}$$

where the variable k is the wave vector, the amplitude of which is the wave number given by $|k| = 2\pi/\lambda$, and the variable ω is the angular frequency given as $2\pi f$ [1-5]. The argument of the exponential of these solutions is what is known as the phase of the individual wave, and leads to the phase velocity v_p and group velocity v_g, shown in equations 4.9 and 4.10, of the waves propagating in the material.

$$v_p = \frac{\omega}{k} \tag{4.9}$$

$$v_g = \frac{\partial \omega}{\partial k} \tag{4.10}$$

The investigated PbSe films are absorptive, so the wave vector will be complex taking the form $\tilde{k} = k_1 + ik_2$ [5]. The index of refraction is a measure of the reduction of the speed of light as it travels through a medium [5-7]. Examining equation 4.9, the phase velocity is related to the speed of light by equation 4.11.

$$\frac{\omega}{k} = \frac{c}{n} \tag{4.11}$$

Therefore, the complex index of refraction for absorptive mediums is given by equation 4.12.

$$m = \tilde{k}\left(\frac{c}{\omega}\right) = \frac{k_1}{|\tilde{k}|} + \frac{ik_2}{|\tilde{k}|} = n + i\kappa \tag{4.12}$$

Equation 4.12 shows that the real part of the refractive index is equivalent to the real part of the wave vector normalized to its magnitude, and the imaginary part of the refractive index is the imaginary part of the wave vector normalized to its magnitude. From this relationship, it is clear that the dispersion relations relating the complex index of refraction to the incident wavelength are equivalent to the dispersion relations that relate the complex wave vector to angular frequency. There is another relationship to be considered, which relates the time variation and the spatial variation of the incident wave according to equation 4.13.

$$k^2 = \varepsilon \left(\frac{\omega}{c}\right)^2 \tag{4.13}$$

From equations 4.11 and 4.13, the complex index of refraction m is the square root of the complex permittivity ε. To further define the components of each, the real part of the complex permittivity can be found by equation 4.14,

$$\varepsilon_1 = n^2 - \kappa^2 \tag{4.14}$$

and the imaginary part can be found by equation 4.15.

$$\varepsilon_2 = 2n\kappa \tag{4.15}$$

These relationships have been used extensively throughout this study, examples of which will be discussed in Chapter 5.

With the components of the complex index of refraction defined, the absorption coefficient α, the square root of which is proportional to detector sensitivity from equation 1.2, can be defined. As stated previously, the imaginary part of the refractive index stems from the attenuation of light as it passes through an absorptive medium. So,

for the imaginary part of the index of refraction, the phase velocity can be rearranged to

yield α by equation 4.16.

$$\alpha = \frac{2\omega\kappa}{c} = \frac{4\pi\kappa}{\lambda} \tag{4.16}$$

4.2 Absorption in PbSe Thin Films

Table 6. Calculated absorption coefficient using the dispersion relations from figure 28 for PbSe films.

Wavelength (μm)	n	k	α (cm^{-1})	Wavelength (μm)	n	k	α (cm^{-1})
2.166	4.7	0.25	14504.12	3.730	4.95	0.22	7412.09
2.237	4.7	0.254	14265.43	3.836	4.95	0.199	6519.07
2.441	4.7	0.238	12251.93	3.950	4.96	0.194	6172.30
2.686	4.7	0.45	21054.37	4.069	4.97	0.189	5837.17
2.797	4.9	0.4	17968.71	4.197	4.98	0.173	5180.31
2.919	4.88	0.25	10763.73	4.332	4.97	0.127	3684.05
2.984	4.883	0.22	9265.79	4.630	4.95	0.0572	1552.53
3.052	4.885	0.22	9058.64	4.796	4.94	0.0353	925.01
3.197	4.895	0.22	8647.44	4.973	4.94	0.00917	231.71
3.275	4.9	0.22	8441.55	5.165	4.94	0.00285	69.34
3.357	4.91	0.22	8234.60	5.371	4.92	0.00154	36.03
3.443	4.85	0.219	7993.46	5.595	4.9	0.00138	31.00
3.534	4.93	0.225	8001.05	5.838	4.83	0.00128	27.55

Using the dispersion relations found in figure 28, the wavelength dependent

absorption coefficient at room temperature for the investigated PbSe films was

calculated. Table 6 and figure 37 show the calculated results for the room temperature

absorption coefficient between approximately 2 μm and 6 μm. The calculated MWIR

absorption coefficient for the investigated films agrees well with the previously reported

value of 10000 cm^{-1} by Baleva [8].
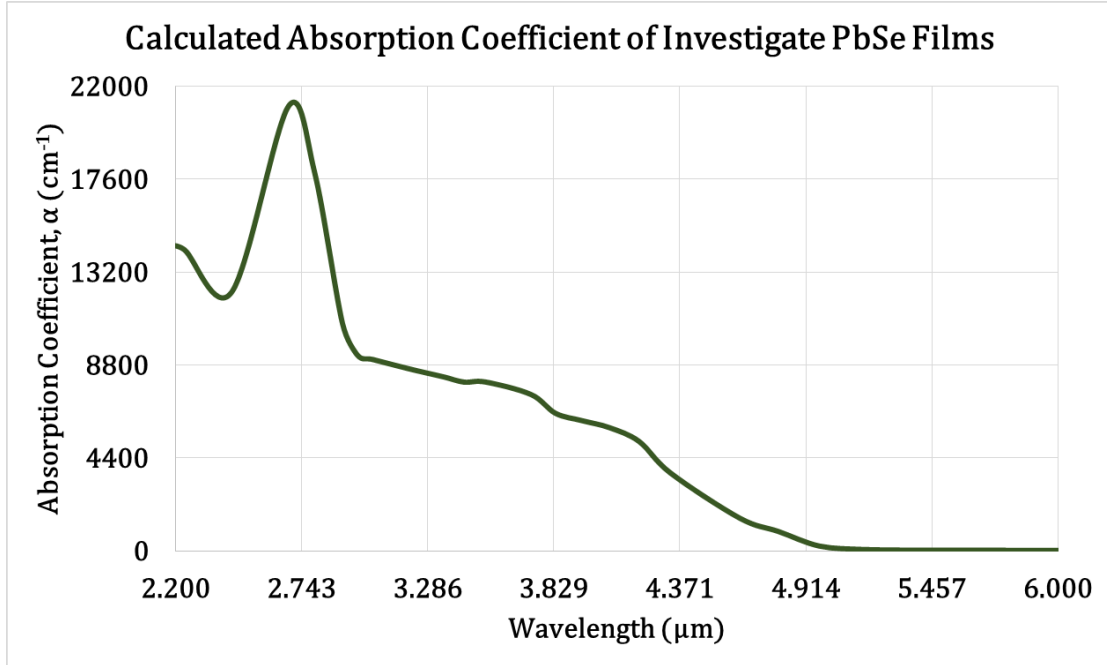
Figure 37. Calculated wavelength-dependent absorption coefficient of PbSe films.

As seen in figure 37, the absorption coefficient between 3 µm and 5 µm is weighted toward lower wavelengths. The Beer-Lambert law, seen in equation 4.17, describes the resulting field intensity I of a wave after it propagates through a finite distance within a medium,

$$I = I_0 e^{-\alpha t} \tag{4.17}$$

where I_0 is the incident field intensity in units of W/cm^2, and t is the thickness through which the wave propagates in cm [5]. Dividing the resulting field intensity by the incident field intensity yields the transmission, which can be used to find the absorption within the material by equation 4.18.

$$A = 1 - \frac{I}{I_0} = 1 - e^{-\alpha t} \tag{4.18}$$
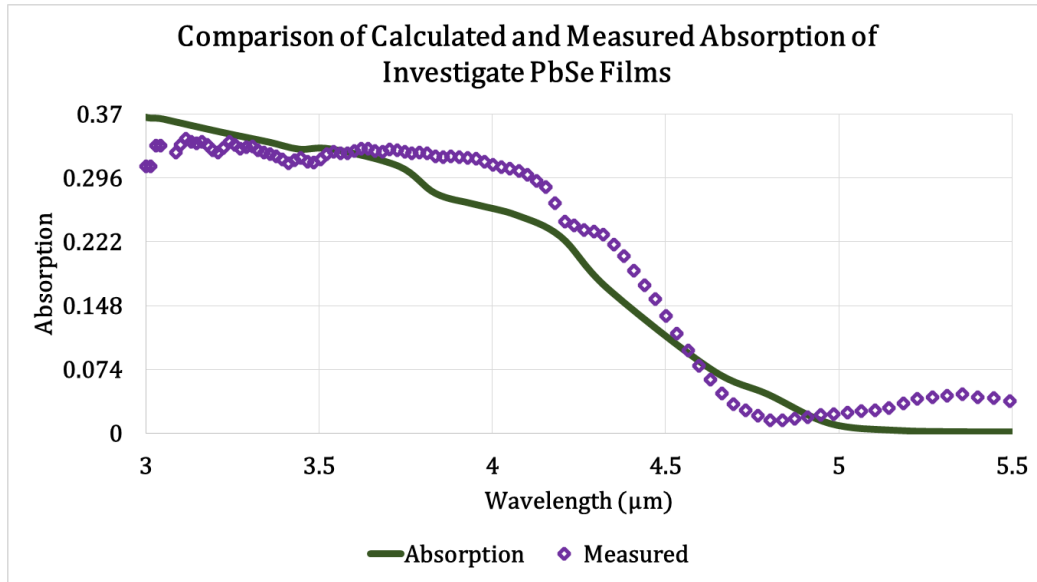
Figure 38. Comparison of absorption calculated from modified PbSe dispersion relations and measured absorption in multi-layer PbSe films.

Stated in Chapter 2, the investigated PbSe films of this study are grown to a thickness of approximately 1 µm, half of which is converted to PbI_2 after sensitization. Therefore, using equation 4.18 and the wavelength-dependent absorption coefficient found in table 6, I calculated the absorption within PbSe films. Shown in figure 38, the absorption of PbSe was calculated to be ~25-37% above the absorption edge. Included in figure 38 is the measured absorption spectrum from figure 20 for comparison. The calculated absorption agrees well with that of the measured up to ~3.6 µm, yet between 3.7 µm and 4.5 µm the measured spectrum has a higher absorption. The calculated spectrum of figure 38 only takes into consideration the dispersion relations of PbSe, yet the films I investigated were engineered to contain multiple layers of alternating values of the index of refraction. As mentioned in Chapter 2, the PbI_2 and SiO_2 layers, as well as the Si substrate, are wide bandgap semiconductors, so are considered to be transparent to MWIR radiation. However, from figure 38 it is clear that these layers have an effect on

107

the absorption of the films that were investigated. Previously described in Chapter 1, this multi-layer structure leads to constructive interference which increases the absorption for wavelengths close to 4 µm in the investigated films. The origin of the interference in multi-layer thin films will now be discussed.

4.3 Thin Film Interference
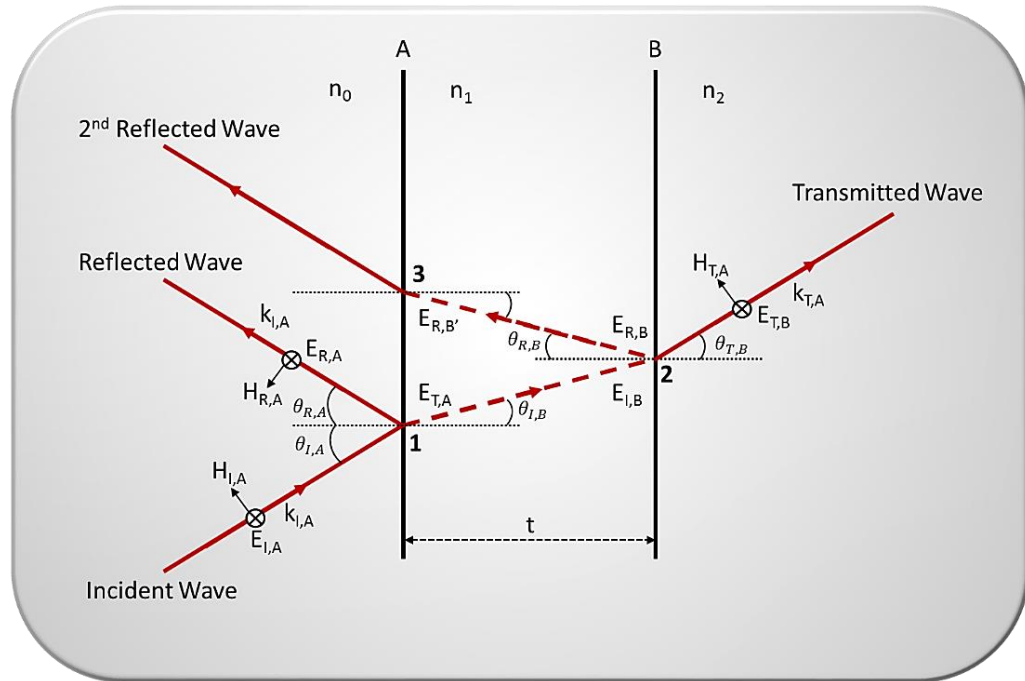
Figure 39. Interaction of a light wave as it transmits through the layers of an optical thin film.

Consider the situation presented in figure 39 in which an incident light wave travels within a three-layer thin film. The index of refraction of the three layers are labeled as n_0 for the incident medium which is considered to be air, n_1 for the intermediate medium, and n_2 for the final medium, which is considered to be a thick substrate. The electrodynamic behavior within the thin film leads to the phenomenon of reflection, transmission, and absorption [2, 5]. Let *A* represent the interface between medium 1 and medium 2, while *B* represents the interface between medium 2 and the

substrate. From the continuity condition of Maxwell's equations the tangential part of the electric and magnetic fields must be continuous across the boundary [5]. However, the normal part of the electric field is not continuous across the interface, due to the differences in the polarizabilities between materials on either side of the boundary. Instead the electric displacement is conserved [9]. Using the continuity condition, and utilizing the propagation vector $\boldsymbol{H} = \sqrt{\frac{\varepsilon_0}{\mu_0}}(n\boldsymbol{k} \times \boldsymbol{E})$, the electric E_A and magnetic H_A field components at A in figure 39 are given by equations 4.19 and 4.20,

$$E_A = E_{I,A} + E_{R,A} = E_{T,A} + E_{R',B} \tag{4.19}$$

$$H_A = \sqrt{\frac{\varepsilon_0}{\mu_0}}(E_{I,A} - E_{R,A})n_0 cos\theta_{I,A} = \sqrt{\frac{\varepsilon_0}{\mu_0}}(E_{T,A} - E_{R',B})n_1 cos\theta_{I,B} \tag{4.20}$$

where $E_{I,A}$, $E_{R,A}$, and $E_{T,A}$ represent the incident, reflected, and transmitted tangential electric field component at interface A. The quantity $E_{R',B}$ represents the tangential electric field component reflected from B, while the n_0 and n_1 are the refractive indices of the incident medium and the single layer film [5]. The prime denotation for the reflected part of the field is to indicate that the component is to be considered at interface A, which is to say it is the reflected component after passing through the film from A to B. The PbSe films and devices we investigated were designed to be illuminated at or near normal incidence, so the term $cos\theta_{I,A}$ can be considered to be 1. The refracted angle θ_B for the ideal case would also be normal to the film surface, however in real films significant scattering can occur which would increase the contribution from other angles of illumination.

Similarly, the components of the tangential part of the electric E_B and magnetic H_B fields are given by equations 4.21 and 4.22,

$$E_B = E_{I,B} + E_{R,B} = E_{T,B} \tag{4.21}$$

$$H_B = \sqrt{\frac{\varepsilon_0}{\mu_0}} \left(E_{I,B} - E_{R,B} \right) n_1 cos\theta_{I,B} = \sqrt{\frac{\varepsilon_0}{\mu_0}} E_{T,B} n_2 cos\theta_{T.B} \tag{4.22}$$

where $E_{R,B}$ is the component reflected from and in the vicinity of B, n_2 is the refractive index of the substrate or subsequent layer, and $\theta_{T,B}$ is the angle at which the beam refracts into the substrate.

Recall that the vacuum wavelength of light is reduced by the index of refraction of the medium in which it propagates. To determine if the first and second reflected waves interfere, consider the optical path length the original wave traverses as it propagates through the film. Referring to figure 39, let the point in which the incident ray enters the medium of index n_1 be denoted as **1**, the point in which the refracted wave enters the medium with refractive index of n_2 be known as **2**, and finally the point at which the second reflected wave exits the medium and enters the incident medium be **3**. The optical path length ΔPL is given by equation 4.23,

$$\Delta PL = \frac{|\overrightarrow{12}| + |\overrightarrow{23}|}{\lambda_n} = \frac{n(|\overrightarrow{12}| + |\overrightarrow{23}|)}{\lambda} \tag{4.23}$$

where $|\overrightarrow{12}|$ and $|\overrightarrow{23}|$ represent the length of the vectors between the points **1** and **2** and **2** and **3**, respectively [10]. In the special case of normal incidence, the sum of the length of the vectors between points **1**, **2**, and **3** is just double the thickness t. Thus, ΔPL then reduces to equation 4.24.

$$\Delta PL = \frac{2nt}{\lambda} \tag{4.24}$$

The numerator in equation 4.24 is known as the optical path length, which is used to determine whether interference will be constructive or destructive. The optical path

length is only part of the picture, however. Above, it was stated that the first wave will undergo a 180° phase shift upon reflection. This can be regarded as an equivalent path difference of $\Delta R = \lambda_0/2$, which must be taken into account. Including this phase shift, the conditions for constructive interference are given by equation 4.25, and those for destructive interference given by equation 4.26.

$$\Delta PL + \Delta R = p\lambda; (p = 1, 2, 3, \dots) \tag{4.25}$$

$$\Delta PL + \Delta R = p\lambda; \left(p = \frac{1}{2}, \frac{3}{2}, \frac{5}{2} \dots \right) \tag{4.26}$$

The importance of equation 4.25 and 4.26 with respect to the PbSe films of this study should be evident. When a light beam travels through the PbSe film, interference can occur due to the layers containing media of alternating high and low refractive index. In fact, this phenomenon can be exploited to increase the absorption and field intensity within the PbSe layer.

Returning to the light wave as it propagates through the film, a phase shift, shown in equation 4.27, will occur as the wave propagates through the film,

$$\frac{k_0(2n_1 t cos\theta_{I,B})}{2} = k_0 g \tag{4.27}$$

where the variable g has been used to simplify the parenthetical argument. The incident and reflected waves at B can then be defined in terms of the transmitted wave and reflected wave from B at A by equations 4.28 and 4.29.

$$E_{I,B} = E_{T,B} e_0^{-ikg} \tag{4.28}$$

$$E_{R,B} = E_{R',B} e^{ik_0 g} \tag{4.29}$$

The fields at interface A and interface B can now be described as in equations 4.30 - 4.33.

$$E_B = E_{T,A}e^{-ik_0g} + E_{R',B}e^{ik_0g} \tag{4.30}$$

$$H_B = \left(E_{T,A}e^{-ik_0g} - E_{R',B}e^{ik_0g}\right)\sqrt{\frac{\varepsilon_0}{\mu_0}}n_1\cos\theta_{I,B} \tag{4.31}$$

$$E_A = E_B\cos k_0g + \frac{H_B(i\sin k_0g)}{\sqrt{\frac{\varepsilon_0}{\mu_0}}n_1\cos\theta_{I,B}} \tag{4.32}$$

$$H_A = E_B\sqrt{\frac{\varepsilon_0}{\mu_0}}i\sin k_0g + H_B\cos k_0g \tag{4.33}$$

It is often more efficient to treat these equations in matrix form, especially when extending to multiple layers [5, 9]. The above relationships in matrix form are given by equation 4.34.

$$\begin{bmatrix} E_A \\ H_A \end{bmatrix} = \begin{bmatrix} \cos k_0g & \frac{i\sin gk_0g}{sqrt\left(\frac{\varepsilon_0}{\mu_0}\right)n_1\cos\theta_{I,B}} \\ \sqrt{\frac{\varepsilon_0}{\mu_0}}i\sin k_0g & \cos k_0g \end{bmatrix}\begin{bmatrix} E_B \\ H_B \end{bmatrix} \tag{4.34}$$

The transformation matrix that relates fields at the second interface to fields at the first is known as the characteristic matrix, which will be denoted as M_j where the subscript j represents the layer under evaluation. The characteristic matrix of a single layer has been given, however the method can be extended to a q-layer film with equations 4.35 and 4.36.

$$M_{film} = \prod_{j=1}^{q} M_j = M_1M_2 \cdots M_q = \begin{bmatrix} m_{11} & m_{12} \\ m_{21} & m_{22} \end{bmatrix} \tag{4.35}$$

$$\begin{bmatrix} E_A \\ H_A \end{bmatrix} = M_{film}\begin{bmatrix} E_{q+1} \\ H_{q+1} \end{bmatrix} \tag{4.36}$$

Returning to the single layer film, it is now possible to determine the reflection and transmission amplitude coefficients in terms of the components of the light wave [5, 9]. The matrix form of equations 4.21 and 4.22 is given by equation 4.37.

$$\begin{bmatrix} E_{I,A} + E_{R,A} \\ (E_{I,A} - E_{R,A})\sqrt{\frac{\varepsilon_0}{\mu_0}}n_0 cos\theta_{I,A} \end{bmatrix} = M_1 \begin{bmatrix} E_{T,B} \\ E_{T,B}\sqrt{\frac{\varepsilon_0}{\mu_0}}n_2 cos\theta_{T,B} \end{bmatrix} \tag{4.37}$$

Let $\tilde{r}$ and $\tilde{t}$ be the reflection and transmission amplitude coefficients, respectively. Relating these coefficients to the incident, reflected, and transmitted waves while expanding equation 4.37 leads to equations 4.38 and 4.39.

$$\tilde{r} = \frac{\left(\sqrt{\frac{\varepsilon_0}{\mu_0}}n_0 cos\theta_{I,A}m_{11} + \frac{\varepsilon_0}{\mu_0}n_0 n_2 cos\theta_{I,A}cos\theta_{T,B} - m_{21} - \sqrt{\frac{\varepsilon_0}{\mu_0}}n_2 cos\theta_{T,B}m_{22}\right)}{\sqrt{\frac{\varepsilon_0}{\mu_0}}n_0 cosAm_{11} + \frac{\varepsilon_0}{\mu_0}n_0 n_2 cos\theta_{I,A}cos\theta_{T,B}\, m_{12} + m_{21} + \sqrt{\frac{\varepsilon_0}{\mu_0}}n_2 cos\theta_{T,B}m_{22}} \tag{4.38}$$

$$\tilde{t} = \frac{2\sqrt{\frac{\varepsilon_0}{\mu_0}}n_0 cos\theta_{I,A}}{\sqrt{\frac{\varepsilon_0}{\mu_0}}n_0 cosAm_{11} + \frac{\varepsilon_0}{\mu_0}n_0 n_2 cos\theta_{I,A}cos\theta_{T,B}\, m_{12} + m_{21} + \sqrt{\frac{\varepsilon_0}{\mu_0}}n_2 cos\theta_{T,B}m_{22}} \tag{4.39}$$

For larger angles of incidence, the reflectance and transmittance amplitude coefficients can be very complex, however typical infrared detection and imaging systems are designed to collect light at small angles near normal incidence. This greatly reduces the complexity of equations 4.38 and 4.39. As an example, for a single layer film assuming normal incidence, equation 4.38 reduces to equation 4.40,

$$\tilde{r} = \frac{n_1(n_0 - n_2)cos k_0 g + i(n_0 n_2 - n_1^2)sin k_0 g}{n_1(n_0 + n_2)cos k_0 g + i(n_0 n_2 + n_1^2)sin k_0 g} \tag{4.40}$$

where n_2 in this case is the substrate refractive index. Finally, the square of the amplitude coefficients gives the overall reflectance R and transmittance T of the film. Therefore, the reflectance of the film is given by equation 4.41,

$$R_1 = r_1 r_1^* = \frac{n_1^2(n_0 - n_2)^2 cos^2 k_0 g + (n_0 n_2 - n_1^2) sin^2 k_0 g}{n_1^2(n_0 + n_2)^2 cos^2 k_0 g + (n_0 n_2 + n_1^2)^2 sin^2 k_0 g} \tag{4.41}$$

where the $*$ denotation represents the complex conjugate operator. Depending on the optical thickness of the film, R can be further simplified. This simplification is used in

113

thin film applications like interference filters, anti-reflection coatings, and dielectric mirrors [11-17].

4.4   **The Back Reflector Structure in PbSe**

Discussed in Chapter 1, interference in the investigated PbSe films is possible in the PbSe and PbI$_2$ layers. The majority of the field intensity enhancement, which directly effects the absorption, from constructive interference will occur within the PbSe layer. It should be noted, however, that the films are sufficiently thin that interference fringes generated in the PbI$_2$ will reach into PbSe offering a small enhancement [5]. From calculations shown in Chapter 1, I found that ~23% of the incident light will transmit through the film into the substrate without being absorbed or reflected. Though the situation presented in figure 2 assumes smooth layers and sharp interfaces, its argument is still valid for the rough films that were investigated. Indeed, figure 38 demonstrates the effects of interference in these multilayer films, yet up to 23% of the incident light is lost to transmission. The intensity of the resultant interference wave is directly related to the amplitudes of the constituent waves of which it is comprised [5, 9-10]. Therefore, the transmission loss through the substrate leads to reduced electric field intensity in the interference fringes created in the PbSe layer. The addition of an embedded metal reflector, in this case platinum, can help to circumvent this transmission loss by reflecting all of the light that transmits through the film without absorption or reflection back into the film. The back reflector is attractive as a PbSe enhancement mechanism due to its ease of fabrication, wide area coverage, wavelength selectivity, and large increase in absorption and field intensity [18-21].

Shown in figure 40, the difference in the PbSe structure with an embedded Pt reflector is minimal. The SiO_2 layer serves as a dielectric spacer with which to change the thickness of the film to selectively tune the resonant enhancement. The effective structure is that of a Fabry-Perot cavity [5, 10].
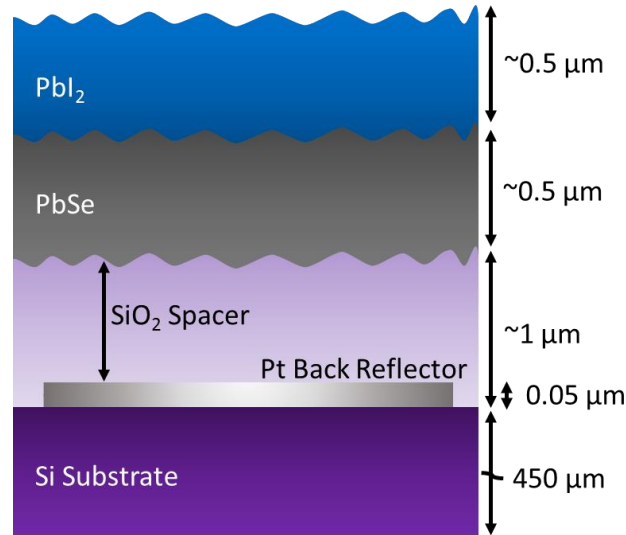
Figure 40. Depiction of PbSe film cross-section with embedded Pt back reflector.

Table 7. Layer thicknesses for modeled PbSe films with Pt back reflector.

Layer	Refractive Index, n	Thickness (nm)
PbI_2	2.5	400
PbSe	4.97	500
SiO_2	1.39	800-1400
Pt	3.23	50
Si substrate	3.49	450000

As an example, consider a PbSe film with an embedded Pt back reflector. The metal of choice would typically be gold due to its high reflectivity and low losses in the MWIR regime. However, our experiments have shown that gold diffuses into the PbSe film during the oxidation and sensitization processes. Therefore, Pt was selected due to

its high melting temperature, and high reflectivity in the MWIR regime [22]. As an aside, a popular configuration for commercial detectors is to back side illuminate them, such that the incident light transmits through the substrate instead of the top of the film. In this configuration, a dielectric spacer and back reflector could be deposited on the PbI_2 layer after the sensitization process, and gold could be used. However, for this study the films and devices were designed for front side illumination.
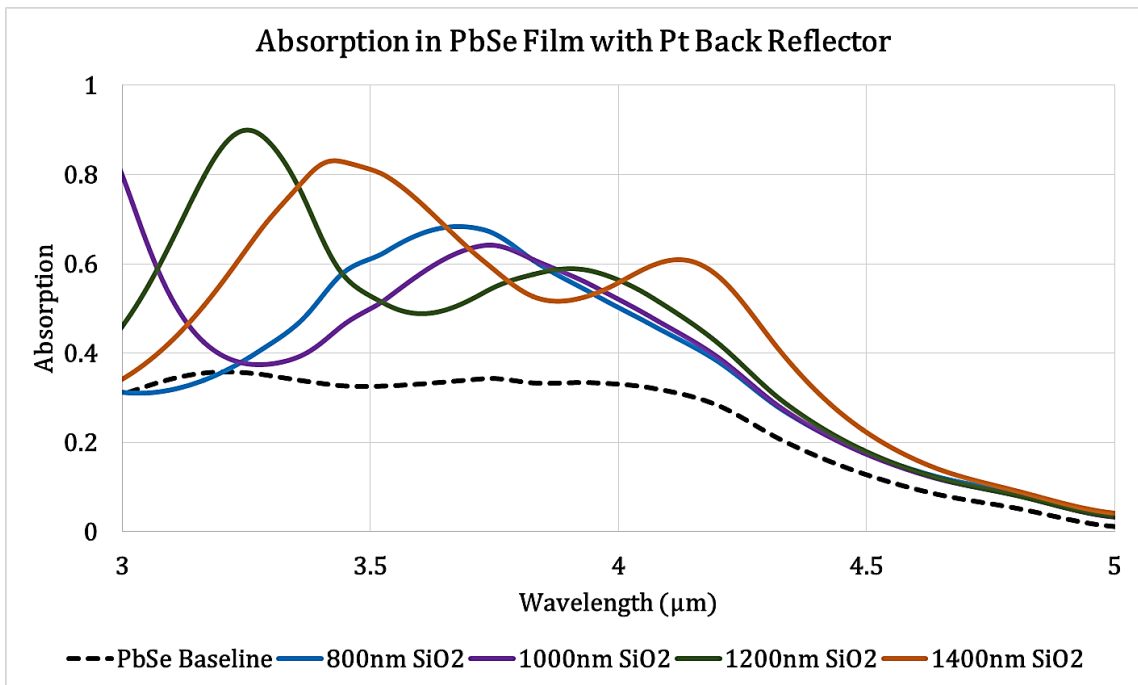
Figure 41. Calculated absorption in modeled PbSe films with Pt back reflector for various SiO_2 thicknesses.

To first order, the film can be modeled numerically using the transmittance and reflectance coefficients derived previously. I modeled PbSe films with *OpenFilters*, an open-source thin film program from Montreal Polytechnique [23]. The SiO_2 layer was varied between 800 nm to 1400 nm to observe how the spectrum shifts with dielectric spacer thickness. The layer thicknesses for the modeled films are shown in table 7.

The calculated absorption in the modeled films is shown in figure 41. The baseline PbSe film absorption (black dashed trace), shown here for reference, agrees well with the measured results of figure 20. For SiO_2 thicknesses of 800 nm (blue trace) and 1000 nm (violet trace), single resonance peaks are observed at 3.64 µm and 3.76 µm, respectively. As the SiO_2 thickness is increased, the single-peaked spectra of 800 nm and 1000 nm become two-peaked spectra for 1200 nm (green trace) and 1400 nm (orange trace). Further, the absorption spectrum red-shifts with SiO_2 thickness, moving one of the resonance peaks to coincide with the absorption edge of PbSe. The presence of multiple peaks and the red-shift are indicative of interference within the films. The SiO_2 spacer changes the length of the cavity setup within the film. When the thickness of the spacer is such that the cavity length corresponds to a longitudinal mode, optical interference will occur and increase the electric field intensity within the films [5]. These results demonstrate that by changing the SiO_2 thickness, the absorption can be selectively tuned to the desired spectral region.

I also calculated the amplitude of the absorption enhancement, shown in figure 42, by dividing the absorption spectrum for each SiO_2 thickness by that of the baseline PbSe film. Here, only the results between 3 µm and 4.5 µm are considered relevant, because the absorption is relatively low and falls off at longer wavelengths. The baseline trace, which represents the absorption in PbSe films without a back reflector, is shown as a black dashed line for reference. The results of these preliminary calculations were used to determine the optimum SiO_2 thickness for back reflector enhanced PbSe devices. In this case, a SiO_2 thickness of 1400 nm was found to be desirable due to the large peak at 3.45 µm and the peak close to the PbSe absorption edge at 4.2 µm. Indeed, the 1400 nm

SiO₂ thickness yields an absorption as high as 2.55-times greater than that of baseline films, as well as a factor of two enhancement at the PbSe absorption edge. Described in Chapter 5, a second, higher fidelity optimization study was conducted utilizing finite element analysis to further refine these initial calculations before fabrication.
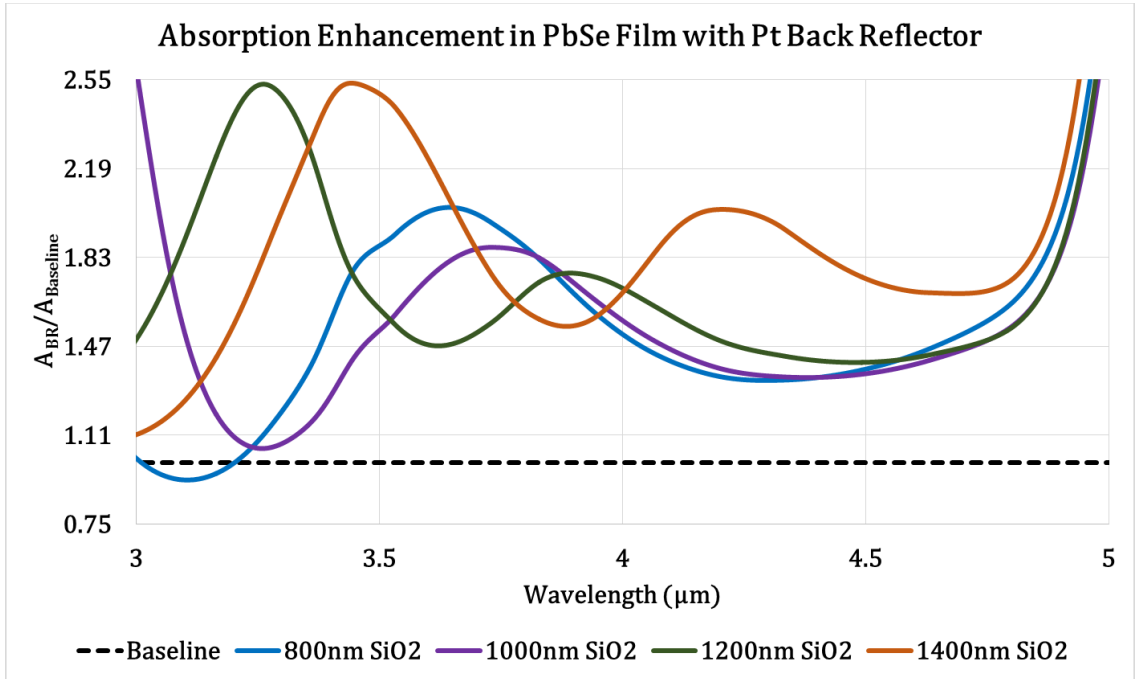
Figure 42. Calculated absorption enhancement in PbSe films with back reflector as a function of SiO₂ thickness.

Chapter 4 References

[1]   J. D. Jackson, *Classical electrodynamics*, New York: Wiley, 1999.

[2]   J. D. Griffiths, *Introduction to electrodynamics*, Upper Saddle River, N.J: Prentice Hall, 1999.

[3]   C. A. Balanis. *Advanced Engineering Electromagnetics*, 1st Ed., Hoboken, NJ: John Wiley and Sons, Inc. 1989.

[4]   D. Sarid and W. Challner, *Modern Introduction to Surface Plasmons: Theory, Mathematical Modeling, and Application*, New York, NY: Cambridge University Press, 2010.

[5]   E. Hecht, *Optics*, 4th Edition. Addison-Wesley, New York, 2002.

[6]   K. Kasunic, Optical Systems Engineering. McGraw-Hill Education, 2011.

[7]   C. J. Willers, Electro-Optical Systems Analysis and Design, Bellingham, WA: SPIE Press, 2013.

[8]   Baleva, et al. "Infrared Absorption of Laser Deposited PbSe Films," J. Physics C, Sol-State Phys., 1987.

[9]   I. Chambouleyron and J. M. Marinez, *Handbook of Thin Films Materials*; ch 12, edited by Nalwa, H.S., Academic Press, 2001.

[10]   OP-Tec: National Center for Optics and Photonics Education, *Fundamental of Light and Lasers*, 2nd ed. Texas: Op-TEC, 2013.

[11]   M. S. Rauscher, et al. "Dual-channel mid-infrared sensor based on tunable Fabry-Perot filters for fluid monitoring applications," Sensors and Actuators B 259, 2018.

[12] E. Gayo, and J. Frutos, "Interference filters as an enhancement tool for infrared thermography in humidity studies of building elements," Infrared Physics and Technology 38, 1997.

[13] L. Fei, et al. "Design and fabrication of composite structure in ZnSe providing broadband mid-infrared anti-reflection," Optical Materials 84, 2018.

[14] H. Wu, et al. "High quantum efficiency N-structure type-II superlattice mid-wavelength infrared detector with resonant cavity enhanced design," Superlattices and Microstructures 105, 2017.

[15] F. Felder, et al. "Lead Salt Resonant Cavity Enhanced Detector with MEMS Mirror." Physics Procedia 3, 2010.

[16] W. Heiss, et al. "Epitaxial Bragg mirrors for the mid-infrared and their applications." Progress in Quantum Electronics 25, 2001.

[17] T. Wood, et al. "Study of the influence of temperature on the optical response of interferometric detectors systems," Sensors and Actuators A 203, 2013.

[18] S. Jain, et al. "Broadband absorption enhancement in ultra-thin crystalline Si solar cells by incorporating metallic and dielectric nanostructures in a back reflector," Pro. Photovolt: Res. Appl., Vol. 23, 2015.

[19] J. Piotrowski and A. Piotrowski, "Uncooled infrared photodetectors in Poland," Opto-Electron. Rev., 14, no. 1, 2006.

[20] J. J. Talghader, A. S. Gawarikar, and P. R. Shea, "Spectral selectivity in infrared thermal detection," Light: Science & Applications, Vol. 1, 2012.

[21] X. Tang, M. Ackerman, and P. Guyot-Sionnest, "Thermal Imaging with Plasmon Enhanced HgTe Collidal Quantum Dots Photovoltaic Devices," manuscript nn-2018-03871g submitted to ACS Nano, 2018.

[22] A. Y-C. Yu and W. E. Spicer, "Optical Properties of Platinum," Physical Review, Vol. 171, No. 3, 1968.

[23] S. Larouche, and L. Martinu, "OpenFilters: open-source software for the design, optimization, and synthesis of optical filters," Appl. Optics, vol. 47, issue 13, 2008.

[24] Evan, Amato. University of California San Diego, Scripps Institute of Oceanography, Department of Atmospheric and Climate Sciences 251: Radiation The Atmosphere Ch3 Class Notes

[25] C. Matzler, "MATLAB Functions for Mie Scattering and Absorption," Institut fur Angewandte Physik, Research Report No 2002-08, 2002.

Chapter 5: Design Methodology and Performance Predictions

We have shown that, depending on the type of resonant structure, there are many

degrees of freedom with which to selectively enhance PbSe films. As we discussed in

Chapter 3, with surface plasmon resonant structures the morphology, metal type, and

surrounding material dictate the resonant condition. In regards to the back reflector

structure discussed in Chapter 4, the metal type and dielectric spacer thickness determine

the resonance. To narrow the design space, I employed a design methodology similar to

that of Choi [1-3]. First, numerical analysis was carried out using *MATLAB* or

OpenFilters to select design parameters. The chosen parameters were inserted into the

finite element modeling (FEM) tool *ANSYS HFSS* to predict the absorption, as well as the

field dynamics, in the PbSe films we investigated [4-10]. I started finite element

modeling efforts with a single unit cell, the results of which were compared with those

obtained with numerical methods for validation. Then, an infinite array of unit cells,

meant to approximate the physical film, was modeled to determine the effect of the

resonant structure on the film absorption. For optimization, I conducted parametric

analyses of structure and film parameters, the results of which were used to choose the

optimum design dimensions. Structures based on the chosen parameters were fabricated

with help from my collaborators, and incorporated into our PbSe photoconductive

detectors. I conducted detector measurements, and compared the results to my models for

concurrence. Moreover, I compared the resonant structure enhanced PbSe

photoconductor measurements to the reference detector measurements, shown in Chapter

2, to verify we had achieved the goal of raising the operating temperature of PbSe

detectors. These last two steps will be described in Chapter 6. In this chapter, the design and optimization of the resonant structure enhanced films will be discussed in detail.

5.1 **FEM and the *ANSYS HFSS* Environment**

The necessary theoretical background for resonant structures based on surface plasmon resonance and interference effects were discussed in Chapter 3 and Chapter 4. The numerical models I constructed and employed for this investigation follow closely with the theoretical background, and thus will not be discussed here. Instead, attention is turned to the finite element analysis method and the *ANSYS HFSS* simulation environment.

Finite element modeling (FEM) is a powerful tool for solving Maxwell's equations for complex objects [11-12]. The solution to these relationships can become intractable, requiring large computing resources and time to produce meaningful results. The FEM method is attractive due to its capability of solving nonhomogeneous regions quickly and efficiently.
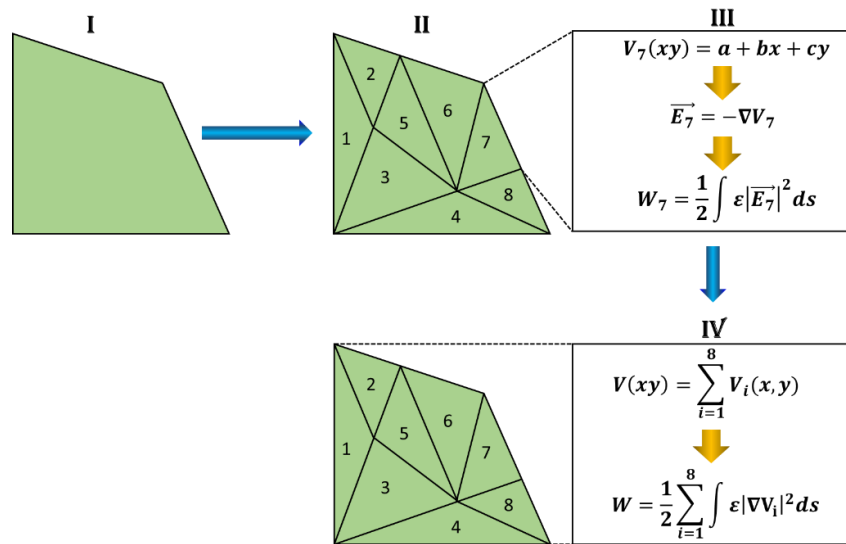
Figure 43. Simple depiction of the finite element method (FEM) for solving electromagnetic problems.

Depicted in figure 43, there are four major steps in the FEM method [12]. In step **I** the object (or objects) under investigation are defined, and in step **II** the region is discretized into smaller volume elements such as hexahedrons, or tetrahedrons. Here, a two-dimensional solution space has been divided into triangular elements for simplicity. The collection of segmented elements forms what is known as the mesh. In **III** the electric potential in a single element is approximated by a polynomial solution of the form found in equation 5.1,

$$V_i(x, y) = a + bx + cy \tag{5.1}$$

where a, b, and c are constants. When solving for the solutions of a single element, the electric potential is assumed to be non-zero inside the element and zero everywhere else. Moreover, the electric potential is assumed to vary linearly, such that the electric field, shown in equation 5.2, is uniform within the element.

$$\boldsymbol{E}_i = -\nabla V \tag{5.2}$$

The energy per unit length, which in this example is the desired quantity, of the element is found by equation 5.3,

$$W_i = \frac{1}{2} \int \varepsilon |\boldsymbol{E}_i|^2 \, ds \tag{5.3}$$

where ε is the permittivity within the element. After finding a solution for each element, step **IV** is to solve for the entire solution space by summing the constituent solutions. For an excellent rigorous explanation and mathematical derivation of the finite element method, the reader is referred to [12].

The high frequency structure simulator available from ANSYS, Inc. (*ANSYS HFSS*) is a full 3-dimensional frequency domain solver for Maxwell's equations [13-14]. Similar to programs such as *COMSOL Multiphysics* and *CST Microwave Studio*, *ANSYS HFSS* is an integrated computer aided design (CAD)-solver environment with a built in graphical user interface in which the user has the ability to draw, model, and simulate nearly any electromagnetic problem imaginable [15]. *ANSYS HFSS* uses the FEM, where solutions for the electric field take on the form of equation 5.4,

$$\nabla \times \left(\frac{1}{\mu_r}\nabla \times \boldsymbol{E}\right) - k_0^2\varepsilon_r\boldsymbol{E} = \boldsymbol{J}_{source} \tag{5.4}$$

where μ_r is the relative permeability, ε_r is the relative permittivity, k_0 is the wave number defined as ω/c, ω is the angular frequency of the wave, c is the speed of light in vacuum, and $\boldsymbol{J}_{source}$ represents the source current density. The magnetic field is calculated using equation 5.5,

$$\boldsymbol{H} = \frac{1}{\omega\mu}\nabla \times \boldsymbol{E} \tag{5.5}$$

and the other electromagnetic properties are derived from equations $3.5 - 3.7$ in Chapter 3. *ANSYS HFSS* finds solutions using a similar approach to that defined in figure 43. However, *ANSYS HFSS* uses a proprietary algorithm in which the approximated solution is then evaluated against pre-defined error criteria, and the mesh is refined into smaller elements to iterate the process until the solution falls below the error threshold [14]. This adaptive mesh process is depicted in figure 44, where between steps **IV** and **V** the difference between S-parameter solutions, defined shortly, of two consecutive iterations are compared to the preset error criterion.
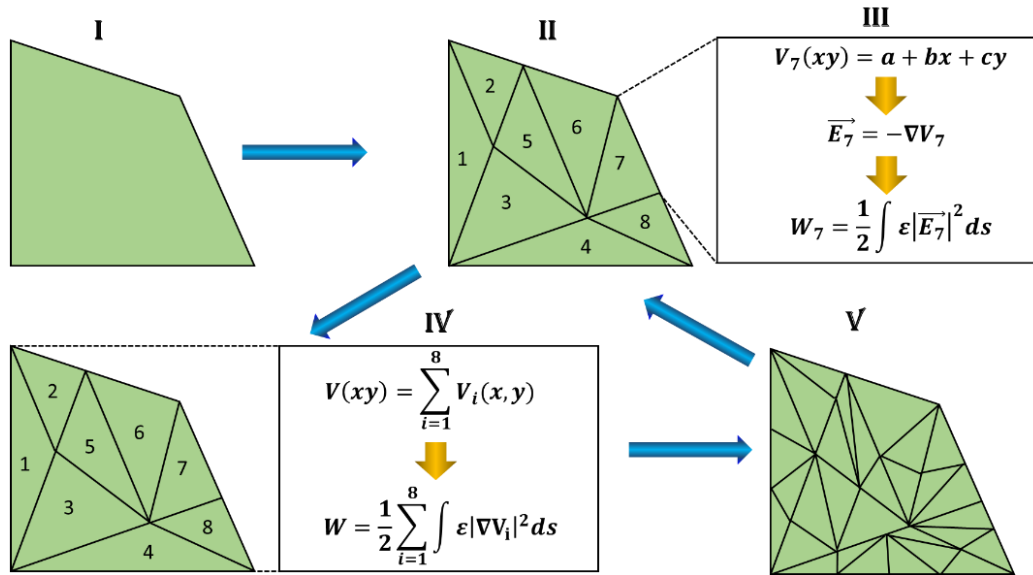
Figure 44. Simple depiction of adaptive mesh process in ANSYS HFSS.
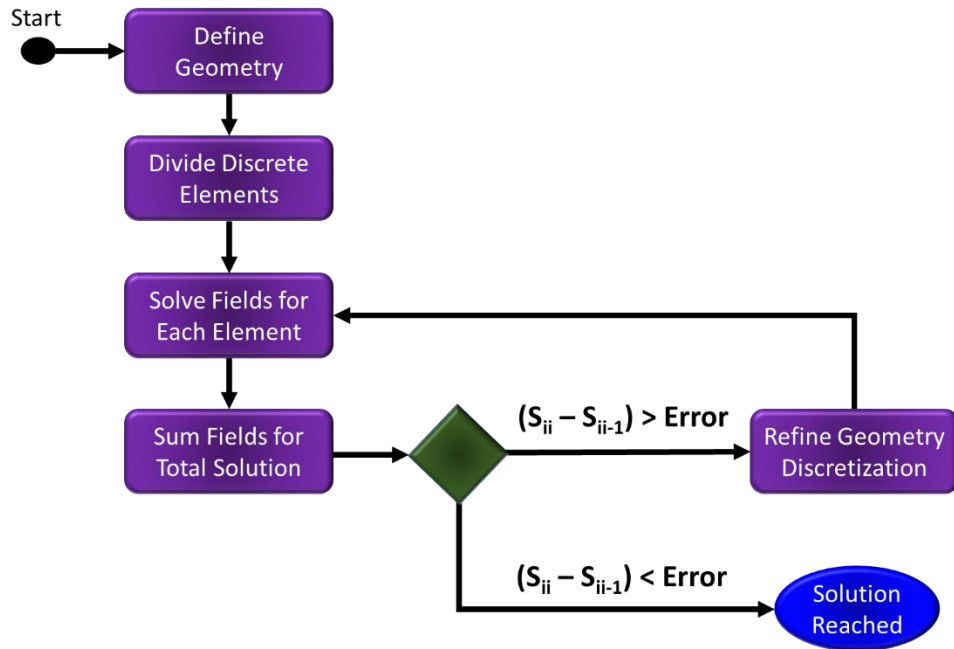
Figure 45. Simple flow block diagram for the FEM and adaptive mesh refinement in ANSYS HFSS.

For clarity, a flow block diagram of the adaptive mesh procedure is shown in figure 45. In the next section, the details of setting up the *ANSYS HFSS* modeling environment will be discussed in the context of the PbSe films we investigated.

5.2 Modeling the PbSe Film with ANSYS HFSS

Layer	Pitch (µm)	Thickness (µm)
PbI_2		$t\_PbI_2 = 0.4$
PbSe		$t\_PbSe = 0.5$
SiO_2	0.5	$t\_SiO_2 = 1.225$
Si		$t\_Si = 0.05$ (Truncated)
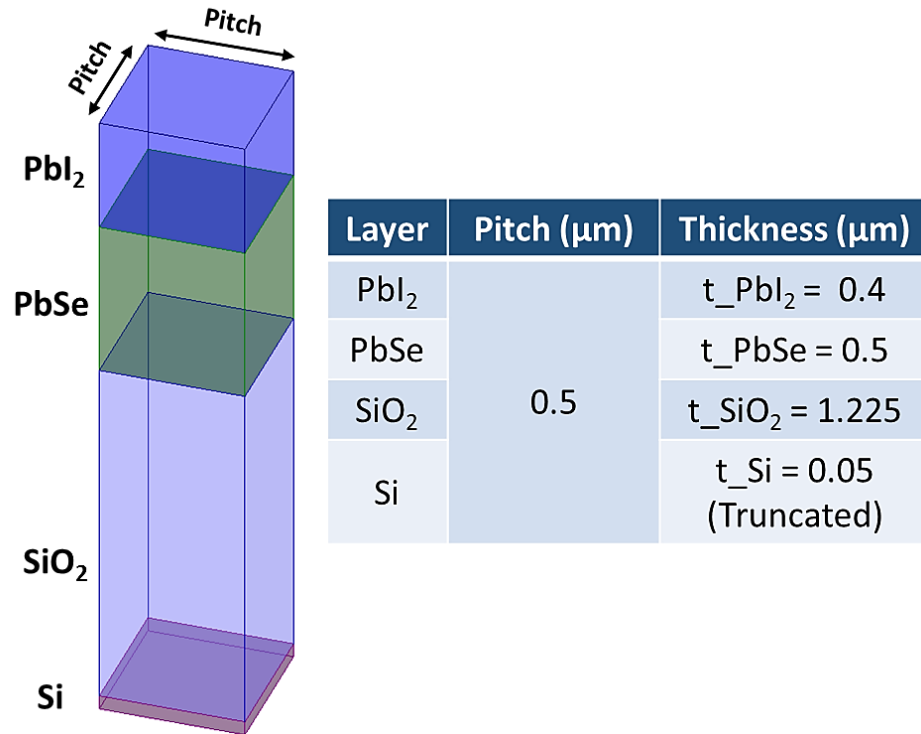
Figure 46. Unit cell of the PbSe films under investigation modeled in ANSYS HFSS.

The PbSe films we investigated, shown in figure 46, were drawn in the GUI of

ANSYS HFSS. A driven modal solution setup was selected to solve for the whole film

[14]. The film was input layer by layer, with the side length of each layer being input as

the variable *pitch*. The thicknesses of each layer are input as *t_"layer/structure"*, where

the "layer/structure" section is replaced by the material of the layer or the structure. For

example, the thickness of the PbSe layer is input as *t_PbSe*. Variable names were used to

enable the use of parametric analysis in the "Optimetrics" feature of *ANSYS HFSS* [4]. It

should be noted that due to the large thickness of the Si layer (450 µm), it was input with

a thickness of only 50 nm. This approximation was used to save computational time.

Further, when the full substrate thickness was input, I observed several erroneous peaks

in the modeled result. Due to the principles described in Chapter 1 and Chapter 4, it was only necessary to model the SiO$_2$-Si interface to observe interference effects. Therefore, the truncation of the substrate was found to be an acceptable approximation.

After defining the geometry, the next step was to specify the material parameters for each layer. In *ANSYS HFSS*, materials are defined by two properties [8]. The first is the real part of the relative permittivity of the material, and the second is either the loss tangent $tan\,\delta$ or the frequency dependent conductivity σ_{AC}. The real and imaginary parts of the complex permittivity have already been defined in equations 4.14 and 4.15 of Chapter 4. The loss tangent and complex conductivity were used to simulate the losses in the material, and are given by equations 5.6 and 5.7, respectively,

$$tan\,\delta \cong \frac{\varepsilon''}{\varepsilon'} \tag{5.6}$$

And

$$\sigma_{AC} = 2\pi f \varepsilon'' \varepsilon_0 \tag{5.7}$$

where ε' and ε'' are the real and imaginary parts of the complex permittivity, f is the frequency of the electromagnetic wave, and ε_0 is the permittivity of free space [16]. Typically, the loss tangent was used in this study for PbSe, while the frequency dependent conductivity was used for Au and Pt. Recall from Chapter 2 that the other semiconductor layers were treated as non-absorbing due to their large bandgaps, and to ensure the absorption in the film is representative of the PbSe active layer. Therefore in the Si, SiO$_2$, and PbI$_2$ layers, only the real part of the relative dielectric constant was utilized.
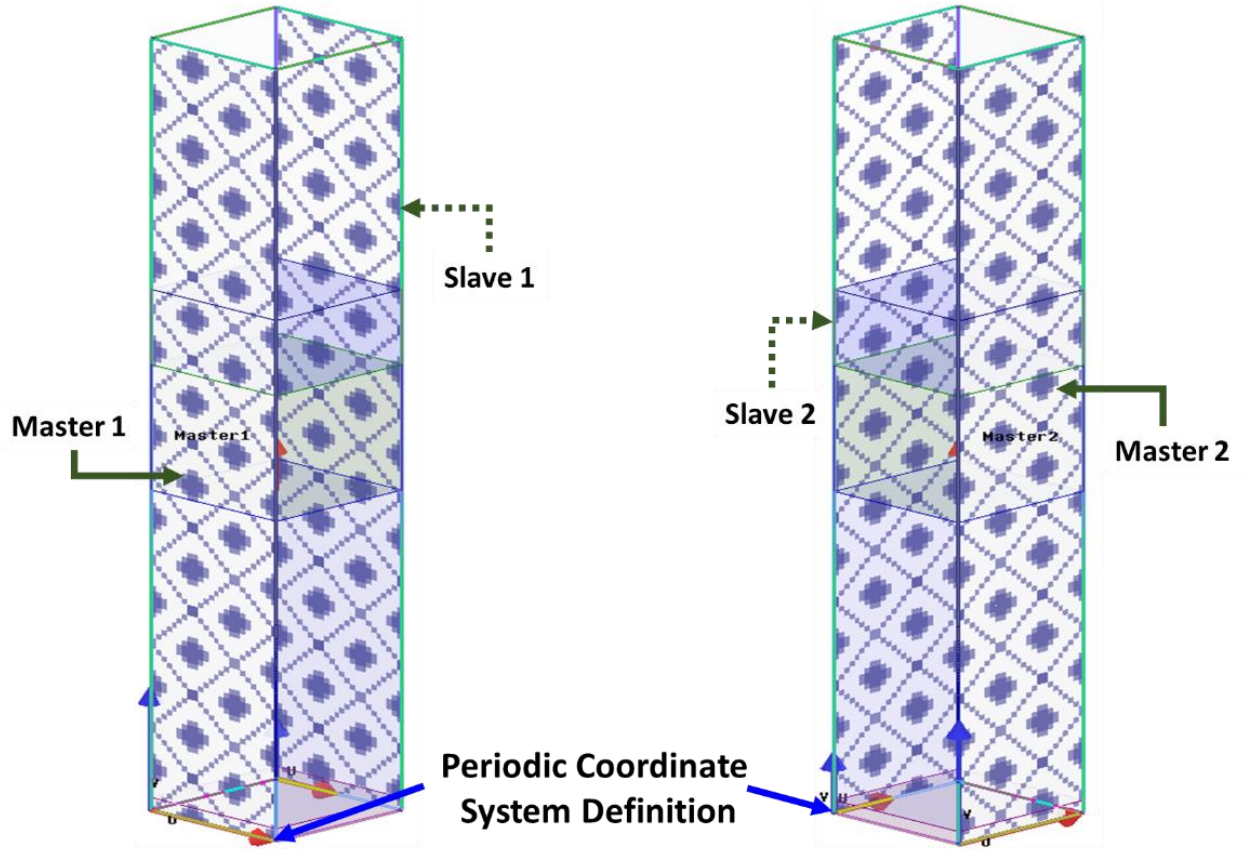
Figure 47. Periodic Master/Slave boundary conditions for modeled PbSe films.

The next step was to select the boundary conditions for the film [17]. Periodic boundary conditions, shown in figure 47, known as Master/Slave boundary conditions were assigned on the faces of the unit cell. To simplify the process of defining the boundary conditions, as well as to the ensure there was enough room between the excitation and the film surface to approximate the far field, a vacuum box $(\varepsilon_r, \mu_r = 1)$ was used around the unit cell with a thickness equal to the sum of the thicknesses of each layer and an additional space of 1 micron. Master boundary conditions were placed on two adjacent faces, labeled *Master1* and *Master2*, while *Slave1* and *Slave2* were placed on the opposite faces. For each master boundary condition, a coordinate system (U,V) was selected to define the direction of periodicity. With this configuration, the solutions

of Maxwell's equations are calculated for a single unit cell, and symmetry is used at the boundaries to approximate them for either a finite or infinite array [17-18]. In the case I simulated the PbSe film as an infinite array to approximate the real film.

Flouquet ports, excitation ports for plane-periodic structures, were used to excite the unit cell. For these ports, the user defines a set of modes that represent plane wave modes with their direction of propagation set by the defined frequency, phase angle, and geometry of the unit cell [19]. Stated in Chapter 2 and Chapter 4, the PbSe photoconductors we investigated were designed to operate at normal incidence. Therefore, the angle of incidence in the models was kept at 0 degrees. Plane wave illumination was assumed in both the TM and TE polarization directions, so only the TE_{00} and TM_{00} modes were used. Flouquet ports offer a relatively simple way to determine the reflection, transmission, and absorption of a modeled structure in the form of S-parameters.

Scattering parameters, known as S-parameters, are defined as a transfer matrix that relates an incoming set of parameters on a multi-port system to the output of the system [20-21]. For simplicity, consider a two port system in which the input is labeled as I_1 and I_2, and the output is labeled as O_1 and O_2. The outputs O_1 and O_2 are defined in terms of the inputs I_1 and I_2 by equation 5.8.

$$\begin{bmatrix} O_1 \\ O_2 \end{bmatrix} = \begin{bmatrix} S_{11} & S_{12} \\ S_{21} & S_{22} \end{bmatrix} \begin{bmatrix} I_1 \\ I_2 \end{bmatrix}$$

(5.8)

Here, S_{11} and S_{22} are the TE and TM reflection coefficients, while S_{12} and S_{21} are the TE and TM transmission coefficients. Similar to the Fresnel reflection and transmission coefficients, to find the percent of the incident excitation reflected R or transmitted T, the

S-parameters must be squared. Therefore, the reflection, transmission, and absorption in the film can be found using equations 5.9-5.11.

$$R = S_{11}^2 \ or \ S_{22}^2 \tag{5.9}$$

$$T = S_{21}^2 \ or \ S_{12}^2 \tag{5.10}$$

$$A = 1 - S_{11}^2 - S_{21}^2 \ or \ 1 - S_{12}^2 - S_{22}^2 \tag{5.11}$$

After the film geometry, boundary, and excitation conditions were established, the analysis setup was defined. In *ANSYS HFSS* the initial solver frequency, error threshold, number of convergence passes, mesh refinement, solver type, and port impedance must be specified. Table 8 shows the analysis setup parameters I used to simulate the fields in the modeled PbSe films. When modeling resonant or frequency dependent structures, if the frequency dependent behavior is unknown the frequency should be set to the highest frequency of interest [7]. The spectral region of interest in these films is from 3 µm to 5 µm, so the solver frequency was set to 100000 GHz. To ensure the solver would reach convergence, the maximum number of iterative passes was set to 15. This number of passes was chosen empirically during the modeling process as a balance between computation time, and convergence time-out. The error threshold was set to be slightly lower than the default value, again chosen empirically. The default maximum refinement, which takes advantage of the *ANSYS HFSS* built-in adaptive mesh algorithm, was found to be sufficient [21]. The mixed-order solver, which is the most accurate of the available solvers, was used. For periodic arrays, *ANSYS HFSS* has a feature called domain-decomposition in which computation time can be reduced using high performance parallel computing to distribute a model's solutions across multiple resources [22]. This feature was utilized to reduce computation time. Finally, an interpolating frequency

sweep with 500 points was defined between 50000 GHz and 120000 GHz. The interpolating sweep provides accurate S-parameter solutions, and is used when the fields are not necessarily the parameter of interest [14]. Later, when discussing the electric fields within the film, we use discrete frequency sweeps, in which the field quantities are saved at each frequency to calculate figures of merit.

Table 8. Specified analysis setup parameters for modeled PbSe film simulations in ANSYS HFSS.

Initial Solve Frequency (GHz)	Convergence Passes	Error Threshold (Max Delta S)	Maximum Mesh Refinement/Pass	Solver
100000	15 Minimum 3 Minimum Converged Passes 2	0.01	30%	Mixed Order; Domain Decomposition
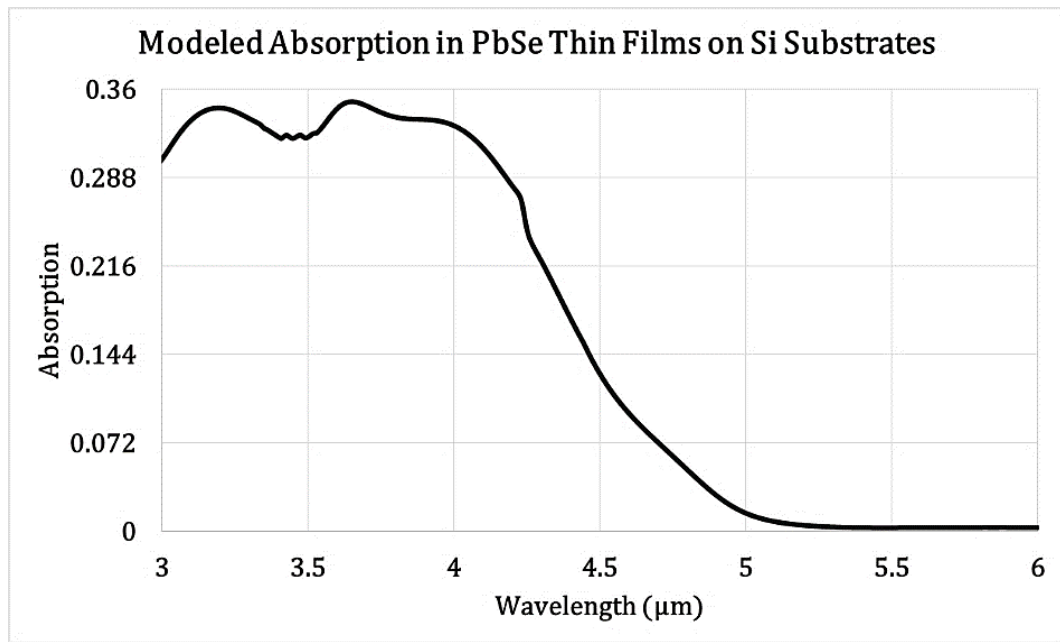
Figure 48. Modeled absorption in PbSe thin films with 1225 nm SiO$_2$, 500 nm PbSe, and 400 nm PbI$_2$.

To determine the absorption of the PbSe film depicted in figure 46, the S-parameters of the TM mode were used. It should be noted that this unit cell has a polarization independent configuration, so the TE mode yielded the same results. A

parametric analysis was conducted to determine which SiO_2, PbSe, and PbI_2 thicknesses

resulted in an absorption spectra in agreement with figure 20. It was found that a SiO_2

thickness of 1225 nm, PbSe thickness of 500 nm, and a PbI_2 thickness of 400 nm resulted

in a closely matched absorption spectrum. Figure 48 shows the absorption of the modeled

film. The decrease in absorption centered at 3.5 µm is associated with interference in the

films, which is also present in figure 20. Moreover, this interference was also found to be

present in the spectral response and quantum efficiency of the baseline detectors shown

in figure 22, suggesting it even plays a significant role in our baseline PbSe detectors.
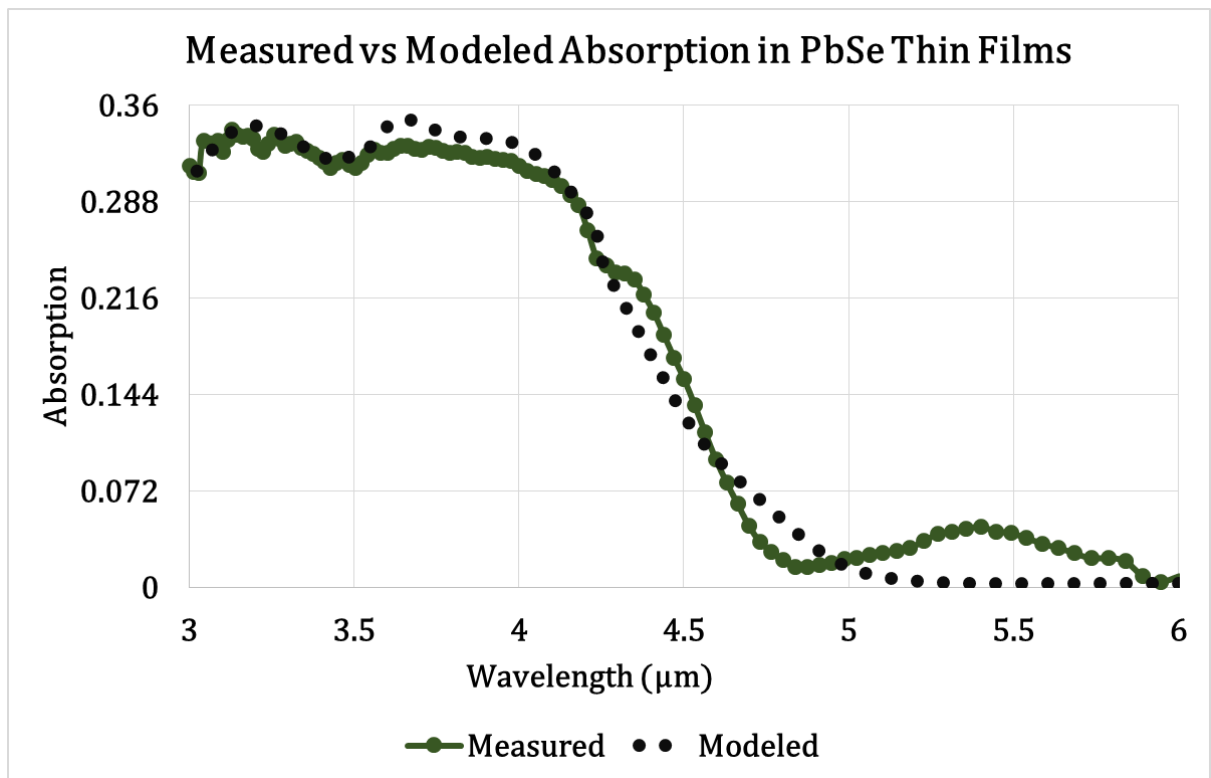
Figure 49. Comparison of modeled to measured absorption in PbSe films for model validation.

Before moving on, it is important to review how the model was validated.

Modeling and simulation are powerful tools used to predict real system behavior, thereby

making the engineering process more efficient. Further, they provide insight into the

underlying mechanisms and working principles in the system under investigation. To this end, I compared the modeled and measured absorption to validate the model. Figure 49 shows that the modeled spectrum agrees well with the measured spectrum, with only minor deviations attributed to surface roughness and impurities as mentioned in Chapter 2. The close agreement between modeled and measured results shows that the model can be used to predict, at least to first order, the absorptive behavior of the investigated PbSe films.

5.3 Predicted Results for Metal Discs in PbSe Films

For surface plasmon resonant structures, the disc shape was chosen for its polarization independence and simplicity of fabrication. To select the aspect ratio, defined as the quotient of disc diameter and thickness, I completed a parametric study using a quasi-static model developed in *MATLAB* (see Appendix B). The Au and Pt discs were modeled with a fixed disc thickness of 20 nm, and a disc diameter varying from 40 nm to 500 nm. This resulted in a disc aspect ratio between 2 and 25. In anticipation of the limitations of fabrication on rough surfaces, the discs were considered at the SiO_2-PbSe interface. The discs would be patterned and fabricated on the SiO_2 before roughening and PbSe deposition. Figure 50 shows an example result from the parametric study. Recall from Chapter 3 that the extinction Q-factor is the sum of the absorption and scattering Q-factors. As seen in figure 50, the absorption Q-factor is very small, and the scattering and extinction Q-factors lie on top of one another. Therefore, the extinction Q-factor is dominated by scattering. As mentioned Chapter 3, this means the evanescent waves generated due to surface plasmon polaritons will be traveling waves. The resonance for Pt discs with a 12.5 aspect ratio was found to be at 3.74 µm.
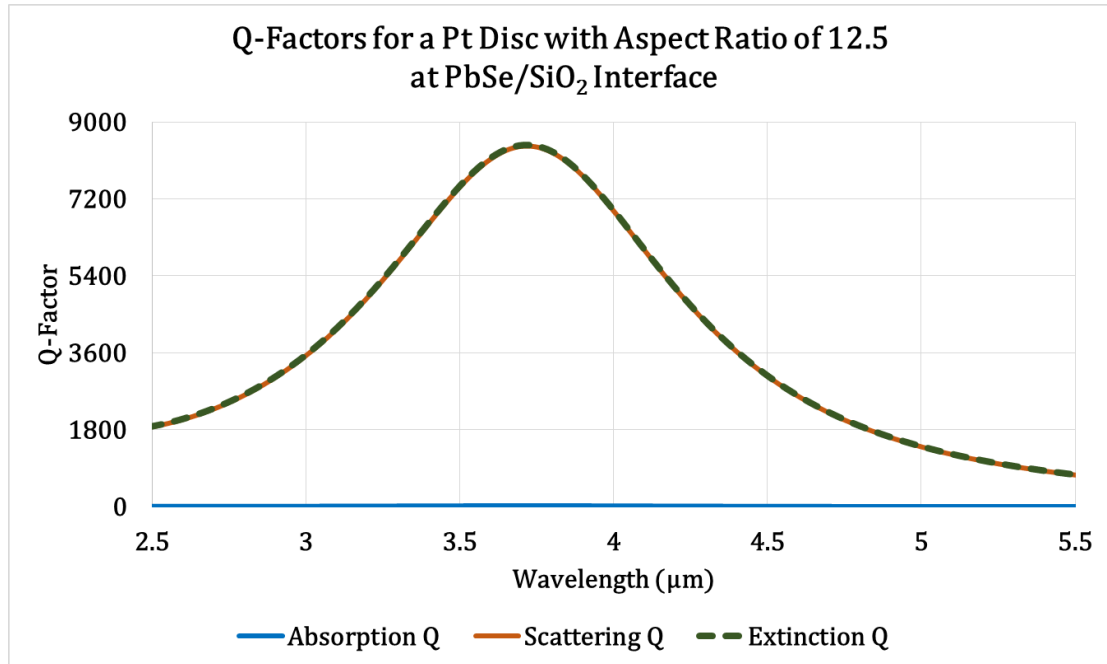
Figure 50. Efficiency (Q) factors of Pt discs at SiO₂/PbSe interface for an aspect ratio of 12.5.

In both Au and Pt, scattering was found to be the dominant surface plasmon phenomenon. In fact, as a general observation, scattering was found to dominate in the plasmonic disc structure regardless of metal. From Mie theory, scattering becomes the dominant mechanism for large structures [24-25]. Therefore, due to the large diameter of the discs, this observation is expected behavior and an excellent reason to choose the disc shape for enhancing PbSe detectors. Figure 51 shows how the efficiency factors for Au and Pt discs vary as a function of disc diameter. For larger aspect ratio discs, the resonance red-shifts, and the amplitude increases. Moreover, the width of the resonance peak, defined as the full width at half maximum, increases. For the Au discs, it increases from an estimated 0.5 µm at an aspect ratio of 15 to 0.8 µm at an aspect ratio of 25. The Pt discs starts with and maintains a larger resonance peak width than the Au; where an aspect ratio of 12.5 resulted in a width of 1.2 µm, and at an aspect of 25 a width of 2 µm.

135
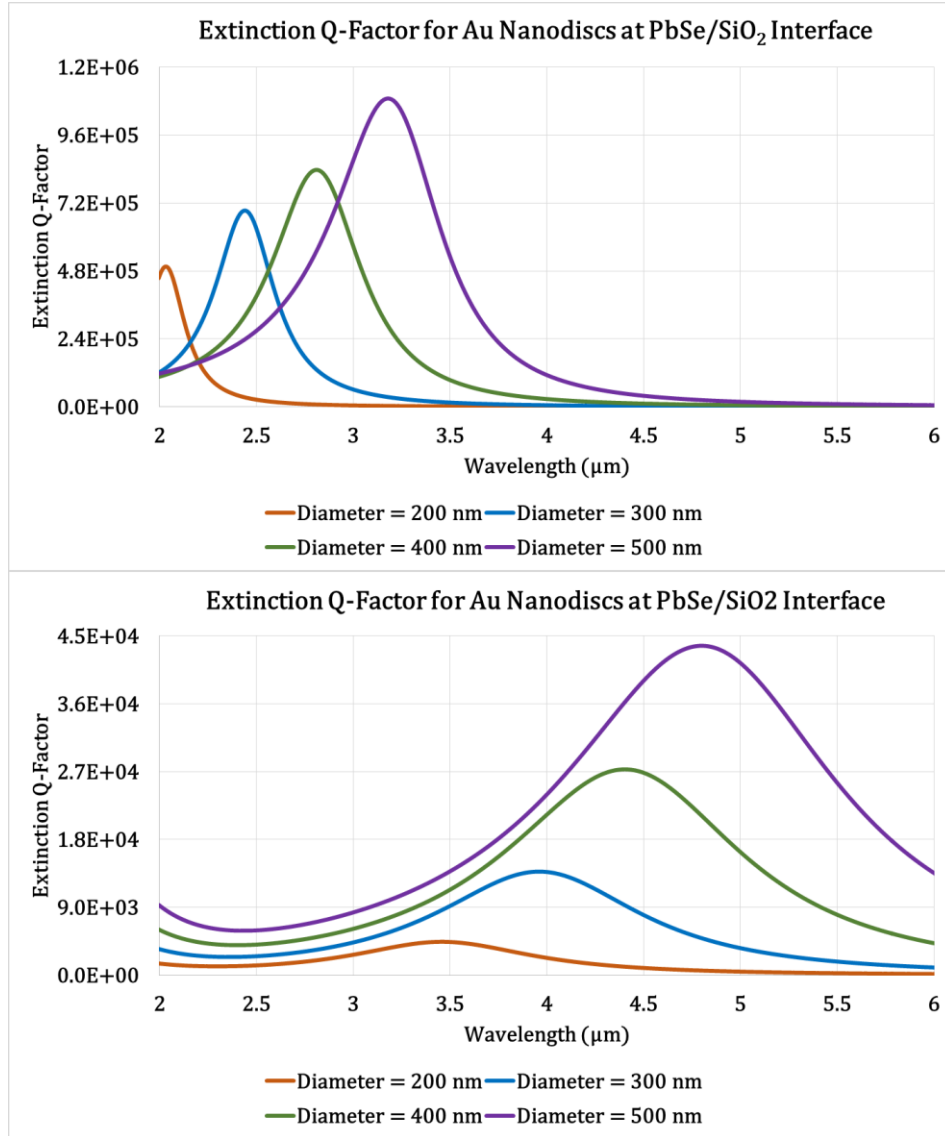
Figure 51. Results of the parametric analysis of the Au and Pt discs embedded at the SiO₂-PbSe interface.

Recall from Chapter 3 that the width of the resonance peak is related to the surface plasmon lifetime, where the longer the lifetime the sharper the resonance peak [23]. When comparing the surface plasmon lifetimes of Au and Pt from figure 36, with respect to the resonance peak width, the results of figure 51 are to be expected. The goal of this investigation was to enhance PbSe performance over the MWIR regime. Therefore, a tradeoff exists between the narrower peaks of Au, which offer an increased extinction efficiency (Q) factor, and the broad peaks of Pt that offer a broader

136

enhancement. For this study, Pt was selected for device fabrication, in part, due to its broad resonance.
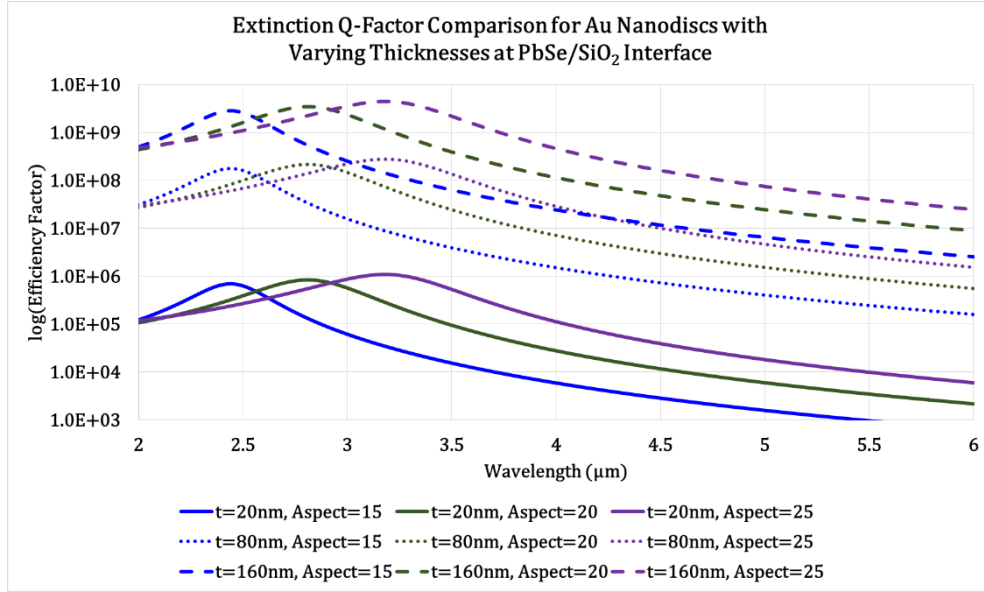
Figure 52. Comparison of 20 nm, 80 nm, and 160 nm thick Au discs with fixed aspect ratios.
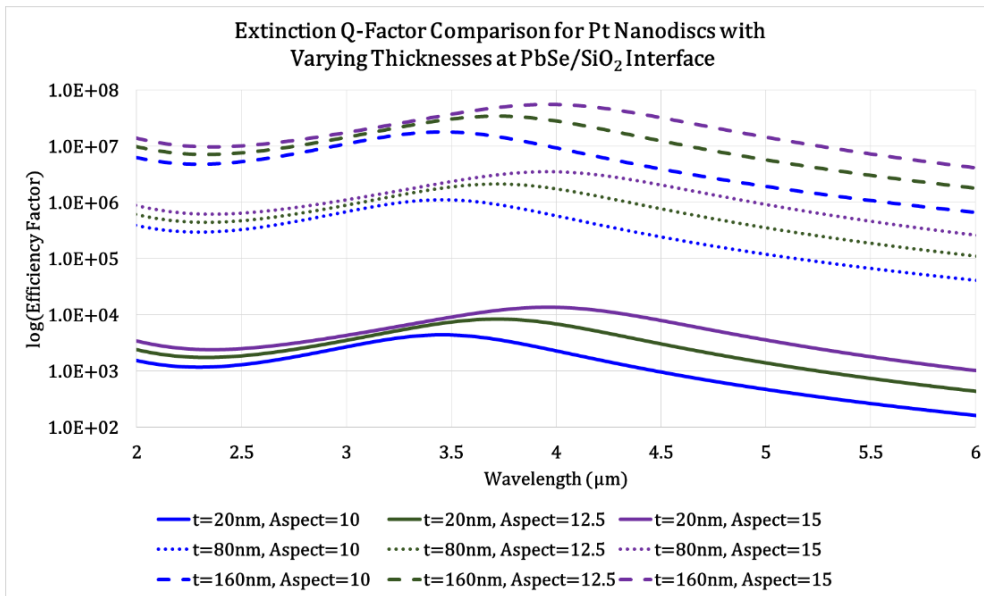
Figure 53. Comparison of 20 nm, 80 nm, and 160 nm thick Pt discs with fixed aspect ratios.

To ensure the resonance peak and majority of the peak width would reside within the spectral response region of PbSe, which has an absorption edge of ~4.3 µm, and to

ensure the resonance peak did not fall within the atmospheric CO_2 absorption notch of 4.1 µm – 4.4 µm, the disc parameters were chosen such that their resonance peaks would be located between 3.5 µm and 4 µm. For Pt, this lead to an aspect ratio of 12.5, which has a resonance of 3.74 µm. However, for Au the resonance peak did not reach this region during the parametric study. It was required to extend the aspect ratio of Au to 30 to reach a resonance wavelength of 3.51 µm.

Though the disc diameters shown in figure 51 have a maximum diameter of 500 nm, larger discs would be used in the real films due to fabrication constraints. To keep the aspect ratio fixed, larger disc diameters necessitate larger thicknesses. To this end, I modeled larger discs to observe the effect of disc diameter on the resonant behavior of Au and Pt discs. Keeping the aspect ratio fixed by scaling the disc diameter, disc thicknesses of 20 nm, 80 nm, and 160 nm were modeled. Figures 52 and 53 demonstrate that increasing the disc thickness for the same aspect ratio does not affect the resonance. This agrees well with the assertion in Chapter 3 that the aspect ratio is the governing parameter for surface plasmon resonance for the disc structure [23]. In-turn, the larger disc diameter necessary to maintain the aspect ratio leads to an increased extinction Q-factor. Therefore, discs of up to 1 µm diameter were considered feasible for fabrication. The selected parameters for finite element modeling are shown in table 9.

Table 9. Selected parameters for finite element method modeling of single Au and Pt discs.

Metal	Aspect Ratio	Diameter	Resonant Wavelength
Au	30	≤ 1 µm	3.51 µm
Pt	12.5	≤ 1 µm	3.74 µm
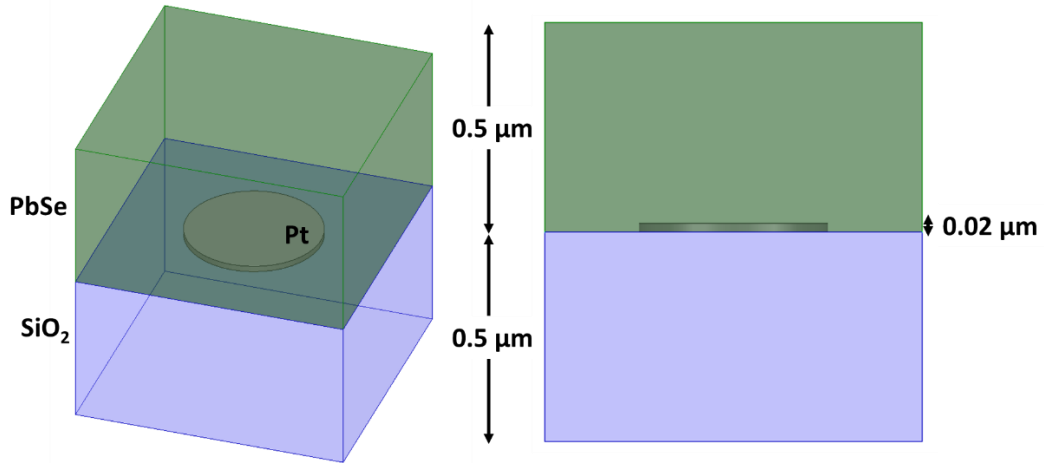
Figure 54. PbSe-SiO₂ interface unit cell with single Pt disc modeled in ANSYS HFSS.
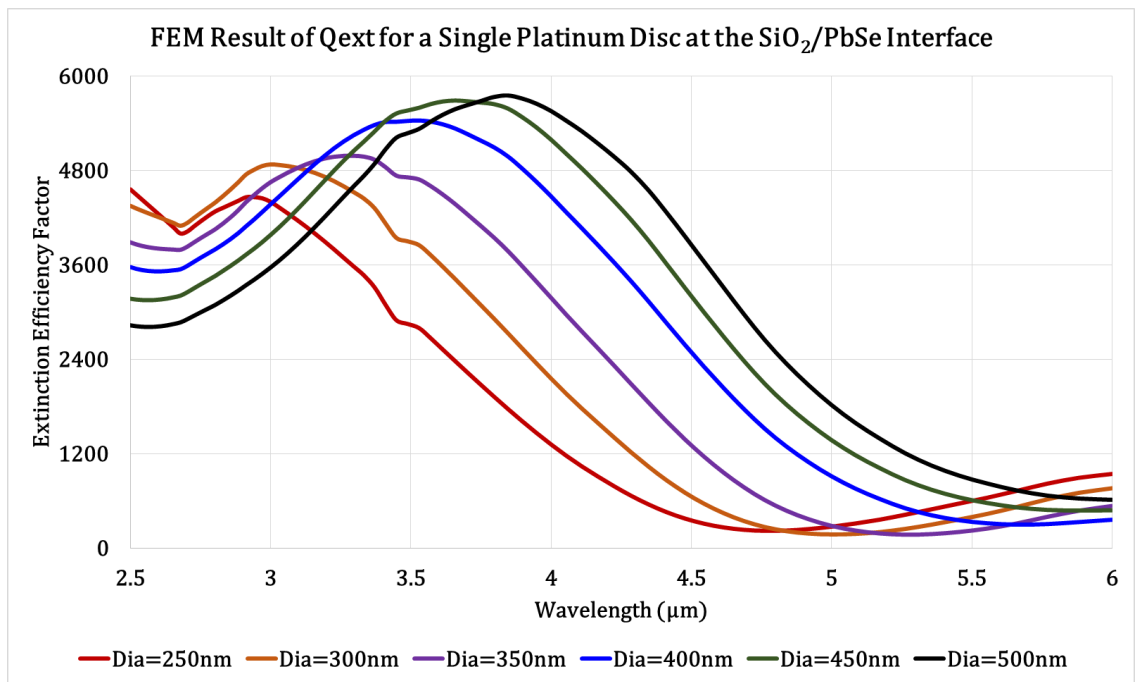
Figure 55. Extinction efficiency (Q) factor, dominated by scattering, of Pt discs at the SiO₂-PbSe interface modeled in ANSYS HFSS.

The aspect ratios of table 9 were found using the quasi-static model for surface plasmon resonant discs. During the parametric analysis described above, the dielectric constant of the host material, in this case the interface between the SiO_2 and PbSe, was considered constant. For higher fidelity results, a single disc at the same interface was modeled with the full dispersion relations in *ANSYS HFSS*. For this simulation, only a

single unit cell was modeled to observe the fields and the Q-factors of the disc structure.

Moreover, to minimize interference effects in the film, only the PbSe and SiO$_2$ layer was

considered. The discs in the context of the whole film will be discussed shortly.
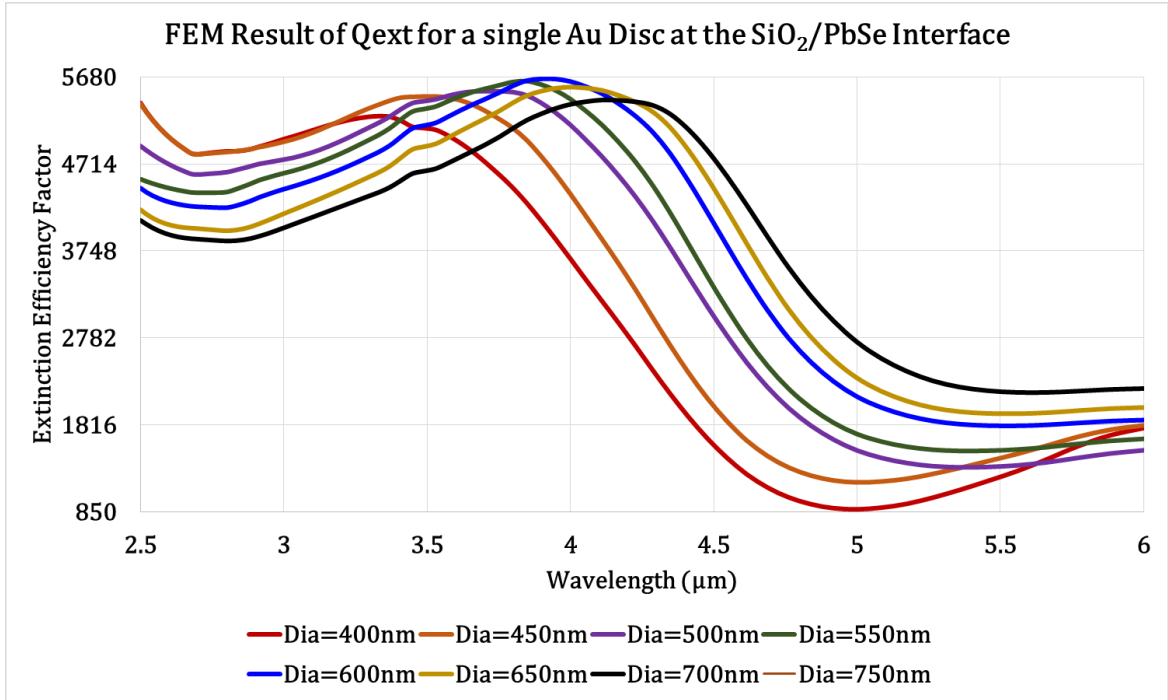
Figure 56. Extinction efficiency (Q) factor, dominated by scattering, of Au discs at the SiO$_2$-PbSe interface modeled in ANSYS HFSS.

Shown in figure 54, the layer thickness of both SiO$_2$ and PbSe were set to 500 nm.

Here, radiation boundary conditions, which are absorbing boundary conditions, were

used at the edge of the unit cell [17]. Excitation was in the form of an x-polarized plane

wave traveling in the −z-direction, and starting 1 µm above the film. The disc radius was

set to be a quarter of the unit cell pitch, such that the disc diameter was half the pitch. The

disc was positioned in the center of the unit cell. A discrete frequency sweep was used to

determine and utilize all of the field solutions necessary for calculating the field intensity

enhancement and efficiency factors. The scattering and absorption efficiency factors were

calculated using equation 5.12 and equation 5.13, and the extinction efficiency factor is given as their sum,

$$Q_{abs} = \frac{\sigma}{\pi r_{disc}^2 c \varepsilon_0 n_0} \iiint_{Disc\ Volume} |E|^2\ dV \tag{5.12}$$

$$Q_{sct} = \frac{2}{\pi r_{disc}^2 c \varepsilon_0 n_0} \iint_{Disc\ Surface} |E \times H^*|\ dS \tag{5.13}$$

where $\frac{c \varepsilon_0 n_0}{2}$ is the intensity of the incident wave, σ is the electrical conductivity of the medium, and πr_{disc}^2 is the geometric cross-section of the disc transverse to the direction of illumination [7, 23].

To observe the effects of the full dispersion relations of PbSe on the surface plasmon resonance of the discs, the pitch was varied from 500 nm up to 1 µm for Pt discs and 500 nm to 1.5 µm for Au. The discs, in turn, were modeled with diameters between 250 nm and 750 nm, depending on the metal. Finite conductivity boundary conditions were used on the disc, which utilize the input conductivity to calculate losses within the metal. These boundary conditions were necessary, because, as described in Chapter 3, the charges inside and outside the disc contribute to the evanescent waves that result from surface plasmon resonance. Figure 55 and figure 56 show the results for the extinction efficiency (Q) factors for Pt and Au discs, respectively. From the quasi-static model, it would be expected that Pt would have a smaller amplitude and a narrower resonance than Au. However, the modeled results show that Au has the smaller amplitude and broader resonance. Further, the resonances of Pt have a more symmetrical shape, while the Au discs exhibit a more asymmetric.
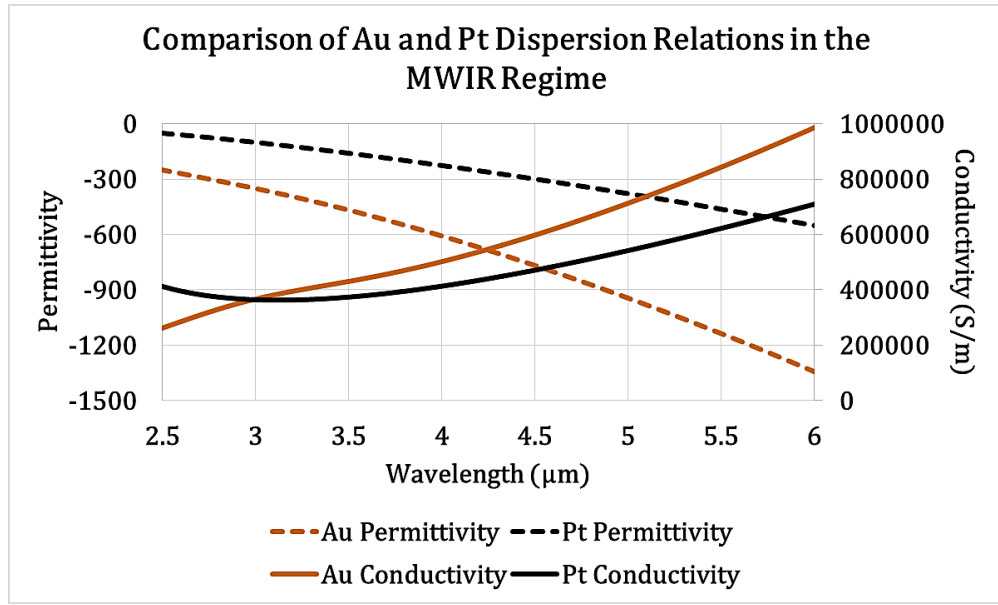
Figure 57. Comparison of Au and Pt dispersion relations from 2.5 µm to 6 µm.

Consider the quasi-static resonance condition for surface plasmons, which considers the host material to have a fixed dielectric constant. Figure 33 shows that Au has long surface plasmon lifetime (up to ~500 ns at the PbSe absorption edge of 4.3 µm), leading to a narrow resonance line width. However, figure 28 shows that the dielectric constant of PbSe is highly frequency dependent in the MWIR region. Therefore, the changes in the dielectric constant of PbSe create a broad background continuum, where for each different value there is a narrow Au resonance condition. Fano resonances describe the asymmetric line shape that arises from the interference between a broad background continuum and a narrow resonance [24-26]. Therefore the asymmetry observed in figure 56 is associated with Fano resonance. Though the Pt absorption spectra is more symmetric, Fano resonances were observed in the spectra of figure 55 as well. However, due to the lower surface plasmon lifetime for Pt, the resonances are broader and so its asymmetry is less pronounced. The Fano resonances observed suggest

that the absorption enhancement in PbSe will be more asymmetric than the results of figure 51 would suggest. As described in Chapter 6, I found this assertion to be true.

For both Pt and Au, it would seem that for the resonance condition to reside between 3.5 µm and 4 µm, the required diameter is between 400 nm to 500 nm. This similarity is perhaps the most startling result, because it suggests that the material of the disc does not change the resonance condition dramatically as the quasi-static model would suggest. Figure 57 shows the differences between the electrical properties of Au and Pt. The Au has a lower permittivity and a higher conductivity than Pt. With its lower conductivity Pt has a higher absorption cross-section than Au, which explains the observed increase in the extinction Q-factor in Pt. Recall from Chapter 3 that the permittivity is an important parameter for surface plasmon resonance. From the difference in the permittivity of Au and Pt, a first assumption would be that the resonances should be different for the same aspect ratio discs. Recall that for discs, the aspect ratio is just as important for resonance. In fact, the results of figures 55 and 56 suggest aspect ratio is more important than the metal type for the resonance condition of these discs in PbSe films.

Along with the increase in extinction, it was important to determine the electric field intensity enhancement at the resonance wavelength. Indeed, the importance of the electric field intensity enhancement was emphasized in equation 3.35 in Chapter 3 while describing the carrier generation rate in photoconductors. The intensity enhancement is found by taking the ratio of the resulting wavelength-dependent electric field intensity to that of the incident intensity. The incident field intensity in these models is that of a unit

amplitude plane wave. I calculated the electric field intensity enhancement in the xz-, yz-, and xy-planes for both Au and Pt discs at the SiO$_2$/PbSe interface using *ANSYS HFSS*.
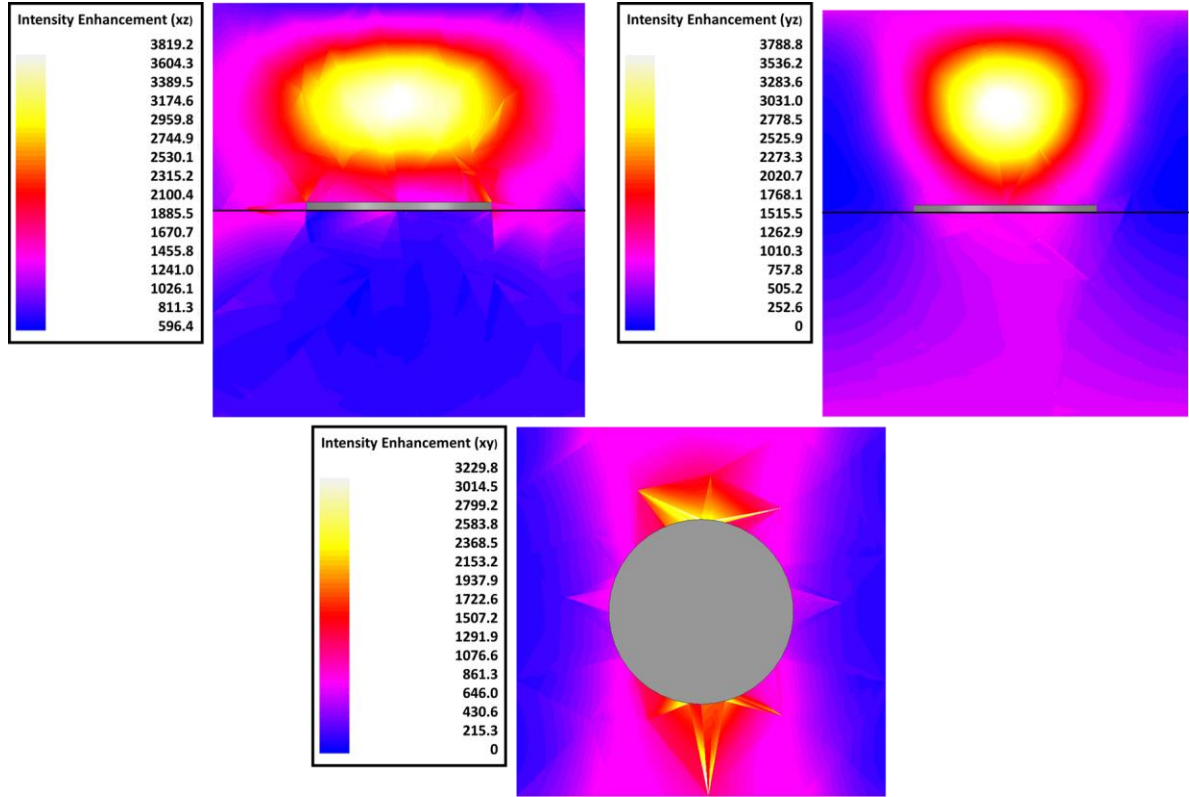
Figure 58. Modeled electric field enhancement plots in the (top-left) xz-, (top-right) yz-, and (bottom) xy-directions for a single Pt disc at SiO$_2$/PbSe interface.

Recall that the plane wave is x-polarized and propagates in the –z-direction. Therefore the largest intensity enhancement is observed in the xz-plane, followed by the xy-plane, and finally the yz-plane. The field intensity plots for both Au and Pt are shown in figure 58 and figure 59, respectively. Both materials produce large intensity enhancements, as seen from the xz-plane, in the middle of the PbSe film. The Au has a slightly higher maximum intensity enhancement of 3944 over Pt at 3819, yet from figure 51 it would be expected that Au would lead to a much larger enhancement than Pt.

The field behavior varies in the yz-plane as well, with both the Au and Pt discs

144

leading to an increase in field intensity in PbSe and throughout SiO$_2$. This same similarity

between Au and Pt discs was observed when comparing figures 55 and figure 56,

reaffirming the assertion made above that aspect ratio is more important for surface

plasmon resonance than the material characteristics of the metal discs. It can be asserted

from these results that embedding either Au or Pt disc arrays into PbSe films would lead

to similar sensitivity enhancement. Indeed, when modeling the full film structure, perfect

electrical conductor boundary conditions, described below, were used, so the results were

metal independent.
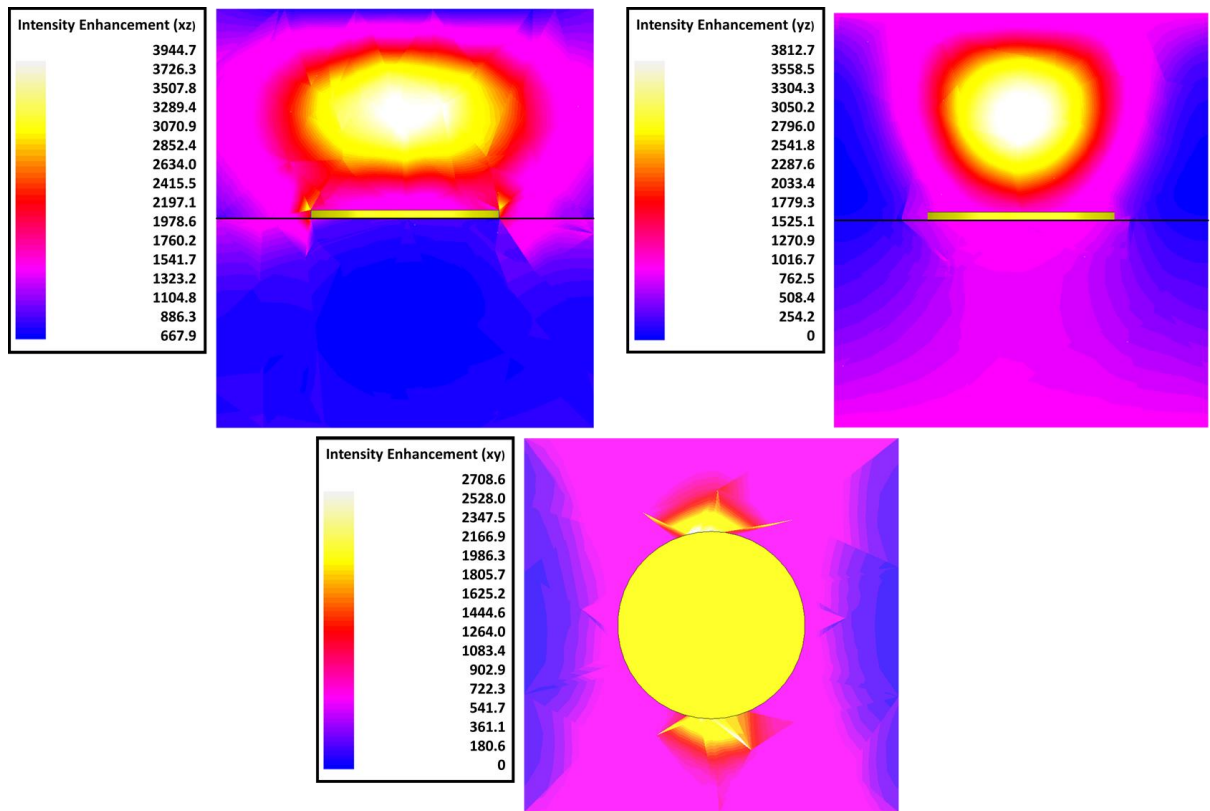
Figure 59. Modeled electric field intensity enhancement plots in the (top-left) xz-, (top-right) yz-, and (bottom) xy-directions for a single Au disc at SiO$_2$/PbSe interface.

My goal in modeling the single discs was to determine the expected field

enhancement in PbSe films. Though the scattering cross-section and field enhancement

are good figures of merit for preliminary studies, the desired effect of embedding surface plasmon resonant structures into the PbSe detectors was to enhance the absorption in the investigated films. To this end, infinite arrays, with a unit cell shown in figure 60, of Pt and Au discs with diameters from 250 nm to 1000 nm and a fixed thickness of 40 nm were modeled in the full PbSe film structure in a similar manner described above. Discs were placed 30 nm below the SiO_2-PbSe interface.
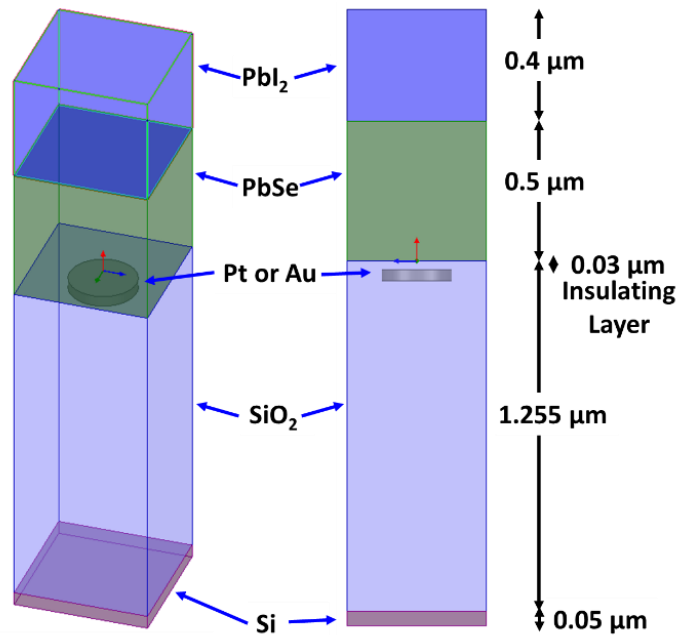
Figure 60. The modeled unit cell of the PbSe film with embedded metallic discs modeled in ANSYS HFSS.

As described in [27], quenching, a process in which surface charges generated during SPR excitation can recombine in the metal, can occur thereby negating the enhancement. Therefore, a 30 nm insulation layer of SiO_2 was inserted on top of the disc to mitigate this potential parasitic process. The perfect electric conductor (PEC) boundary conditions were used for this simulation to separate any losses in the metal from the absorption spectra [17]. Due to this boundary condition, the spectra for both Au and Pt

were found to be the same. However, it should be noted that for Pt discs more losses would be expected, leading to lower overall enhancement. The absorption over the range of 2.5 µm to 6 µm was calculated using an interpolated frequency sweep and equation 5.11.
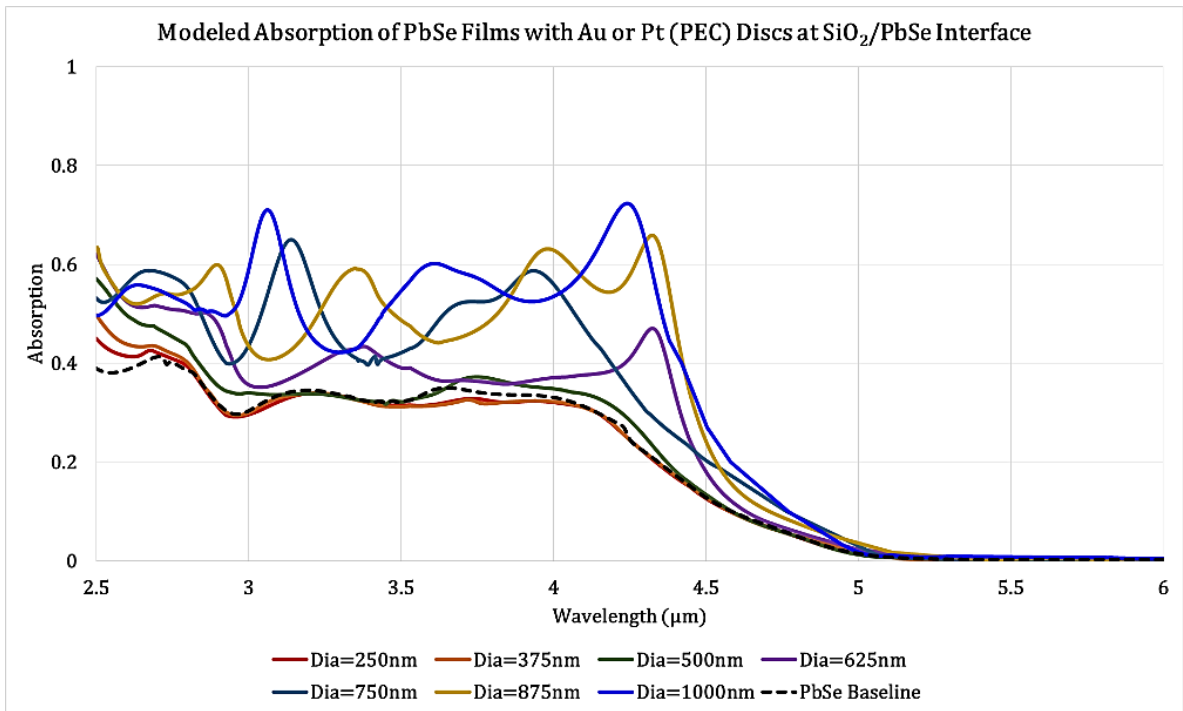
Figure 61. Modeled absorption in PbSe films with metallic (PEC) discs at SiO₂/PbSe interface.

The predicted absorption for various diameters of PEC discs in PbSe films is shown in figure 61. Discs with diameters below 500 nm (aspect ratio smaller than 12.5) are shown to result in an absorption that is similar to the baseline PbSe absorption. Once the aspect ratio reaches 12.5 (green), there starts to be absorption enhancement. As the discs become larger the absorption continues to grow, and multiple resonance peaks develop. Up to a factor of three enhancement over the baseline PbSe absorption was predicted, depending on disc diameter and spectral region of interest. These results predict that surface plasmon resonant discs can lead to a large sensitivity increase in the

147

PbSe films we investigated. Notice how for the 625 nm diameter and 875 nm diameter discs in figure 61 there is a resonance peak at 3.35 µm. This region is close to the previously observed reduction in absorption due to interference in the baseline PbSe films shown in figure 20. For the 750 nm and 1000 nm diameter discs, the peak is red-shifted, and the dip in absorption is again present in the region around 3.4 µm. Therefore, peaks in the vicinity of this region are associated with surface plasmon resonance.

As the disc diameter increases, more peaks appear suggesting that interference starts to play a more significant role. In multilayer films and optical cavities, the separation between interference peaks can be determined by the free spectral range, which gives the wavelength separation between adjacent spectral peaks [28-30]. Using the thicknesses of the film found in figure 60, we can determine the separation between peaks due to interference using equation 5.14,

$$\Delta\lambda \cong \frac{\lambda_0^2}{2ntcos\theta + \lambda_0} \qquad (5.14)$$

where λ_0 is the vacuum wavelength of the peak of interest, and the refractive index-thickness product nt is the optical thickness of the layer. For multiple layers, the effective optical thickness is the sum of the optical thicknesses of each layer. For instance, consider the predicted absorption spectra for the 1000 nm disc in figure 61. The peak centered at 3.6 µm is associated with SPR, and will be ignored for now. There are two other peaks of interest in the 3 µm – 5 µm region. These are centered at 3.07 µm and 4.25 µm, a wavelength span of 1.18 µm. If the free space wavelength is that of the peak at 4.25 µm, the free spectral range is calculated to be 1.2 µm, which is within 1.7% of the modeled distance between peaks. This example serves to reinforce the assertion of

interference in the investigated films, and shows that with embedded discs the SPR and interference work together to provide a broadband absorption enhancement in the PbSe.

5.4 **Predicted Results for an Embedded Reflector Layer in PbSe Films**

Discussed in Chapter 1 and Chapter 4, the back reflector is an attractive structure for PbSe photoconductor enhancement. Consider figure 41 and figure 42 in Chapter 4, which show how varying the SiO_2 thickness in the back reflector structure effects the absorption of PbSe. It was stated that the desired thickness of the SiO_2 layer is around 1400 nm to yield an absorption increase that is a factor of 2.55 and 2 above the baseline PbSe films at 3.45 µm and 4.2 µm, respectively. To observe the resulting field intensity within this configuration, and to verify the numerical results, it was modeled in *ANSYS HFSS*.

A unit cell similar to that of figure 46 was used as the geometry of these simulations. A 50 nm Pt layer was inserted, and given PEC boundary conditions to ensure the only absorption observed in the model would be from the PbSe layer. To further optimize the SiO_2 thickness, the SiO_2 layer in the *ANSYS HFSS* model was varied from 1400 nm to 1500 nm. Due to the fact that the enhancement mechanism in these films is optical interference, the thickness of the films can affect the resonant shape dramatically. Recall that the PbSe deposition process involves growing a layer of PbSe, and then converting approximately half of the layer to PbI_2 for sensitization. Therefore, for these simulations the PbSe thickness is assumed fixed, while the PbI_2 thickness was varied from 300 nm to 400 nm to account for variation in the sensitization process. I observed experimental results that supported the reduced PbI_2 thickness, and were in good

agreement with modeled predictions. Table 10 shows the parameters used for the different film thicknesses modeled.

The modeled results of figure 64 agree well with those of figure 41, which validates the predicted absorption increase in figure 42. For configurations 1 and 2, the increase is even more pronounced. In all three configurations, the peaks of the spectrum are predicted to red-shift for 1500 nm thick SiO_2 over that of the 1400 nm thick layer. For configuration 1 and 2, this red-shift leads to larger peaks at the PbSe absorption (~4.3 µm) edge, which can be beneficial.

The detector sensitivity, specifically the spectral responsivity, is weighted by photon energy hv according to equation 5.15,

$$\Re(hv) = \frac{A\eta_i q i_{photo}}{hv P_{inc}} \tag{5.15}$$

where A is the absorption of the active material, η_i is the internal quantum efficiency defined as the ratio of the absorbed photons to current generating carriers, q is the charge of the electron, i_{photo} is the magnitude of the photogenerated current, and P_{inc} is the power incident on the detector. This relationship shows that there should be higher response at longer wavelengths. Moreover, the photon flux is also weighted toward higher wavelengths for thermal energies close to room temperature (see Appendix C), so the SiO_2 thickness should be designed such that a large enhancement is achieved at longer wavelengths. Therefore, a 1500 nm SiO_2 layer was selected for fabrication. A secondary peak was observed at 3.11 µm, 3.32 µm, and 3.5 µm for PbI_2 thicknesses of 300 nm, 350 nm, and 400 nm, respectively. This secondary peak serves to broaden the absorption enhancement, and lead to even greater response.

Table 10. Thickness parameters for three different configurations of PbSe films used to observe the effect of the PbI$_2$ and SiO$_2$ layer thickness on the absorption in PbSe films with a Pt back reflector.

Configuration	Layer	Thickness (nm)
1	PbI$_2$	300
	PbSe	500
	SiO$_2$	1400-1500
	Pt	50
	Si	50
2	PbI$_2$	350
	PbSe	500
	SiO$_2$	1400-1500
	Pt	50
	Si	50
3	PbI$_2$	400
	PbSe	500
	SiO$_2$	1400-1500
	Pt	50
	Si	50
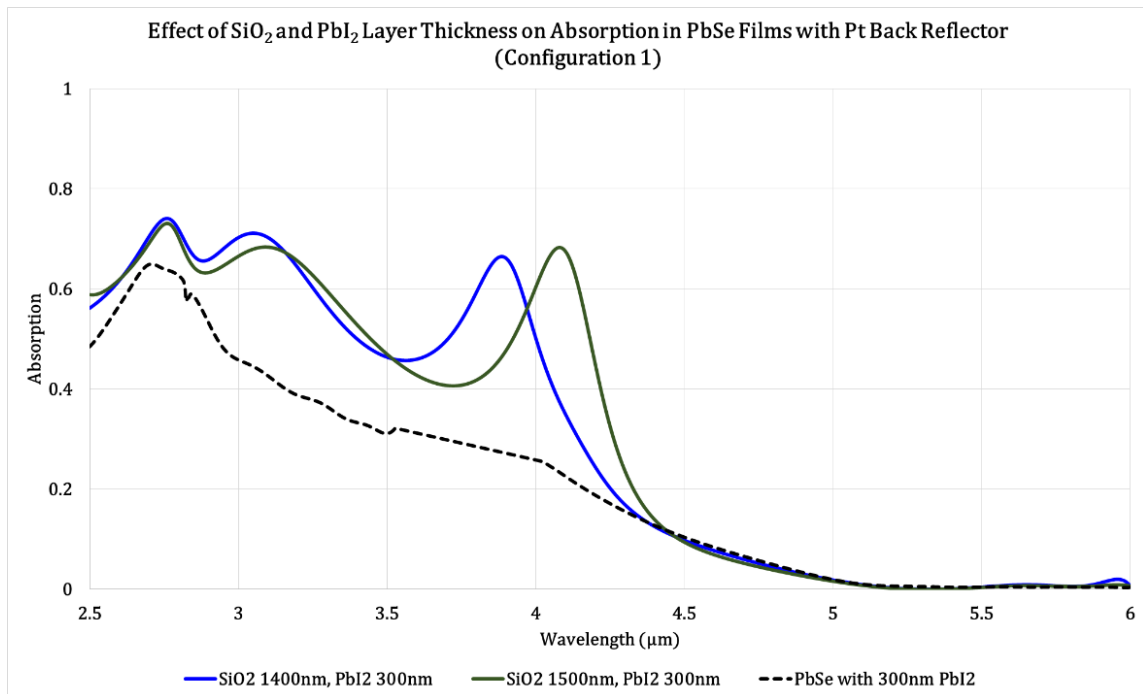
Figure 62. Effect of SiO$_2$ and PbI$_2$ layer thickness on absorption in PbSe Films with Pt back reflector in configuration 1.
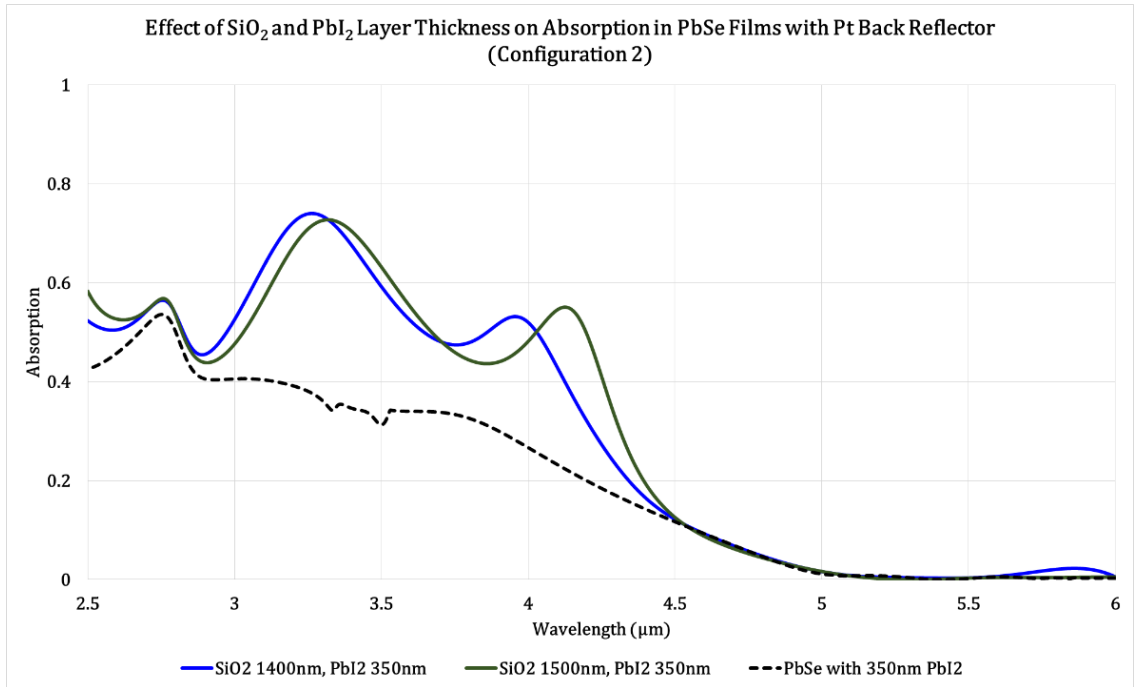
Figure 63. Effect of SiO₂ and PbI₂ layer thickness on absorption in PbSe Films with Pt back reflector in configuration 2.
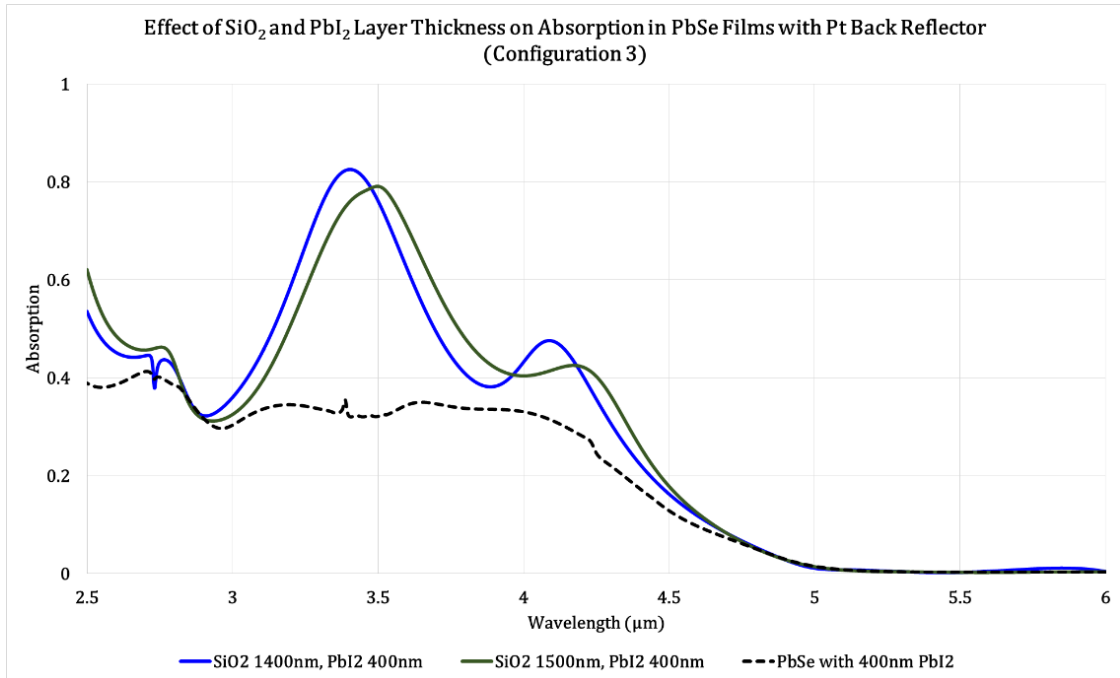
Figure 64. Effect of SiO₂ and PbI₂ layer thickness on absorption in PbSe Films with Pt back reflector in configuration 3.
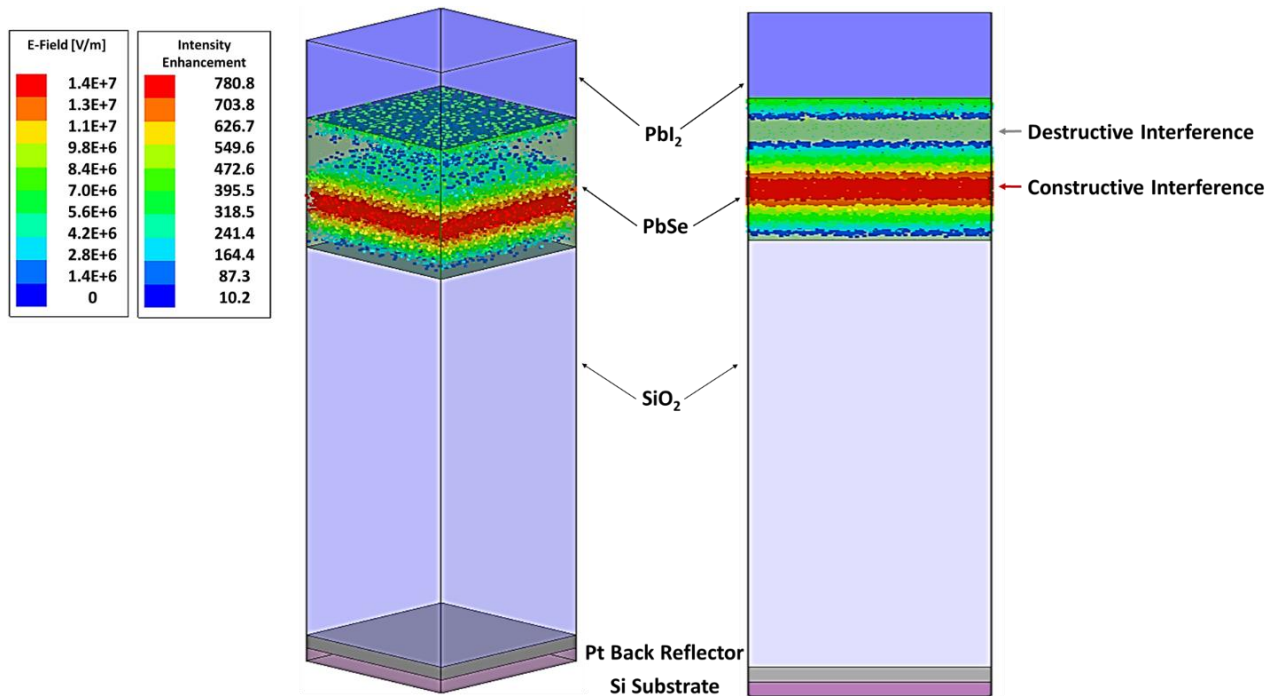
Figure 65. Electric field and field intensity enhancement due to interference at 4.08 μm in PbSe films with Pt back reflector, 1500 nm SiO2, and 300 nm PbI2 thickness

Consider configuration 1 in figure 62 above. The peak near the absorption edge of PbSe (~4.3 µm) is 68% at 4.08 µm. This is nearly a factor of three enhancement over the corresponding PbSe baseline film at the same wavelength. To further investigate this test case, I simulated the electric field intensity in the PbSe layer of the modeled film. Flouquet ports were used for a discrete frequency sweep in which the fields were saved at every 1000 GHz between 50000 GHz and 120000 GHz. Recall that the TE_{00} and TM_{00} mode excitations of the Flouquet port are effectively plane waves, and in this simulation were set to an input power of 1 W. With the unit cell area being 500 nm x 500 nm, the incident intensity was 4 x 10^{12} W/m^2. Figure 65 shows the magnitude of the electric field within the PbSe layer, as well as the field intensity enhancement. From top to bottom, the magnitude of the field within the layer starts at 7 MV/m, and then the field vanishes in the top half of the layer. This disappearance is indicative of destructive interference.

153

Indeed, shortly after the field returns and results in a highly intense region with a field of 14 MV/m near the bottom half of the film, which is due to constructive interference. The predicted electric field intensity enhancement in this region is as large as 780 times that of the incident wave, showing the benefits of this simple configuration. A similar intensity increase would be seen at the 3.11 µm peak; and even in the band between 3.5 µm and 4 µm where the absorption decreases, a small increase over the baseline films is expected.
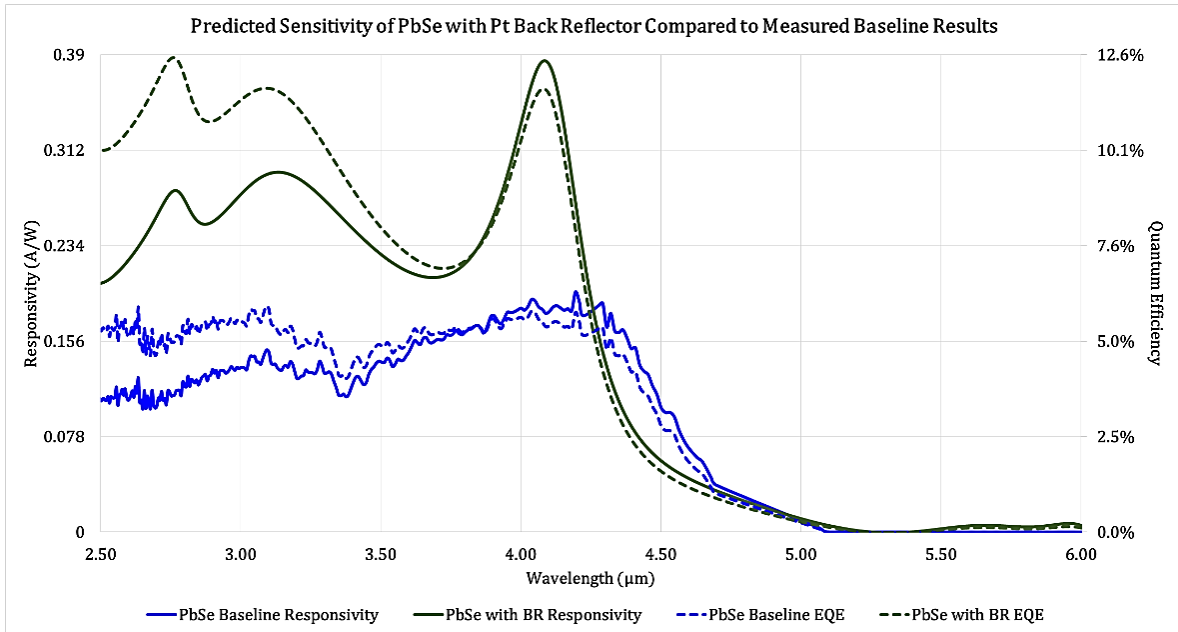
Figure 66. Predicted sensitivity of PbSe detector with Pt back reflector compared to baseline result.

So far, the primary figure of merit discussed for these films has been absorption. However for detectors, responsivity and external quantum efficiency (EQE) were used to gauge the sensitivity; after all, the goal of this investigation was to demonstrate PbSe device sensitivity enhancement such that the room temperature performance is comparable to that of the baseline operated at lower temperatures. Recall from figure 22 that the peak room temperature responsivity and EQE at 4.3 µm for the baseline PbSe

154

detectors was shown to be 0.2 A/W and 6%, respectively. Coupled with figure 20, which shows the PbSe absorption at the absorption edge (~4.3 µm) is 35%, the internal quantum efficiency (IQE), which is the quotient of the EQE and absorption, for these detectors at room temperature is calculated to be 17.14%. I used this IQE to calculate the responsivity from equation 2.15 in Chapter 2 based on the predicted absorption.

The predicted sensitivity for a photoconductor derived from a back reflector film with a 300 nm PbI_2 layer is shown in figure 66. The dip in responsivity at ~3.4 µm in the baseline detector is predicted to red-shift to ~3.5 µm in the back reflector enhanced films. Further, there are three distinguishable peaks at approximately 2.8, 3.3, and 4.1 µm. It would seem that due to resonance the large peak at 4.08 µm blue shifts the response spectrum compared to baseline PbSe. This is evidence of interference, because the wavelengths that match the longitudinal modes of the film will experience the largest absorption enhancement in a plane-parallel cavity. However, as will be shown in Chapter 6, this peak was observed to be much wider due to the roughness of the deposited films. Roughness leads to peak broadening, and, as discussed in Chapter 2, the measured films are very rough compared to the smooth interfaces that were modeled. Of note is the increase in sensitivity over the whole band. At the 4.08 µm peak, the sensitivity is increased by a factor of 2, and over the whole band the responsivity and quantum efficiency are well above that of the baseline detectors. These results predict the responsivity and quantum efficiency of PbSe detectors with embedded back reflectors are indeed comparable to those of the baseline films at lower temperatures. These results were put to the test, and in the next chapter it will be demonstrated that the back reflector enhanced PbSe detectors offer a major improvement over the current state-of-the-art.

Chapter 5 References

[1]   K. K. Choi, et al. "Electromagnetic modeling and resonant detectors and arrays," Infrared Physics & Technology, Vol. 70, 2015.

[2]   K. K. Choi, et al. "Resonant structures for infrared detection," Applied Optics, Vol. 56, No. 3, 2017.

[3]   K. K. Choi, et al. "Resonator-quantum well infrared photodetectors," Appl. Phys. Lett. 103, 2013.

[4]   Getting Started with HFSS: Optimizing a Waveguide T Junction. ANSYS Release 18.2, ANSYS, Inc., 2017.

[5]   ANSYS Metamaterial Summit: Frequency Selective Surfaces. ANSYS 14.0 Release, ANSYS, Inc., 2012.

[6]   Workshop 3-6: RCS of a Cube. ANSYS 2015.0 Release, ANSYS, Inc., 2015.

[7]   N. M. Buford, "Plasmonic Nanostructurres for the Absorption Enhancement of Silicon Solar Cells," Masters Thesis, University of Arkansas, 2013.

[8]   Material Properties. ANSYS, Inc., 2014.

[9]   HFSS Fields Calculator Cookbook. ANSYS Release 17.2, ANSYS, Inc., 2016.

[10]   Modeling Layered Structures with Shell Elements. ANSYS, Inc., 2016.

[11]   K. F. Warnick, *Numerical Methods for Engineers: An Introduction Using MATLAB and Computational Electromagnetics Examples*, SciTech Publishing, Edison, NJ, 2011.

[12]   M. N. O. Sadiku, "A Simple Introduction to Finite Element Analysis of Electromagnetic Problems," IEEE Transactions on Education, Vol. 32, No. 2, 1989.

[13]   M. Jones, "Ansys High Frequency Structure Simulator (HFSS) Tutorial," Pacific

        Northwest National Laboratory, 2017. [Online]. Available:

        https://indico.fnal.gov/event/13068/contribution/10/material/slides/1.pdf.

        [Accessed: Nov. 3, 2018].

[14]   ANSYS, Inc., *An Introduction to HFSS*, Release 18.2, Canonsburg, PA: ANSYS,

        Inc., 2017.

[15]   J. Hoffmann, et al. "Comparison of electromagnetic field solvers for the 3D

        analysis of plasmonic nano antennas," Proc. SPIE. Vol. 7390, 2009.

[16]   C. A. Balanis. *Advanced Engineering Electromagnetics*,1st Ed., Hoboken, NJ:

        John Wiley and Sons, Inc. 1989.

[17]   ANSYS, Inc., "Appenix 5-2: HFSS 3D Boundary Conditions," Technical Note,

        Release 2014.0, Canonsburg, PA: ANSYS, Inc., 2014.

[18]   ANSYS, Inc., "Introduction to ANSYS HFSS for Antenna Design", Presented as

        part of FSS Workshop, ANSYS 14.0 Release, ANSYS, Inc., 2012.

[19]   ANSYS, Inc., "Getting Started with HFSS: Floquet Ports," Technical Note,

        Release 18.2, Canonsburg, PA: ANSYS, Inc., 2017.

[20]   J. O. Sophocles, *Electromagnetic Waves and Antennas*, Rutgers University, 2016.

[21]   Agilent Technologies, Inc., "Topic 5: S-parameter Simulation and Optimization."

        ADS 2009 (version 1.0). Agilent Technologies, Inc., 2009.

[22]   ANSYS, Inc., "HFSS with HPC for Large Finite Antenna Array Design,"

        Canonsburg, PA: ANSYS, Inc., 2011.

[23]   D. Sarid and W. Challner, *Modern Introduction to Surface Plasmons: Theory, Mathematical Modeling, and Application*, New York, NY: Cambridge University Press, 2010.

[24]   F. M. Limonov, et al. "Fano resonances in photonics," Nature Photonics, Vol. 11, 2017.

[25]   Y. Zhang, et al. "Fano resonances in disc-ring plasmonic nanostructure: strong interaction between bright dipolar and dark multipolar mode," Optics Letters, Vol. 37, No. 23, 2012.

[26]   B. Luk'yanchuk, et al. "The Fano resonance in plasmonic nanostructures and metamaterials," Nature Materials, Vol. 9, 2010.

[27]   X. Tang, et al. "Plasmon resonance enhanced colloidal HgSe quantum dot filterless narrowband photodetectors for mid-wave infrared," J. Mater. Chem. C, 5, 2017.

[28]   E. Hecht, *Optics*, 4th Edition. Addison-Wesley, New York, 2002.

[29]   R. E. Fischer, et al. *Optical System Design*, 2nd Edition, SPIE Press, McGraw Hill, 2008.

[30]   I. Chambouleyron and J. M. Marinez, *Handbook of Thin Films Materials*; ch 12, edited by Nalwa, H.S., Academic Press, 2001.

Chapter 6: PbSe Film and Device Measurements

The results presented thus far have assumed smooth interfaces, perfect fabrication and ideal conditions. To determine the achievable enhancement under laboratory conditions, structures were fabricated in PbSe films and test detector devices. The detector fabrication procedures are described in Appendix A. In this chapter, the experimental results of the investigated PbSe devices with embedded resonant structures are discussed.

6.1 Confirmation of Plasmonic Resonance of Metal Discs in PbSe

Before devices with embedded plasmonic structures were fabricated using photolithography, I performed preliminary studies to verify the feasibility of metallic discs in PbSe. With help from my collaborators, Au and Pt discs were fabricated on the SiO_2 layer using electron beam lithography (EBL), which is similar to photolithography with the exception that the exposure is with a concentrated electron beam instead of UV photons [1-2]. We patterned 500 nm and 1000 nm diameter discs into 1mm x 1 mm arrays with a pitch, defined as the center-to-center disc spacing, twice that of the diameter. After patterning and developing the e-beam resist, RF sputtering was performed to deposit a chromium (Cr) adhesion layer and either Pt or Au onto the substrate. In accordance with table 9, the deposited thickness of the Pt and Au discs was selected such that the aspect ratio would be 12.5 and 30, respectively. Liftoff and cleaning was then performed to remove excess metal and contaminates from the surface. Figure 67 shows scanning electron microscope images of the arrays, and table 11 shows the measured disc diameters and pitches.
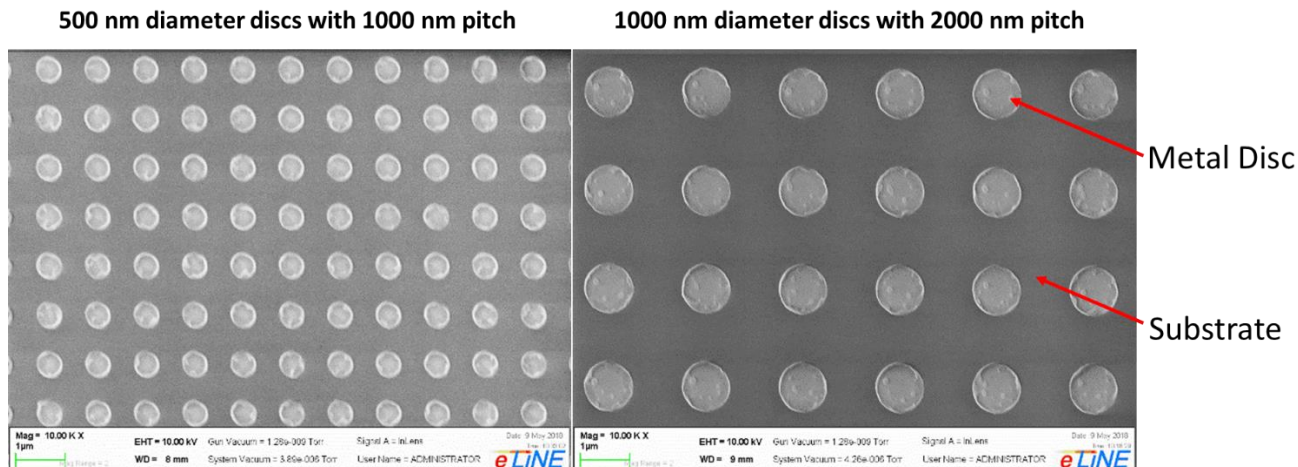
Figure 67. SEM images of 500 nm (left) and 1000 nm (right) disc arrays patterned by EBL.

Table 11. Measured disc diameter and pitch for 500 nm and 1000 nm Au and Pt discs patterned by EBL.

Metal	Designed Dia./Pitch (nm)	Measured x-Dia.(nm)	Measured y-Dia. (nm)	Measured x-Pitch (nm)	Measured x-Pitch (nm)
Pt	500/1000	602.9	502.4	1016.0	846.6
Pt	1000/2000	982.5	960.2	1998.5	1953.1
Au	500/1000	524.8	558.3	937.8	848.6
Au	1000/2000	993.8	1027.0	1965.0	1942.8

Before depositing PbSe onto the disc arrays, I used a *Thermo Fisher Scientific* iS5 tabletop FTIR spectrometer to determine the optical density spectra of the disc arrays. It was important to measure the baseline spectrum from the disc arrays alone for comparison with disc arrays embedded in PbSe. In this case, the integrating sphere method described in Chapter 2 was not used due to the small area of the disc arrays. Instead, the discs were positioned over a 2 mm aperture to ensure the focused black body source would be incident only on the array. The background transmission signal was collected at normal incidence through the aperture alone, and the signal transmission was collected through the disc arrays and aperture. The optical density was calculated using equation 2.13 found in Chapter 2.
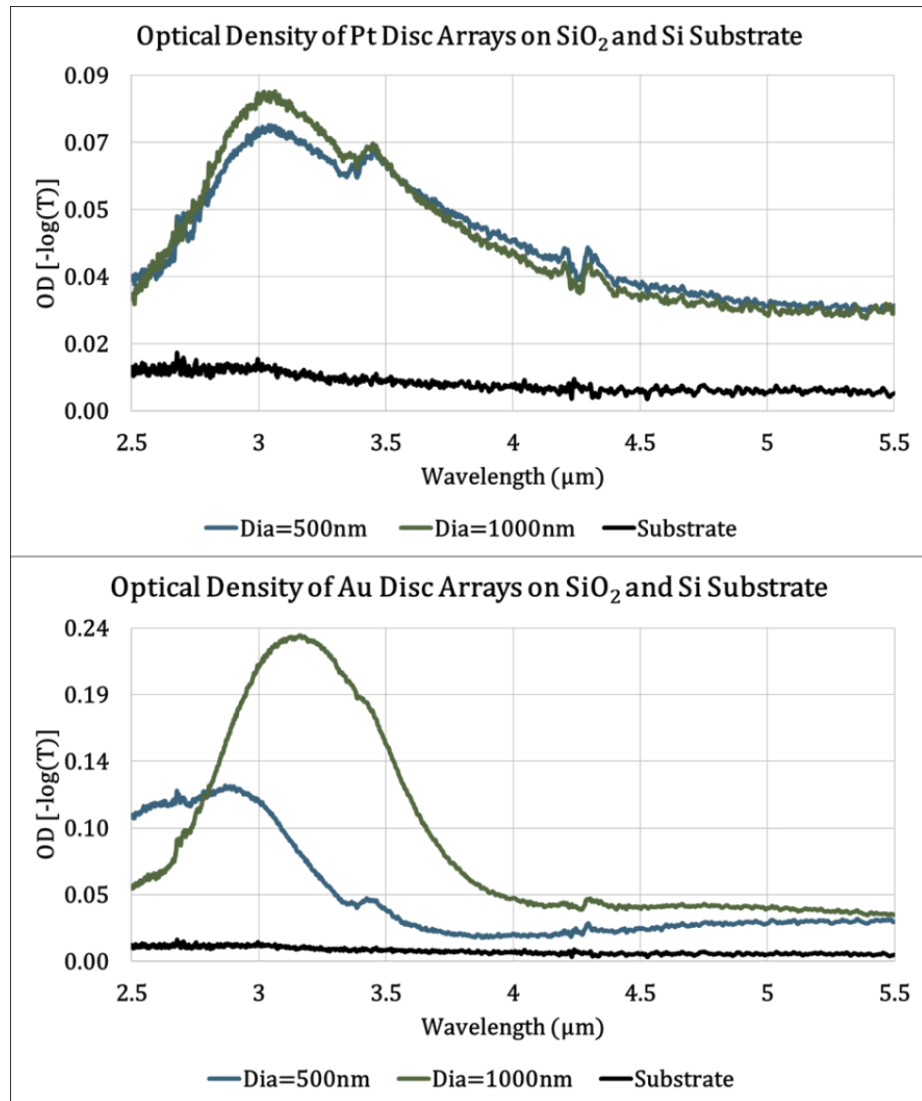
Figure 68. Optical density spectra of Pt (top) and Au (bottom) disc arrays on SiO$_2$ layer and Si substrate.

Figure 68 shows the measured OD spectra of the Pt and Au disc arrays. Considering the 1000 nm discs the width of the Pt peak was observed to be approximately 1.25 µm. In contrast the width of the Au peak is smaller at 0.71 µm. The difference in the peak width is expected due to the longer surface plasmon lifetime shown in figure 33. A more interesting phenomenon is noticed when comparing the difference in how the spectra change with size between the Pt and Au disc arrays. For Pt the size seems to only have the effect of increasing the amplitude, which follows the general rule that

aspect ratio is the dominant parameter for SPR in discs and is consistent with figure 53.

However, in Au the resonance shifts to longer wavelengths as the disc size increases.

This behavior is in contrast with figure 52. The explanation again comes back to the

conductivity of the two metals. As seen in figure 57, Au has a higher electrical

conductivity, and therefore is less lossy than Pt. Less loss equates to higher reflectivity,

and makes Au act like a perfect electric conductor (PEC) in the MWIR regime.

Therefore, aspect ratio, more specifically the thickness of the disc, is not as important a

parameter as the diameter for the resonance in Au discs. This explanation seems to be

consistent with the modeled results of figure 56.
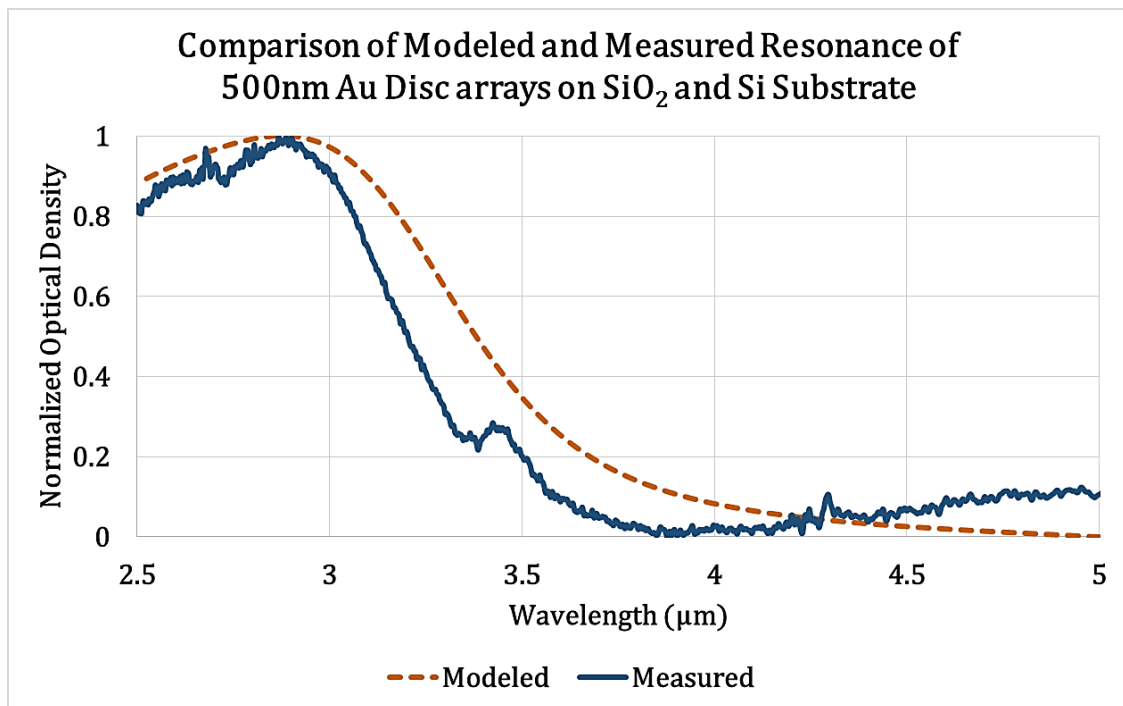
Figure 69. Comparison of modeled and measured results for 500 nm Au disc array on SiO₂ layer and Si substrate at room temperature.

Also of note in figure 68 is the differences in the amplitude of the OD. A

comparison of the 500 nm diameter disc arrays will show that the amplitude of Au is

slightly larger than that of Pt. This again is to be expected due to the larger electrical

conductivity of Au. Yet, the Au has more of an asymmetric resonance. To confirm that

this asymmetry was not an anomaly in the measurement, I modeled the structures in

ANSYS HFSS. Figure 69 shows that the modeled results agree well with the

measurement, and seem to support the assertion made in Chapter 5 that Au will yield a

more asymmetric resonance than Pt.
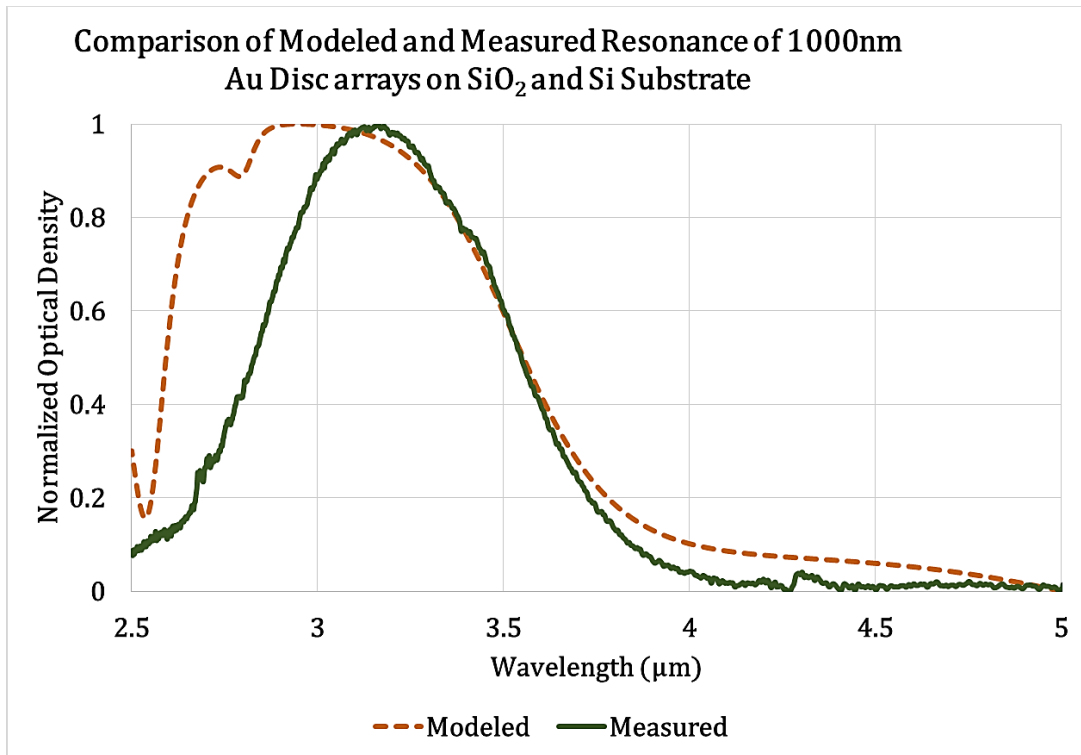
Figure 70. Comparison of modeled and measured results for 1000 nm Au disc array on SiO₂ layer and Si substrate at room temperature.

In contrast, the larger discs for Au, shown in figure 70, have a more symmetric

line shape. Again, I modeled these discs to confirm the legitimacy of my measurements.

The modeled results show a broader resonance than that of the measured, however the

two spectra are still in reasonable agreement. Both show a more symmetric resonance,

yet their peaks are shifted with respect to one another by 170 nm, suggesting the

163

deposited metal discs may have a slightly different diameter than designed. Examining the measured disc diameters in table 11 seems to confirm my hypothesis, because the discs were not perfectly circular.

Our PbSe films were deposited, oxidized, and sensitized on the 500 nm Au disc array, and the OD was measured in the same method described above. The 500 nm Au disc array was chosen for these measurements instead of the 1000 nm disc array to avoid the interference peaks observed in the modeled results in figure 61. Due to the roughness of the films and the substrate, interference effects are difficult to distinguish during a simple FTIR OD measurement. Therefore, larger discs are reserved for PbSe devices described later.
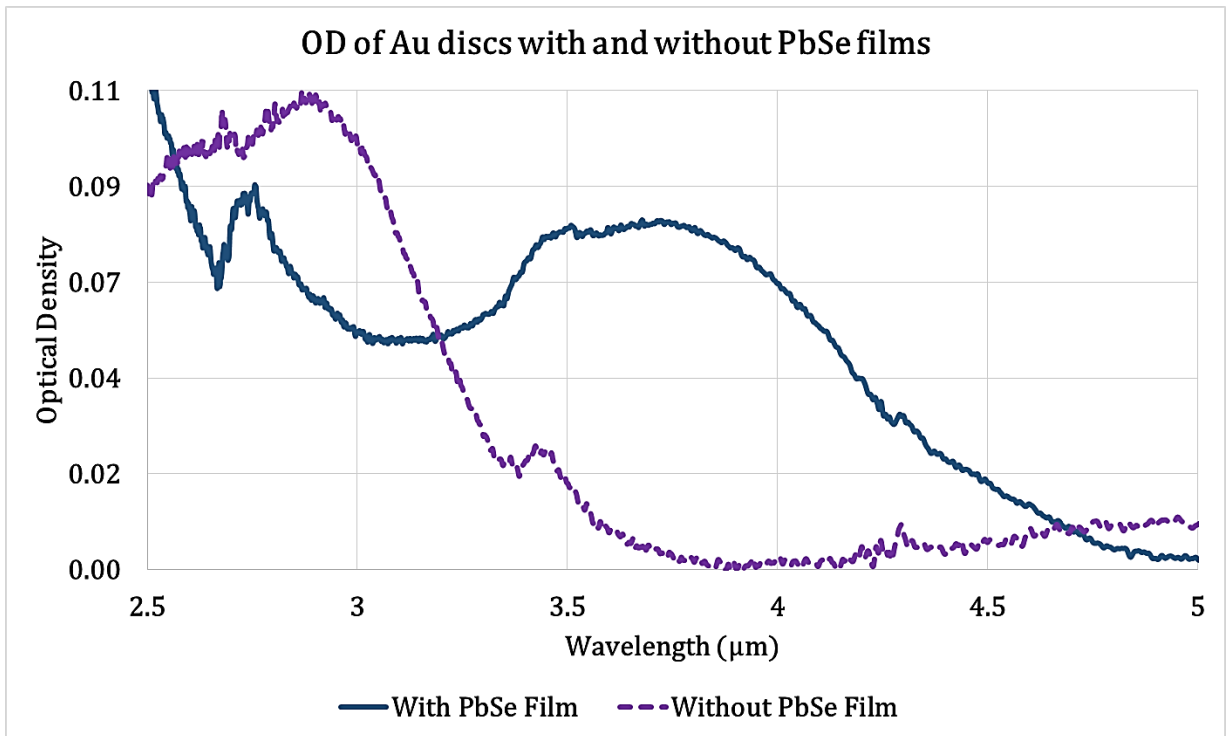
Figure 71. Room temperature comparison of resonance for 500 nm diameter Au disc arrays within and without PbSe films with layer thicknesses of approximately 400 nm, 500 nm, and 1200 nm for the PbI$_2$, PbSe, and SiO$_2$, respectively.

Figure 71 shows the spectra obtained from PbSe films with embedded discs. Inside the PbSe films, the resonance shifts by 860 nm from the discs without PbSe. Further, the amplitude of the optical density decreases due to the decrease in reflectance between the PbSe-Au interface compared to the air-Au interface without PbSe films. This shift, as well as the resonance peak wavelength, is indicative of surface plasmon resonance. Moreover, this shift was predicted when considering the discs modeled without PbSe shown in figure 69, and the disc arrays modeled with PbSe shown figure 56. This shift confirms the surface plasmon resonance effect present in the investigated PbSe films with embedded metallic discs.
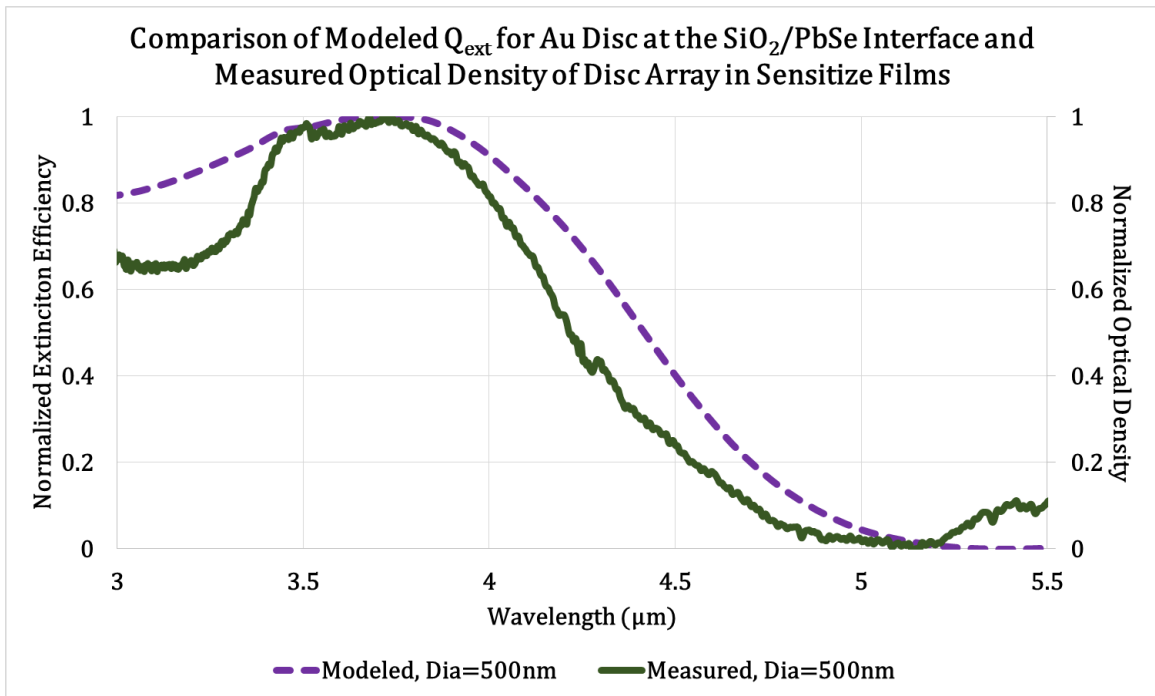
Figure 72. Comparison of modeled and measured spectra of 500 nm Au disc arrays in PbSe films.

For completeness, figure 72 shows the comparison between modeled extinction efficiency in figure 56 and the measured OD. The peak of the measured and modeled spectra match, suggesting that a pitch twice that of the diameter leads to a negligible

amount of coupling between the fields of adjacent discs. The measured discs show a

narrower resonance than that of the modeled spectra, similar to the results presented in

figure 69 and figure 70. This increased broadening in the modeled results is most likely

due to the difference in the dispersion relations of the real film and fabricated gold discs.

Nevertheless, the peak resonance was accurately predicted, so the next step was to

fabricate and measure PbSe photoconductive devices with embedded discs.

6.2 PbSe Detectors with Embedded Pt Disc Arrays
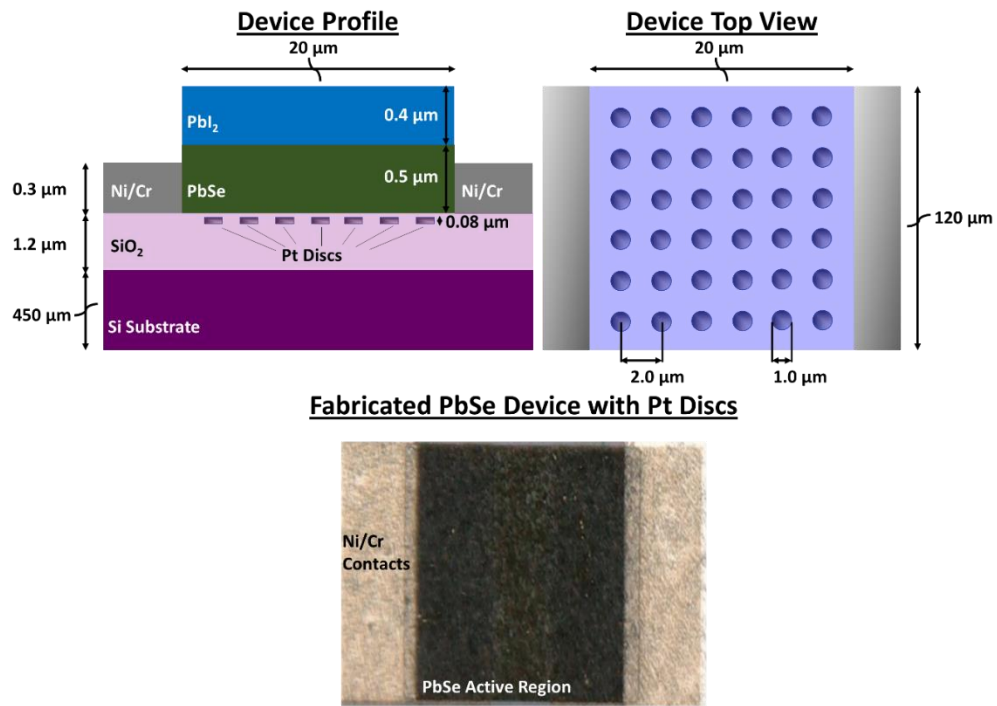
Figure 73. PbSe photoconductive devices with embedded Pt disc array; (top-left) depiction of the designed device cross-section, (top-right) depiction of the top view of device showing the Pt disc arrays, and (bottom) top view of fabricated PbSe device.

Test detector devices with embedded Pt discs at the SiO_2-PbSe interface were

fabricated using photolithography. Gold, though it offers a larger enhancement and is

acceptable for FTIR measurements, was found to have a tendency to thermally diffuse

into the PbSe during the oxidation and sensitization processes. This has been found in

166

previous experiments to lead to leakage current and overall degraded performance in photoconductive PbSe devices. Platinum did not show any signs of diffusion, and so was used for this investigation. Platinum has a higher loss than Au, so the performance would prove to be different than that predicted in figure 61. The resolution of the photomask and photolithography system was limited to ~1 µm features, so discs of approximately 1 µm and aspect ratio between 12.5 and 15 were fabricated. Here the variation in aspect ratio was due to variances in fabricated thickness. Test detectors, depicted in figure 73, were 20 µm (width) x 110 µm (length) in dimension for the disc detectors. To reduce the possibility of quenching, a SiO_2 insulation layer was deposited on top of the discs. For these devices the insulation layer was designed to be 30 nm, however through fabrication errors the insulation layer turned out to be 180 nm. This fabrication error will be discussed in more detail for it is the primary reason that the measurement results did not agree with the modeled spectrum.

I measured the spectral response of these PbSe photoconductive devices with embedded Pt discs using a modified method as that depicted in Chapter 2. For these measurements a *FEMTO* model DLPCA-200 current pre-amplifier was connected in series with the detector, and was used to bias the detector up to a maximum value of 6 V for a field strength, defined as the quotient of the applied voltage and width of the active region between metal contacts, of 3 kV/cm. This pre-amplifier was operated in AC mode, and grounded to the test fixture chassis to reduce noise. Signal current was amplified by a factor of 10^6, and input into a *Stanford Research Systems (SRS)* model SR560 low-noise amplifier. The *SRS* low-noise amplifier converts the signal to voltage, and noise is further reduced by a 300 kHz–1 MHz built in bandpass filter. The signal was further amplified

up to a factor of 100 before being output to the auxiliary detector input of a *Magna-IR*
model 550 spectrometer. The secondary FTIR arm was used to project the black body
source out of the FTIR, where it was reflected off of a parabolic mirror with a 50 cm
focal length and focused onto the detector. Again, a *Thor Labs* FDPSE2X2 2 mm x 2 mm
PbSe photoconductor was used to determine the power of the black body source, and
using equation 2.15 from Chapter 2 the spectral responsivity was calculated.
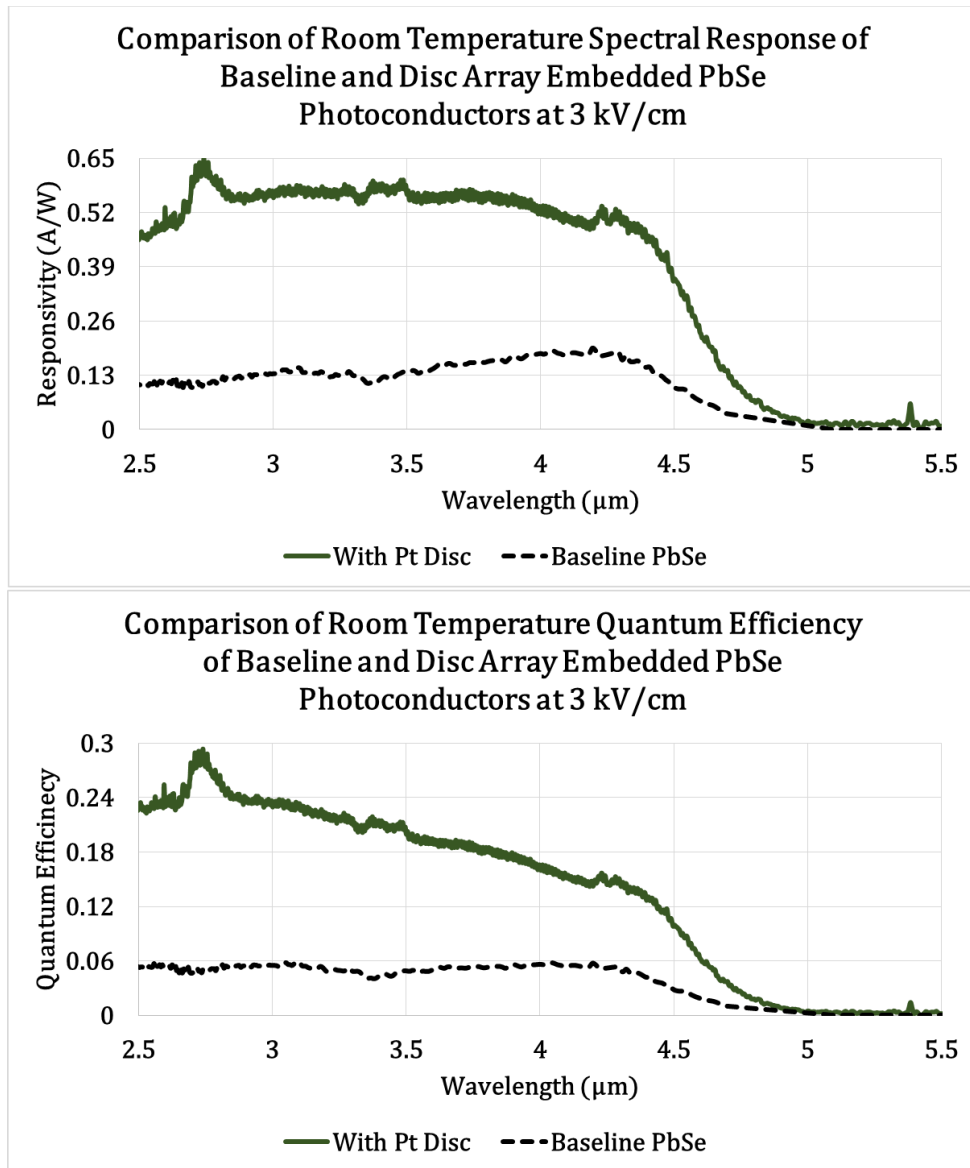
Figure 74. Comparison of room temperature (290 K) spectral response (top) and EQE (bottom) between PbSe with embedded Pt discs and baseline detectors.
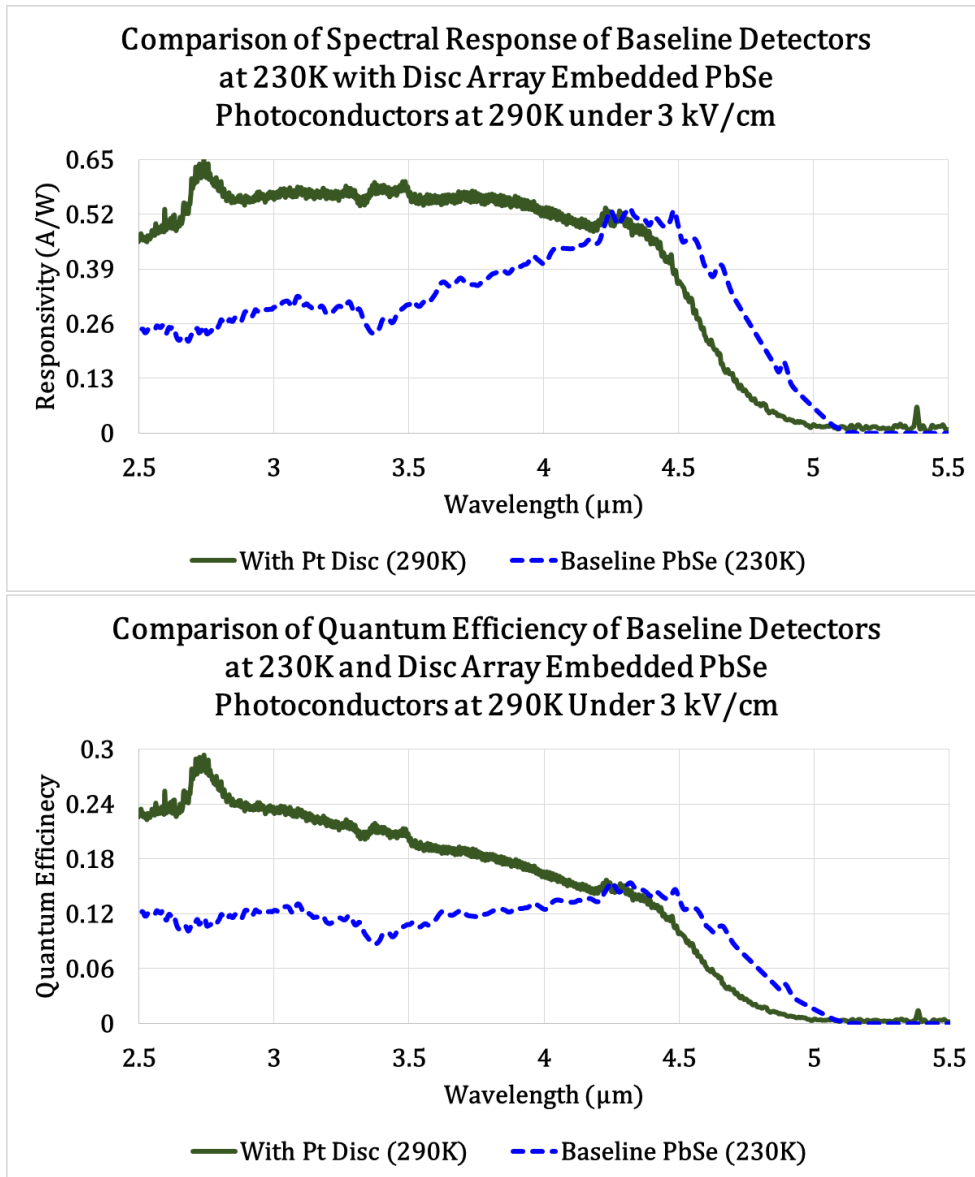
Figure 75. Comparison of room temperature (290 K) spectra of PbSe with embedded Pt discs with that of the 230K spectra of baseline detectors.

The measured room temperature spectral response of these devices is shown in figure 74. The maximum in-band response was found to be 570 mA/W between ~3.4 µm and 3.8 µm as opposed to 180 mA/W at 4.3 µm seen in the baseline detectors. This result shows a factor of three increase, as well as a blue shift in the maximum position. However, the spectrum does not show the predicted behavior of figure 61. From the

169

prediction, it would be expected that there would be distinguishable interference peaks, as well as a peak close to 3.6 µm. This discrepancy between the measured and modeled spectrum shape can be explained by the 180 nm SiO_2 insulation layer. It was designed to be 30 nm, yet through errors in fabrication it was six-times greater. Such a large layer of SiO_2 deposited on top of the discs lead to the surrounding medium having a factor of two lower index of refraction than the effective index of refraction at the interface between the PbSe and SiO_2 layers. It is the authors hypothesis, from the principles described in Chapter 3, that this would blue shift the primary resonance peaks. Furthermore, it would lead to unknown interference effects. This is a point of further investigation for future study.

Though a distinguishable peak was not observed, the decrease close to 3.4 µm indicative of interference in the baseline PbSe spectrum was absent. There are two possible explanations. The first is that the difference in SiO_2 thickness and the placement of the disc spoils the cavity length that leads to interference. The second possible explanation is that the peak that now resides at ~3.4 µm is from plasmonic resonance, which now compensates for the reduction in responsivity due to destructive interference. This second explanation would explain the factor of three increase over the baseline PbSe performance. It has been shown using surface plasmon resonant disc arrays can yield up to a five-fold increase in responsivity [3]. Therefore, it is again the author's hypothesis that should the discs arrays be positioned close to the PbSe-SiO_2 interface, an enhancement of greater than three-times is achievable over this baseline. This would be due to the enhanced electric field intensity leading to excess carrier generation in the PbSe, which would lead to an effective increase in both absorption and internal quantum

efficiency. To reiterate, this is a point of further investigation for future study. It should be noted that the second explanation for the absence of the interference dip at 3.4 µm is consistent with the assertion that peaks in figure 61 in the vicinity of 3.4-3.6 µm are associated with SPR.

Interestingly the peak responsivity of the sample with Pt discs has a value that is similar to that of the 230 K spectrum shown in figure 22. Indeed, figure 75 shows a comparison indicating that the detectors with embedded Pt discs have similar sensitivity to the 230K spectra in the baseline detectors at the PbSe absorption edge of 4.3 µm. Moreover, the sensitivity of the embedded disc samples is greater than that of the baseline detectors over a large portion of the MWIR band. With proper fabrication and optimization, the room temperature samples may have even greater sensitivity over the baseline detectors at lower temperature. Though the disc detectors are not optimized, these results still serve as a proof of concept that surface plasmon resonant structures enable room temperature operation PbSe photoconductors with higher sensitivity.

6.3 PbSe Devices with Embedded Metallic Back Reflector
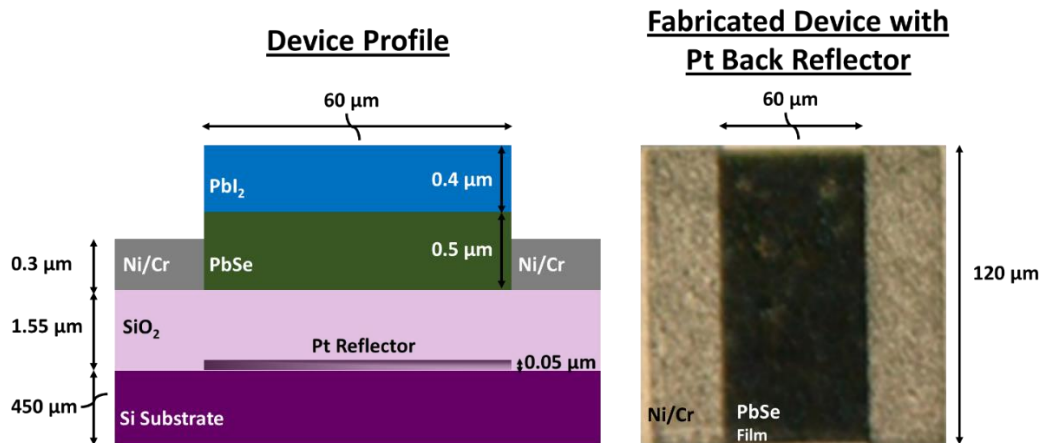
Figure 76. PbSe photoconductive devices with embedded Pt back reflector; (left) depiction of the designed device cross-section, (right) top view of fabricated PbSe device.

In Chapter 5, a large increase was predicted over the baseline detector for PbSe devices with an embedded Pt back reflector. To confirm this prediction, PbSe devices with Pt back reflectors were fabricated. Similar to the metallic disc fabrication process, 50 nm thick Pt back reflectors were deposited on the native SiO_2 layer of the Si substrate. In accordance with the desired resonance discussed in Chapter 5, plasma enhanced chemical vapor deposition was used to grow a 1.5 µm SiO_2 layer utilized as a dielectric spacer. Following this step, the modified baseline process for reduced roughness PbSe detector fabrication (describe in Appendix A) was followed to fabricate 60 µm (width) x 120 µm (length) photoconductive test detectors similar to that of the baseline configuration. Figure 79 depicts the devices with embedded metallic reflectors.
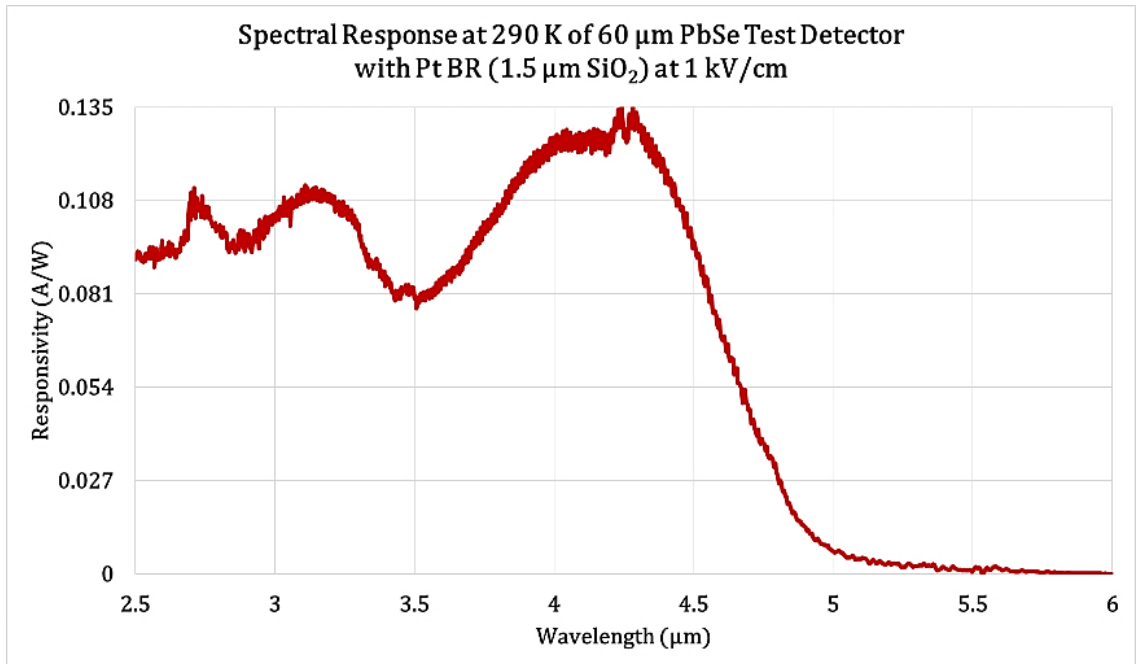
Figure 77. Room temperature (290 K) spectral response of PbSe test detectors with embedded Pt back reflector and 1.5 µm SiO_2 spacer under an applied field of 1 kV/cm.

Detectors with embedded Pt reflectors were tested using the same spectral response method described above for the embedded disc arrays. A 6 V bias was applied to the detector, resulting in a 1 kV/cm electric field. It was found that the spectrum in figure 77 is very similar in shape to that of the predicted spectra in figure 66, which will be discussed in more detail at the end of this chapter. Two peaks from thin film interference were clearly observed at 4.3 µm and 3.2 µm, suggesting a free spectral range of 1.1 µm. This free spectral range was calculated to be within 1.6% of the theoretical value for a film with layer thicknesses of 300 nm for PbI$_2$, 500 nm for PbSe, 1500 nm for SiO$_2$, and 50 nm for Pt. In this case the substrate was excluded from the calculations, because all of the incident light should either be reflected or dissipated in the Pt layer based on previous calculations. Incidentally, this is also why FTIR absorption measurements were not conducted on these samples.

The amplitude of the peak spectral response shown in figure 77 is approximately 1.7 times less than that of the baseline detectors. However, notice that the applied field across these detectors is three-times less than that of the field applied to the baseline detectors. The photo-generated current I$_L$ in a photoconductor is directly proportional to the applied electric field E across the detector by equation 6.1,

$$I_L = J_L A = q G_L \tau (\mu_n + \mu_p) A E \tag{6.1}$$

where J$_L$ is the current density in A/cm^2, A is the detector area in cm^2, q is the charge constant, G$_L$ is the carrier generation rate in cm^{-3}s$^-$, τ is the carrier recombination lifetime in µs, and the mobility of the electrons and holes in cm^2/Vs is given by μ_n and μ_p, respectively [4-5]. The photocurrent scales linearly with applied electric field until the products $\mu_n E$ and $\mu_p E$ reach their saturation velocities. In baseline detectors, we have

observed the photocurrent to continually increase with applied fields in excess of 5
kV/cm, so linearly scaling the data up to 3 kV/cm to predict higher field performance was
considered to be an acceptable approximation.
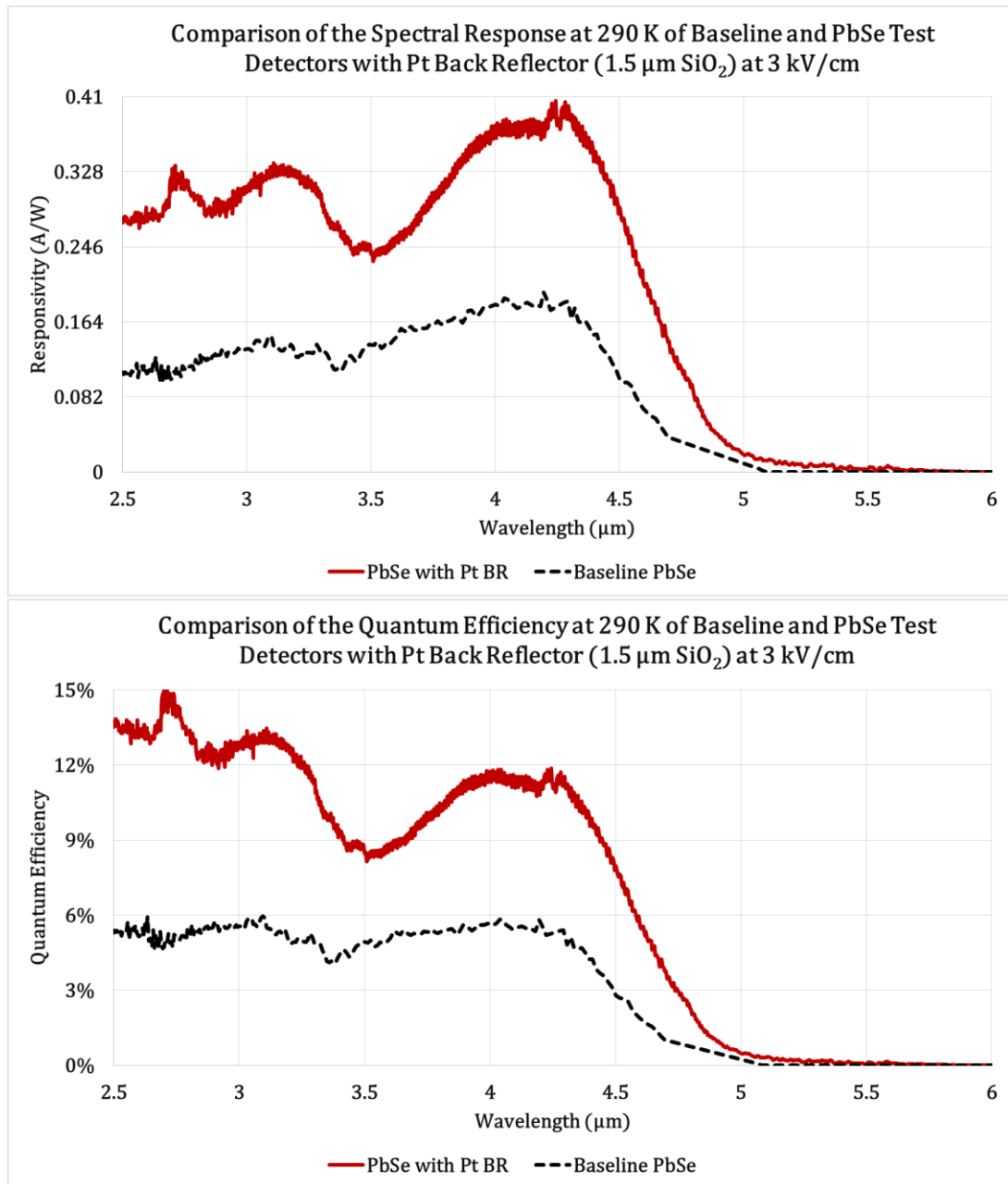
Figure 78. Comparison of room temperature performance of baseline PbSe and predicted performance with Pt back reflector at 3 kV/cm.

174

The amplitude of the spectral response spectrum in figure 77 was linearly scaled to predict and directly compare the performance of the test detector with the embedded back reflector to that of the baseline PbSe detectors at room temperature under an applied field strength of 3 kV/cm. In figure 78, the interference peaks in both the baseline and Pt back reflector test detectors clearly overlap at 3.1 and 4.1 µm. Indeed, when the same free spectral range calculations were performed on the results from the baseline films the value obtained was 1.13 µm, which is within 2% of the distance between peaks in the measured spectra. Considering the similarity between the shapes of the observed responsivity spectra in figure 78, it may be tempting to assume that the design process described in Chapter 4 and Chapter 5 was unnecessary. After all, a back reflector could just as easily be fabricated in the baseline detector configuration. From the modeled results verified in figure 49, the baseline PbSe films have a SiO_2 layer thickness of 1225 nm. However, consider figure 41 in which the absorption spectrum for different SiO_2 thicknesses was presented. For a 1200 nm SiO_2 thickness, the absorption peaks are closer to the lower end of the spectrum. Discussed in Chapter 5, the responsivity is weighted toward longer wavelengths. Therefore, by designing the back reflector configuration to have a SiO_2 thickness of 1500 nm, the detector performance has been optimized for longer wavelengths.

In contrast to the PbSe alone, the majority of the light that would transmit into the substrate is reflected back for a second pass through the film. As can been seen, under the same electric field, this retro-reflective surface leads to a factor of two enhancement in responsivity over the whole MWIR band. Moreover, an examination of figure 79 shows the scaled sensitivity at 290 K in the back reflector embedded detector is similar to that of

the baseline detectors at 250K. Similar to the disc-embedded detectors discussed above, these results serve as confirmation that the back reflector structure is a viable method for increasing the operating temperature of PbSe photoconductors.
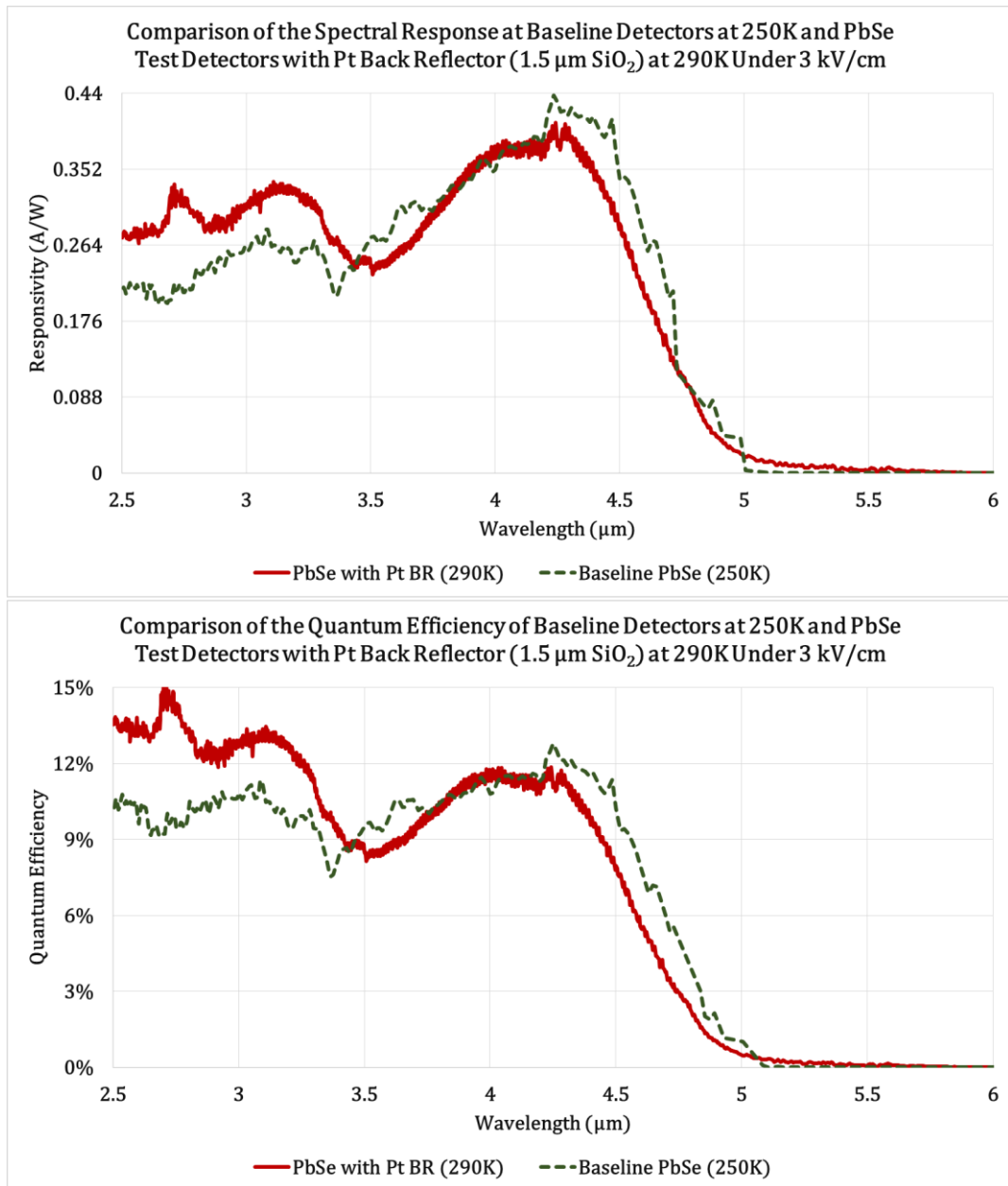
Figure 79. Comparison of 290 K spectra of PbSe with embedded Pt reflector with that of the 250 K spectra of baseline detectors.

It should be noted that part of the enhancement in responsivity and quantum efficiency is likely due to the reduction in roughness, described in Appendix A, from 500 nm peak-to-peak to 100 nm peak-to-peak leading to smoother interfaces and less variance in layer thickness. Even with the reduced roughness, however, the spectrum is broadened when compared to the model predictions.
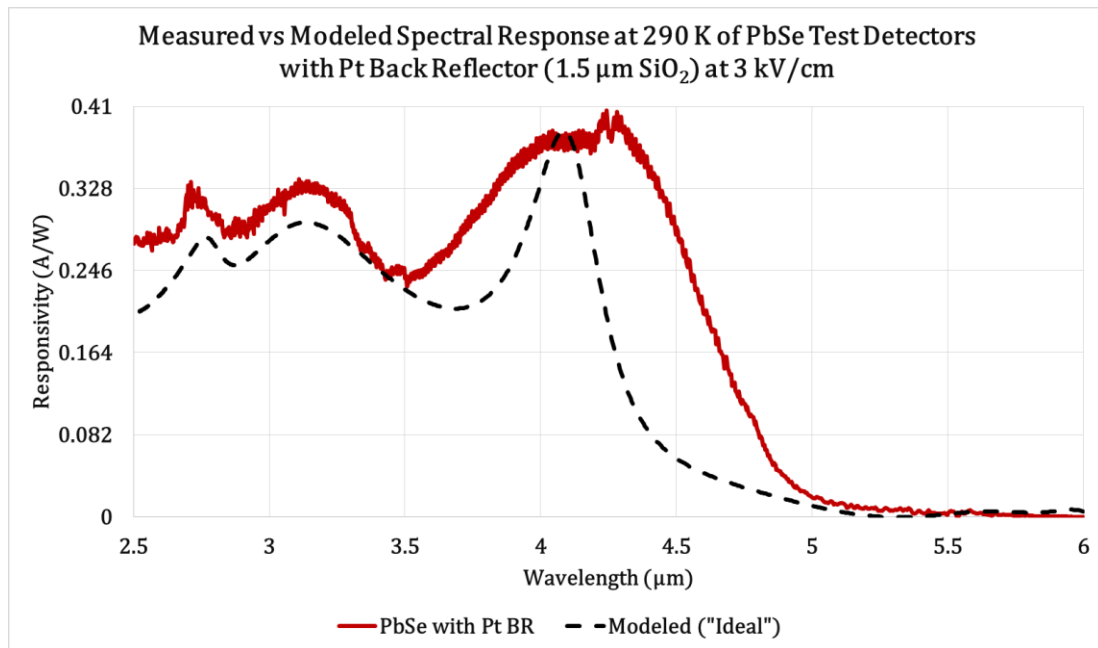
Figure 80. Measured vs modeled spectral response at 290 K of PbSe test detectors with embedded Pt back reflector and 1.5 µm SiO₂ layer.

In figure 80, the measured and modeled spectra are very similar, with their peaks residing in nearly identical locations. The most noticeable difference is that of the width of the primary peak at 4.1 µm. In the predicted results, the peak is narrow having a FWHM of approximately 230 nm. By comparison, the measured results have a FWHM of 750 nm. This broadening is due to the induced and inherent roughness from the polycrystalline grains in the PbSe films. As broadband light travels through the film, it will be scattered by PbSe crystallites, impurities, etc. This scattering increases the path

length within the film, leading to increased absorption and altering the angle of incidence for interference fringes throughout various parts of the beam propagating through the film. An increase in absorption explains the slight increase in spectral response over that of the modeled results, whereas the change in interference due to the increase in path length and incident angle is responsible for broadening. Yet, from figure 80 it is apparent that the majority of the photons that contribute to photocurrent travel without deviation from scattering through the film resulting in constructive interference and the primary peak at 4.1 µm.

Chapter 6 References

[1]   M. J. Madou, *Fundamentals of Microfabrication: The Science of Miniaturization*, Second Edition. CRC Press, 2002.

[2]   S. A. Campbell, *Fabrication Engineering at the Micro- and Nanoscale*, Fourth Edition. Oxford University Press, New York, 2013.

[3]   X. Tang, et al. "Plasmon resonance enhanced colloidal HgSe quantum dot filterless narrowband photodetectors for mid-wave infrared," J. Mater. Chem. C, 5, 2017.

[4]   J. Singh, *Optoelectronics: An Introduction to Materials and Devices,* McGraw-Hill Companies, Inc., 1996.

[5]   D. A. Neamen, *Semiconductor Physics and Devices: Basic Principles, 3rd Ed*, New York, NY: McGraw Hill, 2003.

Chapter 7: Conclusion

The goal of this study was to increase the performance of PbSe photoconductive detectors, such that the sensitivity at room temperature is comparable to that of the current stat-of-the-art at lower temperatures. Discussed in Chapter 5, an absorption enhancement of up to three-times over the baseline was predicted for surface plasmon resonant discs, and an absorption enhancement of up to 2.55-times over that of the baseline PbSe absorption was predicted both numerically and by finite element modeling for the back reflector structure. In Chapter 6 it was shown that the surface plasmon resonant discs embedded in PbSe devices produced a factor of three enhancement in spectral responsivity at room temperature when compared with the baseline detectors under the same applied electric field. Moreover, it was shown that the disc-embedded detectors have performance at room temperature comparable to the baseline detectors at 230K. These results confirm the original hypothesis that surface plasmon resonant structures can be designed and tailored to increase the operating temperature of PbSe photoconductive devices. However, the spectra of the measured devices with embedded discs did not resemble the predicted results due to the large SiO_2 insulation layer. As a subject of future study, this discrepancy can be better understood and corrected. With proper optimization of the fabrication process, even greater room-temperature sensitivity could be achievable.

Also discussed in Chapter 6, the measured responsivity and quantum efficiency of the PbSe devices with embedded back reflector showed remarkable agreement with modeled predictions, and a factor of two sensitivity enhancement over the baseline PbSe detectors. Furthermore, it was shown that the back reflector structure lead to performance

at 290 K that is similar to the baseline detector at 250K, thereby confirming the viability of the back reflector interference structure as a mechanism for raising the operating temperature of PbSe photoconductors from 250 K to 290K. Presented in Chapter 5, FEM predictions demonstrate that the resonance can be tuned to specific wavelengths and regions by changing the thickness of the underlying SiO_2 layer. Indeed, this opens up the possibility for tunable room temperature, low cost infrared sensing devices with excellent performance.

Table 12. Unit cell parameters for modeling the combination of surface plasmon resonant Pt discs and Pt back reflector in PbSe films.

Layer/Structure	Thickness (nm)	Pitch* (nm)
PbI$_2$	300	1000
PbSe	500	1000
Pt Disc (PEC Boundary Conditions)	40	500 (*Diameter)
SiO$_2$	1500	1000
Pt back reflector	50	1000
Si	50	1000
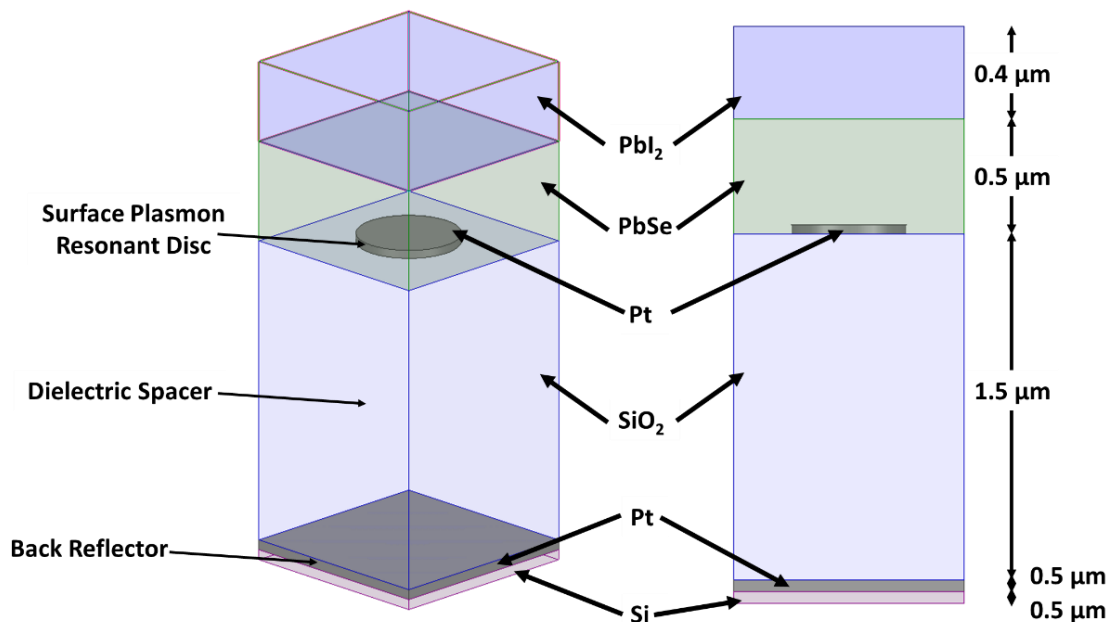
Figure 81. Unit cell of PbSe film with combination of surface plasmon resonant Pt discs and Pt back reflector modeled in ANSYS HFSS.

181

My projections suggest that the back reflector and surface plasmon resonant structures can be combined for even greater enhancement. In fact this configuration has been demonstrated by Tang in HgTe colloidal quantum dot photovoltaic detectors, yielding excellent MWIR imaging capability at cryogenic temperatures [1]. Recall from Chapter 2 that I measured an absorption of 30-35% in the baseline PbSe films. With both the plasmonic discs and the back reflector structure, I observed by analysis that this absorption can be increased by levels between three and seven times in narrow spectral regions within the MWIR regime. Films were modeled in *ANSYS HFSS* with unit cell parameters shown in table 12. The unit cell is shown in figure 81.
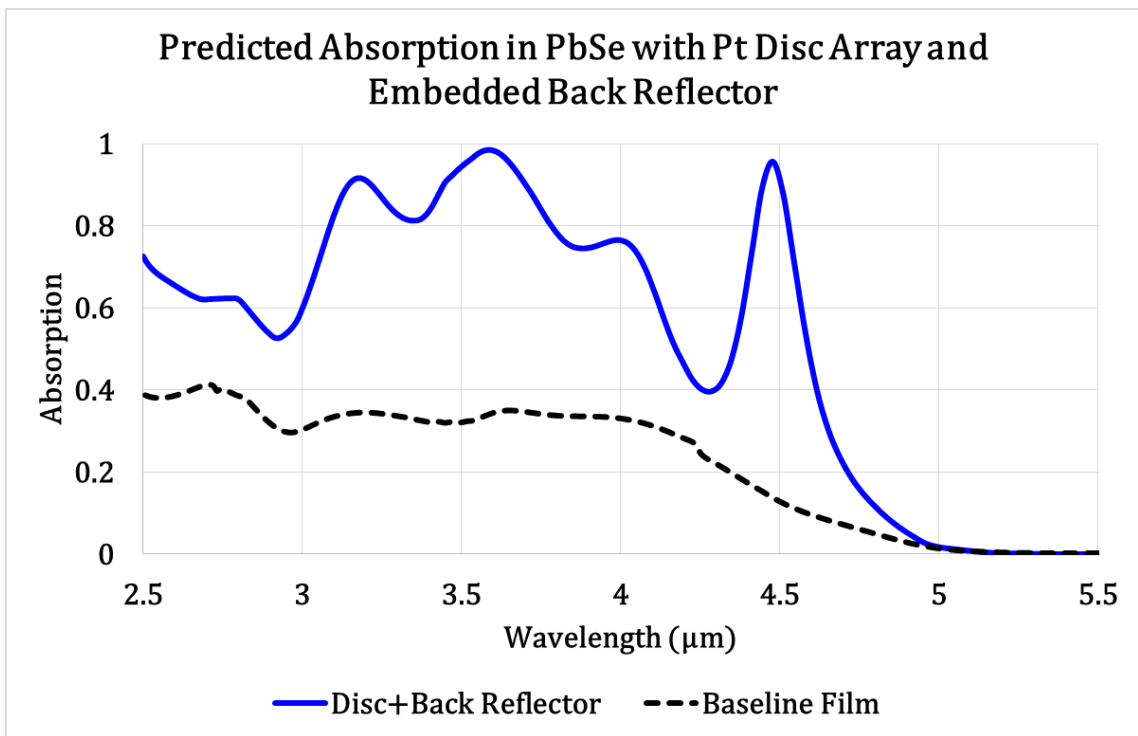
Figure 82. Predicted absorption in PbSe films with combined optical enhancement techniques of SPR and embedded metallic back reflector compared to the modeled absorption in baseline films.

Consider the spectra of figure 82, which show the predicted absorption as a result of combining a Pt disc array with a Pt back reflector in PbSe films, as well as the

modeled baseline absorption at room temperature. The absorption results predict a broadband enhancement over the whole 3 µm - 5 µm band, with maximums reaching nearly 100% at 3.6 µm and 4.5 µm. Further, the disc array is conveniently designed such that there is a decrease in absorption in the CO_2 atmospheric window between 4.1 µm and 4.4 µm. This small region also corresponds to the absorption edge of PbSe (~4.3 µm), so it is the author's hypothesis that the steep reduction in absorption at 4.3µm is due to the steep drop in absorption below the bandgap energy. The sharp increase absorption shortly after 4.3 µm leading the peak at 4.5 µm is due to the large field intensity produced from both surface plasmon resonance and interference. This large field intensity warrants further discussion.
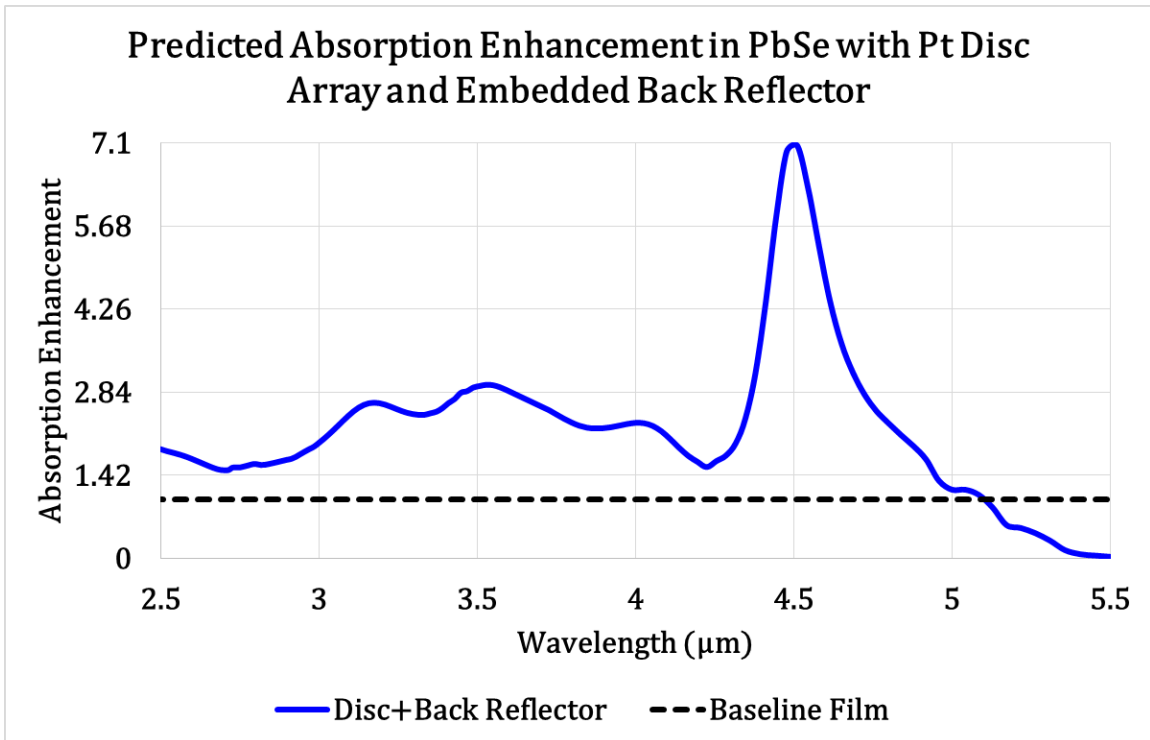
Figure 83. Predicted absorption enhancement in PbSe films with combined optical enhancement techniques of SPR and embedded metallic back reflector compared to the modeled absorption in baseline films.

183

However, before moving on consider figure 83, which shows the predicted absorption enhancement, defined as the absorption of the resonant structure enhanced film normalized to the baseline absorption spectrum, gained by combining surface plasmon resonant disc arrays with the back reflector structure. Compared to the baseline spectrum, the combination of the disc array and back reflector structures yield greater than 1.5-times the absorption over the whole band, three-times the absorption at approximately 3.6 µm, and over a factor of seven times greater absorption at 4.48 µm.
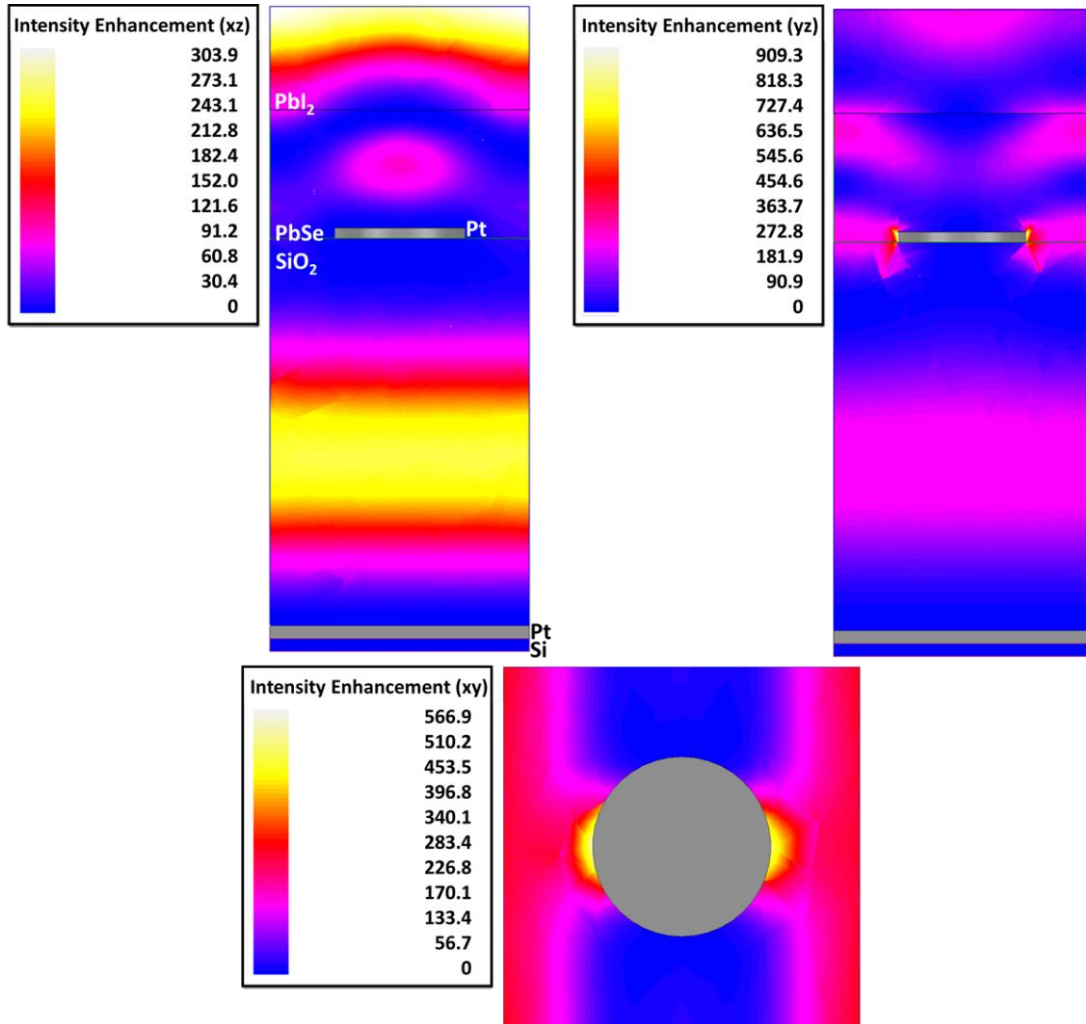
Figure 84. Electric field Intensity enhancement plots for surface plasmon resonant Pt discs and Pt back reflector embedded in PbSe films at an incident wavelength of 3.60 µm. in the (top-left) xz-, (top-right) yz-, and (bottom) xy-directions.
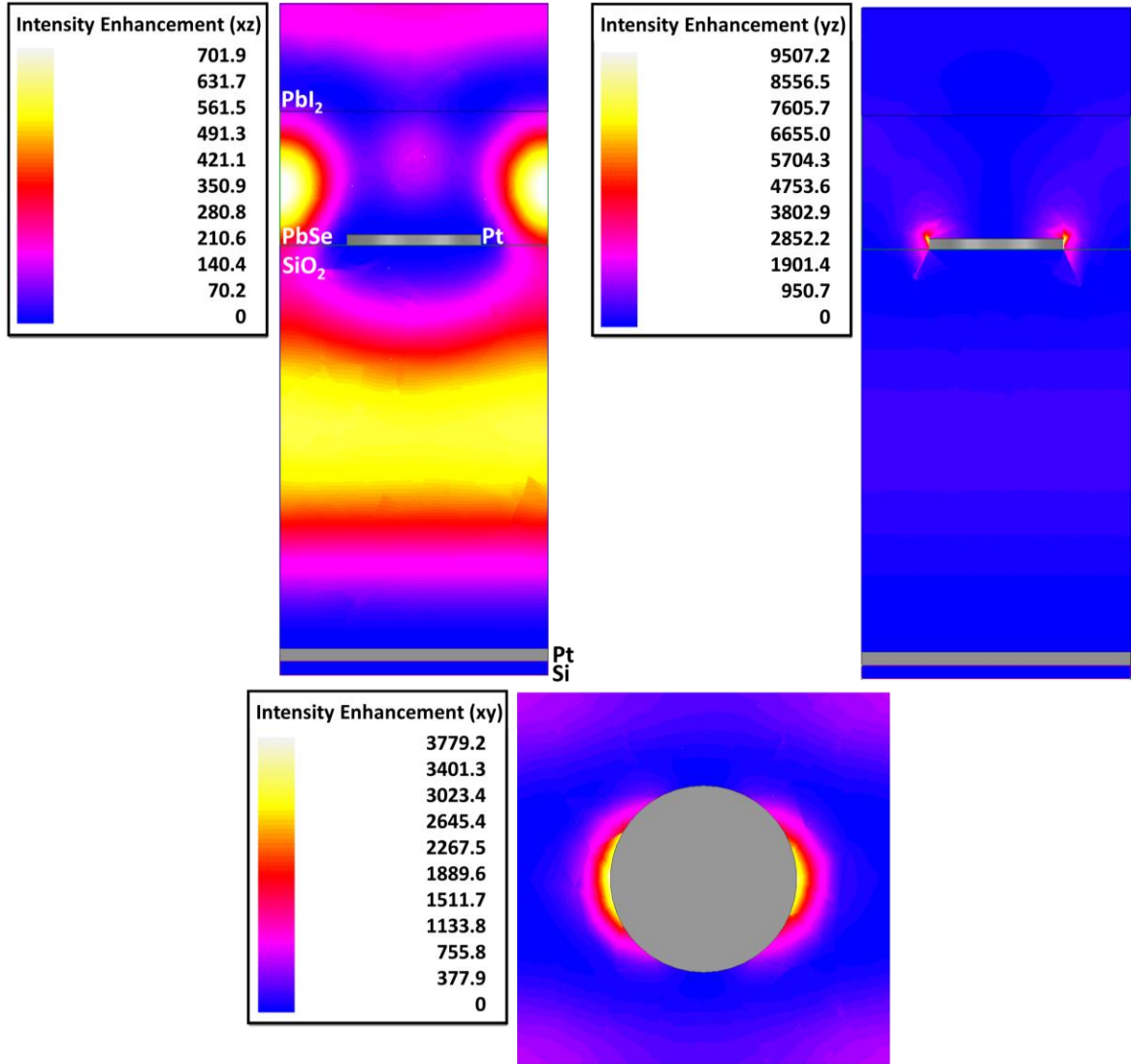
Figure 85. Electric field intensity enhancement plots for surface plasmon resonant Pt discs and Pt back reflector embedded in PbSe films at an incident wavelength of 4.48 µm. in the (top-left) xz-, (top-right) yz-, and (bottom) xy-directions.

To observe the origins of this large absorption increase and gain insight into the increase in electric field intensity offered by this configuration, discrete frequency calculations were performed using *ANSYS HFSS*. Figure 84 and figure 85 show the electric field intensity enhancement, defined as the resulting electric field intensity in the film normalized to the incident electric field intensity, in the PbSe film with an embedded Pt disc array and Pt back reflector for an incident plane wave with free a space

185

wavelength of 3.6 µm and 4.48 µm, respectively. Nearly 100% absorption is predicted at these wavelengths, so they were selected for further analysis. It should be noted, however, that large intensity enhancements are also expected at 3.2 µm and 4 µm. In the xz-plane of figure 84 (top-left), the majority of the intensity enhancement is in the SiO_2 layer, suggesting the Pt disc and Pt back reflector make a plane-parallel (Fabry-Perot) cavity [2-5]. Still, there is an intensity enhancement between 60 and 90 in the middle of the PbSe layer. In the xy-plane (bottom), the effects of both surface plasmon resonance and interference are observed. The field intensity in the vicinity of the disc surface is similar to the intensity shown in Chapter 4 for surface plasmon resonant discs. The intensity observed on the edges of the unit cell in the xy-plane are those associated with interference. To be sure, the fields in the yz-plane (top-right) show the large electric field intensity enhancement expected around the disc, as well as the fringes expected of interference. With a field intensity enhancement of over 900 possible using this configuration, it is clear why the absorption is predicted to be nearly 100%.

Similar phenomena are observed in figure 85. The intensity enhancement at 4.48 µm is much larger than at 3.6 µm. In the xz-plane (top-left), the larger electric field intensity enhancement is again seen in the SiO_2 layer, suggesting the same resonant cavity is produced between the Pt discs and Pt back reflector. The field intensity in the PbSe, however, is much larger reaching the maximum intensity enhancement in the space between discs. This is indicative of the dual-dipole effect described in Chapter 3. In the xy-plane (bottom), surface plasmon resonance is again observed. The interference fringes observed in the xy-plane of figure 84 are absent, suggesting that the dominant enhancement mechanism at 4.48 µm is surface plasmon resonance. This seems to be

186

confirmed in the yz-plane (top-right) of figure 85, with nearly all the field enhancement residing in the near-field of the Pt disc. It would seem that by combining the two techniques, the surface plasmon resonance wavelength has been shifted to 4.48 µm. An alternative explanation, that seems in part to be the case, is that multipole resonances are being excited within the Pt disc leading to multiple peaks from surface plasmon resonance. This phenomenon warrants further study in the future.
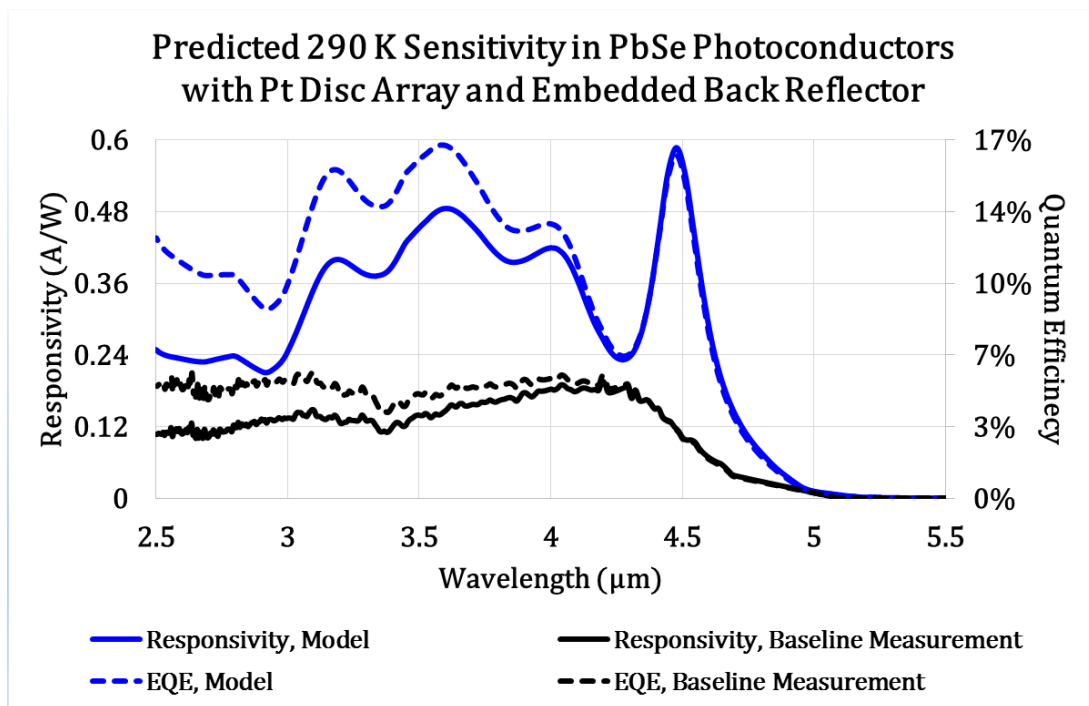
Figure 86. Predicted room temperature spectral responsivity (solid) and quantum efficiency (dashed) of PbSe devices with SPR disc arrays and embedded back reflector compared to the current baseline detector performance.

The large difference between the amplitude of the field intensity enhancement at 3.6 µm and 4.48 µm is of note, especially in the xy- and yz-planes. The field intensity enhancement for illumination of 4.48 µm is ~100-times greater than that at 3.6 µm, yet the absorption at the former is slightly lower than the latter. An examination of the

baseline spectrum in figure 82 shows that the PbSe absorption falls off above the cutoff wavelength. Therefore, it is necessary for the field intensity enhancement to be much larger in this region to achieve such a large absorption. Future investigation into this configuration could yield interesting new avenues for PbSe detectors, such as near room temperature long-wave detection.
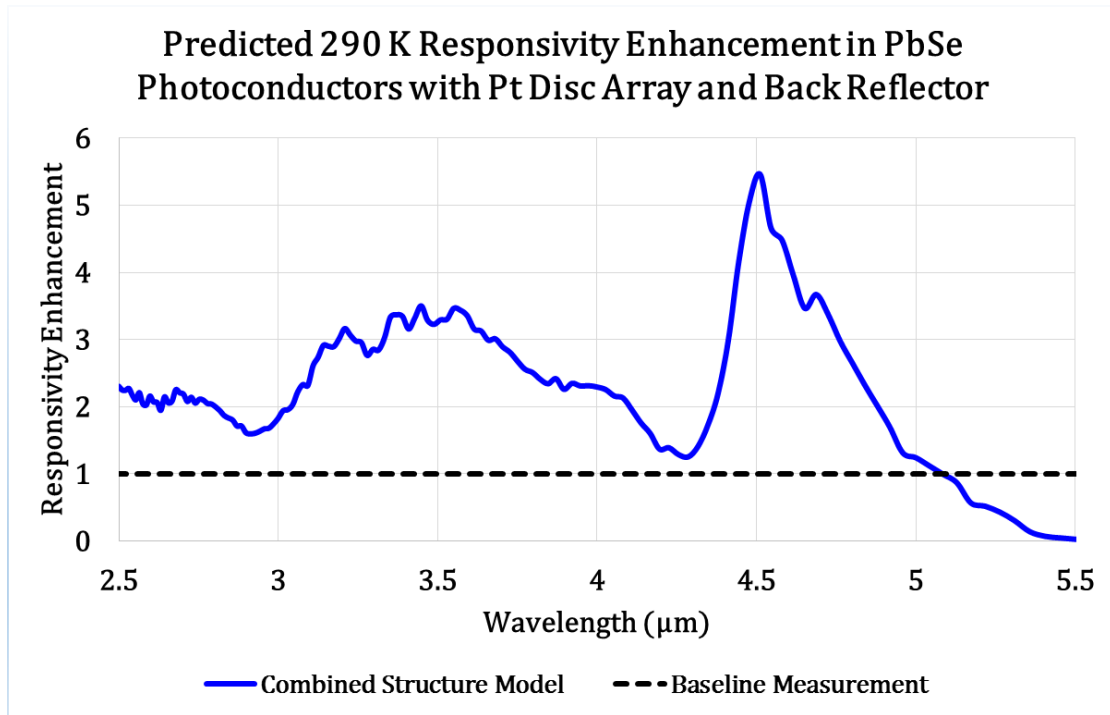
Figure 87. Predicted room temperature spectral responsivity enhancement PbSe devices with SPR disc arrays and embedded back reflector (blue, solid) over the baseline detector performance (black, dashed).

The sensitivity of ideal detectors with these combined techniques has also been predicted by assuming the internal quantum efficiency of the baseline detectors at room temperature (~17%) still holds. Presented in figure 86, the responsivity (blue, solid trace) of the resonant structure enhanced detectors is predicted to reach a maximum of 0.58 A/W at 4.5 µm, with 0.41 A/W, 0.48 A/W, and 0.4 A/W coinciding with peaks at 4 µm, 3.6 µm, and 3.2 µm, respectively. The quantum efficiency (blue, dashed trace) reaches a

high of ~17% at 3.6 µm and 4.5 µm, with greater than 10% over most of the rest of the

MWIR band for the same detector.
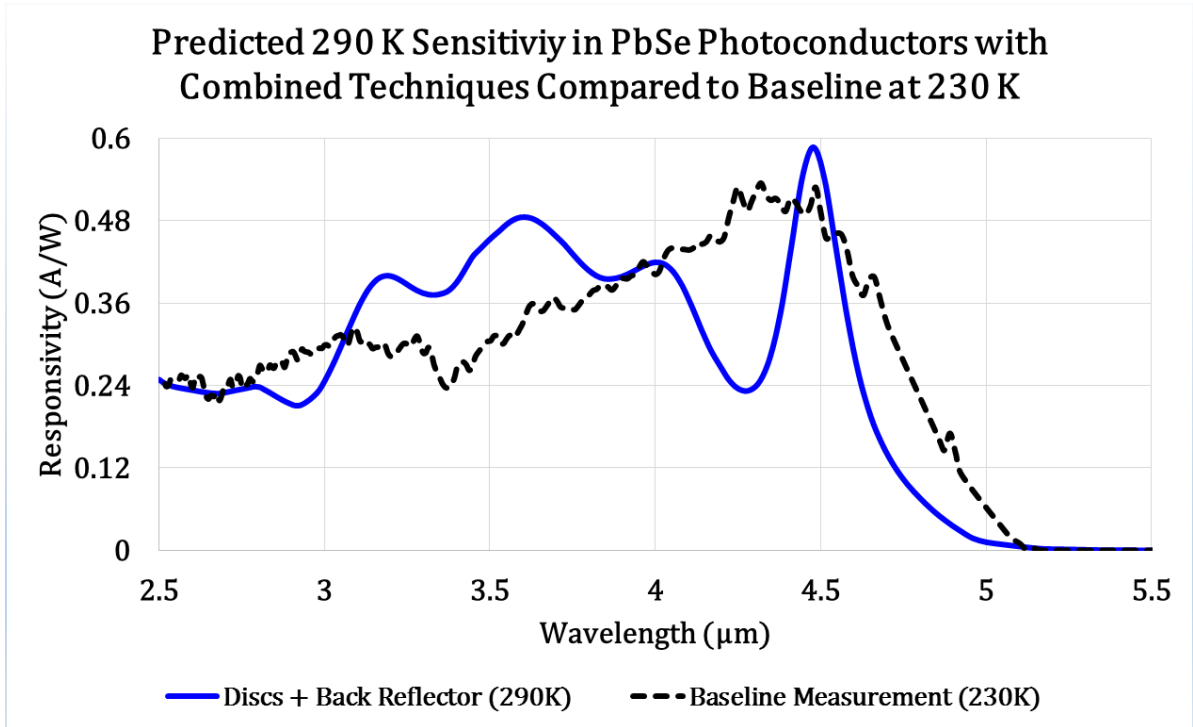
Figure 88. Predicted room temperature (290 K) sensitivity of PbSe detectors with combined Pt disc array and Pt back reflector compared to measured baseline sensitivity at 230 K.

Of note is the fact that the predicted performance at room temperature for this

combination of structures is greater than 3-times that of the baseline detector performance

at 3.6 µm and over 5-times greater at 4.48 µm. In fact, figure 87 shows that the

responsivity is above that of the baseline detector over the whole 3-5 µm band.

Moreover, the predicted performance, shown in figure 88, is greater than that of the

measured baseline at 230 K for a majority of the usable MWIR spectrum. These results,

along with those shown in Chapter 6, show that by proper design and fabrication of these

optical management schemes, the sensitivity of PbSe MWIR detectors can exceed that of

the current state-of-the-art such that their performance is greater at room temperature than

devices with PbSe alone at temperatures as low as 230 K.

Chapter 7 References

[1]   X. Tang, M. Ackerman, and P. Guyot-Sionnest, "Thermal Imaging with Plasmon Enhanced HgTe Collidal Quantum Dots Photovoltaic Devices," manuscript nn-2018-03871g submitted to ACS Nano, 2018.

[2]   E. Hecht, *Optics*, 4th Edition. Addison-Wesley, New York, 2002.

[3]   R. E. Fischer, et al. *Optical System Design*, 2nd Edition, SPIE Press, McGraw Hill, 2008.

[4]   OP-Tec: National Center for Optics and Photonics Education, *Fundamental of Light and Lasers*, 2nd ed. Texas: Op-TEC, 2013.

[5]   W. T. Silfvast, *Laser Fundamentals*, New York, NY: Cambridge University Press, 2000.

[6]   C. C. Davis, *Lasers and Electro-Optics: Fundamentals and Engineering*, 2nd ed. New York, NY: Cambridge University Press, 2014.

Appendix A: Fabrication of PbSe Devices

PbSe Baseline Detector Fabrication

The deposition process starts with a three-inch single side polished <100> Si wafer from *Pure Wafer, a WRS Company* [1] with a $1 - 1.5$ µm thick SiO_2 layer grown by plasma enhanced chemical vapor deposition (PECVD) on top [2]. Reactive ion etching (RIE) was performed on the SiO_2 layer with tetraflouromethane (CF_4) gas to produce a peak-to-peak roughness of $400 - 500$ nm (~177 nm RMS). Described briefly in Chapter 2, we used a chemical bath deposition process to deposit and sensitize PbSe films on the roughened substrates. The process starts by mixing lead acetate trihydrate ($Pb(C_2H_3O_2)_2$) and optical grade selenourea ($(H_2N)_2C{=}Se$) in a chemical bath to produce a ~1 µm thick PbSe film. Films were then introduced into an oxygen furnace at ~450 $^{\circ}$C for oxidation, followed by a halogen furnace at 350 $^{\circ}$C to complete sensitization.

An AZ 1518 photoresist from *Microchemicals Gmbh* with a thickness of 4 µm was spin coated at a rate of 4000 rpm onto the surface for 40 seconds [4]. After a 60 second prebake at 110 $^{\circ}$C, the sample was then put into a Karl Suss MA6 Mid/Deep UV mask aligner under a photomask designed for PbSe test detectors [5]. Upon UV illumination with a wavelength of 350 nm, bonds between the molecules of the resist in the exposed area become weaker, thereby making them soluble in developer [2-3]. The sample was then immersed in a 1:1 solution of general purpose AZ developer and DI water to remove the exposed areas, exposing the PbI_2 layer of the PbSe film in a process called etch-back. The exposed PbI_2 areas were then removed down to the PbSe layer by RIE, an anisotropic technique, defining the areas for metal contact deposition. This process also

defines the detector configuration. The samples were then placed in a bath of acetone to remove the photoresist.
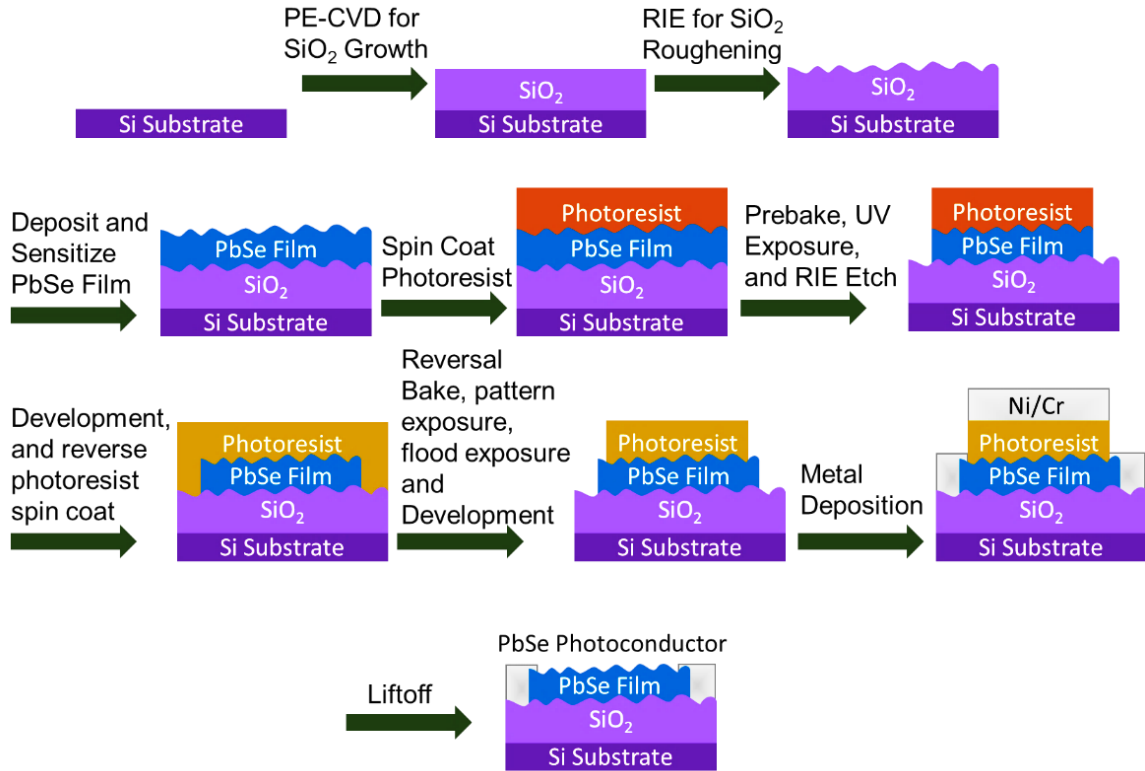
Figure 89. Fabrication process for PbSe photoconductive devices.

After cleaning with IPA and spray drying with N_2, AZ 5214-E was spin coated onto the sample to a thickness of 1.6 µm at 3000 RPM. This compound is a special positive photoresist from *Microchemicals Gmbh* which works on an image reversal process that results in the same profile as a negative resist [6]. Negative resists are typically used for metal liftoff, a process to remove excess metal after deposition. In a similar process to that described in the previous step, the photoresist was baked at 110 °C for 80 seconds, exposed and developed [7]. After developing, a second flood exposure was performed to weaken the bonds in the leftover resist. A 15 nm thick Cr adhesion layer followed by a 150 nm layer of Ni was RF sputtered onto the sample to form metal contacts. The sample

193

was then placed in AZ developer for liftoff. After drying the fabrication process was complete, resulting in baseline PbSe detectors. The process for depositing nanodiscs or back reflectors structures described in Chapter 6 is almost identical, with the exception that the metallic structures are patterned and deposited onto the SiO_2 layer before PbSe deposition. Roughening was then performed around the metallic structures for PbSe adhesion to the substrate. A depiction of the baseline PbSe fabrication process is shown in figure 89.

Preparation for Resonant Structures: PbSe Roughness Reduction

As discussed in Chapter 2, the baseline PbSe films have a peak-to-peak roughness of approximately 500 nm. Surface plasmon modes exist along the metal-dielectric interface, and, in the case of traveling waves, propagate along the metal surface. Due to the fact that these modes are so tightly coupled to the interface, surface roughness of the metal, dielectric, or both can significantly reduce the propagation distance of SPP into the PbSe thereby reducing the enhancement in the films. Indeed, Fadakar and colleagues demonstrated through finite element analysis that the attenuation in SPP modes perpendicular to the interface increases with the surface roughness of the host material [8]. Moreover, surface roughness has an effect on the back reflector as well, due to the localized variances in refractive index and layer thickness. Therefore, we developed a procedure to reduce the roughness of our PbSe films.

Nanosphere lithography is a patterning technique that does not require the exposure of an electro- or photosensitive film for patterning. Instead, in this process nanometer-scale polystyrene spheres are deposited onto the substrate by either the Langmuir-Blodgett method, or through spin coating [9-13]. For the reduced roughening

process, the spin coating method described in [10-11] was used. The process starts by mixing 40 mL of methanol (CH_3OH) with 100 µL of Triton X-100 surfactant ($C_{14}H_{22}$-$O(C_2H_4O)_9OH$) to produce a 1:400 solution [10]. 750 µL of 1 mg/mL polystyrene spheres obtained from *ThermoFisher Scientific* and DI water solution were then added to the mixture [14]. The spheres used for nanoroughening were between 300 nm and 350 nm in diameter. The solution was mixed for 10 min by sonication. Si wafers with SiO_2 grown by plasma enhanced chemical vapor deposition (PECVD) were then cleaned using isopropyl alcohol, acetone, and DI water before being dried with N_2. To further reduce surface contaminants and remove any residue from previous cleaning, the substrates were placed in an O_2 plasma cleaner for 10 min. 100 µL of solution was then pipetted and spin coated at a rate of 1500 rpm onto the substrate for 60 seconds. After the solvent had dried, a CF_4 etch was performed on the samples for 200 seconds to roughen the substrate around the spheres. Nanospheres were then removed using a combination of sonication in acetone and methanol for 10 min each, followed by an IPA rinse for the final cleaning.

Figure 90 shows a 5000x SEM image of the polystyrene spheres on the SiO_2 surface after spin coating. Ideally, the nanospheres would be assembled into a continuous periodic monolayer, however over a 7.62 cm diameter substrate this proved difficult, as large areas were left uncovered. Nevertheless, we empirically concluded that this new roughening process was adequate for PbSe adhesion to the substrate. To determine the reduction in roughness in PbSe films deposited after the new nanoroughening process compared to the baseline process, we measured the surface roughness via atomic force microscopy (AFM) [15]. Figure 91 contains surface roughness maps obtained over a 50 µm area of smooth SiO_2 (top-left), baseline roughened SiO_2 (top-right), and nanosphere

lithography roughened (bottom) SiO₂ substrates. Notice the difference in uniformity between the baseline roughened and nanosphere lithography roughened maps. Furthermore, figure 92 shows a five-fold reduction in peak-to-peak roughness from 500 nm peak-to-peak down to 100 nm peak-to-peak when comparing the baseline to the nanosphere roughened films. This reduction in roughness would prove critical to maximizing the enhancement in the PbSe films due to resonant structures.
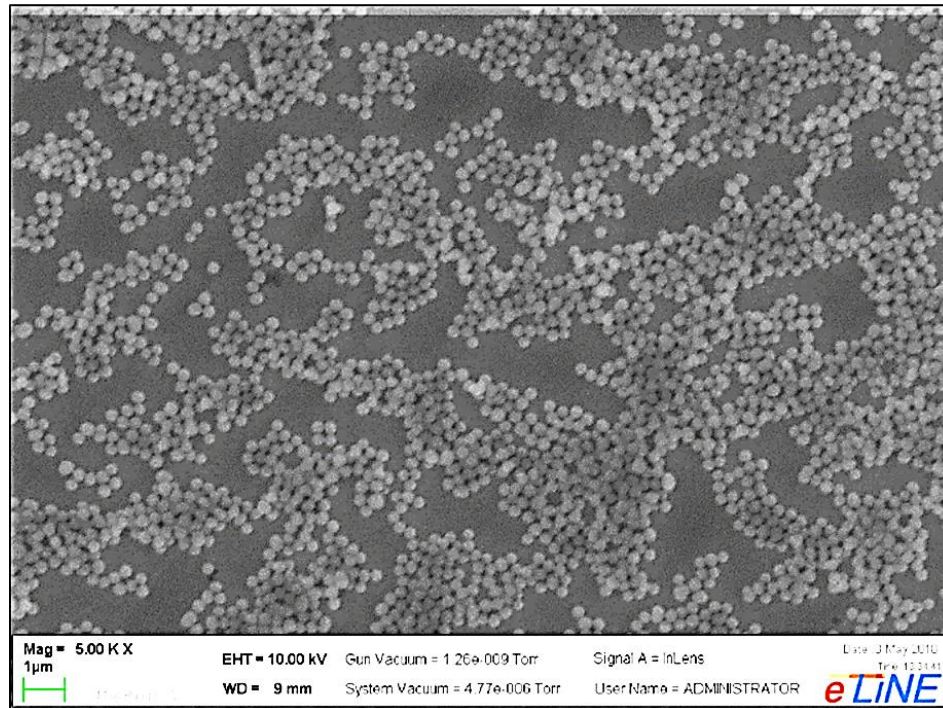
Figure 90. SEM image of SiO₂ surface after polystyrene nanosphere spin coating.

Smooth SiO$_2$ Layer:
Peak-to-Peak Roughness ≈ 10 nm

Baseline SiO$_2$ Layer:
Peak-to-Peak Roughness ≈ 500 nm

Nanosphere Lithography Roughened SiO$_2$ Layer:
Peak-to-Peak Roughness ≈ 100 nm
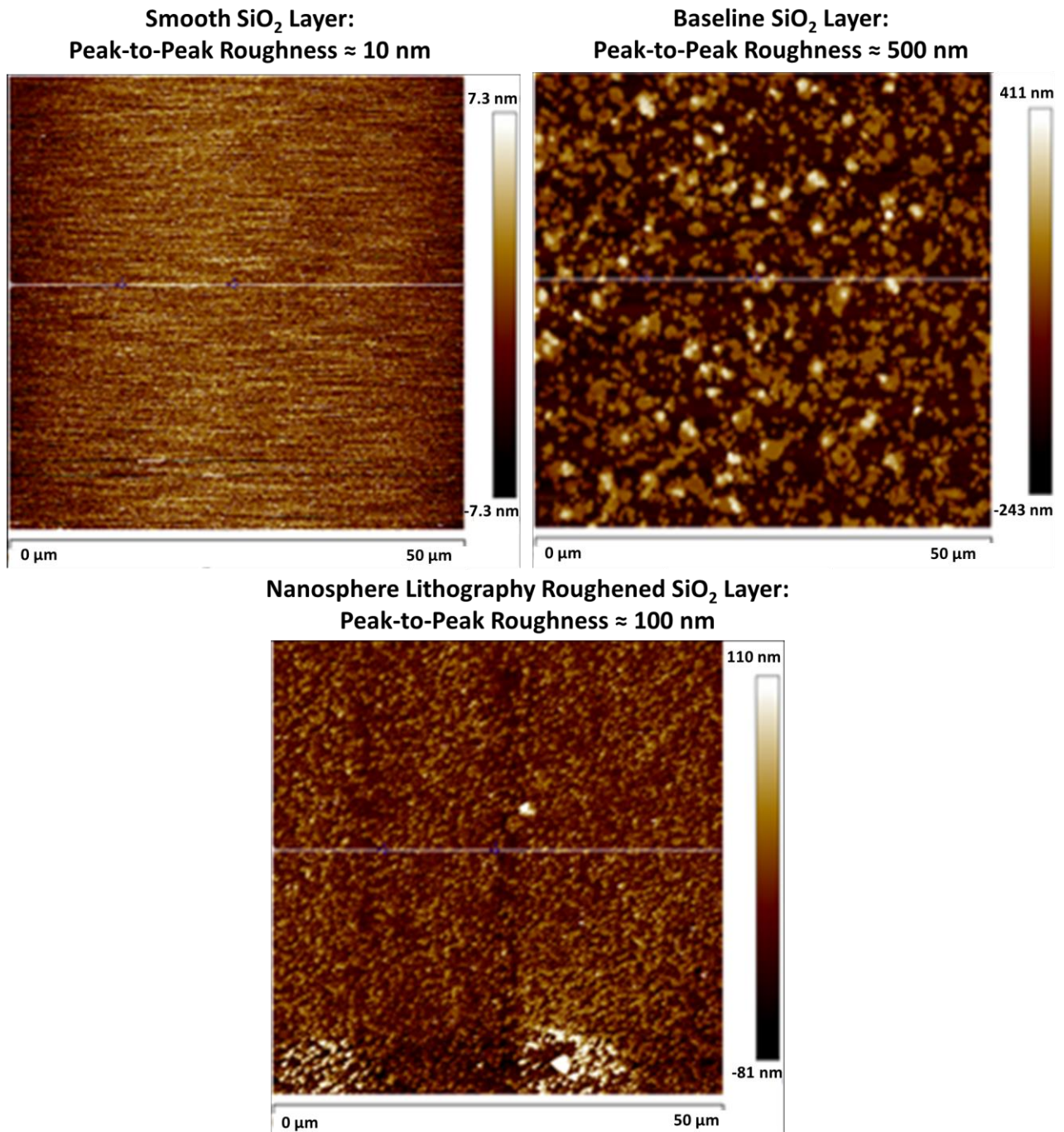
Figure 91. Measured surface roughness maps obtained using AFM of smooth (top-left), baseline roughened (top-right), and nanosphere lithography roughened (bottom) SiO$_2$ on Si substrates.
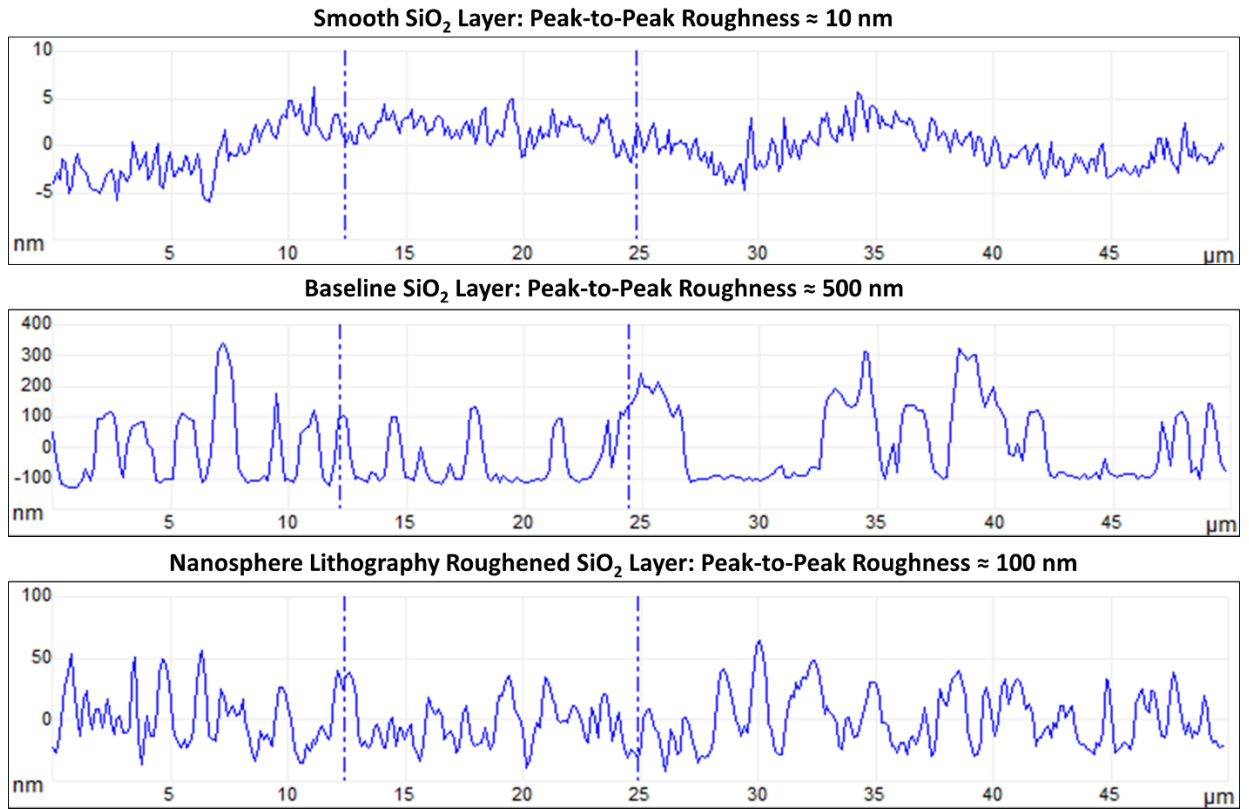
Figure 92. Measured surface profiles obtained using AFM of smooth (top), baseline roughened (middle), and nanosphere lithography roughened (bottom) SiO₂ on Si substrates.

Appendix A References

[1]   Pure Wafer, a WRS Materials Company, "Test Wafers," 2017. [Online].

        Available: https://www.purewafer.com/waferproducts/test. [Accessed Nov. 5,

        2018].

[2]   M. J. Madou, *Fundamentals of Microfabrication: The Science of Miniaturization*,

        Second Edition. CRC Press, 2002.

[3]   S. A. Campbell, *Fabrication Engineering at the Micro- and Nanoscale*, Fourth

        Edition. Oxford University Press, New York, 2013.

[4]   Microchemicals GMBH, "Photoresists," [Online]. Available:

        https://www.microchemicals.com/products/photoresists.html. [Accessed Nov. 5,

        2018].

[5]   Suss MicroTec, "MA/BA6 Mask and Bond Aligner," 2018. [Online]. Available:

        https://www.suss.com/en/products-solutions/mask-aligner/ma-ba-6. [Accessed

        Nov. 5, 2018].

[6]   Microchemicals GMBH, "AZ® 5214 E, [Online]. Available:

        https://www.microchemicals.com/products/photoresists/az_5214_e.html.

        [Accessed Nov. 5, 2018].

[7]   Merick, "AZ 5214 E Photoresist," Merick Performance Materials GmbH.

        [Online]. Available: https://www.microchemicals.com/micro/az_5214e.pdf.

        [Accessed Nov. 5, 2018].

[8]   H. Fadakar, et al. "Effect of surface roughness on propagation of surface plasmon

        polaritons along thin lossy metal films," 19th Iranian Conference on Electrical

        Engineering, 2011.

[9]   Y. Li. *Plasmonic Optics Theory and Applications,* Tutorial Texts in Optical
        Engineering, Vol. TT110. SPIE Press. Billingham, WA., 2017.

[10]   C. L. Cheung, et al. "Fabrication of nanopillars by nanosphere lithography," Barry
        Chin Li Cheung Publications. 4, 2006.

[11]   W. Wu, D. Dey, and O. G. Memis, "Fabrication of Large Area Periodic
        Nanostructures Using Nanosphere Photolithography," Nanoscale Res. Lett. 3,
        2008.

[12]   O. N. Oliveira Jr, "Langumuir-Blodgett Films-Properties and Possible
        Application." Brazilian Journal of Physics, vol. 22, no. 2, 1992.

[13]   L. Chitu, et al. "Modified Langmuir-Blodgett deposition of nanoparticles-
        measurement of 2d to 3D ordered arrays," Measurement Science Review, Vol. 10,
        No. 5, 2010.

[14]   ThermoFisher Scientific, "CML Latex Beads, 4%, 0.3 μm," ThermoFisher, Inc.
        [Online]. Available:
        https://www.thermofisher.com/order/catalog/product/C37237?SID=srch-srp-
        C37237. [Accessed Nov. 5, 2018].

[15]   R. R. L. De Oliveira, "Measurement of the Nanoscale Roughness by Atomic
        Force Microscopy: Basic Principles and Applications," 2012. [Online]. Available:
        http://cdn.intechopen.com/pdfs/33450/InTech-
        Measurement_of_the_nanoscale_roughness_by_atomic_force_microscopy_basic_
        principles_and_applications.pdf. [Accessed Nov. 5, 2018].

Appendix B: Surface Plasmon Resonance Numerical Models

Quasi-static Calculation of the Scattering, Absorption, and Extinction Cross-sections and Q-Factors for Surface Plasmon Resonant Discs

I wrote the following *MATLAB* script to calculate the surface plasmon resonant Q-factors

and cross-sections for oblate spheroids, which was used as a first approximation for disc

calculations [1-3].

```
%Surface Plasmon Resonance of an Oblate Spheroid (Disc)
%Author: Justin Grayer
%Date: 11/05/2018
%This script was used to calculate the scattering, absorption, and
%extinction cross-sections and Q-factors for Surface plasmon resonanct
%discs using the quasi-static method

clear variables; close all;clc;
%Assume a plane wave is polarized along the x-direction
a = (0.5/2); %The disc radius in microns
b = (0.5/2); %The disc radius in microns
c = 0.02/2; %The disc thickness in microns

%Define the effective index of refractoin for the disc host material
n_eff = 5.07; %Index of Refraction of PbSe

rasp = a/c; %Calculate the disc aspect ratio
ecc =sqrt(1-1/rasp^2); %Calculate the disc eccentricity
g_ecc = sqrt(1-ecc^2)/ecc; %Simplificaiton constant for calculating

%Calculate shape factor in x-direction
Sx = (g_ecc/(2*ecc^2))*((pi/2)-atan(g_ecc))-(g_ecc^2/2);
%Calculate shape factor in y-direction
Sy = Sx;
%Calculate shape factor in z-direction
Sz = (1-Sx)/2;

%Loop through all wavelengths of interest (From 3 - 5.5 microns as shown)

for ii = 1:1000 %Number of iteration steps
   lambda(ii) = 2.99749+0.00251*ii; %Wavelength in microns

   %Complex index of refraction loaded from the metal functions entitiled
```

```
%"Drude(metal)" for the current wavelength. Au shown.
m_Au(ii) = DrudeAu(lambda(ii)); %Index of refraction of the metal
eps_m_Au(ii) = m_Au(ii)^2; %Complex permittivity of the metal

%Calculate the polarizability in the x-, y-, and z-directions
alpha_x(ii) = (4*pi*a*b*c*(eps_m_Au(ii)-n_eff^2))/...
   (3*(n_eff^2+Sx*(eps_m_Au(ii)-n_eff^2)));
alpha_y(ii) = (4*pi*a*b*c*(eps_m_Au(ii)-n_eff^2))/...
   (3*(n_eff^2+Sy*(eps_m_Au(ii)-n_eff^2)));
alpha_z(ii) = (4*pi*a*b*c*(eps_m_Au(ii)-n_eff^2))/...
   (3*(n_eff^2+Sz*(eps_m_Au(ii)-n_eff^2)));

%Define the wavenumber
k(ii) = n_eff^2*2*pi/(lambda(ii));

%Calculate the scatterinng, absorption, and extinction Q factors in
%the x-direction. Can be expanded to y- and z- directions by
%replacing the complex polarizability.
Qscat_x(ii) = (k(ii)^4*abs(alpha_x(ii))^2/(6*pi*a*b));
Qabs_x(ii)= (k(ii)*imag(alpha_x(ii))/(pi*a*b));
Qext_x(ii) = Qscat_x(ii)+Qabs_x(ii);

%Calculate the scattering, absorption, and extinction cross-sections.
%Can be expanded to y- and z- directioins by replace the
%polarizability.
Cscat_x(ii) = (k(ii)^4*abs(alpha_x(ii))^2/(6));
Cabs_x(ii)= (k(ii)*imag(alpha_x(ii)));
Cext_x(ii) = Cscat_x(ii)+Cabs_x(ii);
end

%Plot the wavelength dependence of the extinction
%cross-section in units of cm^2.
figure
plot(lambda, Cext_x*1e-8, 'LineWidth',2)
title(['Normalized Extinction Cross-Section for a Single Pt Nanodisc(Aspect = ',
num2str(rasp,3),') at PbSe/SiO_2 Interface'])
xlabel('Wavelength (\mum)')
ylabel('Cross-Section (cm^2)')
set(gca,'FontSize',16)
```

Calculation of the Dispersion Relations of Drude Metals

I wrote the following *MATLAB* script to calculate the dispersion relations of the metals

examined in this investigation. These functions were derived from Rakic's treatment [4].

Silver (Ag)

```
%Calculate the dispersion relations of silver
%Justin Grayer
%11/05/2018
%Takes in wavelength ("lambda") in eV and returns complex index of
%refraction.
function [n] = DrudeAg(lambda)
%Oscillator Strength [eV]
f = [0.845, 0.065, 0.124, 0.011, 0.840, 5.646]; %[eV]
% Damping constant per oscillator[eV]
gamma = [0.048, 3.886,0.452,0.065,0.916,2.419];
%Oscillator Frequency
ww = [0.816,4.481,8.185,9.083,20.29]; %[eV]
%Plasma Frequency [eV]
wp = 9.01;
% Energy of input wavelength [eV]
w = 1.24/lambda;
%Plasm frequency for intraband transitions[eV]
omegap = f(1)^(1/2)*wp;
%Calculate metal permittivity for given wavelength
for ii = 0:5
   if ii == 0
      eps = 1-omegap^2/(w*(w+1*1i*gamma(ii+1)));
   else
      eps = eps+f(ii+1)*wp^2/(((ww(ii)^2-w^2)-1i*w*gamma(ii+1));
   end
end
%Returns the complex index of refraction of Ag for given wavelength
n = sqrt(eps);
```

Aluminum (Al)

```
%Calculate the dispersion relations of Aluminum
%Justin Grayer
%11/05/2018
%Takes in wavelength ("lambda") in eV and returns complex index of
%refraction.
function [n] = DrudeAl(lambda)
%Oscillator Strength [eV]
f = [0.523, 0.227, 0.050, 0.166, 0.030];
% Damping constant per oscillator[eV]
gamma = [0.047, 0.333, 0.312, 1.351, 3.382];
%Oscillator Frequency [eV]
ww = [0.162, 1.544, 1.808, 3.473];
%Plasma Frequency [eV]
```

```matlab
wp = 14.98; %[eV]
% Energy of input wavelength [eV]
w = 1.24/lambda; %[eV]
%Plasm frequency for intraband transitions[eV]
omegap = f(1)^(1/2)*wp;
%Calculate metal permittivity for given wavelength
for ii = 0:4
   if ii == 0
      eps = 1-omegap^2/(w*(w+1*1i*gamma(ii+1)));
   else
      eps = eps+f(ii+1)*wp^2/((ww(ii)^2-w^2)-1i*w*gamma(ii+1));
   end
end
%Returns the complex index of refraction of Al for given wavelength
n = sqrt(eps);
```

Gold (Au)

```matlab
%Calculate the dispersion relations of Gold
%Justin Grayer
%11/05/2018
%Takes in wavelength ("lambda") in eV and returns complex index of
%refraction.
function [n] = DrudeAu(lambda)
%Oscillator Strength [eV]
f = [0.024, 0.010, 0.071, 0.601, 4.384];
% Damping constant per oscillator[eV]
gamma = [0.241, 0.345, 0.870, 2.494, 2.214];
%Oscillator Frequency
ww = [0.415, 0.830, 2.969, 4.304, 13.32];
%Plasma Frequency [eV]
wp = 9.03;
% Energy of input wavelength [eV]
w = 1.24/lambda;
%Calculate metal permittivity for given wavelength
for ii = 0:5
   if ii == 0
      eps = 1-(0.760*wp^2/(w^2+1i*0.053*w));
   else
      eps=eps+f(ii)*wp^2/(ww(ii)^2-w^2-1i*w*gamma(ii));
   end
end
%Returns the complex index of refraction of Au for given wavelength
n = sqrt(eps);
```

Nickel (Ni)

```
%Calculate the dispersion relations of nickel
%Justin Grayer
%11/05/2018
%Takes in wavelength ("lambda") in eV and returns complex index of
%refraction.
function [n] = DrudeNi(lambda)
%Oscillator Strength [eV]
f = [0.096, 0.1, 0.135, 0.106, 0.729];
% Damping constant per oscillator[eV]
gamma = [0.048, 4.511, 1.334, 2.178, 6.292];
%Oscillator Frequency
ww = [0.174, 0.582, 1.597, 6.089];
%Plasma Frequency [eV]
wp = 15.92;
% Energy of input wavelength [eV]
w = 1.24/lambda;
%Plasma frequency for intraband transitions[eV]
omegap = f(1)^(1/2)*wp;
%Calculate metal permittivity for given wavelength
for ii = 0:4
   if ii == 0
      eps = 1-omegap^2/(w*(w+1*1i*gamma(ii+1)));
   else
      eps = eps+f(ii+1)*wp^2/(((ww(ii)^2-w^2)-1i*w*gamma(ii+1));
   end
end
%Returns the complex index of refraction of Ni for given wavelength
n = sqrt(eps);
```

Palladium (Pd)

```
%Calculate the dispersion relations of palladium
%Justin Grayer
%11/05/2018
%Takes in wavelength ("lambda") in eV and returns complex index of
%refraction.
function [n] = DrudePd(lambda)
%Oscillator Strength [eV]
f = [0.330, 0.649, 0.121, 0.638, 0.453];
% Damping constant per oscillator[eV]
gamma = [0.008, 2.950, 0.555, 4.621, 3.236];
%Oscillator Frequency [eV]
ww = [0.336, 0.501, 1.659, 5.715];
```

```
%Plasma Frequency [eV]
wp = 9.72;
% Energy of input wavelength [eV]
w = 1.24/lambda;
%Plasma frequency for intraband transitions[eV]
omegap = f(1)^(1/2)*wp;
%Calculate metal permittivity for given wavelength
for ii = 0:4
   if ii == 0
      eps = 1-omegap^2/(w*(w+1*1i*gamma(ii+1)));
   else
      eps = eps+f(ii+1)*wp^2/(((ww(ii)^2-w^2)-1i*w*gamma(ii+1));
   end
end
%Returns the complex index of refraction of Pd for given wavelength
n = sqrt(eps);
```

Platinum (Pt)

```
%Calculate the dispersion relations of platinum
%Justin Grayer
%11/05/2018
%Takes in wavelength ("lambda") in eV and returns complex index of
%refraction.
function [n] = DrudePt(lambda)
%Oscillator Strength [eV]
f = [0.333, 0.191, 0.659, 0.547, 3.576];
% Damping constant per oscillator[eV]
gamma = [0.080, 0.517, 1.838, 3.668, 8.517];
%Oscillator Frequency [eV]
ww = [0.780, 1.314, 3.141, 9.249];
%Plasma Frequency [eV]
wp = 9.59;
% Energy of input wavelength [eV]
w = 1.24./lambda;
%Plasma frequency for intraband transitions[eV]
omegaP = f(1)^(0.5)*wp;
%Calculate metal permittivity for given wavelength
for ii = 0:4
   if ii == 0
      eps = 1-omegaP^2/(w*(w+1i*gamma(ii+1)));
   else
      eps=eps+f(ii+1)*wp^2/(ww(ii)^2-w^2-1i*w*gamma(ii+1));
   end
end
%Returns the complex index of refraction of Pt for given wavelength
```

```
n = sqrt(eps);
```

Surface Plasmon Propagation Distance, Phase Velocity, and Lifetime

I wrote the following M*ATLAB* script to calculate the surface plasmon propagation

distance, phase velocity, and lifetime for idealized metals within PbSe [1].

```
%Surface plasmon parameters for metals
%Justin Grayer
%11/05/2018
%Calculates the surface plasmon propgation distance, phase velocity, and
%lifetime for a given metal.


clear variables; close all; clc;


%Speed of light (m/s)
c = 3e8;
%Index of effective refractive index of host material(PbSe shown)
n_eff = 5.07;
%Calculate prermittivity of host materials
eps_eff = n_eff^2;


%Loop through all wavelengths of interest (From 2 - 6 microns shown)
for ii=1:40
    %Define wavelength (microns)
    lambda(ii,1) = 1.99+0.1*ii;
    %Define frequency (Hz)
    omega(ii,1) = 2*pi*c/lambda(ii,1);
    %Define wavenumber(microns^-1)
    k0(ii,1) = 2*pi/lambda(ii,1);
```

%Load in complex index of refraction of the metal (Pt shown)

m_metal_Pt(ii,1) = DrudePt(lambda(ii,1));

%Calculate complex permittivity

eps_m_Pt(ii,1) = m_metal_Pt(ii,1)^2;

%Calculate surface plasmon propgation distance (microns)

dsp_Pt(ii,1) = 2*real(eps_m_Pt(ii,1))^2/(eps_eff^(3/2)*imag(eps_m_Pt(ii,1))*k0(ii,1));

%Calculate surface plasmon phase velocity (microns/s)

Vsp_Pt(ii,1) = (c/n_eff)*(1-(eps_eff/(2*real(eps_m_Pt(ii,1)))));

%Calculate surface plasmon lifetime (s)

tau_sp_Pt(ii,1) = 2*real(eps_m_Pt(ii,1))^2/(omega(ii,1)*eps_eff*imag(eps_m_Pt(ii,1)));

end

%Plot surface plasmon propgation distance

figure

subplot(1,3,1)

hold on

plot(lambda, dsp_Pt, 'o','MarkerEdge', [0 0.5 0], 'MarkerFace',[1 1 1], 'LineWidth', 2.5)

title('SP Propagation Distance')

xlabel('Wavelength \mum')

ylabel('Surface Plasmon Propagation Distance (\mum)')

set(gca,'FontSize',16)

hold off

%Plot surface plasmon phase velocity

subplot(1,3,2)

hold on

plot(lambda, Vsp_Pt/c, 'o', 'MarkerEdge', [0 0.5 0], 'MarkerFace',[1 1 1],'LineWidth', 2.5)

```matlab
title('SP Relative Phase Velocity')

xlabel('Wavelength \mum')

ylabel('Relative Surface Plasmon Phase Velocity (V_s_p/c)')

set(gca,'FontSize',16)

hold off


%Plot surface plasmon lifetime

subplot(1,3,3)

hold on

plot(lambda, tau_sp_Pt/1e-9, 'o', 'MarkerEdge', [0 0.5 0], 'MarkerFace',[1 1
1],'LineWidth', 2.5)

title('SP Lifetime')

xlabel('Wavelength \mum')

ylabel('Surface Plasmon Lifetime (ns)')

set(gca,'FontSize',16)

hold off
```

Appendix B References

[1]   D. Sarid and W. Challner, *Modern Introduction to Surface Plasmons: Theory, Mathematical Modeling, and Application*, New York, NY: Cambridge University Press, 2010.

[2]   A. A. Toropov and T. V. Shubina, *Plasmonic Effects in Metal-Semiconductor Nanostructures*, Great Clarendon, Oxford, United Kingdom: Oxford University Press, 2015.

[3]   A. Battaglia, et al. "Light scattering by Gaussian particles: Rayleigh-ellipsoid approximation," J. of Quantitative Spectroscopy and Radiative Transfer, 63, 1999.

[4]   Rakic´, et al. "Optical Properties of Metallic Films for Vertical Cavity Optoelectronic Devices," Applied Optics, Vol. 37, No. 22, 1998.

Appendix C: Infrared Sensor System Considerations

Long range imaging systems have become an important tool for situational awareness and detailed examination of the surrounding environment. Examples of their use include advanced threat warning, surveillance and reconnaissance, and sensing of chemical and biological agents. Electro-optical and infrared systems (EO/IR) cover five major bands of the electromagnetic spectrum. These include visible (0.4 µm - 0.7 µm), near-infrared (0.7 µm – 1 µm), short-wave infrared (SWIR; 1 µm – 3 µm), mid-wave infrared (MWIR; 3 µm – 6 µm), and long-wave infrared (LWIR; 6 µm – 14 µm) [1]. Imaging systems are designed for specific applications, with the primary design choice being the spectral band over which the system will operate. For instance, consider a commercial camera intended for consumer photography. This system would be designed for the visible regime, in which the light from either the sun or an artificial source would be reflected off of a subject into the imaging optics and focused onto the detector. In contrast, an infrared system, specifically those designed for MWIR or LWIR, are designed to collect the emitted electromagnetic radiation from the subject or scene. This emitted radiation is determined by the surface temperature of the subject, and is present in all objects with temperatures above absolute zero. Note that due to its temperature dependent nature, infrared radiation is typically associated with thermal radiation.

The examples above show an important distinction between the visible spectrum, associated with the photopic response of the human eye, and the infrared spectrum. Typically visible systems collect and image the reflected light off of a subject, while infrared systems primarily collect thermally emitted radiation. There is another important difference between the two bands, which is the attenuation due to the atmosphere. When

considering atmospheric effects, the aforementioned five bands of interest are divided

into what are referred to as atmospheric windows [1, 2-3]. Imaging systems are designed

within these windows to mitigate the attenuation from CO_2, moisture, and other

particulates within the atmosphere. Figure 93 shows the atmospheric transmission over a

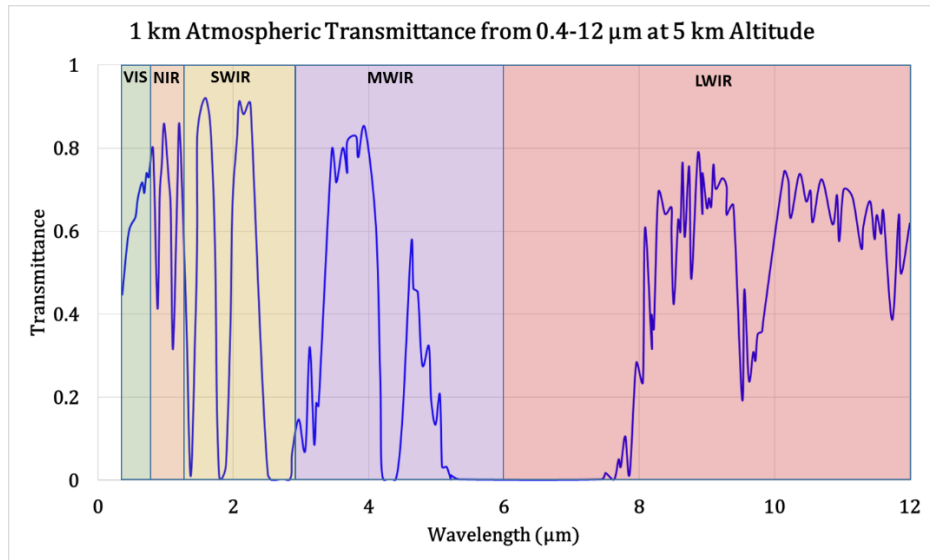1 km horizontal range at an altitude of 5 km [4].

Figure 93. Transmission spectra from visible to LWIR regions of the electromagnetic spectrum over a 1 km range at an altitude of 5 km [4]. Each spectral region contains atmospheric windows through which electromagnetic radiation can propagate without substantial absorption from atmospheric particulates.

For example, in figure 93 the transmission in the visible spectrum is relatively

high, with greater than 70% of photons making it through the 1 km distance. However, in

the SWIR, MWIR, and LWIR bands there are several drops in transmission due to

atmospheric absorption. For systems primarily concerned with sensing the thermal

emission of objects within a scene, the MWIR and LWIR regions are of primary interest.

For systems sensitive to these regions, the solar background is relatively low, and can

even be absent if the system is intended for night-time operation. Systems employing the

212

MWIR and LWIR regimes are typically concerned with what is known as black body radiation.

Black Body Radiation

A black body is an idealization of a perfect emitter and absorber, in which the spectral band of emission or absorption is related to the temperature of the object. The amount of thermal radiation emitted by a real object can be quantified through Planck's law, which relates the spectral emittance, with units of $W/m^2sr\mu m$, of an object to its temperature and emitted wavelength by equation D.1,

$$M(\lambda, T) = \epsilon(\lambda) \frac{c_1}{\lambda^5} \frac{1}{exp\left(\frac{c_2}{\lambda T}\right) - 1} \tag{D.1}$$

where c_1 is a constant with a value of 3.7418 x 10^8 W-μm^4/m^2, c_2 is another constant with a value of 1.4388 x 10^4 μm-K, λ is the wavelength in μm, and T is the temperature in K [1-2]. The emissivity ϵ is a measure of how well an object emits radiation, where an ϵ equal to 1 represents a perfect black body over all wavelengths. Another important relationship that can be derived from Planck's law is Wien's law of displacement in which the peak wavelength of a thermal emitter is related to the temperature of that emitter by equation D.2.

$$\lambda_{peak} \cong \frac{2898 \ \mu m \cdot K}{T} \tag{D.2}$$

As an example, consider the sun which has an average surface temperature of 5778 K. The peak wavelength emitted by the sun is 502 nm, which is in the green portion of the visible spectrum. For infrared applications, a 300 K blackbody, the spectrum of which is shown in figure 94, is often considered because it approximates the background emission

at room temperature. With a peak wavelength of 9.8 µm, the background emission is significant at 300 K. Even in the MWIR regime, where the 300 K emission falls off, the background can overwhelm or degrade the signal of interest. It is this background radiation that limits the performance of infrared detectors, and necessitates the need for a cooling element within the sensing system.
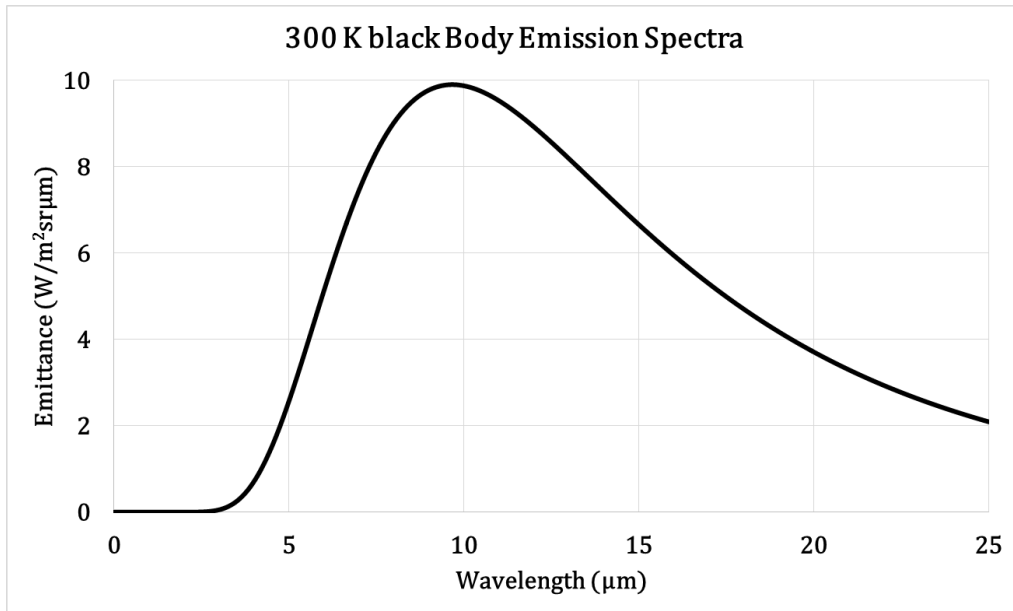

Figure 94. The 300 K black body emission spectrum calculated using Plank's law. Thought the peak of the spectrum is located at 9.8 µm, there is appreciable emission in the MWIR regime which typically drives the need for a cooling element in infrared sensing systems.

Modern Infrared Imaging Systems

An infrared imaging system consists of a receiver, detector, and signal processing electronics [1-3]. The optical receiver includes elements such as a turret for pointing at the subject or scene of interest, telescope optics to transfer and focus the photons from the scene to the detector, and various optomechanical assemblies. The optical detector includes the light sensitive material, detector cooling assembly, and read-out integrated circuit (ROIC). The signal processing electronics are closely tied with the ROIC, and can

214

include analogue-to-digital conversion, image and digital signal processing, and data interpretation. A block diagram representation of the photon flow from the scene through the imaging system is shown in figure 95. Photons are emitted from the scene, and transmitted to the receiver where some may be absorbed by compounds in the atmosphere. The photons are then further attenuated as they transmit through and are focused by the telescope, which usually consists of both reflective and refractive optics. Photons are imaged onto the detector, which in modern imaging systems is a focal plane array consisting of thousands or even millions of detector elements called pixels.
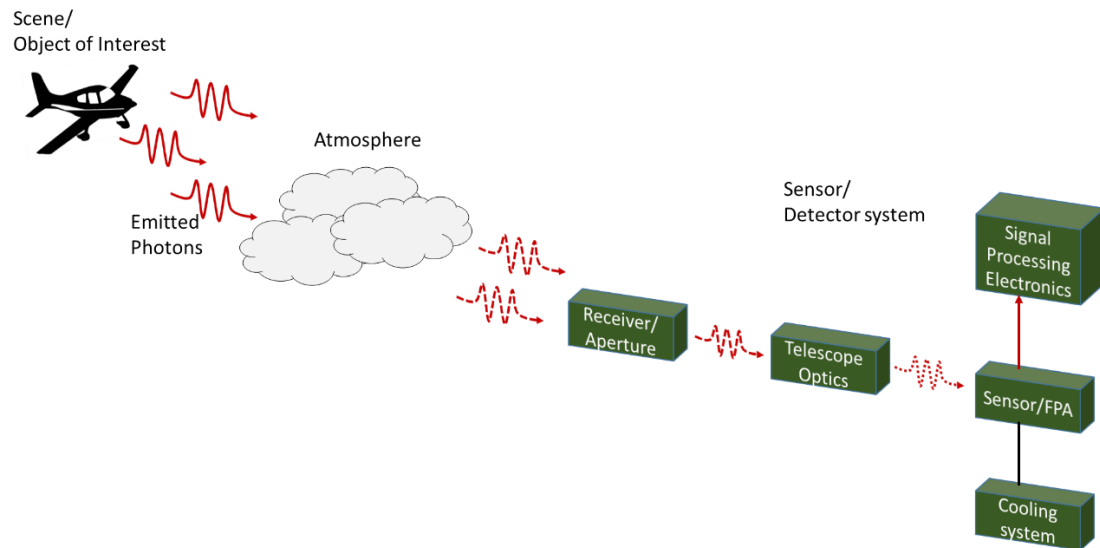
Figure 95. Block diagram showing emitted photons from an object of interest as they transmit through the atmosphere into a long-range sensing system. Photons are attenuated by atmospheric particulates, as well as the optical elements of the sensing system.

The sensitivity of a detector element starts with the material of which it is made. For instance, in the visible spectrum materials like mercury cadmium telluride (HgCdTe), cadmium sulfide (CdS), and Si are utilized as detector materials [5]. In the SWIR region HgCdTe, indium gallium arsenide (InGaAs), and lead sulfide (PbS) are utilized [2, 7]. For the MWIR band HgCdTe, indium antimonide (InSb), and lead selenide (PbSe) are

popular materials [5, 7], and in the LWIR region HgCdTe, quantum well infrared photodetectors (QWIP), and vanadium oxide (VOx) are used [8]. All of the aforementioned materials, regardless of the spectral band, are semiconductors, which are governed by the composition and quantum mechanical properties of the material [3, 9, 10-12].

Appendix C References

[1]   J. C. Leachtenauer, and R. G. Driggers, *Surveillance and reconnaissance imaging systems: Modeling and Performance Prediction*. Norwood, MA: Artech House, Inc, 2004.

[2]   K. Kasunic, *Optical Systems Engineering*. McGraw-Hill Education, 2011.

[3]   C. J. Willers, *Electro-Optical Systems Analysis and Design*, Bellingham, WA: SPIE Press, 2013.

[4]   Spectral Sciences, Inc. [online] Available: http://modtran.spectral.com/modtran_home#plot. [Accessed Sept. 11, 2018]

[5]   P. R. Norton, "Photodetectors," in *McGraw-Hill's Handbook of Optics,* 3rd ed., Vol. 2, New York: McGraw-Hill, 2010, pp. 24.3-24.100.

[6]   E. Hergert, "Detectors: Guideposts on the Road to Selection," in *the Photonics Directory*, 5nd Ed. Laurin Publishing, 2006.

[7]   R. A. Smith, "Detectors for Ultraviolet, Visible, and Infrared Radiation," Applied Optics, Vol. 4, No. 6, 1965

[8]   A. Rogalski, M. Kopytko, and P. Martyniuk, *Antimonide-based Infrared Detectors: A New Perspective*, Bellingham, WA: SPIE Press, 2018.

[9]   D. A. Neamen, *Semiconductor Physics and Devices: Basic Principles, 3rd Ed*, New York, NY: McGraw Hill, 2003.

[10]   R. A. Serway, C. J. Moses, and C. A. Moyer, "The Solid State," in *Modern Physics*, 3rd ed, Belmont, CA: Borrks/Cole-Thomson Learning, 2005.

[11]   C. Kittel, *Introduction to Solid State Physics*, Hoboken, NJ: John Wiley and Sons, Inc. 2005.

[12]   M. P. Marder. *Condensed Matter Physics,* 2nd ed. Hoboken, NJ: John Wiley and

Sons, Inc. 2010.

VITA

Justin S. Grayer was born to Carla and Carl Grayer in Columbia, Missouri. Upon completing secondary education at Rock Bridge High School, he attended Indian Hills Community College in Ottumwa, Iowa. There, he studied Laser Electro-Optics Technology, earning an associate of applied science (A.A.S) degree. Upon completion of his degree, Justin was recruited by Raytheon Space and Airborne Systems in El Segundo, CA as a laser technician. After working his way up to Senior Laser Technician, he began his studies again by taking courses on physics as a part-time student at Santa Monica College. He would eventually move back to Columbia, Missouri to pursue an undergraduate degree in physics from the University of Missouri (MU).

Shortly after the start of his first semester at MU, Justin joined Dr. Gavin King's single-molecule biophysics group. There, he was an integral team member in the setup, alignment, and test of the second generation ultra-stable atomic force microscope. Justin graduated with honors, earning a B.S. degree in Physics in 2012. He remained in Dr. King's group, and earned a M.S. Physics in 2013. Following this achievement, Justin transitioned to Dr. Gregory Triplett's group in the MU department of Electrical and Computer Engineering. There, he would study and grow quantum cascade lasers by molecular beam epitaxy.

Justin earned his second Master's degree, this time in engineering, in the summer of 2014. He started a position as a Senior Systems Engineer in the EO/IR Design Department at Raytheon Space and Airborne Systems in El Segundo, CA shortly after graduating. While at Raytheon, he worked on projects such as star trackers, high energy

laser, and precision photonic oscillators. While working on these projects he was co-inventor on three invention disclosures related to holographic imaging systems for wave front sensing and correction, which as of this writing are under review by the United States patent office.

Also while at Raytheon, Justin pursued a professional certificate in optical engineering from University of California-Irvine. He continued to do so when he took a position as a Senior Systems Engineer at Northrop Grumman in Rolling Meadows, IL early in 2016, and would eventually earn the certificate in optical engineering at the beginning of 2017. Justin's projects at Northrop Grumman have included the characterization and test of 3D Geiger-mode APD cameras, field testing of laser illuminated 3D linear mode APD cameras, and systems design work for the LITENING program area. In 2017 he transitioned to the Advanced Concepts group and the role of Physicist. Since then, he has primarily been focused on infrared detectors and infrared countermeasure systems.

While working at Northrop Grumman, Justin re-entered the PhD program in the Electrical and Computer Engineering Department at the University of Missouri under Dr. Randy Curry. His PhD research was focused on the design and incorporation of optically resonant structures into high operating temperature PbSe photoconductors for enhanced mid-infrared sensitivity. These structures included surface plasmon resonant structures, interference cavities, and anti-reflection coatings. His work was supported by the Defense Advanced Research Projects Agency (DARPA) and the Air Force Research Laboratory (AFRL) as part of the Wafer-scale Infrared Detectors (WIRED) program. Moreover, in addition to his WIRED teammates, Justin has collaborated with Dr. Mool Gupta's and

Avik Ghosh's group at the University of Virginia, as well as Philippe Guyot-Sionnest's group at the University of Chicago. As of this writing, Justin continues to work as a Physicist at Northrop Grumman, where his focus and passion are on electro-optical systems for infrared countermeasures. Justin is also an adjunct professor in the Lasers, Photonics, and Optics department at the College of Lake County in Grayslake, IL, where he teaches aspiring students the skills they need to either become laser technicians or pursue higher educational goals.